Novel Routes To Nanodispersed Semiconductors

A Thesis Presented by

Mark A. Green

In partial fulfilment of the requirements for the awards of the degree of

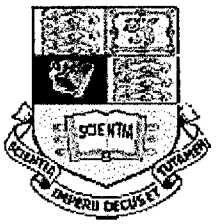
Doctor of Philosophy

of the

University of London

and the

Diploma of the Imperial College



Department of Chemistry,

Imperial College of Science, Technology and Medicine,

London SW7 2AY.

July 1999.

Abstract

Novel synthetic routes to nanodispersed compound semiconductors using organometallic precursors have been developed. The quantum dots have been studied by optical absorption spectroscopy, photoluminescence spectroscopy, transmission electron microscopy, high resolution transmission electron microscopy, infra red spectroscopy and nuclear magnetic resonance. Precursors were studied by NMR, single crystal analysis, microanalysis, mass spectrometry and high temperature GC-MS.

Polar Lewis base solvents such as tri-*n*-octylphosphine oxide and 4-ethylpyridine were utilised as both passivating agent and dispersing medium. In the search for new solvent systems and passivating agents, an investigation was also made into the use of different oxide Lewis Bases as reaction solvents and capping agents. Existing routes using metal alkyls and silylated precursors in hot TOPO were improved by substituting the metal alkyl with a metal alkyl adduct. Cadmium monothiocarbamate and a related precursor, cadmium thioacetate were investigated as possible single source precursors to nanometer sized CdS.

The thermolysis of single source precursors in a Lewis base co-ordinating solvent (alkylpyridine) has been investigated, including studies of decomposition routes and mechanisms, with quantum dots of Cd_3P_2, Zn_3P_2, InP and GaP being prepared. The synthesis of InAs using the metal chloride and an arsenic precursor in an alkylpyridine has also been developed. A simple method for the organisation of III-V materials into glass-like aggregates and thin films has been described.

Contents

Title page 1

Abstract 2

Contents 3

List of tables 8

List of figures 10

Abbreviations and symbols 18

Acknowledgements 21

Chapter 1 - Introduction 24

1.1 Introduction 25

1.2 LCAO and band theory 27

1.3 Band structures 30

1.4 Nanodispersed semiconductors 35

1.5 Absorption, luminescence and oscillator strength 38

1.6 Methods of preparation 45

1.7 TOPO capped nanoparticles 45

1.8 General organometallic routes 52

1.9 Colloidal routes 54

1.10 Synthesis in confined matrices 55

1.11 Nano-heterostructures 58

1.12 Nanocrystal processing 60

1.13 Applications and conclusions 61

Chapter 2 - Synthesis of nanodispersed II-VI compounds 68

2.1 Introduction 69

2.2 Synthetic methodology 70

2.3 Optical properties of Q-CdSe and Q-CdS 74

2.4 Luminescence of Q-CdSe and Q-CdS 78

2.5 Structural properties of Q-CdSe and Q-CdS 82

2.6 Different solvent systems 93

2.7 Conclusions 97

Chapter 3 - Synthesis of nanodispersed II_3-V_2 compounds 98

3.1 Introduction 99

3.2 Synthetic methodology 102

3.3 Potential precursors for Cd_3P_2 103

3.4 Thermolysis of diorganophosphides 105

3.5 Optical properties of Q-Cd_3P_2 112

3.6 Luminescence of Q-Cd_3P_2 117

3.7 Structural characterisation of Q-Cd_3P_2 122

3.8 Potential precursors for Zn_3P_2 136

3.9 Optical properties of Q-Zn_3P_2 137

3.10 Luminescence of Q-Zn_3P_2 140

3.11 Structural characterisation of Q-Zn_3P_2 143

3.12 Conclusions 154

Chapter 4 - Synthesis of nanodispersed III-V compounds 156

4.1 Introduction 157

4.2 Synthetic methodology 158

4.3 Optical properties of Q-InAs 160

4.4 Structural characterisation of Q-InAs 164

4.5 Manipulation of Q-InAs 167

4.6 Thermolysis of gallium and indium diorganophosphides 170

4.7 Optical properties of Q-InP 174

4.8 Structural characterisation of Q-InP 177

4.9 Optical properties of Q-GaP 181

4.10 Structural characterisation of Q-GaP 184

4.11 Conclusions 188

Chapter 5 - Experimental 189

5.1 Chemicals 190

5.1 Manipulation of air sensitive compounds 190

5.2 Solvents 191

5.3 Synthesis of CdS precursors 192

5.4.1 Bis(N,N-diethyl)monothiocarbamato-cadmium(II) 192

5.4.2 Bis(N,N-diethyl)dithiocarbamato-cadmium(II) 192

5.4.3 Cadmium thioacetate·TMEDA adduct 193

5.4.4 dimethylcadmium·triethylamine adduct 193

5.5 Synthesis of diorganophosphide single molecular precursors 194

5.5.1 $[MeCdP^tBu_2]_3$ 194

5.5.2 $[MeCdPR_2]_3$, R = Cp, Cy, Ph 195

5.5.3 $In(P^tBu_2)_3$ and $Ga(P^tBu_2)_3$ 197

5.6 Synthesis of nanoparticulates in TOPO 197

5.6.1 Cd_3P_2/TOPO 197

5.6.2 Zn_3P_2/TOPO 198

5.6.3 CdS and CdSe/TOPO and DMSO 199

5.7 Synthesis of nanoparticulates in 4-ethylpyridine 200

5.7.1 Cd_3P_2/4-etpy 200

5.7.2 Zn_3P_2/4-etpy 200

5.7.3 InP and GaP/4-etpy 201

5.7.4 InAs/4-etpy 201

5.8 Size fractionation 202

5.9 Manipulation of 4-etpy capped nanoparticulates into glasses and thin films 202

5.10 Instrumentation and physical measurements 203

5.10.1 UV (electronic) spectroscopy 203

5.10.2 Photoluminescence spectroscopy 203

5.10.3 Infra-red spectroscopy 204

5.10.4 Mass spectrometry 204

5.10.5 NMR spectroscopy 204

5.10.6 X-ray powder diffraction 205

5.10.7 Electron microscopy (HRTEM, TEM) 205

5.10.8 Atomic force microscopy (AFM) 205

5.10.9 Elemental analysis 206

5.10.10 Inductively coupled plasma atomic emission spectrophotometry (ICPAES) 206

5.10.11 Thermogravimetric analysis (TGA) and gas chromatography mass-spectrometry analysis (GC-MS) 206

5.10.12 X-ray single crystal analysis 207

Appendix 1 - Selected information on studied systems 208

Appendix 2 - Single crystal analysis of $[MeCdP^tBu_2]_3$ 211

Appendix 3 - Single crystal analysis of *mer*$[In(4\text{-ethylpyridine})_3Cl_3]$ 217

References 223

List of tables

2.1 Powder XRD data for nanocrystalline CdS and comparison to the literature 83

2.2 Solution state and solid state NMR data for Q-CdS prepared by various methods 91

2.3 Solution state and solid state NMR data for Q-CdSe prepared by various methods 92

3.1 Exciton diameters as calculated from equation 1.4 99

3.2 Selected major peaks from GC-MS studies of $[MeCdP^tBu_2]_3$ at two different temperatures 110

3.3 Comparison of synthesis temperature, band edge and emission maxima. for Cd_3P_2 capped with TOPO 119

3.4 Comparison of optical properties of different fractions of Cd_3P_2 121

3.5 Diameter as a function of band edge, with predicted and actual diameters for some fractions of Q-Cd_3P_2 129

3.6 Selected IR data on 4-ethylpyridine and 4-ethylpyridine capped Cd_3P_2 131

3.7 Solution and solid state ^{31}P NMR data for TOPO capped Q-Cd_3P_2 134

3.8 Solution and solid state ^{31}P NMR data for 4-ethylpyridine capped Q-Cd_3P_2 135

3.9 ^1H NMR data for 4-ethylpyridine and 4-ethylpyridine capped Q-Cd_3P_2 135

3.10 IR data for 4-ethylpyridine and 4-ethylpyridine capped Q-Zn_3P_2 151

3.11 Solid state and solution state ^{31}P NMR data for 4-ethylpyridine capped Q-Zn_3P_2 153

3.12 Solid state and solution state ^{31}P NMR data for TOPO capped Q-Zn_3P_2 153

4.1 Selected information on optical properties of Q-InAs 163

4.2 Selected GC-MS data for the thermolysis of $Ga(P^tBu_2)_3$

and $In(P^tBu_2)_3$ at different temperatures 173

4.3 Selected IR data for 4-ethylpyridine capped Q-GaP 187

A1 Electrical properties of studied semiconductors 208

List of figures

1.1 LCAO approach to bonding and anti-bonding orbitals 28

1.2 Combination of orbitals leading to the formation of a band 28

1.3 Diagram showing the formation of a band gap from molecular orbitals for silicon 29

1.4 The numbering and assignment of basic function in a chain of H atoms 30

1.5 Assignment of the Bloch function of a H atom chain 31

1.6 Band structure of H atom chain, consisting of one dimensional *s* orbitals only 32

1.7 Promotion of an electron from the valence band to the conduction band for a direct and indirect semiconductor 33

1.8 Spatial electronic state diagram for bulk semiconductor and nanoparticles 35

1.9 Energy of the first excitonic state as a function of particle size as calculated by different authors for CdS 37

1.10 Optical spectra of cadmium sulphide, cadmium selenide, and cadmium telluride nanocrystals, 20-30 Å in size 38

1.11 Oscillator strength as a function of particle size for CdS 39

1.12 Emission from bulk and nanometer CdS 41

1.13 Optical spectrum and luminescence spectrum of Q-CdSe, showing the red shift of the luminescence peak relative to the band edge 42

1.14 Electronic structure of Q-CdSe nanocrystals, showing the relaxation of an electron into a dark state resulting in a stokes shift in the optical spectrum 43

1.15 Reversible shift in optical spectrum for CdS 44

1.16 Scheme for Q-PbS synthesis and HRTEM image of TOPO capped Q-PbS 50

1.17 Reaction scheme for synthesis of polymer bound CdSe nanocrystals 57

1.18 Possible structures of Mixed CdS and CdSe systems 59

1.19 Diagram showing Mn doping and activating of Q-ZnS with a simplified electronic diagram 64

1.20 Schematic and energy diagrams for the Gratzel Cell 66

1.21 Diagram of a single electron transistor 67

2.1 Decomposition scheme for the TMEDA adduct of cadmium thioacetate, showing the increase in band gap with smaller particles 72

2.2 Optical absorption spectra of CdS synthesised by the thermolysis of $Cd(SCOCH_3)_2 \cdot TMEDA$ 73

2.3 Optical absorption spectra of Q-CdS, grown by different methods 75

2.4 Optical spectra of CdS prepared by the thermolysis of cadmium monothiocarbamate at 250 °C, 1 hour, various fractions 75

2.5 Optical absorption spectra for Q-CdSe synthesised by the thermolysis of $Me_2Cd \cdot TEA$ and TOPSe at different temperatures for 30 mins 78

2.6 Optical absorption and luminescence spectra of Q-CdS
synthesised from Cadmium (MTC), showing band edge and deep trap emissions 80

2.7 Luminescence spectra of Q-CdS prepared from Me_2Cd·TEA
and $(TMS)_2S$ at different temperatures 81

2.8 Luminescence spectrum of Q-CdSe synthesised by the
thermolysis of Me_2Cd·TEA and TOPSe at 250 °C for 30 mins 81

2.9 Luminescence spectra of Q-CdSe prepared by the thermolysis
of Me_2Cd·TEA and TOPSe at a)200 °C; b) 120 °C 82

2.10 XRD pattern of Q-CdS prepared by the thermolysis of Me_2Cd·TEA and
$(TMS)_2S$ at 250 °C, with Miller indices indicated 84

2.11 XRD pattern of Q-CdSe prepared by the thermolysis of Me_2Cd·TEA
and TOPSe at 250 °C 85

2.12 a) HRTEM image of an array of Q-CdSe nanoparticles, bar = 5 nm;
b) HRTEM image of a CdSe nanocrystal, showing a hexagonal
lattice, bar = 1 nm 85

2.13 HRTEM image an array of Q-CdS, bar = 5 nm 86

2.14 TEM image of Q-CdS synthesised by the adduct method at 150 °C 86

2.15 TEM Image of Q-CdSe synthesised by the adduct method at 150 °C 87

2.16 Optical absorption and photoluminescence spectra of Q-CdS capped
with DMSO; Inset, determination of band edge by direct band gap method 95

2.17 Reaction scheme for cadmium dithiocarbamate in DMSO showing the suggested bonding of the capping group 96

3.1 TGA analysis of $[MeCdP^tBu_2]_3$ 106

3.2 Suggested decomposition pathways for $[MeCdP^tBu_2]_3$ 108

3.3 Suggested orbital interactions in different organic groups, explaining why β hydrogen elimination occurs for some groups but not others 111

3.4 Optical absorption spectra of nanoparticulate solutions made from three different precursors after 1 hour thermolysis (167 °C) in 4-ethylpyridine 112

3.5 Optical band edge (direct band gap method) of Q-Cd_3P_2 synthesised from $[MeCdP^tBu_2]_3$ in 4-etpy at 167 °C for 24 hours 114

3.6 Optical absorption spectra of a 4-etpy solution of Q-Cd_3P_2 and six size fractions 114

3.7 Optical spectra of Q-Cd_3P_2/TOPO synthesised at different temperatures for 30 mins 116

3.8 Direct band gap measurement of Q-Cd_3P_2/TOPO synthesised at 90 °C for 30 mins 116

3.9 Excitation and emission for Cd_3P_2 118

3.10 Luminescence spectra of TOPO capped Q-Cd_3P_2 prepared at different temperatures (λ_{exc} = 300 nm) 120

3.11 Luminescence spectra of Q-Cd_3P_2/4-ethylpyridine synthesised at 167 °C for 24 hours and various size fractions (λ_{exc} = 300 nm) 120

3.12 HRTEM image of a Cd_3P_2/TOPO nanocrystal (90 °C, 30 mins.),
approx. 4 nm diameter, showing lattice fringes 123

3.13 HRTEM images of a) Q-Cd_3P_2/4-etpy (167 °C, 24 hours) bar = 3 nm.
b) Close up of a dot showing lattice fringes 123

3.14 TEM image of Q-Cd_3P_2/4-etpy (167°C, 24 hours), bar = 20 nm 124

3.15 TEM of Cd_3P_2/TOPO, synthesised at 90 °C for 30 mins.
bar = 20 nm; Inset: Histogram of particle size distribution 124

3.16 Optical absorption spectrum, TEM (bar = 20 nm) and
histogram of particle size for 1st size fraction of Cd_3P_2/4-etpy 127

3.17 Optical absorption spectrum, TEM (bar = 20 nm) and
histogram of particle size for 7th size fraction of Cd_3P_2/4-etpy 128

3.18 EDAX analysis of a) Q-Cd_3P_2/4-etpy b) Q-Cd_3P_2/TOPO 130

3.19 Optical absorption spectra of different samples of Q-Zn_3P_2:
a) TOPO capped synthesised at 150 ° C;
b) TOPO capped synthesised at 250 ° C 138

3.20 Optical absorption spectra of 4-ethylpyridine capped Q-Zn_3P_2,
synthesised at 167 ° C; a) 4 hours, b) 30 hours 138

3.21 Comparison of two size fractions of Q-Zn_3P_2 capped with 4-ethylpyridine 139

3.22 Luminescence spectra of Q-Zn_3P_2/TOPO synthesised at two different
temperatures; Inset, optical absorption band edge and luminescence spectrum
of TOPO capped Q-Zn_3P_2 synthesised at 250 °C, showing the large Stokes
shift (λ_{exc} = 300 nm) 141

3.23 Luminescence spectra of Q-Zn_3P_2 capped with 4-ethylpyridine, showing emission from the solution prior to fractionation and the 8^{th} size fraction (λ_{exc} = 400 nm) 142

3.24 HRTEM image of hexagonal zinc metal by - product obtained from Me_2Zn and HP^tBu_2 in 4-etpy for 50 hours 144

3.25 HRTEM image of Zn_3P_2 capped with 4-ethylpyridine obtained from Me_2Zn and HP^tBu_2 in 4-etpy for 50 hours, bar = 10 nm 144

3.26 HRTEM image of Zn_3P_2 capped with 4-ethylpyridine from Me_2Zn and HP^tBu_2 in 4-etpy for 50 hours, bar = a) 5 nm; b) = 1nm 145

3.27 Optical absorption spectrum, TEM and histogram of particle size for 2^{nd} size fraction of Zn_3P_2/4-etpy 147

3.28 Optical absorption spectrum, TEM and histogram of particle size for 5^{th} size fraction of Zn_3P_2/4-etpy 148

3.29 Optical absorption spectrum, TEM and histogram of particle size for 8^{th} size fraction of Zn_3P_2/4-etpy 149

3.30 TEM image of Q-Zn_3P_2 capped with TOPO, synthesised at 150 °C for 4 hours. Bar = 20 nm 150

3.31 EDAX analysis of a) 4-ethylpyridine capped Q-Zn_3P_2; b) TOPO capped Q-Zn_3P_2 151

4.1 Crystal structure of *mer*[In(4-ethylpyridine)$_3$Cl$_3$] 159

4.2 Optical absorption spectra of Q-InAs synthesised under different conditions 162

4.3 Emission spectra from 3 samples of Q-InAs 163

4.4 XRD pattern for Q-InAs, showing the major Miller indices
expected for InAs. Inset; EDAX analysis of InAs nanocrystals 165

4.5 TEM image of Q-InAs synthesised at 167 °C for 6 days, bar = 100 nm 166

4.6 HRTEM image of Q-InAs synthesised at 167 °C for 6 days, bar = 20 nm.
Inset; Close up of a single nanocrystal showing amorphous character 166

4.7 AFM image of Q-InAs spin coated on glass 168

4.8 Photo of Q-InAs powder (left) and Q-InAs glass (right)
from a 4-ethylpyridine solution 168

4.9 TGA analysis of $In(P^tBu_2)_3$ and $Ga(P^tBu_2)_3$ 171

4.10 Optical electronic spectrum of Q-InP, a) = 167 °C, 4 days;
b) 167 °C, 7 days. Inset; Measurement of the band edge by the
direct band gap method 175

4.11 Luminescence spectra of Q-InP (167 °C, 4 days),
with optical absorption edge showing a slight Stokes shift 176

4.12 XRD pattern for Q-InP (167 °C, 4 days), showing the major
Miller indices expected for InP. Inset; EDAX analysis of InP nanocrystals 178

4.13 TEM images of Q-InP (167 °C, 4 days); a) bar = 200nm;
b) Close up of boxed section, bar = 20 nm 180

4.14 Optical absorption spectra of Q-GaP; a) 167 °C, 7 days.
b) 167°C, 1 hour; inset; determination of band edge for sample (b) 182

4.15 Emission spectrum of Q-GaP (167°C, 1 hour) in relation
to the optical band edge 183

4.16 XRD pattern for Q-GaP (167 °C, 1 hour), showing the major Miller indices expected for GaP. Inset; EDAX analysis of GaP nanocrystals 185

4.17 a) HRTEM Image of a GaP (167°C, 1 hour) nanoparticle, bar = 10 nm; b) HRTEM image of Ga particles, bar = 1nm 185

4.18 TEM image of Q-GaP (167°C, 1 hour), bar = 100 nm. Inset: Histogram of particle size distribution 186

A1 Two possible crystal phases of II-VI materials 209

A2 Crystal lattice of Cd_3P_2 209

A3 Unit cell of M_3P_2 (M = Zn, Cd) stretched along the c axis. Atoms at ideal positions 210

A4 Crystal structure of $[MeCdP^tBu_2]_3$ 211

A5 Crystal structure of *mer*$[In(4\text{-ethylpyridine})_3Cl_3]$ 217

Abbreviation and symbols

Chemical

bipy	bipyrimidine
^{t}Bu	*tertiary* butyl group
Cy	cyclohexyl group
Cp	cyclopentyl group
Oct	octyl group
Ph	phenyl group
Et	ethyl group
etpy	ethylpyridine
TEA	triethylamine
TOP	tri-*n*-octylphosphine
TOPO	tri-*n*-octylphosphine oxide
TOPS	tri-*n*-octylphosphine sulphide
TOPSe	tri-*n*-octylphosphine selenide

Techniques

AFM	atomic force microscopy
EDAX	energy dispersive X-ray analysis
GC-MS	gas chromatography-mass spectrometry
HRTEM	high resolution transmission electron microscopy
ICPAES	inductively coupled atomic emission spectrophotometry
IR	Infra-red spectroscopy

MAS	magic angle spinning
MOCVD	metal-organic chemical vapour deposition
NMR	nuclear magnetic resonance
TEM	transmission electron microscopy
XRD	X-ray powder diffraction

Symbols and constants

α_B	Bohr radius
σ^*	anti-bonding orbital
σ	bonding orbital, conductivity, size distribution
$\boldsymbol{k}$	wave vector
f	oscillator strength
R	radius
h	Planck constant
m^*_e	effective mass of an electron
m^*_h	effective mass of a hole
e	elementary charge
ε	dielectric constant
$n_{e,h}$	concentration of electrons, holes
$\mu_{e,h}$	mobility of electrons, hole
E	energy
E_g	band gap
λ	wavelength
$\lambda_{exc.}$	Excitation wavelength

Acknowledgements

Firstly I would like to thank my supervisor, Professor Paul O'Brien for giving me an interesting set of problems to work on, helping me out and turning the occasional blind eye when I may have done the odd naughty thing. I would also like to acknowledge my alternative supervisor, Dr. Nick Long for help in Paul's absence. My thanks to Dr. Garry Rumbles and group for help with physical chemistry and the use of the PL machine.

I'd like to thank Dick Sheppard (IC), Paul Hamilton (IC), David Butler (ULIRS) and Abil Alieev (ULIRS) for solution and solid state NMR. I acknowledge Hillary O'Callaghan (Chemistry, IC) and Barry Cole (Geochemistry, IC) for elemental analysis and ICPAES. I thank Marianne Odlyha for thermal analysis, Majid Motevalli and Andrew White for single crystal analysis. I would like to acknowledge the considerable efforts of the amazing Keith Pell with TEM, SEM and EDAX analysis. I'd like to thank Graeme Briars (IC, Materials), Jerome Bhat and Rekha Nayak (Univ. of Oxford, Engineering science) for electron microscopy. Thanks also go to Dr. Philip Moriarty (Physics, Univ. of Nottingham) for AFM work. I would like to thank EPSRC and BT for funding. I also thank Mike Burt and Steve Kershaw (British Telecom).

A special thanks to Dr. Tito Trindade for baby sitting me for three years, even when in Portugal. Much appreciated. I'll send you the dry cleaning bill for Exeter. Again, special thanks to Dr. Mike Lazell for in-depth proof reading and a million other things above and beyond the call of duty, including dressing me in Italy. Thanks to the post docs in the Barton lab, namely John Walsh, David Smyth-Boyle, Mikey Mike Lazell, David Otway and Jim Chapman. I'd like to thank my fellow final year postgrads in the Barton lab; Mo Chungazze for showing me the basics of vac line chemistry and clearing out of

the way on the last night in Florence - *Loser*!! and Graeme Horley for teaching me lots of rude words. I also thank the Barton lab basketballers - Seb, Chico, Neerish, Col, Kirst, Jin-ho, Babs and Saleem. Special thanks also go to Jeff Martin, Ange Martin, dangerous Paul Speyer, Elle Tarbuck, Narm, Fi, Carl Redshaw, Wardy and Yank.

I apologise to the Rumbles group about spilling pyridine everywhere - I'm the one whose sterile, your lab just smells a bit.

No acknowledgement's would be complete with out a deep bow to the team - Richard, Steven, Dave, Eleanor, Gordon and Cheryl. My thanks also go to David and Christine Wilson, Brenda Porter, Colleen Phythian, Ally Moyes and Juliet Rana. And anyone else I've forgotten to mention.

My deepest thanks and love to Mum, Dad and Neil who have given freely of their time, money, petrol, *etc.* and asked for nothing in return.

To Mum, Dad and Neil.

Chapter 1 - Introduction

1.1 Introduction

Modern research into small particles can be traced back to Faraday's work on gold colloids in 1857.[1] Ostwald's publication of "The World Of Neglected Dimensions" suggested the size of colloidal particles and the idea of a gradual transition between molecular and colloidal states.[2] Colloidal particles of semiconductors less than 20 nm in diameter are now often referred to as quantum dots, Q-particles, artificial atoms (because of their hydrogen like electronic structure) and microelectrodes (due to the similarity in reactions of colloidal particles and compact electrodes).[3] The synthesis of stable robust colloidal particles is a considerable challenge to chemists and material scientists. Even the most advanced methods of atomic manipulation (scanning tunnelling microscope) cannot produce devices smaller than 10 nm, therefore chemical methods need to be employed to produce materials exhibiting quantum behaviour.[4]

Preparation of nanometer sized materials originally relied on traditional colloidal chemistry, using kinetics to control nucleation and arrest particle growth. Although colloidal particles are small, most retain a degree of crystallinity and can be thought of as fragments of the bulk material. Recently, organometallic and metalorganic routes have been developed for the preparation of passivated quantum dots. Such methods will be discussed in some detail later. The physical properties of colloidal particles differ from those of the bulk lattice. For example small particles predominantly interact with light by absorption, not scattering. Powerful optical methods can therefore be used for analysis of their properties, for example, kinetic studies for the detection of short lived

intermediates.[3] The study of small particles includes quantum dots of semiconductors which are reported to have unusual properties.[5]

The properties of a bulk semiconductor are not determined by the properties of single atoms, but are a result of a periodic array of a large number of molecules or atoms in a crystal lattice. A transition from bulk semiconductor behaviour to molecular properties is observed as increasingly smaller particles are investigated. In this transitionary range, catalytic,[6,7] electronic[8] and optical properties[9] change drastically. Non linear optical properties have been reported in quantum dots due to the presence of charge carriers trapped in surface defects.[10,11]

The catalytic properties of metal quantum dots have also been investigated.[12-14] A 10^{-4} M dispersion of 7 nm diameter Ag colloids in an organic solute yields free radicals when exposed to UV light. Each radical transfers an electron to a colloidal particle which can store a large number of electrons. Under static conditions, a number of electrons can reside on a particle producing a negative potential high enough for hydrogen evolution.

$$2(CH_3)_2COH + Ag_n^{X-} \longrightarrow 2(CH_3)_2CO + 2H^+ + Ag_n^{(X+2)-} \qquad (1.1)$$

$$Ag_n^{(X+2)-} + 2H^+ \longrightarrow Ag_n^{X-} + H_2 \qquad (n = \text{agglomeration number})$$

$$2(CH_3)_2COH \longrightarrow 2(CH_3)_2CO + H_2$$

Nanoparticles of semiconductors are also the subject of intense current research. The electronic structure of a semiconductor alters as the dimensions of the solid are reduced. The restriction of an electron in a well defined box results in what are referred to

as quantum size effects and are of considerable interest. The synthesis of semiconductor nanoparticles started in the 1980's, with the aim of splitting water, reducing it to hydrogen by photo-induced electrons and oxidising it to oxygen by photo-induced holes but was unsuccessful.[15,16]

1.2 LCAO and Band Theory

Band theory is used to explain the electronic properties of a bulk semiconductor.[17,18] A semiconductor exists in an ordered network of atoms, with a specific unit cell being repeated throughout the structure, the single dimension of a cubic unit cell being the lattice constant, *a*. The electronic properties of semiconducting materials can be explained by band theory, which can be viewed as an extension of the linear combination of atomic orbitals (LCAO). A simple explanation can be evolved by considering di-hydrogen, (H_2), as an example.[19] The electron in a hydrogen atom exists in the 1*s* orbital, and has a wave function, ψ, which can be obtained as a solution from the Schrodinger wave equation. This is the amplitude, or displacement from the x, y, or z plane where x, y, and z are spatial co-ordinates. The wave function can be either positive or negative. When two 1s orbitals are combined in di-hydrogen they form a bonding (σ) and an anti-bonding orbital (σ^*), depending on the combination of signs of the wave function. In the ground state, the electrons will occupy the bonding orbital, which is lower in energy (Figure 1.1).

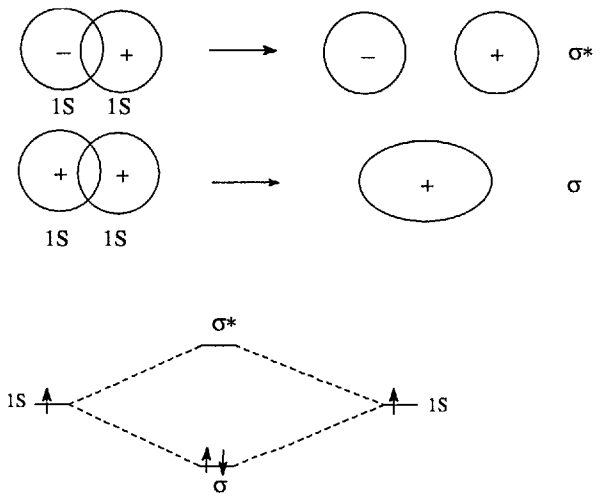


Figure 1.1: LCAO approach to bonding and anti bonding orbitals.

We can then consider a hypothetical linear chain of hydrogen atoms. As the atoms build up, so do the number of molecular orbitals, however they must occupy different energy levels in accordance with Pauli's exclusion principle (Figure 1.2).

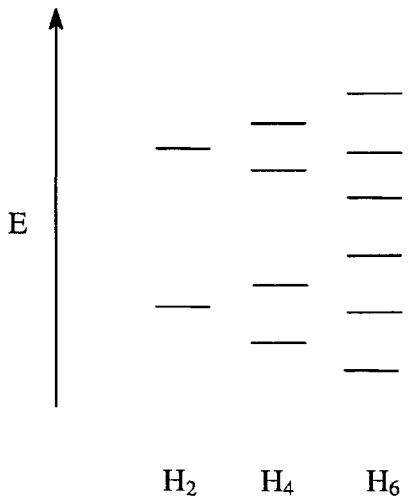


Figure 1.2: Combination of orbitals leading to the formation of a band.

If this could be extended to a solid lattice, there would be a large amount of orbitals separated by relatively small amounts of energy (Figure 1.3). We can therefore assume a continuous band. In considering the electronic properties of more complicated materials, the *s*, *p* and often *d* orbitals are often involved. In metals there are enough electrons to only partially fill the lower energy band, referred to as the valence band. The electrons can however move into the unfilled energy levels, giving rise to conductivity.

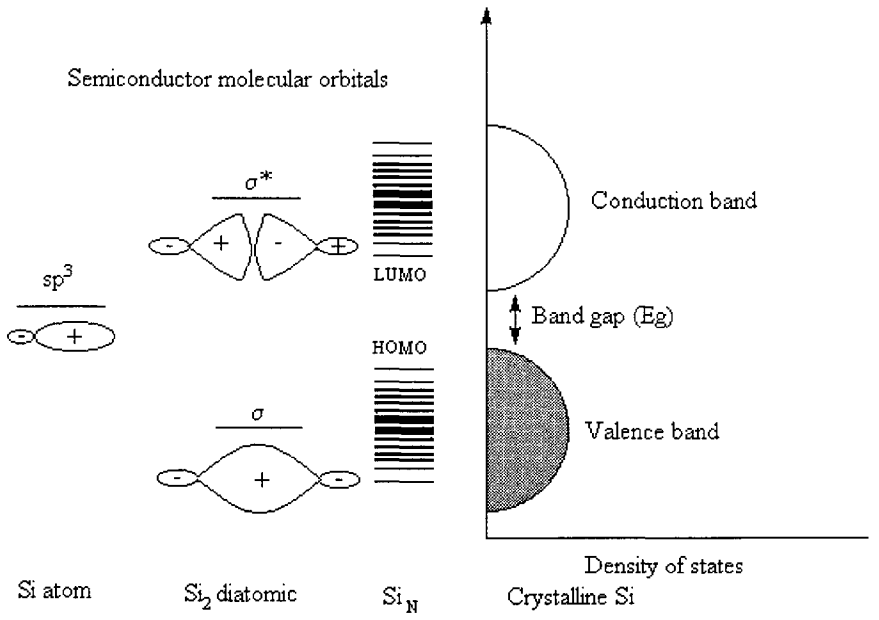


Figure 1.3: Diagram showing the formation of a band gap from molecular orbitals for silicon.[9]

In non metals, there are enough electrons to occupy all the energy levels of the valence band. The next band available is higher in energy and at 0 K, has no electrons. This is referred to as the conduction band and is separated from the valence band by a forbidden region, or band gap (Eg). No electrons may reside within the bandgap, but may be promoted to the conduction band if sufficient energy is supplied. For example, GaAs is a semiconductor with a band gap of 1.43 eV.[20] The valence band is considered to be

composed of n*s* orbitals, and the conduction band can be considered to be composed of n*p* orbitals. Any promotion of an electron is therefore an n*s* → n*p* transition. The electron is then free to move in the conduction band. The band gap varies with different compounds. Compounds composed of heavy atoms, and with small electronegativity differences between the relevant atoms (*i.e.,* less ionic) result in smaller band gaps. Semiconductors are generally defined as having band gaps up to 4.0 eV, anything larger is normally considered an insulator.

1.3 Band Structures

The band structure of a semiconductor is usually displayed graphically as Energy (eV) against ***k***, the wave vector.[19]

The wave vector is derived thus; Numbering the chain of H atoms results in arrangements as shown in figure 1.4, where χ = the basic function of that atom, and a = the lattice constant.

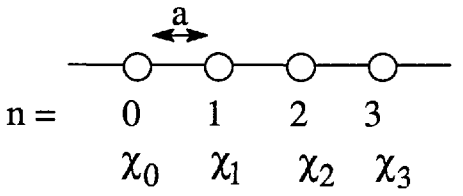


Figure 1.4: The numbering and assignment of basic function in a chain of H atoms.

Taking k from;

$$\psi_k = \sum_n e^{ikna} \chi_n \qquad (1.2)$$

The most anti-bonding and most bonding orbitals are obtained when $k = \pi/a$ and 0 respectively (Figure 1.5). This is described as assigning a Bloch function.

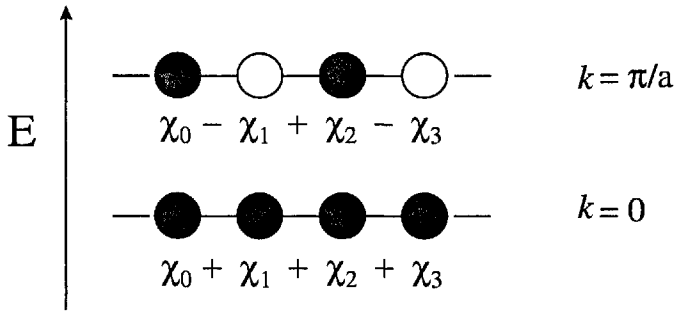


Figure 1.5: Assignment of the Bloch function of a H atom chain.

Therefore k is an index of the various levels in the band, *i.e.*, the larger the value of k, the more nodes. The wave vector is considered between $-\pi/a$ and π/a, and is termed the first Brillouin zone which is represented graphically as the band structure shown in figure 1.6.

This is a one dimensional example, and can be applied to three dimensions using the same principles, giving k a vector nature. The band structure alters for different orbitals due to their topology, and get more complex when dealing with a number of different orbitals. The valence and conduction bands can be seen with possible transitions (Figure 1.7).

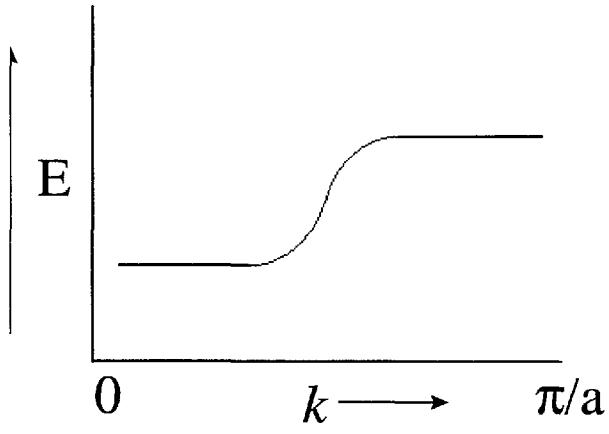


Figure 1.6: Band structure of H atom chain, consisting of one dimensional s orbitals only.

If an electron is given sufficient energy to be promoted to the conduction band, *i.e.*, > Eg, the electron may move through the unoccupied orbitals in the conduction band. It however leaves behind a hole, which can be considered as a particle in its own right, with a positive charge. The electron may recombine with a hole and release a photon of light. Both the electron and the hole are considered charge carriers and can separate and move through the lattice independently.

Certain semiconductor materials (such as silicon) require a change in wave vector (as well as sufficient energy to promote an electron to the conduction band) for a band gap transition. These materials are referred to as indirect band gap semiconductors, and are generally slower in generating charge carriers. Direct band gap semiconductors require only a sufficient energy input for a band gap transition with no change in wave vector.

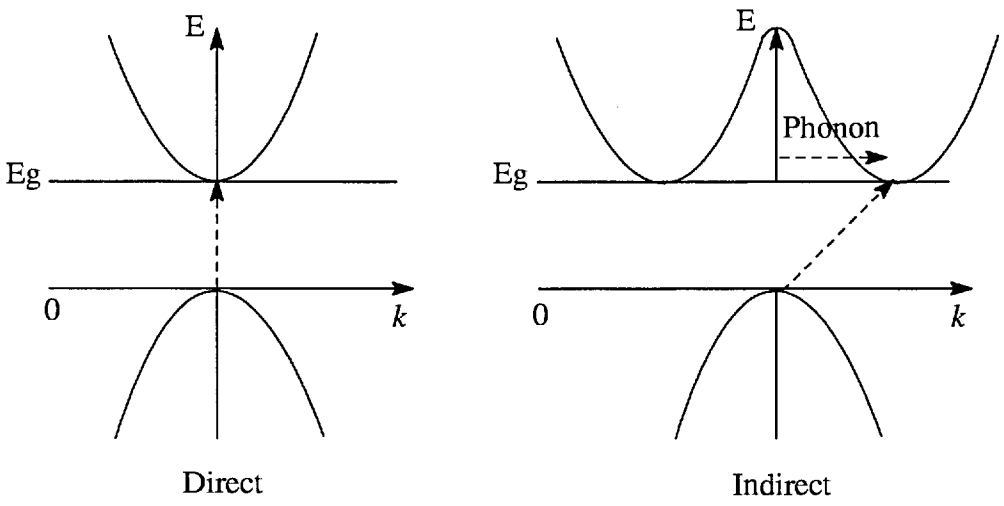


Figure 1.7: Promotion of an electron from the valence band to the conduction band for a direct and indirect semiconductor.

The conductivity (σ) is dependant upon the carrier concentration (n) expressed as particles/cm^3 and their mobility (μ). This can be expressed as

$$\sigma = qn_e\mu_e + qn_h\mu_h \qquad (1.3)$$

Where q = charge carrier.

Although electrons and holes can move independently through the lattice, they can form a bound state by coulombic attraction, forming a Wannier Exciton, which is analogous to the hydrogen atom.

This exciton is considered the first electronic excited state. The Bohr radius of this exciton can be expressed by;

$$\alpha_B = \frac{h^2\varepsilon}{e^2} \left[(1/m^*_e) + (1/m^*_h)\right] \qquad (1.4)$$

Where ε = Bulk optical dielectric coefficient e = Electron charge

m^*_e = Effective mass of an electron m^*_h = Effective mass of a hole

The effective masses of the electron and hole are used because of the excitons interactions with core level electrons. The effective mass can be considered as the ratio of the masses of the electron and hole in a semiconductor, to the mass of the electron and hole in a vacuum. Because the effective mass is small and the crystals electrons screen the exciton, the binding energy for the exciton is small and its radius large.

The small binding energy results in the exciton forming separate charge carriers at room temperature which can de-localise through a semiconductor lattice. Low temperature studies on bulk semiconductors have revealed the presence of excitonic features in electronic spectra. At such temperatures, the exciton has insufficient thermal energy to separate and remains as a bound entity.

1.4 Nanodispersed semiconductors

The two major features, which control the properties of nanoparticle semiconductors, are the quantum size effect on the electronic structure and the high percentage of atoms at the surface, especially important when the effects of surface traps are considered. The quantum size effect is exhibited when the excitonic radius becomes comparable to the size of the crystal. In such a situation, the charge carriers can be treated as particles in a box.[21] The electron's wavelength is restricted to the edges of the nanoparticles, therefore only half integral wavelengths are allowed, resulting in discrete energy levels. Reducing the diameter reduces the size of the box. The electron therefore must exist at a smaller wavelength, increasing the energy and hence widening the band gap. (Figure 1.8).

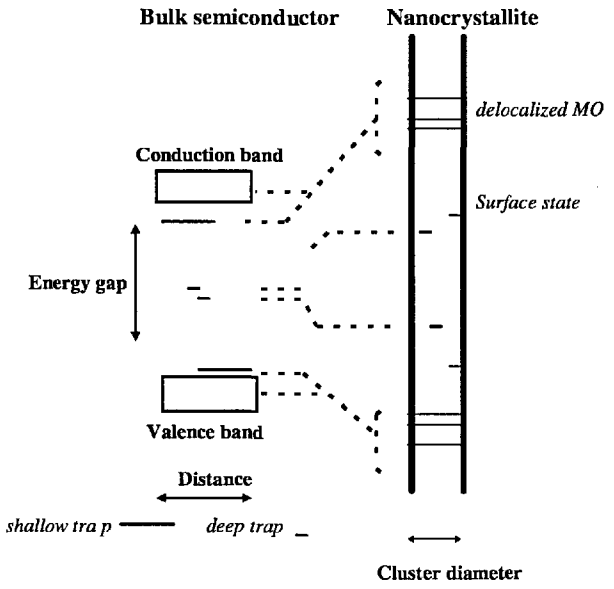


Figure 1.8: Spatial electronic state diagram for bulk semiconductor and nanoparticles, after Brus.[22]

It can therefore be stated that size quantization occurs when

$$R \approx \alpha_B \tag{1.5}$$

Where R = Radius of a spherical nanocrystal, α_B = Bohr radius of the exciton.

When the electron and hole are forced together, Brus showed that by using the effective mass approximation, the particle size can be deduced from the shift in optical band edge;[23]

$$\Delta E = \frac{h^2 \pi^2}{2R^2} \left[(1/m^*_e) + (1/m^*_h)\right] - \frac{1.8e^2}{\varepsilon R} \tag{1.6}$$

This equation gives an approximation of the energy difference between the ground state and the first excited state. Estimations of nanoparticulate diameters derived from the Brus equation give close approximations to experimentally observed diameters for a wide range of nanodispersed semiconductors.[8,9,24,25] However, the equation does not take into account any phenomena in a real system, such as surface defects (trap sites). The effective mass values and dielectric constants are also taken from macrocrystalline solids. The approximation deviates for smaller particles, but is overall a useful model to demonstrate quantitatively the quantum size effect and shows the band gap shift with particle size.

Different theoretical models exist to estimate nanoparticle dimensions.[23,27-32] Most use a 'particle in a box' approximation where the charge carriers are confined in three dimensions by the crystalline size. As shown previously, all give good approximation down to 4 nm.

The differences in most calculations are primarily the complexity and the parameters (Figure 1.9). The first approximations assumed spherical particles and ignored coulombic interaction.[33] Calculation of dimensions from line widths in X-ray powder diffraction patterns using the Scherrer equation[34] tend to give smaller diameters than are actually observed, attributed to the fact that line width is dictated by the crystalline regions in the particle. In quantum dots, the crystalline domain may not extend over the full area and poor crystallinity is often observed. The Krishna-Friesner approximation,[32] which uses a pseudo potential approach, correlates closely with diameters calculated from X-ray diffraction data.

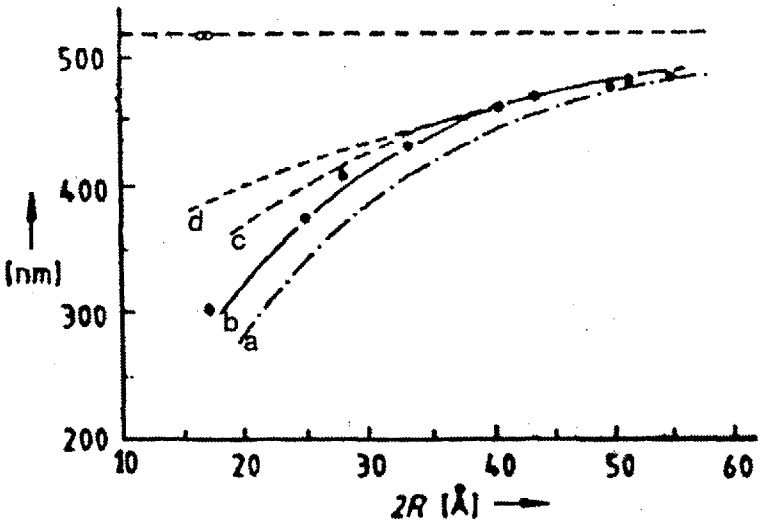


Figure 1.9: Energy of the first excitonic state as a function of particle size as calculated by different authors for CdS.[5]

a. Brus[21] *b. Weller*[28] *c. Lippens*[31] *d. Friesner*[32] *·. experimental.*

1.5 Absorption, Luminescence and Oscillator Strength

Electrons in nanodispersed semiconductors are transported across the band gap by the same process as in macrocrystalline semiconductors. Confinement of electrons in a semiconductor nanoparticle leads to a widening of the band gap. An electron trapped in a box must have wavelengths of half integrals (or multiples there of) which results in quantization of the energy levels. As the box gets smaller, electrons can only exist at smaller wavelengths (higher energy) and so the band gap widens. Evidence of quantum confinement can be seen in an electronic spectrum where the absorption edge of the semiconductor quantum dot is shifted to higher energies relative to the macrocrystalline solid. Other evidence of quantum confinement is the presence of an excitonic peak in an electronic spectrum (Figure 1.10).[35]

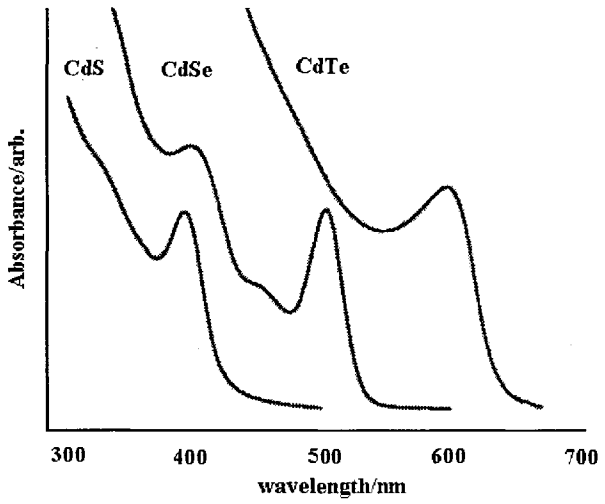


Figure 1.10: Optical spectra of cadmium sulphide, cadmium selenide, and cadmium telluride nanocrystals, 20-30 Å in size, after Bawendi.[35]

The presence of an excitonic peak in an electronic spectrum can be attributed to confined charge carriers being pushed closer together, leading to an increase in oscillator strength (Figure 1.11). Excitonic peaks are often found in bulk materials at low temperature, where the exciton has insufficient thermal energy to separate.

Oscillator strength has been found to increase as particle size decreases,[36] and can be shown (when $R<\alpha_B$) as;

$$f/ f_{ex} = ¾ (\alpha_B /R)^3 \qquad (1.7)$$

Where R = particle radius, f = Oscillator strength, f_{ex} = Oscillator strength in bulk material, α_B = Excitonic Bohr radius

The change in oscillator strength is found to correlate well with experimental data from CdS, CdSe and CdTe nanoparticles.

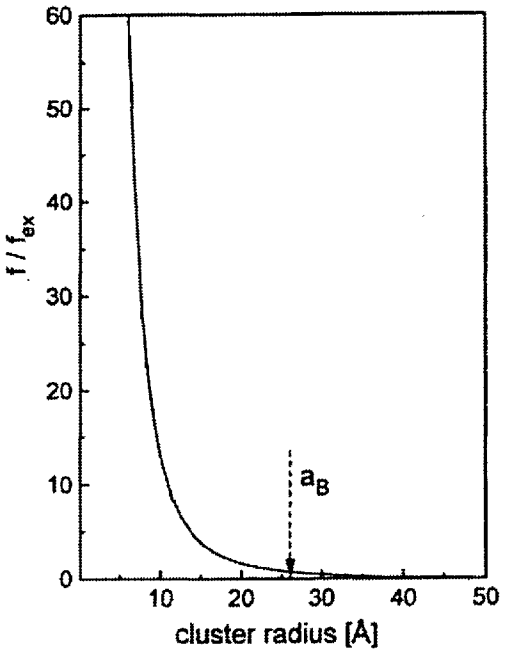


Figure 1.11: Oscillator strength as a function of particle size for CdS.[36]

The luminescence process observed in nanoparticles is complex. In a key paper, Brus investigated the luminescence properties of nanocrystalline and bulk semiconductors.[22] Taking macrocrystalline cadmium sulphide as an example, the surface is usually sulphur deficient, (S^{2-} defects) termed V_S^{2+} (Figure 1.8). The V_S^{2+} defect extracts an electron from the valence band, producing a V_S^{+} defect (essentially an F centre) and a trapped hole which is localised away from the defect. The V_S^{+} state cannot energetically remove another electron and becomes a deep trapping site (*ca.* 0.07 eV). Electrons excited to the conduction band then relax to the V_S^{+} giving a V_S^{0} centre. Emission is from recombination of the relaxed electrons (V_S^{0}) to the nearest pre-existing trapped hole (Figure 1.12). The result is low energy emission, significantly shifted from the band edge.

Early work on CdS nanocrystals resulted in materials which had bulk like emission attributable to the trapping mechanism described above. The synthesis of nanoparticles with passivated surfaces has resulted in the blocking of surface sites. Electron transfer to the S^{2-} defect is minimised, and electron-hole recombination leads to emission close to the absorption edge.

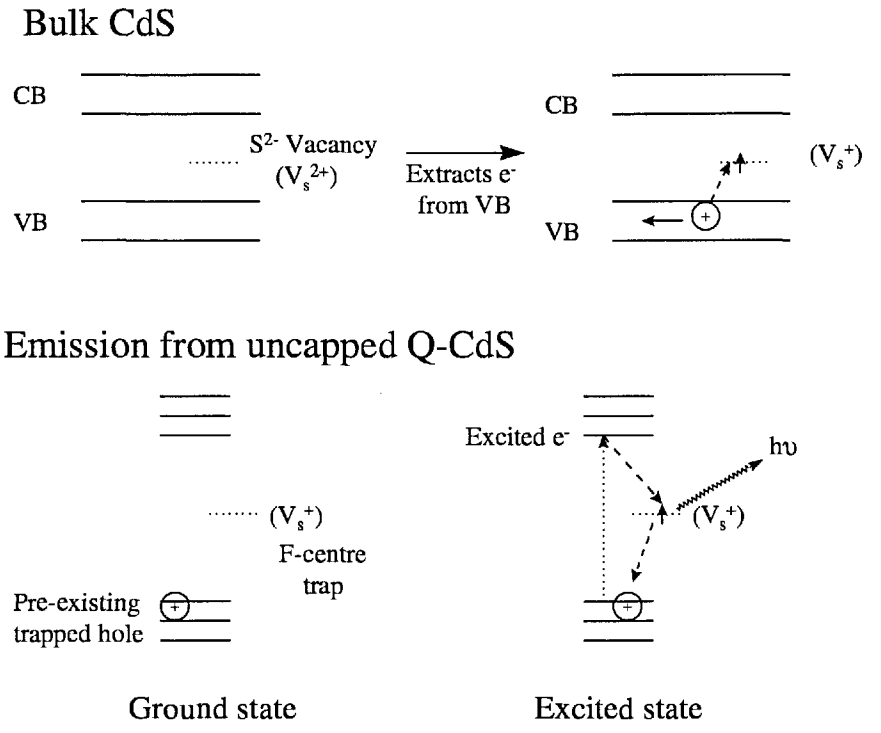


Figure 1.12 : Emission from bulk and nanometer CdS.[22]

This hypothesis is in agreement with experimental evidence, where surface passivation of luminescing semiconductor nanocrystals with other inorganic phases,[37-39] organic ligands such as TOPO (tri-*n*-octylphosphine oxide), and/or oxidation of surface molecules resulted in the blocking of surface defects, allowing only sharp near band edge recombination and emission (Figure 1.13).[35]

The luminescence spectra of nanoparticles passivated with a surface species appear to be slightly red shifted relative to the absorption band edge (Figure 1.13). This was originally attributed to relaxation into shallow traps,[22] however further research suggested the presence of a so-called 'dark exciton' which is responsible for the observed Stokes shift.[40,41]

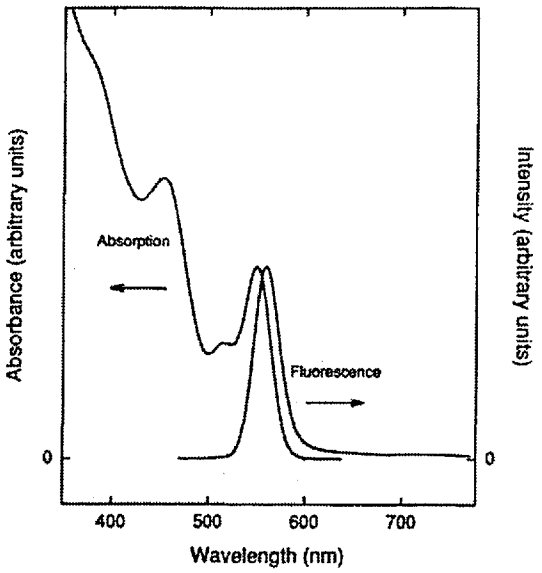


Figure 1.13: Optical spectrum and luminescence spectrum of Q-CdSe, showing the red shift of the luminescence peak relative to the band edge.[35]

The band edge exciton of TOPO passivated CdSe nanoparticles was calculated to be eight fold degenerate. This splits further into five sub-levels when considering the effects of the hexagonal lattice and its intrinsic crystal field splitting, the non spherical shape and the electron - hole exchange interactions (Figure 1.14). These sub-levels are labelled $|N_m| = 0_U$, 0_L, 1_U, 1_L, and 2. Levels $|N_m| > 0$ are twofold degenerate. Two of these sub levels are optically passive ('dark excitons'), whilst the other three have optically allowed transitions ('bright excitons'). These bright and dark states can be explained by taking into account the change in angular momentum required for excited electrons to return to the ground state. The dark states require a change of two units of angular momentum to return to the ground state, and since emitted or absorbed photons cannot have an angular momentum of ± 2, the transition is dark. The bright states require only a change of ± 1 and are thus observed. Excited electrons which occupy the $|N_m| =$

1_L level relax into the $|N_m| = 2$ level, which is optically dark. This accounts for the Stokes shift observed. The dark state is therefore the emitting state, by the less efficient phonon assisted transition, which has been used to explain the long radiative lifetime.

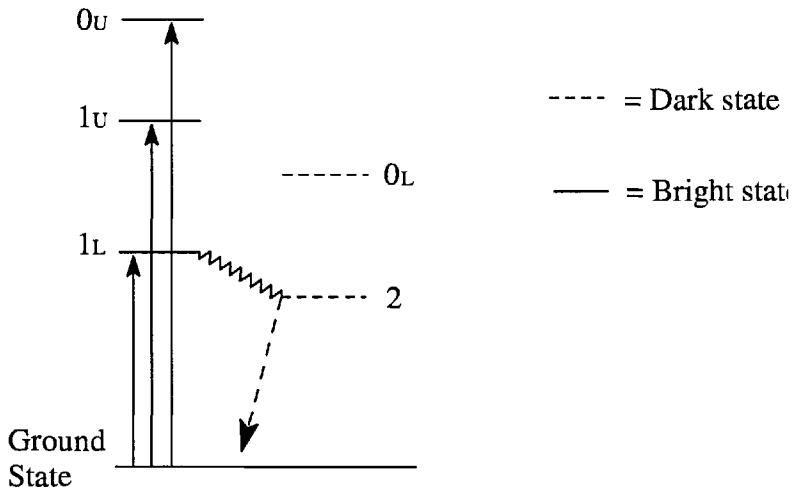


Figure 1.14: Electronic structure of Q-CdSe nanocrystals, showing the relaxation of an electron into a dark state resulting in a stokes shift in the optical spectrum.[41]

Another interesting observation is the red shift in the optical spectrum when a solution of quantum dots is spin coated into a thin film.[36] The shift, of *ca.* 50 meV (for a large cluster of CdS) is reversible, and shifts back to its original position when converted back to a solution (Figure 1.15).

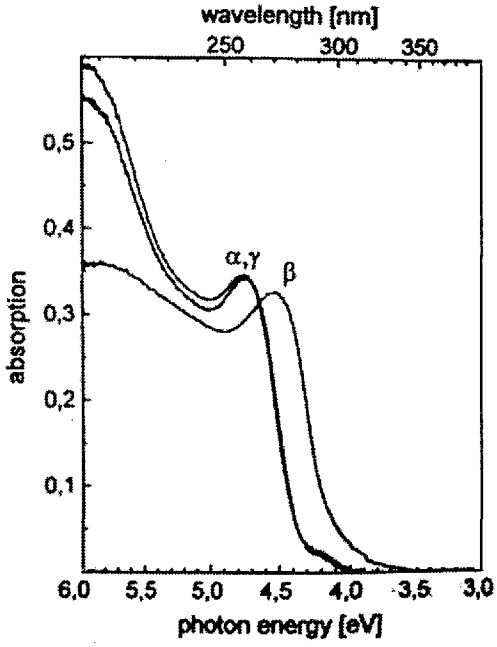


Figure 1.15: Reversible shift in optical spectrum for CdS.[36]

α = Original solution; β = Film made from sol.α; γ = solution made from film.

1.6 Methods of preparation

Many synthetic methods for nanoparticles have been reported in the literature. The majority use either colloidal or organometallic routes. An ideal route should result in pure, monodispersed, crystalline particles with robust surface passivation. Nanoparticles of metals[42-45] and metal oxides,[42] carbides, borides and nitrides have also been produced and have been reviewed elsewhere.[46]

Elemental semiconductors play a key role in the electronics industry. Germanium nanoparticles have been produced by the reaction of $GeCl_4$ and lithium naphthalide in tetrahydrofuran.[47] The quantum dots formed were between 60 Å and 200 Å in diameter. Laser illumination of a hexane solution resulted in further growth and increased crystallinity. Oxide coated silicon nanoparticles have also been produced by the combustion of silane.[48]

1.7 TOPO capped nanoparticles

One of the most recent advances in the synthesis of semiconducting quantum dots, and part of the basis of this thesis, is what shall be referred to as the Bawendi method. In this route, the relevant precursors (*e.g.* dimethylcadmium and a chalcogen source, *i.e.* tri-*n*-octylphosphine selenide/telluride or silylated precursor) are dispersed in tri-*n*-octylphosphine (TOP) and injected into tri-*n*-octylphosphine oxide (TOPO), a high boiling point, co-ordinating solvent at a temperature between 120 °C and 250 °C.[35]

Nucleation was achieved by the sudden introduction of the concentrated reagents resulting in abrupt supersaturation and hence the formation of nuclei, followed by slow growth and annealing, consistent with Ostwald ripening. Steigerwald[49] and Trindade[50] have investigated other possible solvents, both reaching the same conclusion that a polar co-ordinating Lewis base solvent is required to passivate particles when growth has terminated.

After sufficient growth, the heat source was removed and a non solvent added. This increased the average polarity of the solution and decreased the energetic barriers to flocculation. Centrifugation was used to obtain solid nanoparticles and decomposition by-products. The solids were then dispersed in a hydrocarbon, *e.g.,* toluene, and centrifuged further to dispose of the by-products, yielding an optically clear colloidal solution of nanoparticles. Gradual addition of a non solvent (*e.g.*. methanol for a toluene solution), followed by centrifugation resulted in size fractions of nanoparticles, with the larger particles precipitating out of solution first.

TOPO is not only the solvent but also acts as a capping and dispersing agent. The reaction produced TOPO capped nanoparticles, with 30-70% surface coverage. *Bis*(trimethylsilyl)selenium, *bis*(trimethylsilyl)sulfide, *bis*(*tert*butyldimethylsilyl)tellurium and tri-*n*-octylphosphine terlluride have been used as precursors, with no difference observed in the quality of nanocrystals produced.[35] The effect of alternative precursors on the surface properties has also been investigated, with no obvious differences observed.[51] Using TOPSe as a precursor resulted in the species passivating the surface as well as acting as a Se source, as detected by MAS ^{31}P NMR.[52]

The particles produced by this method were nearly monodispersed (σ = 5 %) and crystalline. By varying the temperature of synthesis, the diameter can be controlled between 24 Å and 230 Å. The organic surface cap can be replaced by other organic groups such as pyridine, 4-picolene, *tris*(2-ethylhexyl)phosphate, and 4-(trifluoromethyl)thiophenol.[51] Exposure to a large excess of the new group resulted in surface exchange. Computer modelling of XRD patterns suggests Q-CdSe prepared at temperatures up to 300 °C have one defect per nanocrystal.[35] Alivisatos produced similar quantum dots without crystal defects by using a higher synthesis temperature (350 °C) and tributylphosphine instead of tri-*n*-octylphosphine.[53]

TOPO capped CdSe nanocrystals have also been manipulated into superlattices by controlled crystallisation in a mixture of octane and octanol (9:1 ratio) at 80 °C under reduced pressure.[54] Langmuir Blodgett techniques have been employed to make monolayers on different substrates.[55] Nanocomposites and thin films of CdSe capped with ZnSe have also been produced by electrospray organometallic CVD.[56]

Alivisatos *et al.* have also investigated the effects of mixing organically capped CdSe with the conjugated polymer poly(2-methoxy,5-(2'ethyl)-hexyloxy-*p*-phenylenevinylene) (MEH-PPV).[57] TOPO capped nanoparticles had the surface ligand exchanged for pyridine. The pyridine capped dots were then mixed with a solution of polymer and were then spin coated onto indium tin oxide (ITO) coated glass. Excitation on the polymer resulted in the electron being transferred onto the nanoparticle. This resulted in quenching polymer luminescence, consistent with charge separation at the polymer/quantum dot interface. The resulting Q-CdSe/MEH-PPV composite luminescence efficiency was found to be 12% when loaded with high concentrations of

quantum dots. TEM demonstrated a distinct interconnected network forming at concentrations around 90 % CdSe. The incorporation of quantum dots into a conducting medium is an essential step towards device fabrication.

The idea of incorporation was further advanced by the removal of surface TOPO and replacement with a polymer back bone, rather than a simple dispersion.[58,59] In this method, the nanoparticles of either CdSe or CdSe coated with ZnSe, were prefabricated by the normal method and added to a solution of copolymer containing phosphine/phosphine oxide norbornene blocks. The addition of $[MTD]_{300}$ [NBE-$CH_2O(CH_2)_5P(oct)_2]_{26}$ (where MTD = methyltetracyclododecene, and NBE = 5-norbornen-2-yl) resulted in excellent take up of the quantum dots, and lead to increased fluorescence, whilst the addition of $[MTD]_{300}$ alone had negligible results. Further addition of the polymer resulted in an increase of 2% for the quantum yield, indicating passivation of the quantum dots by the polymer bound phosphine. TEM experiments showed networks of nanoparticles segregated by phosphine rich domains. An investigation was also taken into potential competition between TOPO and TOP to passivate the crystal's surface. Further addition of TOPO resulted in a small increase in luminescence, whilst addition of TOP doubled the emission. This suggests TOP binds to the unpassivated selenium sites, whilst TOPO specifically binds to cadmium.

Hines *et al.* developed the TOPO route further by using diethylzinc and TOPSe in TOP and hexadecylamine, giving crystalline nanodispersed ZnSe between 2.7 and 9.5 nm diameter.[60]

Another interesting compound is a quantum dot homodimer.[61] TOPO capped Q-CdSe was prepared as normal, and then the surface ligand was replaced with a more

robust, strongly binding group, *N*-methyl-4-sulfanylbenzamide (MBAA). The hydrazide capped dots were then cross linked by the addition of *bis*(acylhydrazide) at elevated temperatures. Size selective precipitation removed larger aggregates leaving mainly cross linked dimers.

Trindade and O'Brien have produced CdSe,[62] CdS,[62] PbS,[63] and PbSe[63] TOPO passivated nanoparticles by the use of single source precursors.[50] The use of single source precursors is well established in conventional MOCVD, with added benefits that they provide primarily ease of use and increased safety, as single source precursors tend to be less air sensitive and less toxic.[64] The properties of the II-VI nanoparticles produced by a single source route are comparable to those produced by the Bawendi method. PbS and PbSe quantum dots showed unusual morphologies, with a variety of shapes being observed (Figure 1.16). Size fractionation was reported to be difficult, due to the large size of nanoparticles obtained. Nanocomposites have also been produced where nanocrystals were bridged by molecules such as 2,2'-bipy.[62,50] This was also extended to produce mixed composites of ,*i.e.*, Q-CdSe/ Q-CdS.[50]

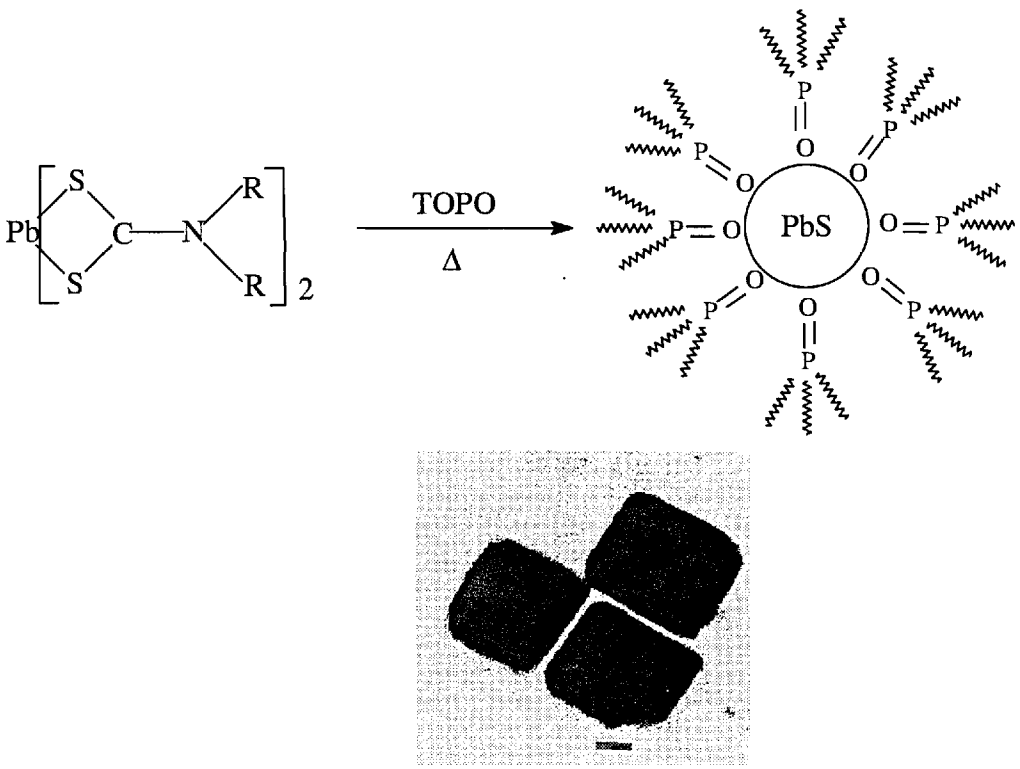


Figure 1.16: Scheme for Q-PbS synthesis and HRTEM image of TOPO capped Q-PbS (bar = 10 nm).

A similar method has been used to synthesise TOPO capped Q-InP.[65] $InCl_3$ was complexed to TOPO prior to reaction. Addition of *tris*(trimethylsilyl)phosphine to the TOPO complex at 100°C resulted in nanocrystal nucleation, which was followed by growth and annealing at high temperatures (265 °C) for days. The temperature was then lowered to 100 °C and a surface capping agent added (dodecylamine). The quantum dots obtained were of high quality, 20-50 Å in size, and crystalline. Luminescence of Q-InP was found to be near band edge, similar to the analogous II-VI materials. The nanoparticles were reported to luminesce only after exposure to air. It is assumed that the stable surface oxide blocks surface traps and promotes band edge emission. A notable

point was their unusual method of isolation. Unlike the original Bawendi work,[35] the reaction mixture was totally dissolved in toluene, which was then size fractionated by the gradual addition of methanol. The method however, resulted in large amounts of In_2O_3 and the resulting crystals were relatively poly-dispersed (standard deviation of *ca.* 20 % prior to size fractionation).

Problems with III-V system can be attributed to the increased covalent nature of the material relative to the analogous II-VI compounds, and the precursor-solvent interactions.[65] Atoms or ions of group III metals are not chemically stable, so strongly complexed organometallic precursors ($InCl_3$-TOPO) are employed. Nucleation and growth are therefore high temperature processes and temporal separation of the two is difficult, resulting in polydispersed products. The decrease in crystallinity of III-V nanoparticles has been attributed to their increased covalent nature.[66]

InP,[65,67] GaP,[67] and GaInP[67,68] nanoparticles have also been produced by precursor thermolysis in TOPO, using an adaptation of the Bawendi route. III-V compounds are also expected to show increased quantum behaviour, as the excitons are generally larger, *i.e.*, excitonic diameter of InP = 150 Å, CdSe = 70 Å. In these routes, a metal halide(s) or a chloro-oxalate was mixed with *tris*(trimethylsilyl)phosphine in either CH_3CN or toluene, and injected into mixtures of TOPO and TOP at high temperatures.

The choice of precursors was an adaptation of Wells' dehalosilylation reaction.[69] High temperature annealing for long periods of time resulted in crystalline nanoparticles, between 20 and 65 Å in size. These were characterised by UV spectroscopy, luminescence spectroscopy, TEM, and X-ray powder diffraction. The crystallinity of the InP dots was also found to be dependent on the indium precursor. Replacing

chloroindium oxalate with indium chloride gave amorphous products.[68] This phenomenon is found in biomineralisation and in microscale inorganic colloids, where the choice of precursor can dictate morphological properties.[70] Replacing TOPO with triphenylphosphine or *tris*(2-diphenylphosphinoethyl)phosphine resulted in nanoparticles which had limited solubility in toluene, indicating poor surface capping.

InAs nanoparticles, 25 to 60 Å in size, have also been produced by thermolysis of $InCl_3$ and *tris*(trimethylsilyl)arsine in TOP alone, which served as both solvent and capping agent.[71]Luminescence was found to be independent of surface oxidation.

Over capping of TOPO passivated nanoparticles has also been achieved, with CdSe being capped with CdS,[72] ZnS,[73] ZnSe[74] and will be discussed later.

These methods are important as almost all quantum dot devices to date have used nanoparticles produced by these routes, due to their robust nature, ease of manipulation and possibly due to their anaerobic method of manufacture.[75-78]

1.8 General organometallic routes

Q-GaP and Q-GaAs have been synthesised by refluxing $GaCl_3$ with either $P(Na/K)_3$ or $As(Na/K)_3$ in toluene/glyme to give crystalline glyme capped quantum dots.[79] The same reaction in aromatic solvents alone again yields nanoparticles which are capped with methanol upon extraction. Q-GaP has also been produced through the thermolysis of a single source precursor $[X_2GaP(SiMe_3)_2]_2$ (X=Br, I) and $(Cl_3Ga_2P)n$, both decomposing at relatively low temperatures under vacuum to yield crystalline Q-GaP.[80] Q-GaP and Q-GaAs have also been produced by thermolysis of $[H_2GaE(SiMe_3)_2]_3$ (E = P, As) at 450 °C

in xylenes, giving nanoparticles approximately 5 nm in diameter. The capping agent is not discussed.[81]

Alivisatos[82] and Nozik[83] used a similar method to Bawendis' to produce GaAs nanoparticles, by refluxing $GaCl_3$ and *tris*(trimethylsilyl)arsine in quinolene at 240 °C for 3 days. Flame annealing at 450 °C followed to improve crystallinity, but resulted in a slight loss of solubility.

Crystalline InAs nanoparticles, 1-8 nm in size have been fabricated by the reaction of $In(acac)_3$ with *tris*(trimethylsilyl)arsine in triglyme at 216 °C for 70 hours. Investigations were also carried out into their non-linear optical properties.[10] The same method was applied successfully to GaAs, where $Ga(acac)_3$ was used instead of the In precursor, using the same conditions.[84] These methods are attractive because they present routes that do not use hazardous precursors, *i.e.*, phosphine or arsine.

Q-CdSe has been also been synthesised by pyrolysis of a single source precursor, $Cd(SePh)_2$, and by $[Cd(SePh)_2]_2[Et_2PCH_2CH_2PEt_2]$ in 4-ethylpyridine.[49] Q-Cd_3P_2 has been produced by the methanolysis of $Cd[P(SiPh_3)_2]_2$.[85,86] Nanometer sized antimonide compounds have been largely overlooked, despite having potentially useful properties. GaSb nanocrystals have been synthesised by refluxing *tris*(trimethylsilyl)antimonide and gallium chloride in toluene. The particles, 20-30 nm in diameter, were analysed by HRTEM and X-ray powder diffraction.[87]

1.9 Colloidal routes

Colloidal work on nanocrystal semiconductors is based on controlled precipitation of dilute colloidal solutions by stopping the growth after nucleation. The synthesis of monodispersed colloidal solutions was explained in the 40's by La Mer *et al.* who theorised that seeds formed that could eventually grow into larger particles.[88-90] These seeds are the nanocrystals that are of current interest, and have been isolated by growth control using various methods. Small crystals are less stable, dissolve then re-crystallise on larger more stable crystals. This is known as Ostwald ripening. Therefore the quantum dots must have a low solubility, which can be achieved by the correct choice of solvent, pH, temperature and passivating agent. Highly monodispersed samples are obtained if the processes of nucleation and growth are distinctly separated, *i.e.,* fast nucleation and slow growth. The colloidal stability of these crystals was improved by using solvents with low dielectric constants, or by using stabilisers such as a styrene/maleic acid copolymer. Henglein,[91] Brus[92,93] and Weller[24] have made large contributions to this field, especially with CdS. A typical example involved mixing aqueous solutions of $CdSO_4$ and $(NH_4)_2S$ and subsequent control of the size of crystalline Q-CdS by alteration of nucleation kinetics using pH.[92] Although an efficient method, some important semiconductors cannot easily be synthesised, *i.e.*, CdSe, GaAs, InSb. Annealing of amorphous colloidal particles is also a problem. Many aqueously prepared nanoparticles are insufficiently stable at high temperatures.

CdS and ZnS have also been produced in methanolic media without the use of an organic ligand to stabilise, using the repulsion of the electrostatic double layer to stop agglomeration.[93]

Zn_3P_2 and Cd_3P_2 have both been produced by aqueous methods, by the injection of phosphine gas into a solution of the relevant metal perchlorate.[94,95] The quantum dots obtained displayed a wide range of colours, ranging from white for small Cd_3P_2, to brown for the larger particles. The white particles were reported to have band gaps of up to 4.0 eV. Luminescence was reported to be good at short wavelength, with little attention paid to crystal morphology.

Murphy has produced manganese activated (occupying surface sites) and manganese doped (occupying lattice sites) ZnS dots, displaying increased quantum yields and orange emissions respectively.[38]

1.10 Synthesis in confined matrices

Materials with small distinct porous structures have been used to synthesise quantum dots. The well defined pores have been used as nanometre sized reaction vessels. Solids such as zeolites,[96] micelles,[97] molecular sieves[98] and polymers[99] have all been used as methods of restricting growth above a certain size. In such circumstances, the matrix also plays a role in determining the final properties of the particle, for example, the lability of micelles. CdSe, ZnS, CdSe/ZnS and ZnS/CdSe nanoparticles have been produced using inverse micelle solutions.[100, 101] A microemulsion containing the metal ion was reacted with a silylchalcogenide, resulting in nanoparticles. The surface was then

capped by phenyl groups or another semiconductor. The surface composition of the crystals are interesting due to their ability to react further with other silyl groups due to the excess Cd^{2+} sites, effectively growing larger and developing a different surface capping.

Growing particles in the internal cavities of zeolites also limits the particle size, with quantum dots generally being no larger than 20 nm. CdS has been synthesised in two different zeolites by ion exchange from the sodium cationic form to the cadmium cationic form, followed by exposure to H_2S gas. Depending upon the amount of cadmium used, different sized particles were obtained.[96]

Q-GaP has also been synthesised in the pores of zeolite Y.[102] Vapour transfer of Me_3Ga into dry Na^+ /H^+ exchange zeolite, resulted in methane evolution and the formation of $(Me)_{3-x}Ga$ sites. An excess of PH_3 at various temperatures (200 °C to 400 °C) resulted in particles in the size range of 10 - 12 Å. The nanocrystals formed were analysed by EXAFS and solid state NMR.

Q-PbS was obtained by exchanging Pb^{2+} into ethylene/methacrylic acid copolymer, followed by exposure to H_2S.[99] The size of the particles was again controlled by Pb^{2+} concentration , with sizes ranging from 13 Å to 125 Å.

An organometallic route to an in-grown polymeric composite of CdSe and ZnSe has also been developed (Figure 1.17).[103-105] 2-pyridyl-polybutadiene polymer was reacted with the relevant group II metal alkyl, giving an adduct. A toluene solution of the polypyridine bound metal alkyl was exposed to H_2Se gas, giving a coloured precipitate. The size of the nanoparticles was determined by the solvent and reaction temperature (-76 °C to 60 °C), with quantum dots synthesised at lower temperatures being smaller.

Hexagonal CdSe was obtained in the size regime 1-6 nm, with the use of light petroleum instead of toluene giving larger particles. The particles were characterised by HRTEM, powder XRD, UV and photo-acoustic spectroscopy (PAS).

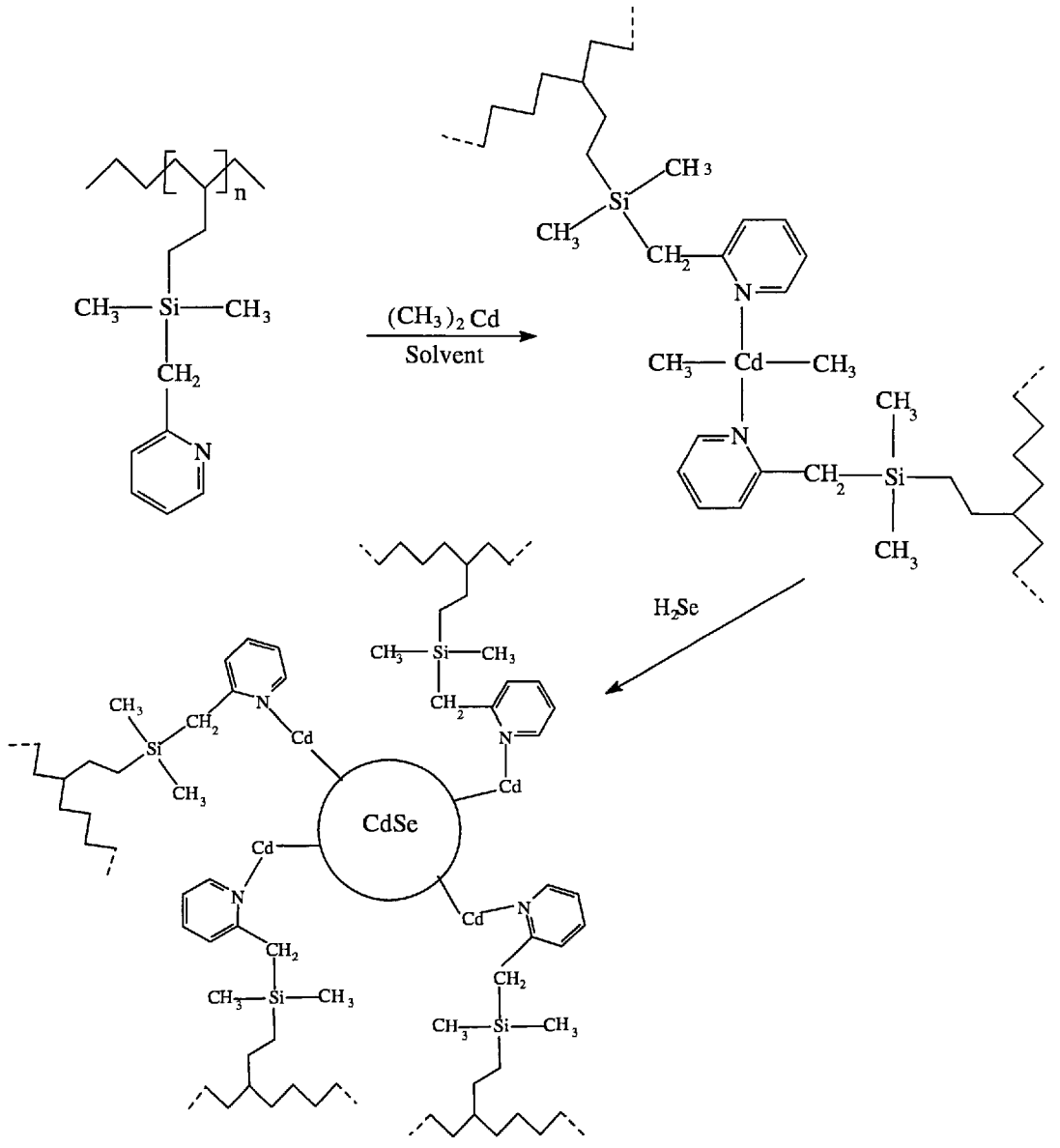


Figure 1.17: Reaction scheme for synthesis of polymer bound CdSe nanocrystals.[103-105]

1.11 Nano-heterostructures

The surface states of nanoparticles play an important role in luminescence and since many applications will be luminescence dependent, heterostructures have been extensively researched leading to improved emission and enhanced charge transfer. Alivisatos reports no significant luminescence in Q-InP until the surface is oxidised, blocking surface defects.[65] This demonstrates the importance of the surface state. In the production of heterostructures, a small particle of one compound acts as a seed for the nucleation of another, resulting in a core of one semiconductor, and a shell of another. These compounds are important as inorganically overcoated dots are more robust and resistant to oxidative degradation than ligand passivated nanocrystals, making them better candidates for electroluminescent devices. Materials that have been reported are $CdS/Cd(OH)_2$,[37] ZnS/CdS,[39] CdS/HgS,[106] CdS/HgS/CdS,[107,108] CdS/PbS,[109] HgS/CdS,[110] CdSe/ZnS,[100,73] CdSe/CdS,[72] CdSe/ZnSe,[112,74] and ZnSe/CdSe.[113] Restraints on these systems are primarily mismatches in lattice constants, and product solubility. The growth of these compounds has to be carefully regulated, or capping becomes irregular. With the epitaxial growth of CdS on the outer shell of a TOPO capped CdSe nanoparticle, the strongly bound organic ligands needed to be replaced with a more labile group, such as pyridine.[72] Further addition of a stock solution of dimethylcadmium and *bis*(trimethylsilyl)sulfide with a specific Cd:S ratio resulted in epitaxial shell growth. Deviation from the ratio resulted in growth of separate CdS nanocrystals and clusters. The inorganically capped particles were soluble in chloroform and dichloromethane.

Photo-physical experiments showed that with excitation, the hole was confined to the core, with the electron de-localised over the entire structure.

The actual structures formed by these systems are highly sensitive to reaction conditions. Figure 1.18 shows other theoretical structures, previously suggested by Fendler.[114]

Weller[115] and Alivisatos[116] have shown separately, by HRTEM, that some colloidal heterostructures of the type CdS/HgS have the morphology shown in figure 1.18 as E and F, giving imperfect capping. Example B/C can be achieved by controlled growth, with incorrect conditions giving example A as discussed above.

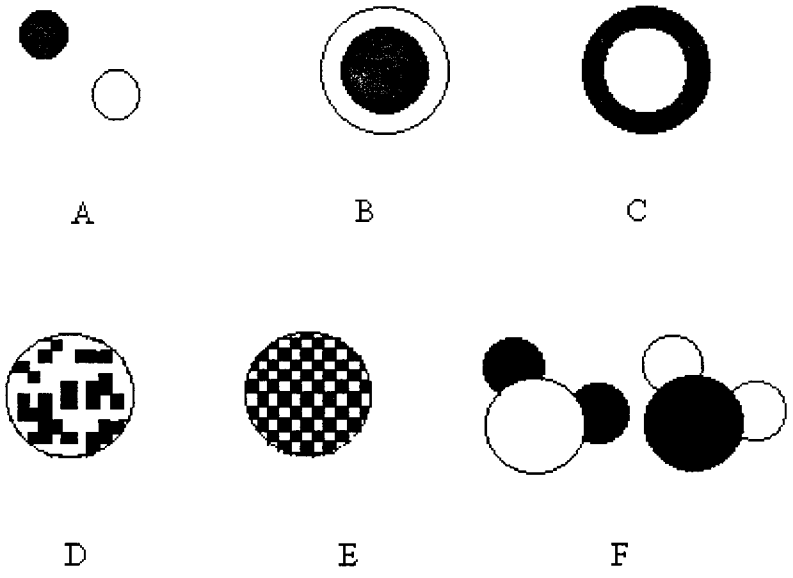


Figure 1.18: Possible structures of Mixed CdS and CdSe systems where A= distinct phases of CdS and CdSe ; B= CdSe capped with CdS; C= CdS capped with CdSe; D= irregular CdSe/CdS mix; E= regular CdSe/CdS mix; F= sandwich CdS/CdSe.

There is also a report of a CdS/HgS/CdS heterostructure, termed a quantum dot quantum well.[107,108] This colloidally synthesised structure has a 5 nm core of CdS,

followed by a shell of 1-3 monolayers of HgS. The shell is grown by the addition of $Hg(ClO_4)_2$ to the aqueous solution of CdS, resulting in displacement of surface Cd by Hg. Mismatch in lattice constants for CdS and HgS is low, at 0.56 %. The final passivation with 1-5 monolayers of CdS is achieved by the dropwise addition of a dilute H_2S solution, giving particles in the size range 6.5 nm to 8.9 nm.

1.12 Nanocrystal processing

As mentioned, TOPO capped nanocrystals have been organised into Langmuir-Blodgett films,[55] and similar manipulations have been carried out on quantum dots synthesised by other methods.[25] Langmuir-Blodgett structures can be built during the formation of nanoparticles, where an amphiphilic layer and a cadmium or lead salt is treated with H_2S, resulting in a layered organic matrix.[117]

Nanocomposites of TOPO capped nanocrystals have been produced by Trindade and O'Brien, as mentioned earlier, by replacing the majority of surface TOPO with a bidentate organic ligand such as 2-2'bipy or 4-4'bipy. Mixed composites could be formed by mixing toluene solutions of two species of nanocrystals with the bridging ligand.[50] TOPO capped CdSe has also been prepared as a thin film by organometallic chemical vapour deposition. The luminescence of the film increased markedly when the surface was passivated by a ZnSe layer.[56] Bawendi has also reported a method to produce a colloidal superlattice of TOPO capped CdSe.[54] Weller has reviewed other quantum dot superlattices.[118]

Polymers have been attached to the surface of nanocrystals to produce large structures. CdS[119] and GaAs[120] were processed into polyvinyl alcohol films using electrostatic deposition and films of anionic PbI_2 in bipolar pyridinium have also been reported.[121]

Other recent advances worthy of note are the uses of DNA in nanocrystal processing, with possible applications to chemical biosensors.[122] Mirkin has used thiol capped, non complementary DNA oligonucleotides to assemble 13 nm Au quantum dots into a macroscopic material.[123] In similar work, Alivisatos synthesised *ca.* 3 nm Au nanocrystals which were then attached to single strand oligonucleotides, which organised into spatially defined structures, dimers and trimers on addition of a single complementary DNA strand, due to Watson-Crick interactions.[124]

1.13 Applications and Conclusions

Alivisatos has produced an electroluminescence device using TOPO capped CdSe nanocrystals with sizes between 3 and 5 nm, and a semiconducting polymer, *p*-paraphenylene vinylene (PPV).[77] The device was fabricated by multiple exposures of an indium tin oxide (ITO) plate or ITO/PPV plate, pre-treated with hexane thiol to a toluene solution of nanocrystals. For stability, the layer was built up to 1000 Å. Electrical contact were made by silver coated magnesium. The colour of the emission was controlled by the particle sizes giving red to yellow emissions. At increased voltage, green luminescence from the polymer layer was predominant. This was then improved upon by fabrication of a LED using CdSe nanocrystals capped with CdS instead of the organic ligand.[75] The

device was produced by using the same basic techniques but using a pre-PPV polymer precursor deposited on ITO coated glass. This film was then annealed at 300 °C for three hours before having CdSe/CdS spin deposited onto the PPV. The use of CdSe/CdS instead of CdSe/TOPO results in an increase in efficiency by a factor of 8 and a factor of 10 increase in lifetime. This is attributed to the inorganically capped particles being resistant to photo-oxidation.

Electroluminescence has been reported from TOPO capped CdSe when incorporated into thin films of polyvinylcarbazole (PVK) and an oxadiazole derivative.[125] The film was then sandwiched between ITO and Al electrodes. The device was tuneable from *ca.* 530 nm to 650 nm by varying the size of the dots. Low temperature studies (77 K) also indicated that only the nanocrystals luminesced at low voltage, whilst at higher voltages both the dots and the PVK matrix electroluminesce. Electroluminescence efficiency was also found to increase at 77 K.

The anaerobic conditions employed to manufacture TOPO capped quantum dots used in device fabrication have the advantage of avoiding potential O_2 doping. For this reason, aqueous routes to nanocrystals were often assumed to be unfavourable. However, Gao *et al.* fabricated a device using CdSe nanocrystals. The quantum dots were synthesised using a Cd salt and H_2Se in aqueous solution with thiolactic acid, at pH 11.[126] The thiolactic acid acted as a capping agent, effectively giving the particle a negatively charged surface, which is essential for adsorption onto the relevant substrate. The size of the particles was controlled by altering the molar ratios between Cd^{2+} and H_2Se, with intense fluorescence obtained by adding an excess of Cd^{2+} shortly after synthesis. Optical glass and ITO coated glass were used as substrates, which had been coated with PEI

(poly-ethyleneimine) to give a positively charged surface. The next step involved the exposure of the substrate to a solution of the nanoparticles for a defined time giving a monolayer of quantum dots. Positively charged PAH (poly(allylaminehydrochloride)) or a precursor for poly-(*p*-phenylene-vinylene) (pre-PPV) were then adsorbed on top. The application of a number of inorganic and organic layers was repeated, until 20 double layers had been applied. The CdSe/PPV multi-layer film was then obtained by heating the CdSe/pre-PPV at 130 °C under a vacuum for 11 hours. The device was finished by the evaporation of an aluminium electrode on the top layer. The device produced almost white light electroluminescence (500 nm to 850 nm) under a forward bias of 3.5 to 5 V with the positive pole on the ITO electrode. Such a broad emission, similar to that of the CdSe solution, was attributed to deep traps, surface defects and a large size distribution. It is interesting to note that a device incorporating aqueous derived nanocrystals has a broad emission, which may be attributable to O_2 doping. The device is reported to have a longer life time than similar simple organic devices.

Another potential application is a quantum dot solid state laser, the patent rights of which are held by Bawendi *et al.*[127] In this patent, II-VI nanoparticles (ZnTe) are held in a polymeric material such as polymethylmethacrylate.

This opens the way for quantum dot devices to be fabricated, in which the size of the nanocrystal dictates the emission. Manganese doped zinc sulfide is already used as a phosphor, and now quantum dots of such a material have been grown although no device has yet been fabricated.[38] The material showed band edge blue emissions from ZnS (*ca* 350 nm) with Mn^{2+} spatially localised, activating the surface and blocking surface traps.

Doping resulted in Mn^{2+} occupying interstitial sites leading to orange emissions (*ca.* 585 nm) along with band edge blue emission (Figure 1.19).

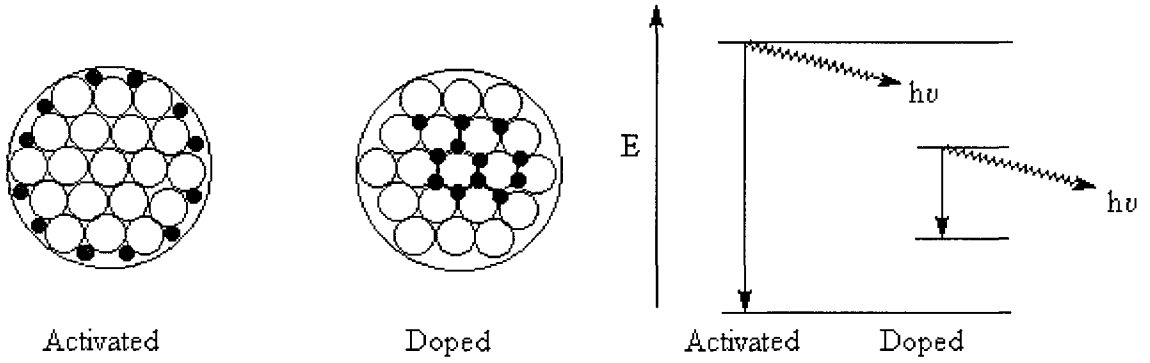


Figure 1.19: Diagram showing Mn doping and activating of Q-ZnS, with a simplified electronic diagram.

Grätzel *et al.* have also used nanocrystalline TiO_2 to construct a photovoltaic cell (Figure 1.20).[128-130] Light absorption is achieved by a monolayer of dye (S) adsorbed to the surface of a thin film of TiO_2. When the dye, usually a complex of a transition metal, is excited (S*) by a photon of light, it injects an electron into the conduction band of the TiO_2, oxidising the metal complex (from +2 to +3 in the case of ruthenium dyes). The positive charge is countered by transfer of charge to a redox mediator (R/R^+) which reduces the complex back to its initial state. The redox mediator is present in the electrolyte and hence in contact with the counter electrode. With electron transfer through the semiconductor layer and eventually to the counter electrode, the circuit is closed, and the mediator returns to its reduced state. The cell therefore acts as a regenerative electrochemical cell, converting light to electricity without undergoing permanent chemical change. The reason for using nanocrystalline particles is primarily the large surface area of Q-TiO_2, allowing nanocrystalline films to have a large number of dye

molecules attached giving a large cross section of light capture. This is an important feature and gives the cell its high conversion efficiency. The role of the dye is similar to that of chlorophyll in green plants and has been used as such to model photosynthesis.

The novel optical and electronic properties are not the only phenomena of nanocrystals to be exploited. The ability to control the size and morphology of quantum dots lend to potential applications in nanotechnology. A single electron transistor has been developed, (Figure 1.21) using a TOPO capped CdSe nanocrystal.[78] The device consists of two gold electrodes, which act as the source and drain of the transistor, separated lithographically by 50 Å, on a doped silicon wafer which acts as the gate electrode. Bifunctional linker molecules such as 1,6-hexanedithiol on the gold electrodes bind any nanocrystals, and can trap a single quantum dot, 55 Å in diameter, between the gap ensuring measurable conductance. Other single electron transistors have been reviewed by Feldheim and Keating.[132]

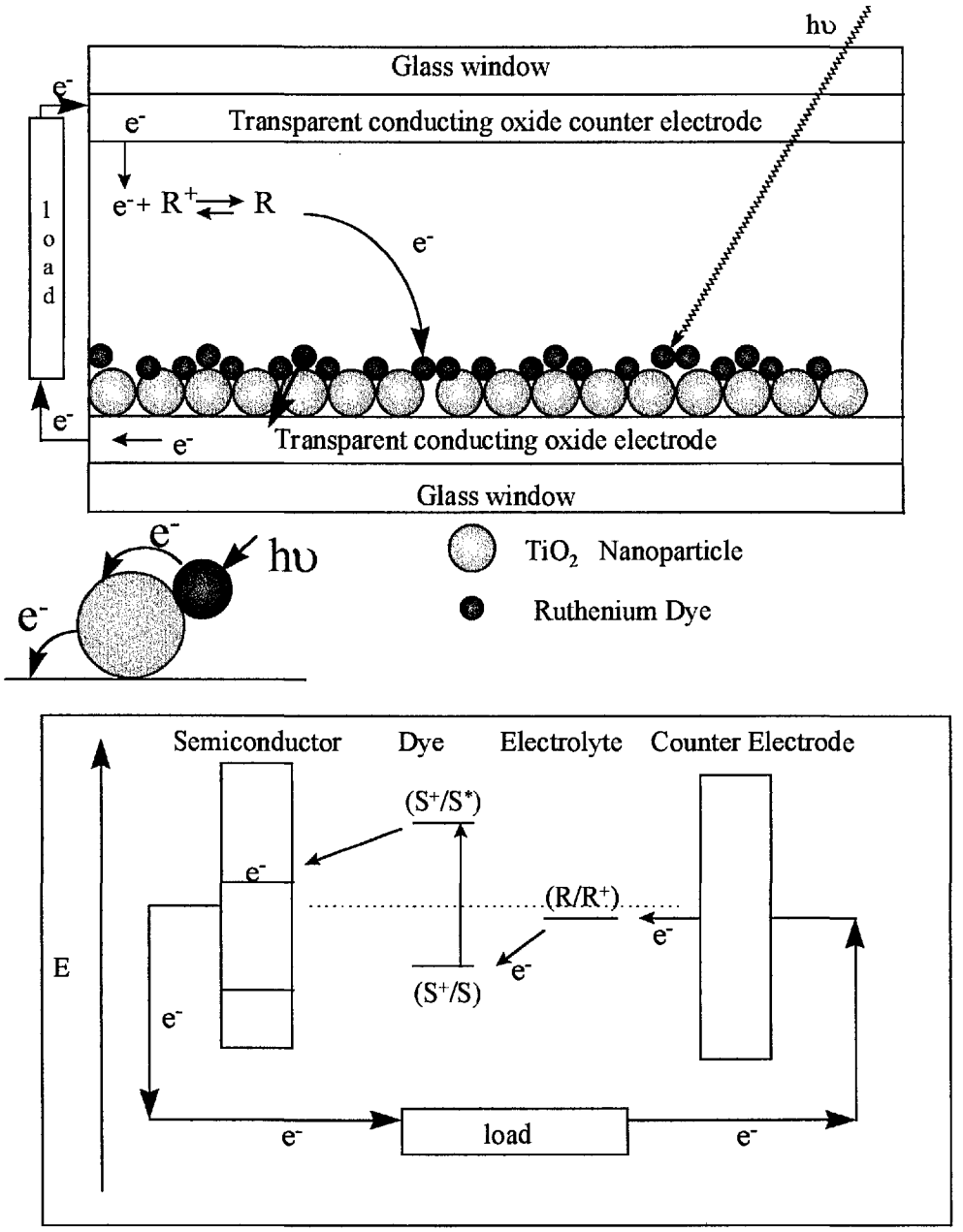


Figure 1.20: Schematic and energy diagrams for the Gratzel Cell.

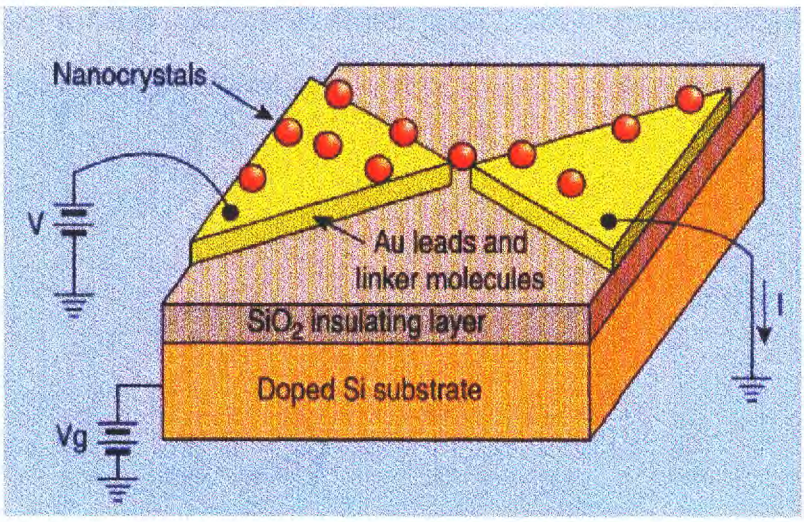


Figure 1.21: Diagram of a single electron transistor.[78]

The ability to synthesise highly luminescent, nearly monodispersed nanocrystals and their manipulation into simple devices offers simple routes to, for example, tunable diodes and highly efficient solar cells. The band gap of a semiconductor quantum dot can be altered by controlling the particle's dimensions (often referred to as band gap engineering) and has opened up possible new areas of electronic research with a wide range of applications.

Chapter 2 - Synthesis of nanodispersed II-VI compounds

2.1 Introduction

II-VI compounds have been the most investigated class of nanodispersed compound semiconductors, presumably because they are easily prepared by various methods.[3,5,8] The development of the TOPO method[35] (see chapter 1) resulted in a simple route to high quality, crystalline, nearly monodispersed, and easily manipulated quantum dots. However, the Bawendi route uses precursors similar to those used by Manasevit in the original MOCVD work, *i.e.*, a volatile metal alkyl and toxic chalcogen source at elevated temperatures.[133] Whilst these precursors are useful, they are toxic and systems such as PbS or HgS would require the use of a lead or mercury alkyl. One answer to such problems lies in the use of single source molecular precursors, in which the metal-chalcogenide bond is already present. The use of such precursors is common in low pressure MOCVD,[64,134] often giving high quality thin films without the need for toxic precursors such as H_2Se or H_2S. For less toxic, but more volatile, systems such as ZnE, (E = Se, S) an adduct of the metal alkyl can be used, as this gives stable species such as $Me_2Zn{\cdot}TEA$ (TEA = triethylamine).[135]

The first reported use of a single source molecular precursor for nanodispersed CdSe was by Steigerwald, in which $Cd(SePh)_2$ was thermolysed in 4-ethylpyridine.[49] This approach was further developed by Trindade, in which a range of metal (Cd, Pb, Zn) dithio- and diseleno- carbamates were decomposed in TOPO and 4-ethylpyridine to give high quality, organically capped, nanoparticles.[50] The TOPO capped particles produced by the single source route was comparable in structural and optical quality to the

analogous Bawendi dots. However, infra-red spectroscopy indicated a surface difference, which has yet to be investigated further.[50]

In this chapter, different precursors and an alternative Lewis base solvent to II-VI nanocrystals are described.

2.2 Synthetic methodology

Metal complexes such as dithiocarbamates have been reported to be effective single molecular precursors.[50] The complex *bis*(N,N-diethyl)monothiocarbamato-cadmium(II), $Cd(SCOCNR_2)_2$ (cadmium monothiocarbamate) appeared to be a potential precursor for nanodispersed CdS. A related compound, the TMEDA adduct of cadmium thioacetate, has previously been used in aerosol assisted chemical vapour deposition (AACVD) and is also a suitable potential precursor.[136] An improvement in the Bawendi system might be achieved if an adduct of dimethylcadmium could be used rather than the simple metal alkyl, especially as the current trend is towards high temperature (350 °C) synthesis, resulting in nanoparticles with no defects.[53] A stabilised metal source is therefore desirable. In this chapter the thermolysis of *bis*(N,N-diethyl)monothiocarbamato-cadmium(II) and cadmium thioacetate·TMEDA in TOPO is described. An adapted Bawendi method where the use of a triethylamine adduct of dimethylcadmium, and trioctylphosphine selenide/*tris*(trimethylsilyl)sulfide is also described.

The *bis*(N,N-diethyl)monothiocarbamato-cadmium(II) (Cd(MTC) hereafter) was prepared as described in the literature,[137] and its identity was confirmed by NMR, IR and

mass spectrometry. Cadmium thioacetate·TMEDA (Cd(TA) hereafter) was synthesised by the reaction of $Cd(OH)_2$, $HSOCCH_3$ and TMEDA in toluene at room temperature. NMR, IR and elemental analysis confirm the formula and are in agreement with cadmium thioacetate·TMEDA synthesised by Nyman *et al.*[136]

The adduct $Me_2Cd{\cdot}NEt_3$ was synthesised by the direct combination of dimethylcadmium and triethylamine in toluene.

In a typical preparation a single source precursor, either Cd(MTC) or Cd(TA), was dissolved in tri-*n*-octylphosphine (TOP). The precursor solution was then injected into hot TOPO stabilised at a temperature between 100 °C and 250 °C. The precursor was expected to decompose producing nuclei of CdS. The nucleii grew into nanocrystalline CdS (consistent with Ostwald ripening) and were finally passivated with the organic ligand (Figure 2.1). After 30 minutes growth the quantum dots were isolated by addition of a non-solvent (methanol), which increased the average polarity of the solution resulting in a decrease in the energy barriers to flocculation.[35] The resulting precipitate was isolated by centrifugation and re-dispersed into a hydrocarbon solvent, resulting in an optically clear nanoparticulate solution. The solution varied in colour depending upon the size of the dispersed dots. Thermolysis of Cd(MTC) and isolation of the resulting products gave a bright yellow solution.

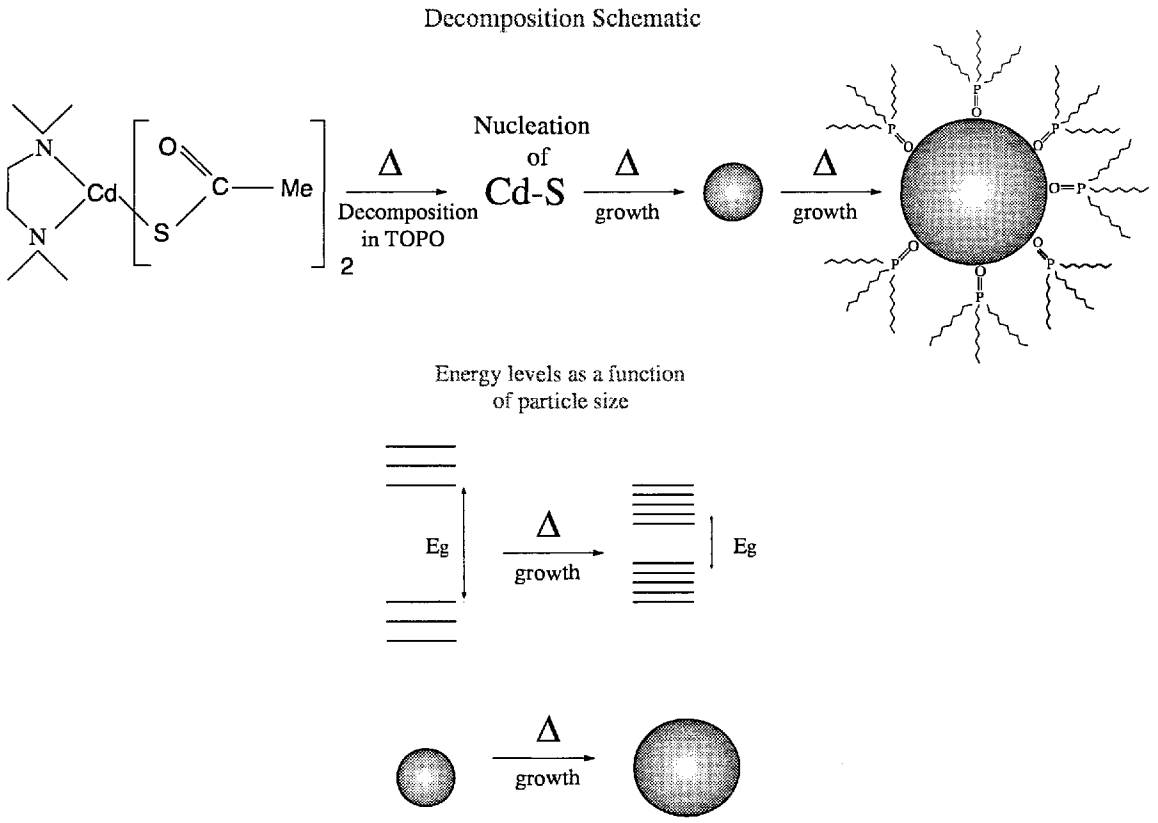


Figure 2.1: Decomposition scheme for the TMEDA adduct of cadmium thioacetate, showing the increase in band gap with smaller particles.

Material obtained by thermolysis of Cd(TA) at a range of temperatures (100 °C to 250 °C) for various times (30 mins to 2 hours) yielded a material which was slightly soluble in toluene. The electronic spectrum shows a band edge of 2.49 eV, similar to bulk CdS (Figure 2.2, Appendix 1), as determined by the direct band gap method described by Pankove,[134] in which absorption data are fitted in the equation:

$$\alpha(h\nu) \propto (h\nu - E_g)^{1/2} \qquad (1.8)$$

The CdS synthesised by thermolysis of Cd(TA) is therefore assumed to be larger than the excitonic radius of CdS (*ca.* 40 Å diameter) as it is exhibiting bulk behaviour. The insolubility of the material in hydrocarbons, with the band edge at a value associated with bulk material, strongly indicates macrocrystallite CdS.

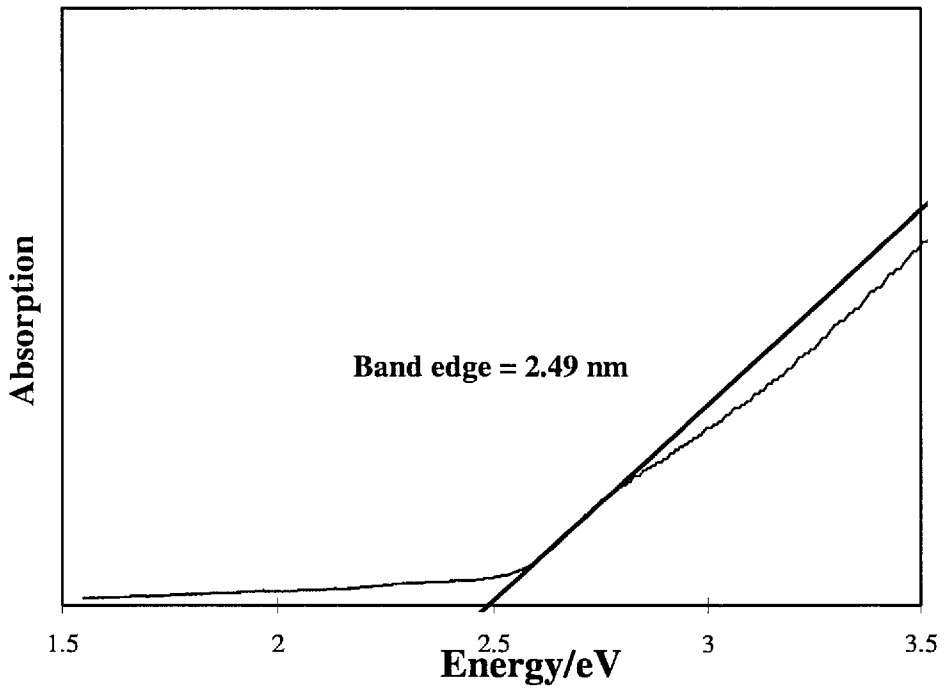


Figure 2.2: Optical absorption spectra of CdS synthesised by the thermolysis of $Cd(SCOCH_3)_2$·TMEDA.

An adaptation of the Bawendi method was developed which involved mixing dimethylcadmium·triethylamine with trioctylphosphine selenide or *bis*(trimethylsilyl)sulfide in TOP. This was then injected into TOPO at temperatures between 100 °C and 250 °C and left to grow. Isolation of the nanocrystals in hydrocarbons again resulted in optically clear coloured solutions.

2.3 Optical properties of Q-CdSe and Q-CdS

Macrocrystalline CdSe and CdS are reported to have optical band gaps of 1.74 and 2.42 eV respectively (716 and 512 nm).[139] Nanodispersed semiconductors can be easily characterised by the shift in the band gap to higher energies by optical spectroscopy. Figure 2.3 shows the optical spectrum of nanocrystalline CdS obtained from the thermolysis of Cd(MTC) (250 °C, 1 hr), and Me_2Cd·TEA with $(TMS)_2S$ in TOPO at various temperatures (30 mins. at 150 °C, 200 °C and 250 °C). The band edge of samples prepared at 200 °C and below is *ca.* 480 nm, typical of CdS with dimensions smaller than the bulk excitonic diameter.

CdS from the monothiocarbamate was found to have a band edge at 2.66 eV (465 nm) from the direct band gap method. The particle size was estimated using the effective mass model (Equation 1.6, Appendix 1) predicting a diameter of 4.78 nm. Size fractionation was attempted on CdS prepared by the thermolysis of Cd(MTC) by gradual addition of methanol to a toluene solution of dots until the solution became turbid. Centrifugation yielded a solid which was re-dispersed in toluene. The seventh fraction showed a shift in optical band edge to higher energies (2.81 eV, 441 nm), and a distinct excitonic peak at 411 nm (3.01 eV). The shift of the band edge and the excitonic peak are consistent with smaller particles with a narrower size distribution relative to the initial solution (Figure 2.4).

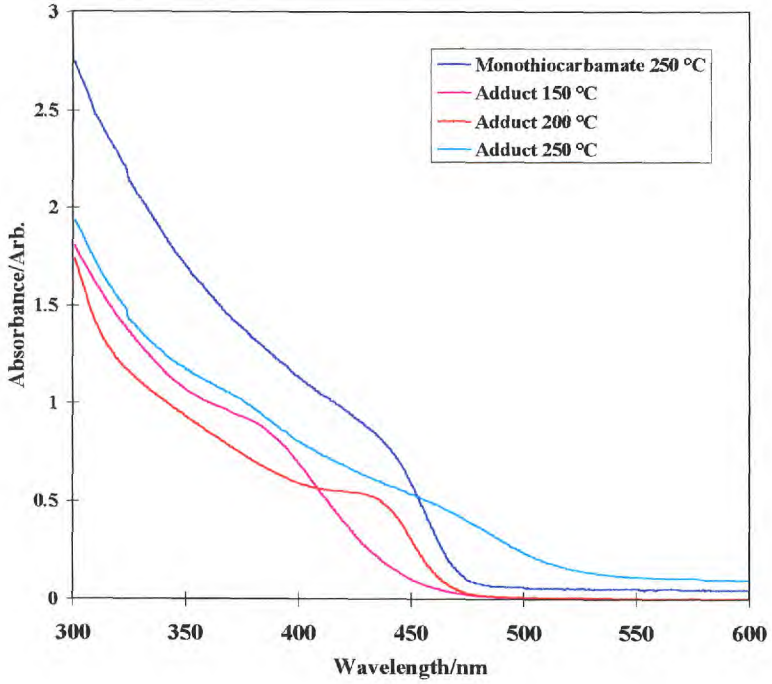


Figure 2.3: Optical absorption spectra of Q-CdS, grown by different methods.

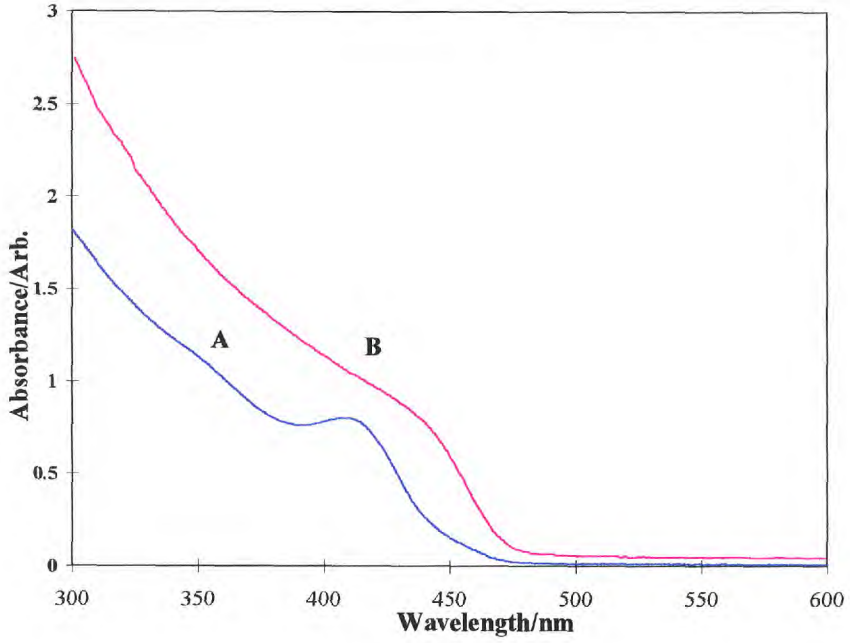


Figure 2.4: Optical spectra of CdS prepared by the thermolysis of cadmium monothiocarbamate at 250 °C, 1 hour: A) Seventh size fraction.; B) Initial solution prior to fractionation.

CdS produced by thermolysis of Me_2Cd·TEA and $(TMS)_2S$ had different diameters depending upon the synthesis temperature as shown by the optical spectra (Figure 2.3). The nanoparticles exhibit a higher energy band edge in the optical spectra with decreasing temperature of synthesis, indicating that lower synthesis temperatures resulted in the growth of smaller particles. Synthesis at lower temperatures (150 °C and 200 °C) gives rise to particles with distinctly blue shifted band edges of 2.88 eV (430 nm) and 2.69 eV (460 nm) respectively (as determined by the direct band gap method). The narrow size distribution is evident from the sharp band edge and excitonic features at 3.21 eV (385 nm) and 2.84 eV (435 nm) respectively.

Nanoparticles synthesised at 250 °C have optical spectra consistent with larger particles and a larger size distribution, giving a broad absorption with a band edge of 2.42 eV. This value is consistent with particles with diameters larger than the excitonic diameter. The high solubility in hydrocarbons, however, points to the possibility of the material still being nanodispersed, as bulk CdS capped with TOPO has previously been reported to be insoluble in toluene and much darker in colour than the bright yellow samples obtained in these experiments.[50]

Figure 2.5 shows spectra of Q-CdSe obtained from the thermolysis of Me_2Cd·TEA and TOPSe in TOPO at various temperatures (30 mins. at 120 °C, 180 °C, 200 °C and 250°C) and are consistent with previously reported spectra. The sample prepared at 250 °C shows a spectrum consistent with a highly monodispersed system, with two excitonic peaks clearly visible and a sharp band edge. Other samples prepared show an increasing blue shift with increasing temperature of synthesis, consistent with the theory that lower synthesis temperatures produce smaller particles.[35]

The absorption spectra of samples synthesised at 120, 180 and 200 °C are broader than the absorption spectra from samples prepared at 250 °C. Lower temperatures should ideally produce a monodispersed range of particles. CdSe described in this thesis appears to grow non-uniformly at lower temperatures. Other factors have previously been reported to produce non-uniform growth such as short alkyl chains on the capping agent.[35] It can be assumed that there is an optimum point at which nucleation occurs at a steady enough rate to allow slow growth. Below such a point, nucleation would be sporadic and chaotic. CdS may grow uniformly at a much lower temperature than CdSe. Work on TOPO capped CdSe reported by Bawendi *et al.*[35] and Alivisatos *et al.*[53] report injection temperatures of not less than 250 °C. The band edge of the sample synthesised at 250 °C, determined by the direct band gap method was found to be 2.23 eV (555 nm), an increase of 0.49 eV from macroscopic CdSe (Figure 2.5, inset). Using the Brus equation (Equation 1.6), the estimated diameter for such particles of CdSe is found to be 4.72 nm. The low temperature synthesis (120 °C) gave samples with a band edge of 2.72 eV (455 nm) with a predicted particle diameter of 3.48 nm.

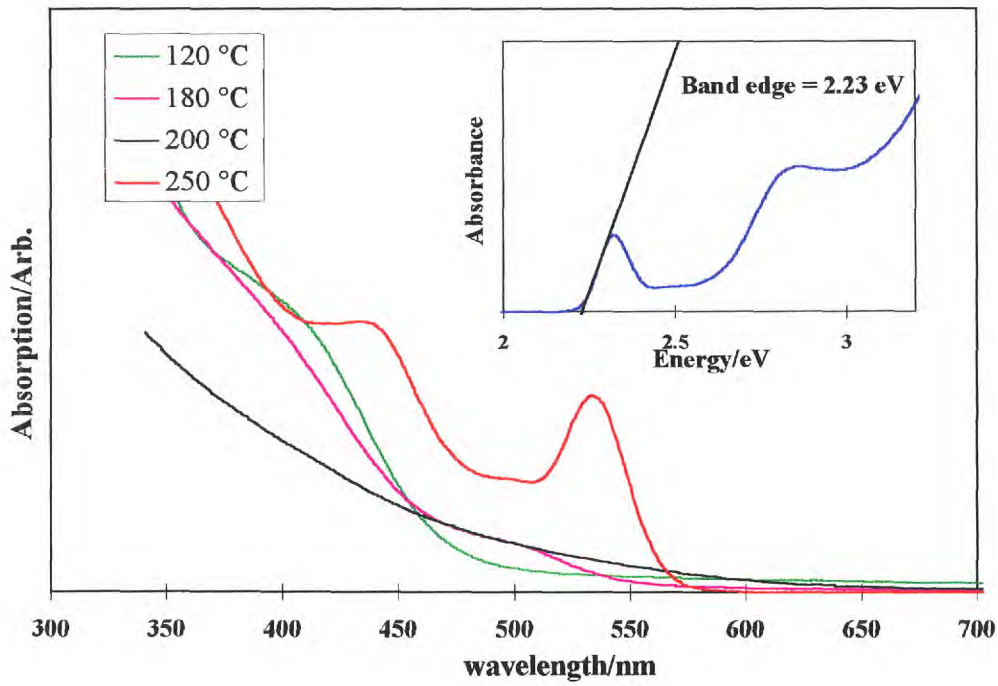


Figure 2.5: Optical absorption spectra for Q-CdSe synthesised by the thermolysis of Me_2Cd·TEA and TOPSe at different temperatures for 30 mins. Inset; Optical band edge of Q-CdSe synthesised at 250 °C.

2.4 Luminescence of Q-CdSe and Q-CdS

The thermolysis of Cd(MTC) and the adducts of dimethylcadmium with the relevant chalcogenide source in TOPO all yielded II-VI nanoparticles, as determined by optical spectroscopy, showing shifts in band edges to higher energies. Similar nanocrystals synthesised by the simple metal alkyl and chalcogen source report excellent band edge luminescence, consistent with small particles with no surface traps.[35]

Bulk cadmium sulfide is reported to have a broad emission between *ca.* 500 and 700 nm, attributed to the surface sulfur vacancies being efficient trapping sites for

electrons.[22] Recombination to an existing hole results in a broad red emission. Early work on nanocrystalline CdS reported bulk type emission despite having an increased band gap.[22,37] It was suggested that as the particles decreased in size, a larger number of surface traps evolved due to the large surface to volume ratio of atoms. The unpassivated surface sites then resulted in red emissions. The advent of the Bawendi route to nanocrystals resulted in the surface traps being blocked by the capping agent, resulting in strong band edge emission.[35] The nanoparticulate II-VI compounds presented in this thesis all exhibit strong band edge emission, some with evidence of trapping states.

Luminescence spectra of the seventh fraction of Q-CdS prepared from Cd(MTC) show band edge emission with a substantial lower energy emission between 550 and 750 nm (Figure 2.6). The red emission is usually attributed to surface defects, however surface passivation should reduce luminescence from such states. Oxygen doping from the precursor is a possible reason for such a low energy emission.

Luminescence spectra from Q-CdS prepared from the dimethylcadmium adduct and $(TMS)_2S$ show strong band edge emission with little evidence of surface states (Figure 2.7). The emission profiles show strong narrow luminescence, with low energy tails attributed to surface defects. The sample prepared at 150 °C had a band edge of 2.88 eV (430 nm), and an emission maximum at 2.90 eV (426 nm). Samples prepared at 250 °C had a band edge of 2.42 eV (512 nm), and an emission maxmum at 2.27 eV (546 nm).

Figure 2.9 shows typical luminescence spectra obtained from CdSe synthesised from dimethylcadmium·TEA and TOPSe at 250 °C for 30 minutes, with a $\lambda_{max.}$ at 564 nm (2.19 eV). The sample has a band edge of 555 nm (2.23 eV), therefore the emission may be classed as band edge. The Stokes shift of *ca.* 10 nm can be attributed to the emitting

state being a dark exciton[40,41] (chapter 1) and the associated relaxation of an excited electron into a dark state. Weak luminescence in the red end of spectrum indicates emission from traps, probably surface defects. Samples prepared at 120 and 200 °C (Figure 2.9) had band edge emissions at 2.68 eV (462 nm) and 2.54 eV (487 nm) respectively, with little evidence of surface traps. The broad emissions are consistent with the electronic spectra, which also indicated a wide size distribution.

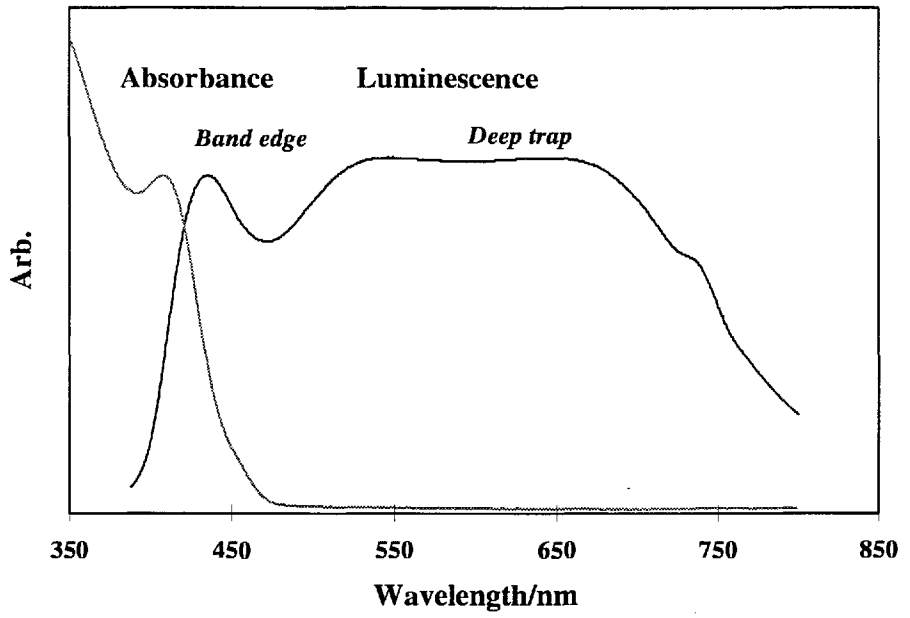


Figure 2.6: Optical absorption and luminescence spectra of Q-CdS synthesised from Cadmium (MTC), showing band edge and deep trap emissions.

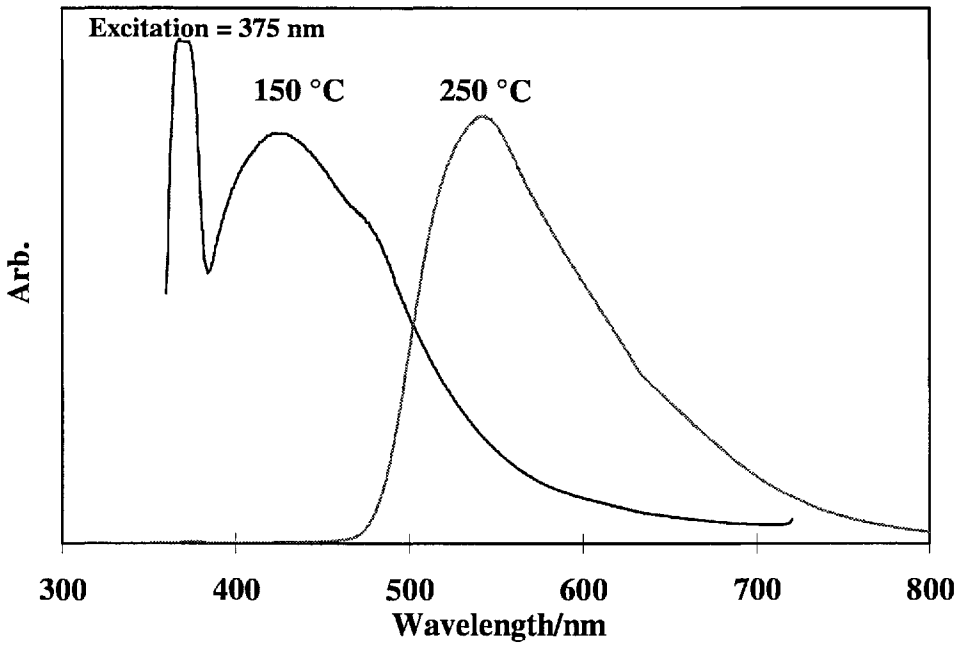


Figure 2.7: Luminescence spectra of Q-CdS prepared from Me_2Cd·TEA and $(TMS)_2S$ at different temperatures.

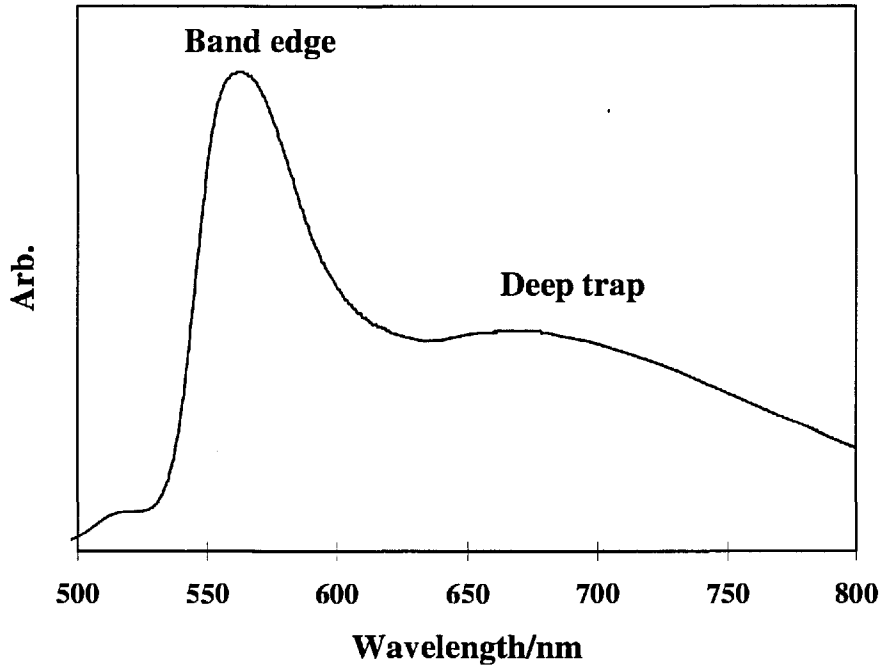


Figure 2.8: Luminescence spectrum of Q-CdSe synthesised by the thermolysis of Me_2Cd·TEA and TOPSe at 250 °C for 30 mins.

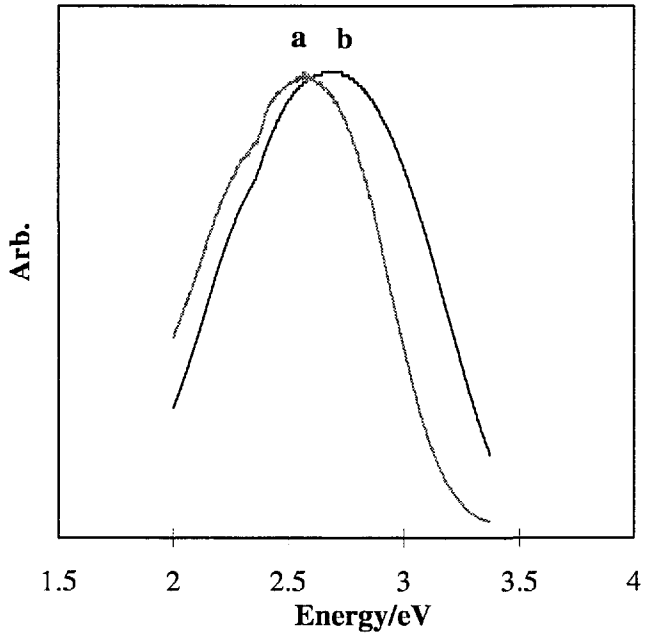


Figure 2.9: Luminescence spectra of Q-CdSe prepared by the thermolysis of Me_2Cd·TEA and TOPSe at a) 200 °C; b) 120 °C.

2.5 Structural characterisation of Q-CdSe and Q-CdS

Cadmium selenide and cadmium sulfide are reported to exist in two phases, zinc blende (cubic) and wurtzite (hexagonal) (Figure A1, appendix 1). X-ray powder diffraction on Q-CdSe and Q-CdS reported in this thesis show typical broadened diffraction patterns for nanoparticulate cadmium chalcogenides.[140] CdS prepared from Me_2Cd and $(TMS)_2S$ at 250 °C for 30 mins showed patterns for typical wurtzite material, showing broad clear reflections from the 110, 103 and 112 planes (Table 2.1, Figure 2.10). The broadness of the peaks are attributed to the small dimensions of the particle.

Nanocrystalline CdSe however, shows reflections typical of a smaller particle, in which the core has no specific crystalline phase and the distinction between zinc blende

and wurtzite is meaningless (Figure 2.11). A single broad reflection is observed between 2θ angles of 20 and 30° which normally indicates the 100, 101 and 002 planes. Two more broad reflections are observed between 2θ angles of 40 and 55° normally indicative of reflections from the 110, 103 and 112 planes.

HRTEM images of Q-CdSe and Q-CdS (Figures 2.12a and 2.13) prepared by the thermolysis of the adduct of dimethylcadmium and TOPSe/$(TMS)_2S$ at 250 °C/150 °C respectively show mono-dispersed crystalline particles with a clearly hexagonal lattice (Figure 2.12b). TEM images provide us with an array of nanoparticles, from which an average diameter and standard deviation can be calculated.

For CdS, synthesised by the adduct of dimethylcadmium and *bis*(trimethylsilyl)sulfide at 150 °C, a band edge of 2.88 eV was observed. Using the new band edge, a particle diameter of 3.7 nm was predicted (Equation 1.6). TEM shows an average particle diameter of 3.54 nm ± 0.18 nm (5.0 %) (Figure 2.14).

Material	*d* (experimental)/Å	*d* (literature)/Å	*hkl*
CdS	3.59	3.58	100
	3.33	3.36	002
	3.16	3.16	101
	2.44	2.45	102
	2.06	2.07	110
	1.88	1.89	103
	1.76	1.76	112
	1.39	1.39	203

Table 2.1: Powder XRD data for nanocrystalline CdS and comparison to the literature.

Q-CdSe synthesised at 150 °C gave particles with a diameter of 3.65 nm and a standard deviation of 0.25 nm (6.7 %) (Figure 2.15). The absorption edge has been used to predict the particle's diameter using the effective mass approximation (equation 1.6) giving an estimated diameter of 3.48 nm. The diameters observed in this work are comparable to dimensions observed in the II-VI nanoparticles prepared by Bawendi[35] or Trindade.[50] The observed nanoparticle's diameters correlate favourably with estimates from the effective mass approximation[23] and the standard deviation was found to be *ca.* 5 %.

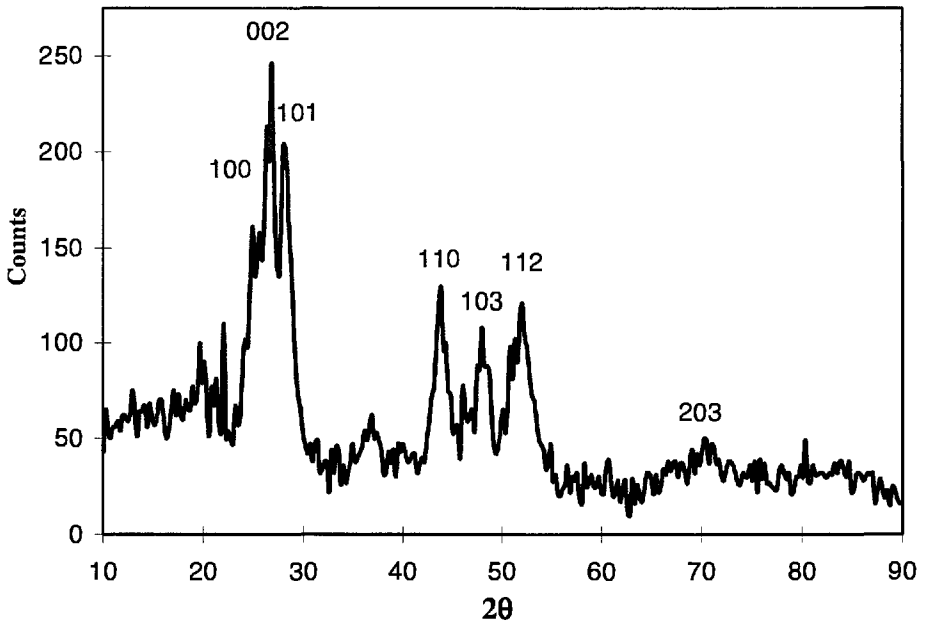


Figure 2.10: XRD pattern of Q-CdS prepared by the thermolysis of Me_2Cd·TEA and $(TMS)_2S$ at 250 °C, with Miller indices indicated.

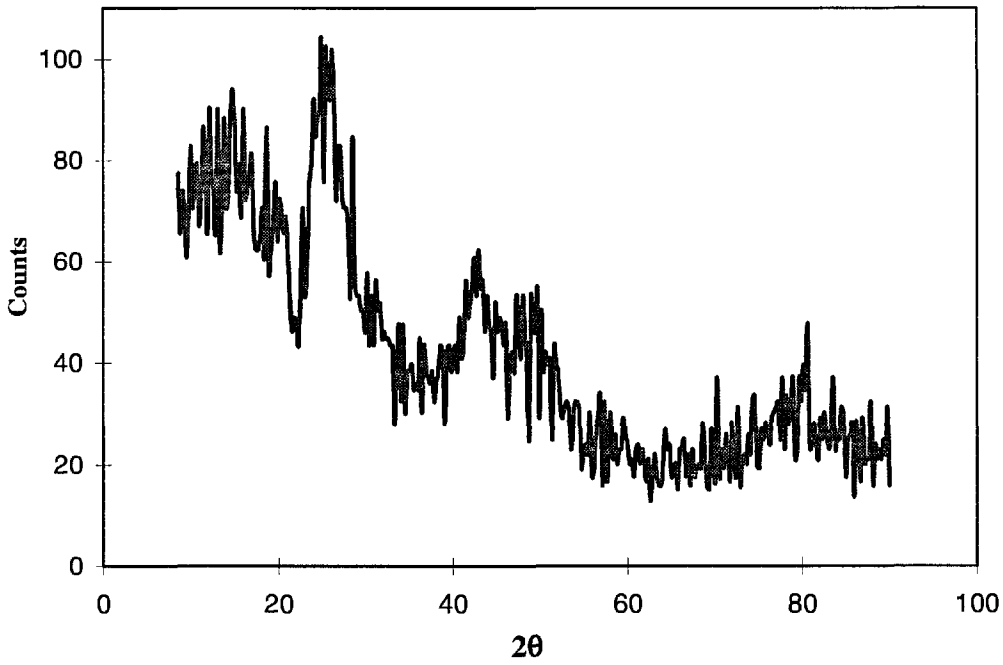
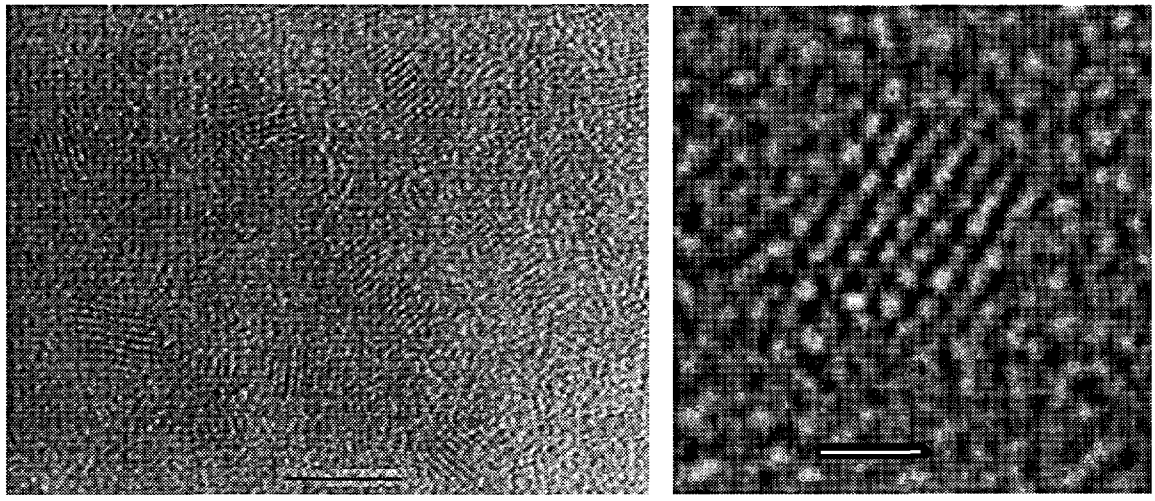


Figure 2.11: XRD pattern of Q-CdSe prepared by the thermolysis of Me_2Cd·TEA and TOPSe at 250 °C.



a *b*

Figure 2.12: a) HRTEM image of an array of Q-CdSe nanoparticles, bar = 5 nm; b) HRTEM image of a CdSe nanocrystal, showing a hexagonal lattice, bar = 1 nm.

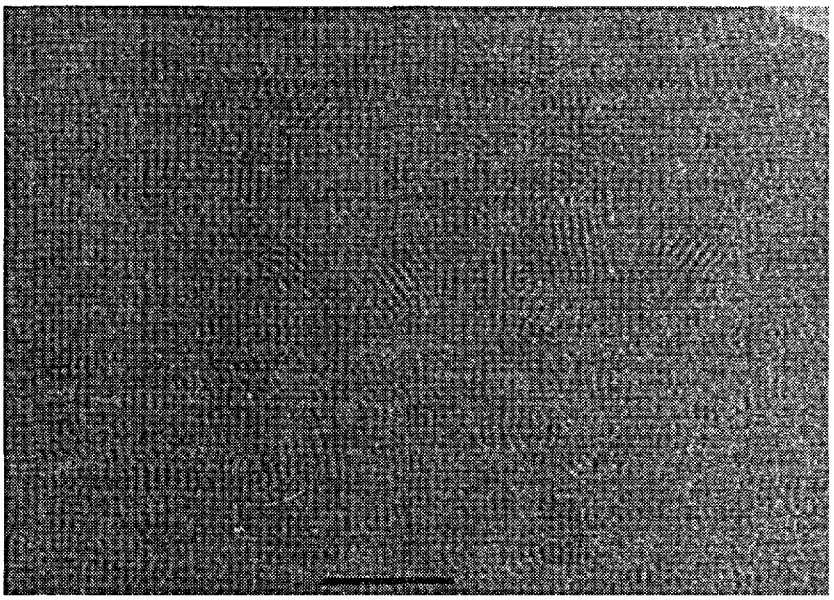


Figure 2.13: HRTEM image an array of Q-CdS, bar = 5 nm.

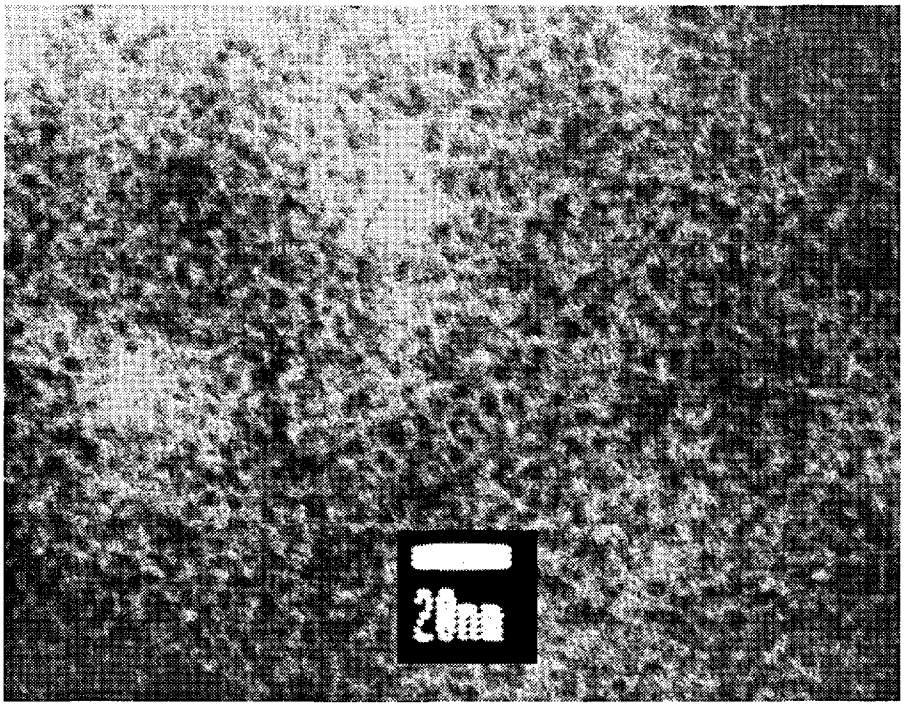


Figure 2.14: TEM image of Q-CdS synthesised by the adduct method at 150 °C.

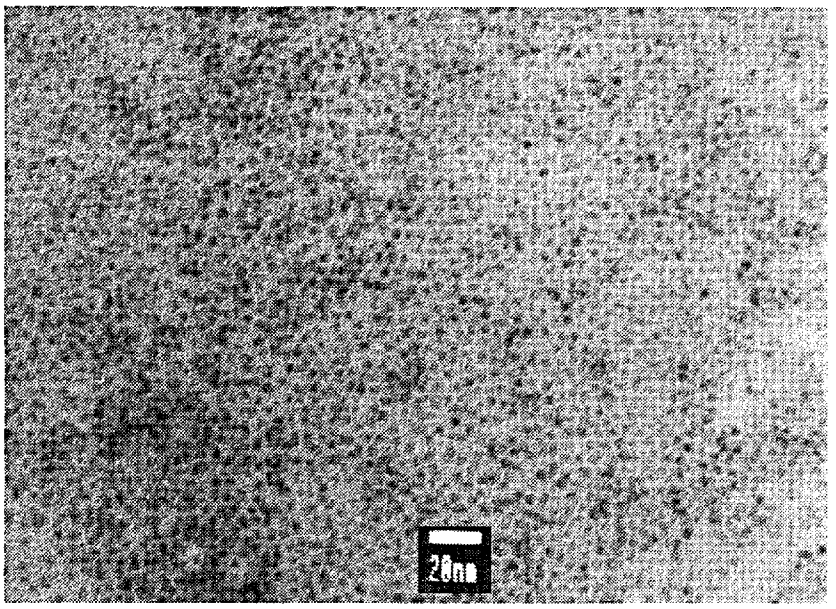


Figure 2.15: TEM Image of Q-CdSe synthesised by the adduct method at 150 °C, bar = 20 nm.

Nuclear magnetic resonance (NMR) spectroscopy of quantum dots has also been used to investigate the capping group and surface bonding properties of TOPO. Solution and solid state MAS ^{31}P NMR of six samples prepared by various methods have been investigated. Single source precursors, such as those described by Trindade[50] have a metal atom bound to five chalcogen atoms. With the metal-chalcogen bond in place, a simple thermolysis mechanism could leave a nanoparticle with a chalcogenide rich surface. Nanoparticles prepared by Murray *et al.* use a 30 % excess of Me_2Cd, possibly giving the particle a metal rich surface for TOPO to bind to.[35] Differences in bonding to various surface moieties could possibly be seen by NMR. The effect of TOP as both a medium for which to deliver the precursors into the reaction vessel and as a capping agent could be investigated. As a Lewis base, TOP should bind to metal sites, and selenium sites

through a simple covalent bond. The addition of TOPSe to single source routes to CdSe may show an increased resonance for the TOP binding to the selenium sites on the surface. For these studies, nanocrystals were synthesised by six methods:

CdSe was prepared by the thermolysis of;

1) Me_2Cd·TEA adduct and TOPSe
2) $NpCd(Se_2CNEt_2)_2$[50]
3) $NpCd(Se_2CNEt_2)_2$ with TOPSe.

CdS was prepared by thermolysis of;

1) Me_2Cd·TEA adduct and $(TMS)_2S$
2) $MeCd(S_2CNEt_2)_2$[50]
3) $NpCd(S_2CNEt_2)_2$[50]

Attempted preparation of Q-CdS by thermolysis of a single source precursor with $(TMS)_2S$ to see the effect of the silylated precursor failed, producing macroscopic CdS.

To aid identification, ^{31}P solution state NMR of TOPO, TOP, TOPSe, and TOPS[141] was obtained. Free TOPO (purified as described in the literature[142]) showed a strong resonance at 49.22 ppm. Impurities were present and were observed at 53.55 and 55.38 ppm. A detailed chromatographic study by Kolosky *et al.*[143] revealed that TOPO generally has impurities such as dioctylphosphine oxide, dioctylmonophosphinic acid and monoctylphosphonic acid, which may be the source of other resonances. TOP has a resonance at -30.34 ppm, TOPSe has a resonance at 36.84 ppm, and TOPS, which is not a precursor, but could be a surface species, has a resonance at 48.49 ppm, with an impurity at *ca.* 57 ppm.

Solid state ^{31}P NMR of CdSe/TOPO previously reported by Becerra *et al.* show one broad resonance between 20 and 35 ppm.[52] The resonance consists of two components, TOPO at 29.3 ppm, and TOPSe at 22.2 ppm. Free TOPO and TOPSe were reported to have isotopic lines at 54.2 and 46.9 ppm respectively.

Trindade performed similar ^{31}P MAS NMR experiments on Q-CdS prepared by a single source route and bulk CdS bound with TOPO.[50] Q-CdS/TOPO displayed resonances at 47.81, 25.39, 6.20 and -5.68 ppm. Bulk CdS/TOPO displayed resonances at 32.6, 11.8 and -3.8 ppm. The resonance at 47.88 ppm was assigned as free TOPO, with the resonances between 20 and 30 ppm assigned as TOPO bound to the nanocrystal surface. The difference in resonances for bonded TOPO was attributed to different surface states, however the broad resonance prevents distinguishing between the two and they may in fact be the same species.

From our MAS NMR results (Tables 2.2 and 2.3), we observe a range of resonances, which we tentatively assign. Trindade[50] and Becarra[52] have previously investigated ^{31}P MAS NMR and their results have been considered whilst assigning resonances. The resonances below 40 ppm can be attributed to the bound Lewis base species, however further identification is difficult. The solid state NMR resonance at *ca.* 47 ppm is attributed to free TOPO and not free TOPSe as this resonance also appears in CdS spectra. Small amounts of impurities are observed at 50 ppm and above.

Solution ^{31}P NMR spectra (Tables 2.2 and 2.3) also provide information about the bonding state. The resonance at *ca.* 35 ppm is assigned as bound TOPO (not free TOPSe, as these peaks again appear in NMR studies on CdS particles), with no contribution observed from TOPSe or TOP bound to the nanoparticle surface. No difference in

resonances was observed in the sample with excess TOPSe. Kuno *et al.* have since confirmed these results by conducting experiments with and without TOP.[51] Broad resonances between 28 and 35 ppm were attributed to bound TOPO, the width of the resonance being due to the inhomogeneous distribution of magnetic environments on the particle surface. Kuno also assigned a peak at -20 ppm as bound TOP.[51]

From our NMR studies, we cannot determine surface differences in metal rich and chalcogen rich quantum dots through NMR, but can assign bound and free Lewis base capping agents.

Q-CdS from Me_2Cd·TEA and $(TMS)_2S$				
Solution state ^{31}P NMR			^{31}P MAS NMR	
δ ppm	assignment		δ ppm	assignment
32.93	Bound TOPO		32.02	Bound TOPO
35.07	Bound TOPO		45.72	Free TOPO
48.63	Free TOPO		47.79	Free TOPO
52.99	Impurity		50.00	Free TOPO
57.68	Impurity		54.82	Impurity
			56.25	Impurity

Q-CdS from $NpCd(S_2CNEt_2)_2$				
Solution state ^{31}P NMR			^{31}P MAS NMR	
δ ppm	assignment		δ ppm	assignment
35.29	Bound TOPO		34.28	Bound TOPO
37.09	Bound TOPO		35.96	Bound TOPO
48.92	Free TOPO		39.54	Bound TOPO
53.25	Impurity		45.85	Free TOPO
57.88	Impurity		47.80	Free TOPO
			50.00	Free TOPO

Q-CdS from $MeCd(S_2CNEt_2)_2$				
Solution state ^{31}P NMR			^{31}P MAS NMR	
δ ppm	assignment		δ ppm	assignment
35.30	Bound TOPO		47.83	Free TOPO
48.96	Free TOPO		51.03	Impurity
53.30	Impurity			

Table 2.2: Solution state and solid state NMR data for Q-CdS prepared by various methods.

Q-CdSe from Me_2Cd·TEA and TOPSe				
Solution state ^{31}P NMR			^{31}P MAS NMR	
δ ppm	assignment		δ ppm	assignment
35.32	Bound TOPO		34.27	Bound TOPO
37.06	Bound TOPO		37.16	Bound TOPO
48.96	Free TOPO		45.91	Free TOPO
53.30	Impurity		47.85	Free TOPO
			55.00	Impurity

Q-CdSe from $NpCd(Se_2CNEt_2)_2$ with TOPSe.				
Solution state ^{31}P NMR			^{31}P MAS NMR	
δ ppm	assignment		δ ppm	assignment
37.05	Bound TOPO		37.09	bound TOPO
48.80	Free TOPO		45.18	Free TOPO
53.15	Impurity		47.82	Free TOPO

Q-CdSe from $NpCd(Se_2CNEt_2)_2$				
Solution state ^{31}P NMR			^{31}P MAS NMR	
δ ppm	assignment		δ ppm	assignment
35.32	Bound TOPO		46.19	Free TOPO
37.06	Bound TOPO		47.81	Free TOPO
48.96	Free TOPO		50.35	Free TOPO
53.30	Impurity			

Tables 2.3: Solution state and solid state NMR data for Q-CdSe prepared by various methods.

IR spectroscopy of TOPO shows a strong absorption at 1466 cm^{-1}, attributed to $\nu(CH_3)$.[53] The ν(P=O) stretch is found to shift from 1146 cm^{-1} to 1120 cm^{-1} upon complexation of the phosphine oxide to the surface cadmium.[53] All II-VI nanoparticles presented in this work exhibited this shift, which indicates binding to the surface metal sites by the P=O moiety. Nanocrystals prepared by the thermolysis of single source molecular precursors were reported not to have this shift, indicating a possible surface difference.

2.6 Different Solvent Systems

Lewis base solvents such as TOPO and pyridine have proved to be successful capping agents and reaction solvents. The criteria for such a solvent/passivating agent has been defined as a polar species with at least one lone pair of electrons available to form a bond with a surface molecule, with ideally, a boiling point high enough to facilitate the thermolysis of organometallic precursors.[49,50]

Dimethylsulfoxide (DMSO) is a common commercially available chemical used in all branches of chemistry as a solvent and reagent. Its physical and chemical attributes at first glance appear to make it ideal as a capping agent. DMSO is well known to form co-ordinate complexes through either the lone pair on the sulphur atom,[144,145] or the two lone pairs on the oxygen atom.[146,147] The boiling point is high enough (189 °C) to allow decomposition of precursors such as metal dithiocarbamates, giving, in theory, DMSO passivated nanocrystals.

Thermolysis of cadmium diethyldithiocarbamate in DMSO at 189 °C for 1 hour resulted in the formation of a bright yellow solution. Isolation of the nanocrystals as a solid was achieved by the addition of methanol (a non-solvent) followed by centrifugation. The powder was found to be soluble in DMSO only. Attempts to disperse the powder in toluene caused immediate irreversible flocculation resulting in a solid which was completely insoluble in all solvents, including DMSO. This is attributed to the removal of surface DMSO by toluene. Colloidal stability was found to be poor, with the particles staying in solution for only a matter of hours.

Optical absorption spectroscopy of a DMSO colloid showed a shift in the optical band edge to 2.55 eV (485 nm), with an excitonic shoulder visible at *ca.* 450 nm as shown in figure 2.16. The shift in band edge is consistent with particles of 5.87 nm diameter (Effective mass approximation, equation 1.6). Photoluminescence spectroscopy showed band edge emission with little evidence of surface trapping states, with a maximum of *ca.* 480 nm (2.58 eV).

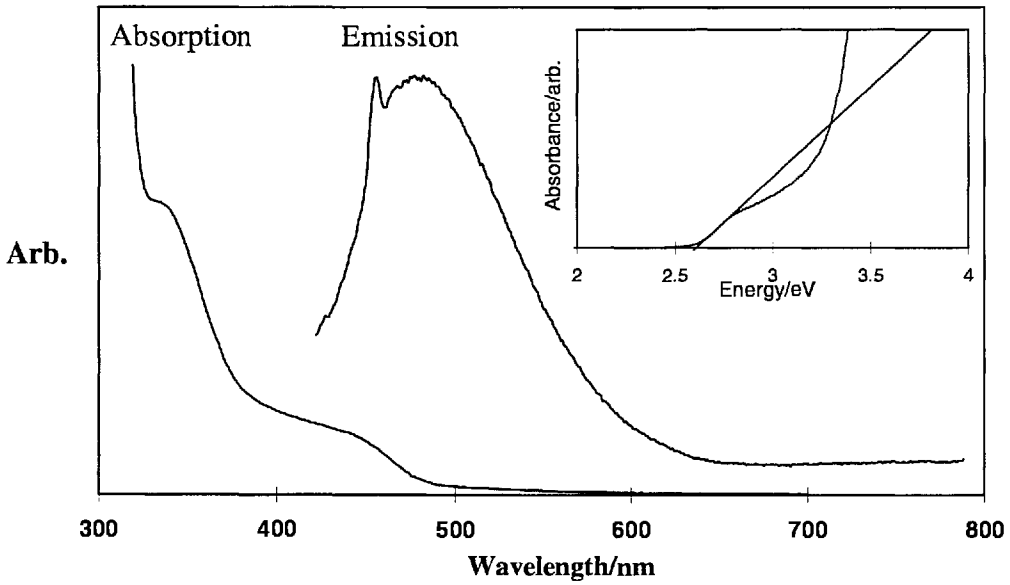


Figure 2.16: Optical absorption and photoluminescence spectra of Q-CdS capped with DMSO; Inset, determination of band edge by direct band gap method.

^{1}H NMR of the powder shows a resonance at 2.5 ppm indicating the presence of DMSO. The ν(S=O) IR stretch in dimethylsulfoxide capped dots is expected to shift due to complexation to surface cadmium, in the same manner as the ν(P=O) stretch in TOPO capped dots shifts.[148] DMSO is unusual, however, as two atoms in the molecule can act as electron donors (lone pair on the sulfur and two lone pairs on the oxygen). Infra red studies can show us which atom is acting as the surface bonding species. Cotton *et al.* studied bonding modes in sulfoxide complexes.[149] Free DMSO has a ν(S=O) stretch at 1055 cm^{-1}.[148] Shifts to wave numbers lower than this are indicative of oxygen bonding, whilst shifts to higher wave numbers indicate bonding through the sulfur atom.

The cadmium complex $CdCl_2$·DMSO is reported to have a ν(S=O) stretch at 950 cm^{-1}, implying bonding through the oxygen atom, which is common for metal complexes of DMSO.[148]

DMSO capped Q-CdS has a sharp feature at 1097 cm^{-1}, indicating bonding through the sulfur atoms. This at first appears surprising, as the reported cadmium complex reports oxygen bonding. The surface of CdS however, is reported to be sulfur deficient, and the Lewis base sulfur in DMSO may bond preferentially over the expected O atom to fill the sulfur vacancy (Figure 2.17). The two methyl groups are not large enough to be considered sterically important. Bonding through the sulfur atom may also explain the insolubility in hydrocarbons, as the alkyl groups will be pressed close to the nanocrystal, and not available for dispersion in similar hydrocarbon solvents.

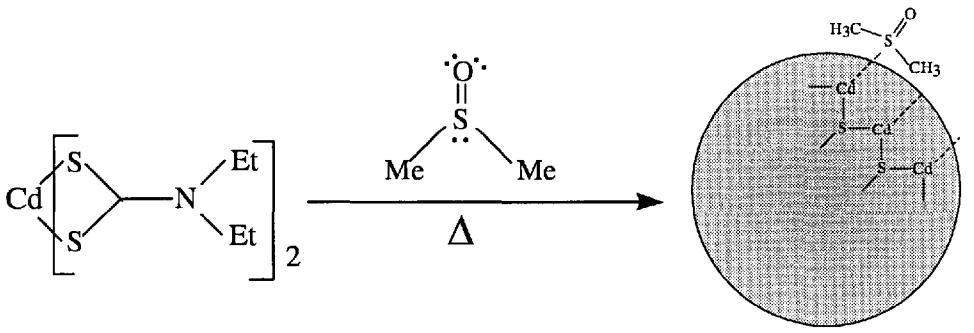


Figure 2.17: Reaction scheme for cadmium dithiocarbamate in DMSO showing the suggested bonding of the capping group.

2.7 Conclusions

In this chapter we have shown that the single source precursor cadmium monothiocarbamate can be used in the preparation of nanoparticulate CdS. A related precursor, cadmium thioacetate·TMEDA adduct was not a suitable precursor, yielding what appeared to be bulk CdS.

A route to CdS and CdSe by using the adduct of the metal alkyl and a chalcogen source was successfully developed and the optical and structural properties investigated. The use of a solvent/capping system not previously employed for passifying nanocrystals (DMSO) was investigated giving nanocrystalline CdS using a precursor previously employed for TOPO capped quantum dots.

The single source route to nanodispersed particles appears to have distinct advantages over existing routes. The choice of precursor appears paramount and the correct choice of solvent appears equally important. The difficulties encountered during this study led to the work described in the following chapters.

Chapter 3 - Synthesis of nanodispersed II_3-V_2 compounds

3.1 Introduction

Bulk II_3-V_2 compounds have many potential applications within devices such as infra red detectors, lasers and also in the field of solar cell technology.[150-155] Due to the large excitonic radii of these compounds, they are expected to exhibit strong size quantization effects. An electron in such a compound will become confined at crystal sizes much larger than in analogous II-VI or III-V materials (Table 3.1). However, many methodologies previously employed for the preparation of bulk II_3-V_2 compounds, such as direct combination of stoichiometric amounts of the desired elements in a multi-zone furnace, are not adaptable to nanocrystal synthesis.[156]

Compound	$*m_n$	$*m_p$	ε	exciton diameter/ Å
Cd_3P_2	0.05	0.5	15.5	360.9
Zn_3P_2	-	-	11	-
GaP	0.1	0.86	9.1	107.5
InP	0.07	0.65	12.7	212.7
CdSe	0.13	0.45	6.1	64.0
CdS	0.19	0.8	5.7	39.3

Table 3.1: Exciton diameters as calculated from Equation 1.4. Constants taken from sources in Appendix 1. Values for effective mass are in units of the free electron mass. Zinc phosphide has no effective mass data.

Synthetic routes to phosphide semiconductors are usually defined by one of three methods;

1] Phosphinolysis, in which a metallorganic compound reacts with phosphine gas.[157]

2] Thermolysis/Alcoholysis of a silylated precursor, which takes advantage of the well studied labile P-Si bond.[158,159]

3] Elimination reactions between $P(SiMe_3)_3$ and a metallorganic compound or a metal halide (dealkylsilylation or dehalosilylation).[69,158]

To date, little research has been conducted on nanodispersed group II phosphides, with arsenides being almost completely overlooked. Cadmium phosphide exists in an anti-Mn_2O_3 structure (Appendix 1), with a band gap of 0.5 eV, the minimum direct transition being at point Γ in the Brillouin zone.[156,160]

Buhro has developed a number of organometallic routes to both Q-Cd_3P_2 and Q-Zn_3P_2, using the methods described above.[158] One particularly successful route involves the methanolysis of a silylated single source precursor;[85,86]

$$Cd[P(SiPh_3)_2]_2 + 4/3\ MeOH \longrightarrow Q\text{-}Cd_3P_2 + \text{other products.}$$

The resulting nanocrystals were capped by Ph_3Si at the phosphide sites and by OMe at the metal sites. Replacement of the phenyl groups on the precursors for methyl groups resulted in bulk material being formed. The reaction mixture was left to anneal in toluene at 60 °C for 15 hours. The same reaction with the zinc precursor resulted in the formation of $Zn(OMe)_2$.[158] The X-ray powder diffraction pattern for Cd_3P_2 was reported, but was later held to be inaccurate as the dots appeared to have annealed in the electron beam of the electron microscope during characterisation.[161] Other organometallic routes, including the reaction of metal perchlorates/halides with *tris*(trimethylsilyl)phosphine resulted in quantum dot formation but no diffraction data could be obtained.[158,85,86]

TEM studies on Q-Cd_3P_2 to date provide evidence for the production of a mixture of crystalline and amorphous materials.

Weller has described an essentially colloidal route to Q-Cd_3P_2 using a variety of metal salts and phosphine gas in triethylamine and methyl methacrylate, followed by room temperature vacuum polymerisation in a sealed quartz cuvette.[162] Earlier work was based upon an aqueous route using hexametaphosphate as a stabiliser.[163] The dots were characterised primarily by measurements of lattice fringes with no X-ray diffraction data reported. Difficulties associated with this route include the use of hazardous phosphine gas and limited manipulation of the particles due to their air sensitivity. However, these nanoparticles decomposed upon exposure to air and illumination.

Zinc phosphide (Zn_3P_2) is a relatively new and poorly characterised compound, with most of the research carried out during the last decade in the search for novel optoelectronic materials.[164,165] The bulk material has the same structure as Cd_3P_2 and a band gap of 1.40 eV.[156,160] Pseudopotential calculations of the band structure are complicated by the unusual structure and these data remains uncertain.[166] Using the band structure presented in the literature, the direct transition is located at point Γ in the Brillouin zone.[156,160] Zinc phosphide nanocrystallites have been briefly reported in the literature including an optical spectrum from a colloidal route,[163] TEM data from the reaction between zinc alkoxide and *tris*(trimethylsilyl)phosphine,[158] but no experimental details in either case.

3.2 Synthetic methodology

This chapter describes the synthesis of Cd_3P_2 and Zn_3P_2 nanocrystals, following the work of Bawendi,[35] Steigerwald,[49] Trindade[50] and Cowley.[167] The Bawendi method, discussed in chapter 1 involves the thermolysis of organometallic precursors by injection into a hot co-ordinating solvent, producing high quality II-VI materials.[35] This method is adapted to the synthesis of M_3P_2 (M = Cd, Zn) by injecting precursors dissolved in TOP into hot TOPO. Steigerwald has produced CdSe nanocrystals by refluxing $Cd(SePh)_2$ in 4-ethylpyridine, to produce organically capped dots.[49] The route is of particular interest in the work reported here as the capping group possesses no phosphorus moiety, which overcomes the problems of analysing phosphide nanocrystals capped with phosphorus containing ligands. Trindade's work on single source routes to TOPO/4-ethylpyridine passivated II-VI quantum dots has previously been discussed.[50]

Cadmium Phosphide

3.3 Potential precursors for Cd_3P_2

Diorganophosphides were chosen as potential single source precursors for the preparation of phosphide semiconductors. A 'one pot' synthetic process is more attractive than a multi-step series and has the advantage of avoiding the use of hazardous phosphine gas and metal alkyls at elevated temperatures. Compounds such as $M(PPh_2)_2$ (M = Hg, Zn) were prepared in the 1960's using lithiated phosphine and the relevant metal chloride.[168] These materials were found to be polymeric which made analysis problematic, extending no further than confirmation of the empirical formula. However these compounds have poor solubility, an essential prerequisite for homogeneous precursor delivery into the reaction vessel. Cowley has prepared a relevant cadmium diorganophosphide, $[MeCdP^tBu_2]_3$, containing both the group II metal and phosphorus moiety in a distorted ring conformation.[169] The route reported involved a transmetallation reaction between $Ga(P^tBu_2)_3$ and Me_2Cd, followed by fractional crystallisation, to afford the pure product in 75 - 95 % yield.

However, the possibility of contamination from the gallium species made it necessary to develop a simpler route in this present study, using the metal alkyl and dialkylphosphine in a methane elimination reaction.

$$3\ Me_2Cd + 3\ HP^tBu_2 \longrightarrow [MeCdP^tBu_2]_3 + 3\ CH_4$$

The reaction gave a crystalline product in toluene, trioctylphosphine and hexane with yields of *ca.* 98 %. Due to the insoluble nature of the isolated compound, a sample for NMR was prepared using the method previously described by Beachley *et al.* in which the reaction is conducted in deuterated solvent.[170] The ^{1}H NMR and ^{31}P NMR data correlate with previous reports.[169] The ^{13}C NMR was not previously reported. In our studies no ^{13}C resonance corresponding to the methyl group was observed. Single crystal analysis confirmed the structure which is reported in Appendix 2.

Whilst investigating routes to other potential precursors, reactions between dimethyl cadmium and either dicyclohexylphosphine or dicyclopentylphosphine in various solvents were carried out, giving $[MeCdPCy_2]_3$ or $[MeCdPCp_2]_3$ (Cy = cyclohexyl and Cp = cyclopentyl). Analysis of the products proved difficult due to the extreme air sensitivity of the compounds and the tendency of the solvent to co-ordinate, making microanalyses unreproducible.

Similar compounds prepared by Wright *et al.*[171,172] were analysed by single crystal analysis and ^{1}H and ^{31}P NMR. The analogous compounds reported here compare favourably with the diorganophosphide previously described. The metallation reaction between diphenylphosphine and dimethylcadmium appeared to produce a different complex, in which two $HPPh_2$ ligands act as donors in the complex. The NMR data suggest a structure similar to $\{[EtZn(\mu\text{-}PPh_2)]_3(HPPh_2)_2.thf\}$, previously reported by Wright *et al.*[172] The compound was assigned as $[MeCd(\mu\text{-}PPh_2)]_3(HPPh_2)_2$.

No ^{13}C NMR data has previously been reported for any group II diorganophosphide compounds making comparison difficult. No *ipso* carbon resonance was observed for the phenyl groups in $[MeCd(\mu\text{-}PPh_2)]_3(HPPh_2)_2$. NMR studies on metal

salts of diphenylphosphine show a major shift in the *ipso* carbon resonance of up to 30 ppm with metals.[173] Studies also showed an increased shift with increasingly large metals. A large metal such as cadmium is expected to attenuate such a shift in the *ipso* resonance. No methyl resonance was observed.

The three new compounds, $[MeCd(\mu\text{-}PPh_2)]_3(HPPh_2)_2$ and $[MeCdPCy_2]_3$ and $[MeCdPCp_2]_3$ were investigated as potential precursors to Cd_3P_2 along with $[MeCdP^tBu_2]_3$.

3.4 Thermolysis of Diorganophosphides

Decomposition mechanisms of precursors are important. Assignment of a correct mechanism can lead to the optimisation of growth conditions often resulting in high purity crystalline end products. Compounds such as dithio- and diseleno- carbamates have been found to be excellent precursors for II-VI compounds, yet appear to have complex decomposition mechanisms, with products dependent upon the specific organic groups attached to the precursor.[174,175] This type of molecular design, leading to precursors for electronic materials, has been extensively researched over the past decade with input from chemists applying knowledge of typically organic mechanisms to such systems.[64,176]

There is only one previous report on decomposition products of a diorganophosphide.[177] Mercury *bis*(dibutylphosphide) was previously reported to undergo photo-reductive elimination at room temperature, to yield elemental mercury and $P_2{}^tBu_4$.

TGA analysis of $[MeCdP^tBu_2]_3$ (Figure 3.1) provided evidence for two distinct phases of decomposition. The first phase is found between room temperature and *ca.* 100 °C, and the second in the temperature range 100 °C to 250 °C.

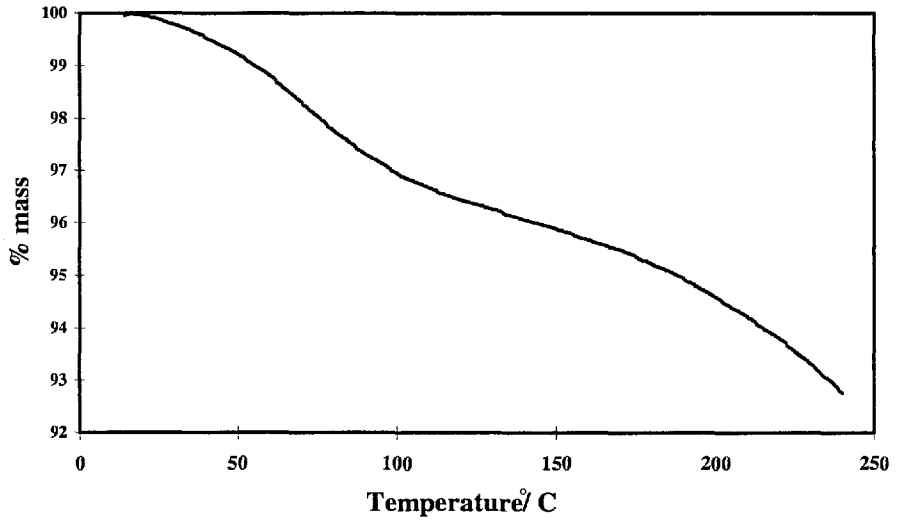


Figure 3.1: TGA analysis of $[MeCdP^tBu_2]_3$.

The two different phases of decomposition can be elucidated when comparing thermolysis products. Injection of $[MeCdP^tBu_2]_3$ into hot TOPO below 100 °C resulted in effervescence and a coloured solution of nanoparticles. Synthesis at temperatures of 150 °C and above yielded a coloured solution of Cd_3P_2 nanoparticles and a black solid, identified by X ray diffraction as elemental cadmium. Traces of elemental cadmium were also found at synthesis temperatures below 150 °C.

This can be explained by a process involving two competing mechanisms (Figure 3.2). Low temperatures (100 °C and below) promote β-hydrogen elimination as the major decomposition pathway, with small amounts of reductive elimination as a minor pathway. Higher temperatures (150 °C and above) result in both β-hydrogen elimination and

reductive elimination. This can be rationalised in terms of the energy required to induce both processes. β hydrogen elimination is a low energy process in contrast to cadmium-phosphorus bond cleavage which is a relatively high energy process.

GC-MS studies on $[MeCdP^tBu_2]_3$ at two different temperatures (90 °C and 250 °C) showed the precursor decomposed over *ca.* 20 mins., with the majority of decomposition occurring within the first 10 mins. The major thermolysis products from GC-MS experiments are shown in table 3.2 and indicate the expected β-elimination product; the alkene $(CH_3)_2C=CH_2$ (m/z = 56) occurs initially in the first few minutes at both temperatures investigated (90 °C and 250 °C). The predominant thermolysis product at both temperatures however appears to be $C(CH_3)_3$ (m/z = 57). The peak at m/z 57 also appears in the room temperature mass spectrum of $[MeCdP^tBu_2]_3$, and therefore is not necessarily a thermolysis product. A species indicative of reductive elimination P^tBu_2 (m/z = 145) appears at both temperatures, predominantly at 250 °C. A signal at 146 has been assigned as HP^tBu_2, a product from β-elimination on one phosphide group followed by elimination (Figure 3.2)

Low temperature GC-MS studies (90 °C) suggest a simple mechanism, with few thermolysis products and none with a mass higher than 176. The pattern of results provide good evidence that β-hydrogen elimination may be the major pathway, with minor contributions from reductive elimination. Evidence was found for the previously reported reductive elimination product, $P_2{}^tBu_4$, as the signal at m/z = 176 occurs consistently and can be attributed to $P_2{}^tBu_2$, a possible by-product of $P_2{}^tBu_4$.

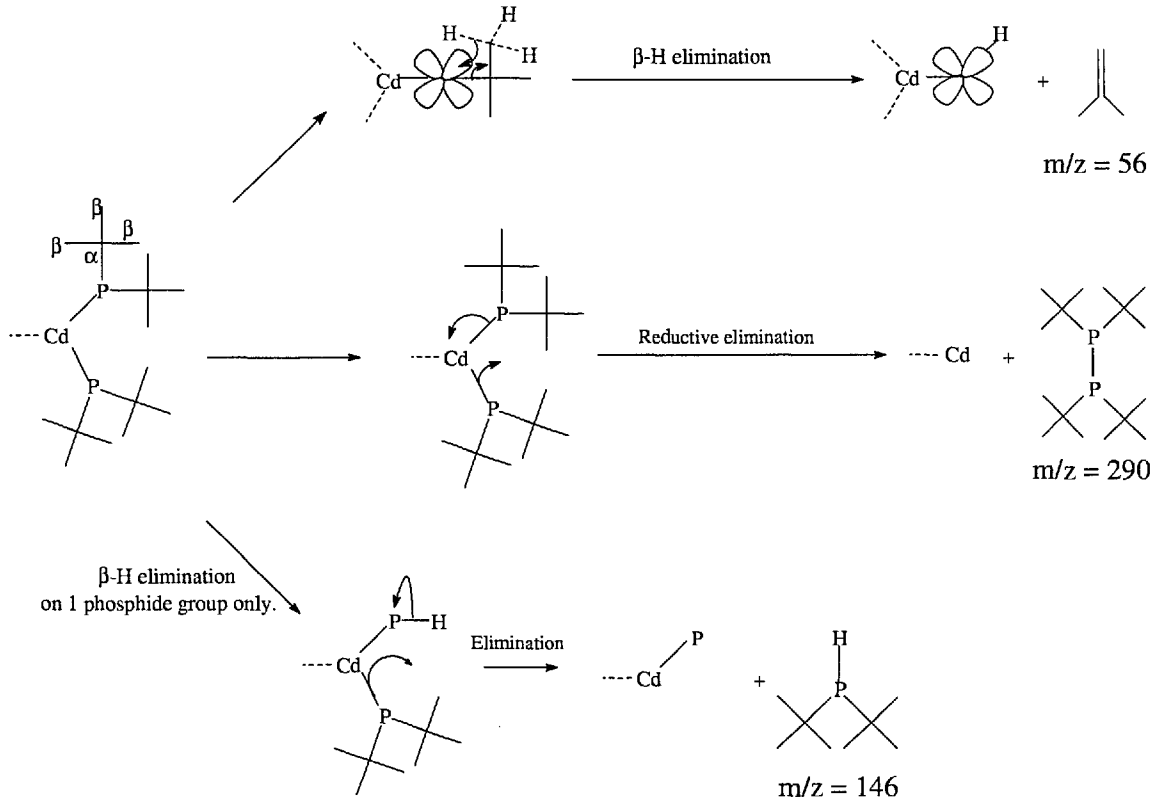


Figure 3.2: Suggested decomposition pathways for $[MeCdP^tBu_2]_3$.

GC-MS results from higher temperature (250 °C) studies are consistent with those expected for β-hydrogen elimination, but not necessarily as the major pathway. The signals for P^tBu_2 (m/z =145) appears more frequently, suggesting a greater contribution from reductive elimination processes. Higher molecular mass (*ca.* 300 m/z) fragments are revealed after 10 minutes. Experiments at 250 °C (retention time 18.19 mins.) gave signals at 176, 233 and 290 amu, consistent with $P_2{}^tBu_4$ and related fragments. There is also evidence of P^tBu_3 (m/z = 202) as shown in table 3.2.

Although not conclusive, GC-MS is supportive of the two mechanism hypothesis. Key fragments at m/z = 57, and 145 also appear in room temperature mass spectrometry

studies, which prevents the definite assignment of mechanisms. The presence of both $(CH_3)_2C=C(H)_2$ and $P_2{}^tBu_4$ are consistent with β-elimination and reductive elimination but does not conclusively establish the two mechanisms.

Corroborating results are obtained when the precursor is thermolysed in 4-ethylpyridine. The period of thermolysis appears to play a significant role, prolonged exposure to heat resulting in an increased metallic content in the product. Aliquots taken after 30 mins of refluxing at 120 °C, followed by isolation with a non-solvent, were established to have a Cd:P ratio of 1.6:1 ($Cd_{3.2}P_2$), as determined by ICPAES. Thermolysis for over 1 hour at 167 °C resulted in an increase in the Cd content, consistent with reductive elimination. Ratios of Cd:P were found to be as high as 7:1 for compounds thermolysed at 167 °C for 24 hours.

Further evidence was obtained from experiments involving thermolysis of a compound in which the tertiary butyl groups (*i.e.*, all hydrogen are in the β position) were replaced with phenyl groups. Thermolysis of $[MeCd(\mu\text{-}PPh_2)]_3(HPPh_2)_2$ in TOPO at 100 °C and 250 °C resulted in the formation of a black solid, with no evidence of nanoparticulates. All solids were isolated by addition of non solvent and centrifugation (*cf.* chapter 5, section 5.6.1) and were found to consist of at least 90 % elemental bulk cadmium with *ca.* 1 % phosphorus. No evidence was found for the compound Cd_3P_2. Following these results, compounds without β hydrogen's were no longer investigated.

Temperature of thermolysis/ °C	Retention time/ minutes	m/z	assignment
90	2.39	56	$H_2C=C(CH_3)_2$
	2.57	56	$H_2C=C(CH_3)_2$
	5.83	57	^tBu
		131	$P^tBu\ (C(CH_3)_2)$
		146	HP^tBu_2
		176	$P_2{}^tBu_2$
250	0.84	56	$H_2C=C(CH_3)_2$
	5.56	57	^tBu
	9.83	57	^tBu
	12.17	106	-
		131	$P^tBu\ (C(CH_3)_2)$
		146	HP^tBu_2
	12.21	202	P^tBu_3
	18.19	176	$P_2{}^tBu_2$
		233	$P_2{}^tBu_3$
		290	$P_2{}^tBu_4$

Table 3.2: Selected major peaks from GC-MS studies of $[MeCdP^tBu_2]_3$ at two different temperatures.

Thermolysis of $[MeCdP(Cp)_2]_3$ (for which only 4 hydrogens out of 9 on the organic moiety are β-H) produced a solution containing only a small amount of nanoparticulate species. A comparison of the precursors highlights the importance not only of the organic groups, but also steric factors and reaction by-products. It is interesting to note that phenyl groups have β hydrogens in the same sense as cyclic compounds, but are planar and therefore are unlikely to interact with the available *d* orbitals on the phosphorus atom. Cyclic compounds have twisted conformations with axial or equatorial hydrogens in positions where interaction is possible. The process of β

hydrogen elimination within a phenyl group would also require the production of benzyne as a reaction by-product which is unlikely, whereas cyclic alkanes would produce an alkene (Figure 3.3).

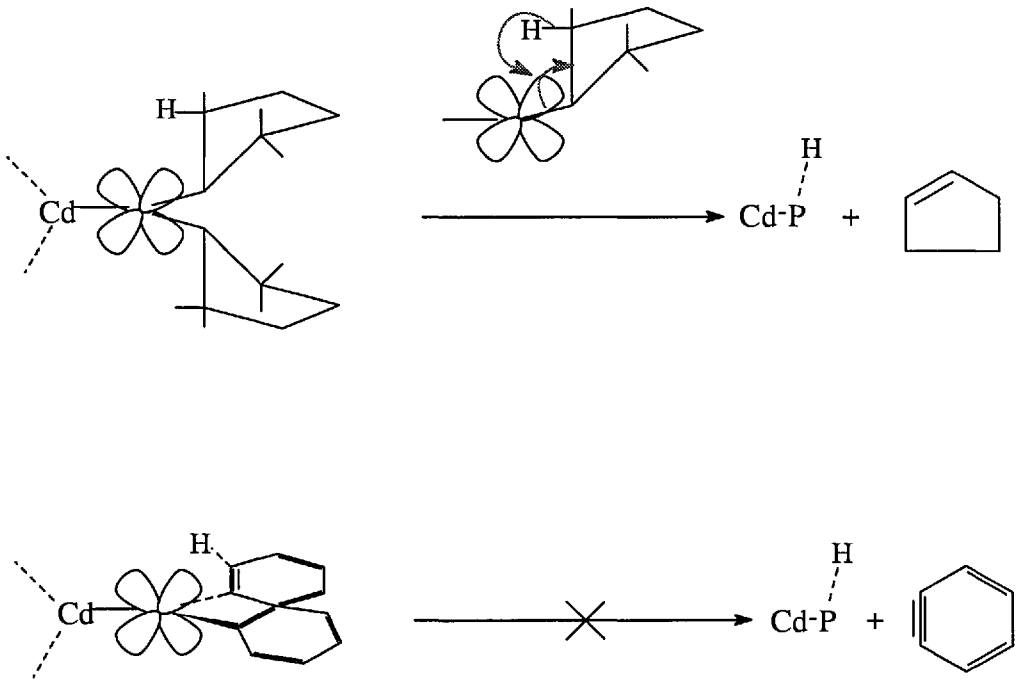


Figure 3.3: Suggested orbital interactions in different organic groups, explaining why β hydrogen elimination occurs for some groups but not others.

In summary it is apparent that high temperatures and excessive reaction times yield elemental cadmium as a by-product; Together with the observation that precursors are required to have β hydrogens, parameters were established and optimised to yield nanoparticulate solutions of Cd_3P_2 with minimal contamination.

3.5 Optical properties of Q-Cd_3P_2

Controlled thermolysis of $[MeCdP^tBu_2]_3$, $[MeCdP(Cp)_2]_3$ and $[MeCdP(Cy)_2]_3$ in co-ordinating solvents resulted in nanoparticulate Cd_3P_2 which could be isolated and re-dispersed in various solvents. All three precursors gave nanoparticulate powders with similar optical band edge after 1 hour thermolysis in 4-ethylpyridine (Figure 3.4). Thermolysis of $[MeCdP(Cp)_2]_3$ and $[MeCdP(Cy)_2]_3$ produced a large amount of insoluble material in addition to a small amount of nanoparticulate material. The superior yields and efficiencies of precursors possessing ^{t}Bu provided the starting basis for further studies.

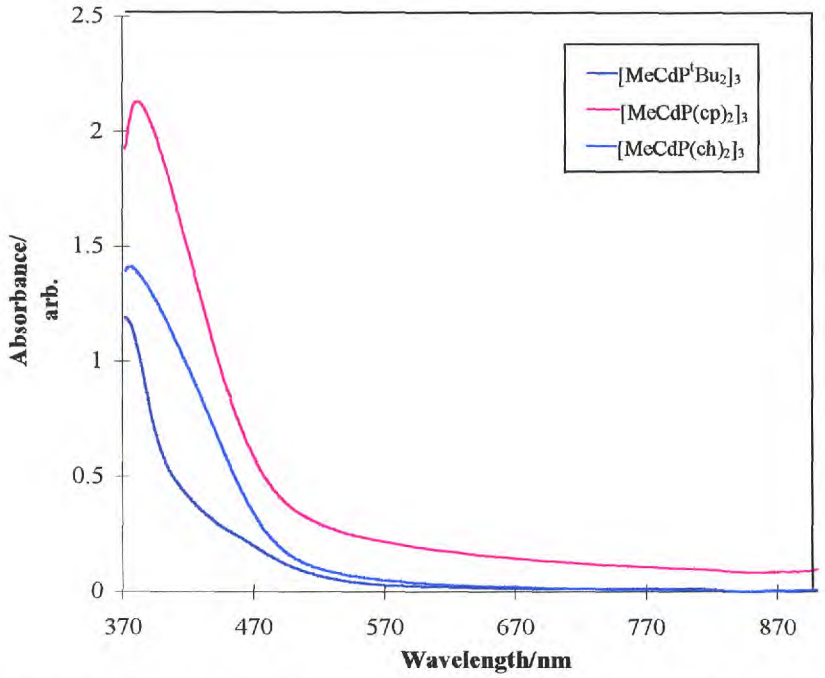


Figure 3.4: Optical absorption spectra of nanoparticulate solutions made from three different precursors after 1 hour thermolysis (167 ℃) in 4-ethylpyridine.

Bulk cadmium phosphide is reported to have a direct band gap of 0.5 eV.[160] However, nanodispersed particles of Cd_3P_2 have blue shifted band edges indicating the increase in band gap due to quantum confinement. This shift is a function of particle size which can be controlled by experimental parameters. Thermolysis of $[MeCdP(^tBu)_2]_3$ in 4-ethylpyridine at 167 °C for 24 hours resulted in a solution containing nanoparticulate material which exhibited a significantly blue shifted optical spectrum, with an excitonic peak ($\lambda_{max.}$) at 2.71 eV (457 nm) (Figure 3.5). The band gap was estimated to be 2.44 eV using the direct band gap method of Pankove (Equation 1.8)[138] and corresponds to particles much smaller than the of the bulk excitonic diameter of 361 Å.

Size fractionation of the sample was achieved by gradual addition of light petroleum to a 4-ethylpyridine solution until the sample became cloudy. Centrifugation yielded solid particulates which were re-dispersed in 4-ethylpyridine. The initial fraction was a deep red/brown, with the final fraction being yellow, indicating different sizes in different fractions. The optical band edges of these fractions (Figure 3.6) show an increase in the observed blue shift, suggesting larger particles precipitate first, followed progressively by increasingly smaller particles. The band edge for the seventh fraction was determined to be 3.07 eV (403 nm).

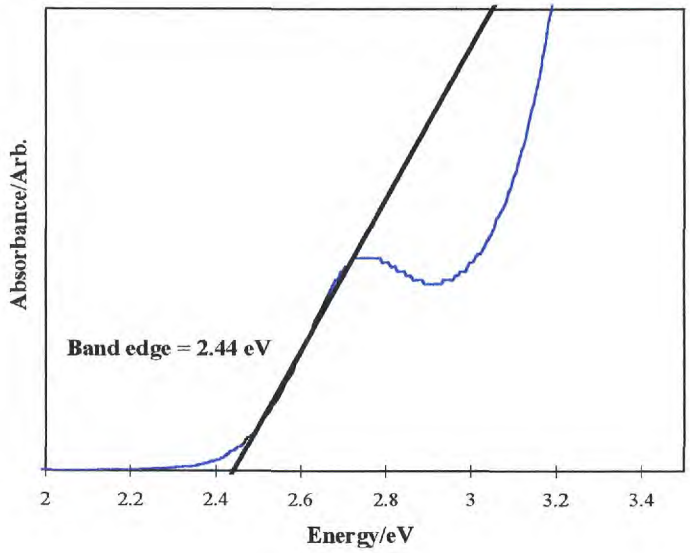


Figure 3.5: Optical band edge (direct band gap method) of Q-Cd_3P_2 synthesised from $[MeCdP^tBu_2]_3$ in 4-etpy at 167 °C for 24 hours.

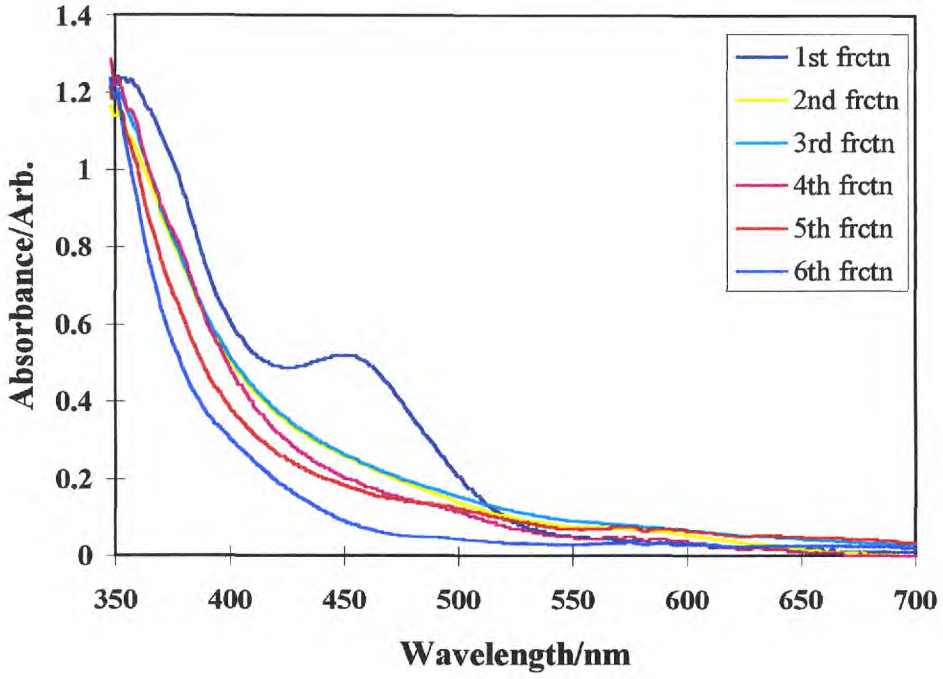


Figure 3.6: Optical absorption spectra of a 4-etpy solution of Q-Cd_3P_2 and six size fractions.

An unusual feature is the decrease of the excitonic feature, which usually becomes more pronounced as the fractions become smaller and the size distribution became narrower, attributed to an increase in oscillator strength.[36] However, optical spectra of TOPO capped CdSe synthesised by Murray *et al.* shows an excitonic feature that eventually decreases with size selective precipitation.[35] It can therefore be assumed that the excitonic feature does not in fact disappear but is masked by the increased blue shift of the absorption band edge.

Thermolysis of $[MeCdP(^tBu)_2]_3$ in TOPO gave a different initial optical spectrum to that observed for 4-ethylpyridine capped particles. Samples prepared at 90 °C were yellow in colour in contrast to samples prepared at 250 °C which exhibited a red/brown colour. The observed optical band edges for all samples prepared were similar and distinctly blue shifted from the bulk band edge of 0.5 eV (band edges *ca.* 2.79 eV, figures 3.7 and 3.8) suggesting that the particles were smaller than those synthesised in 4-ethylpyridine.

Variations in the temperature of synthesis did not result in a major significant difference in band edge position except for the sample prepared at 250 °C. Absorption spectra from samples prepared at 90 °C had a band edge of 2.79 eV (444 nm). Samples prepared at 220 °C had an absorption band edge of 2.60 eV (476 nm). Samples prepared at 250 °C displayed a lower energy onset of absorption at *ca.* 2.40 eV (516 nm). Optical absorption spectra from samples prepared at low temperature (90 °C) had pronounced

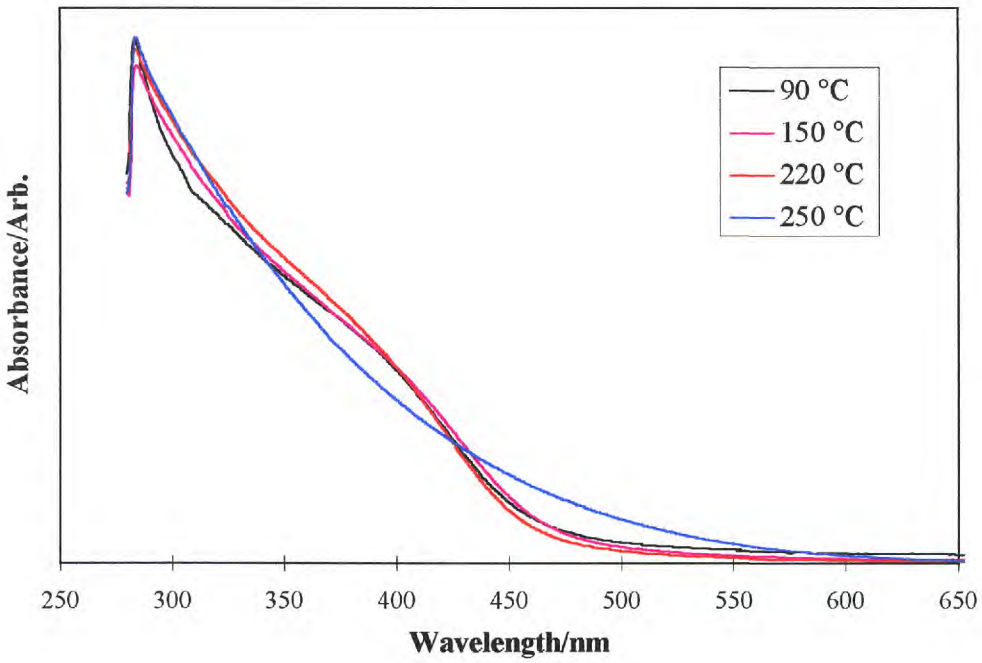


Figure 3.7: Optical spectra of Q-Cd_3P_2/TOPO synthesised at different temperatures for 30 mins.

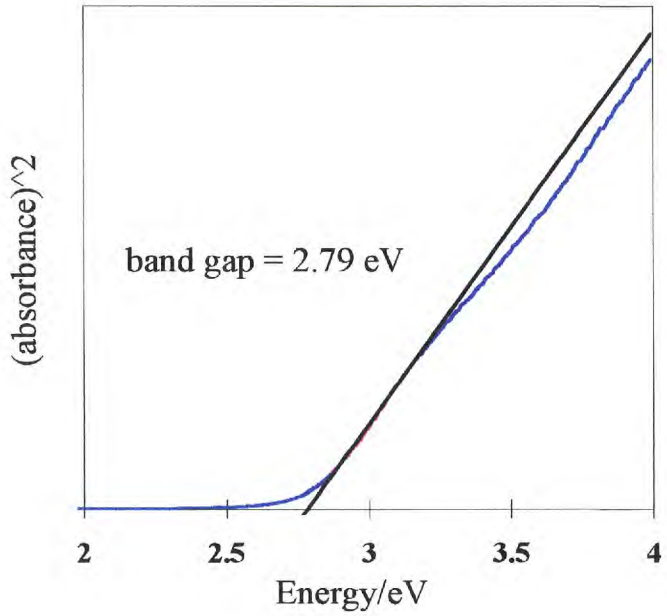


Figure 3.8: Direct band gap measurement of Q-Cd_3P_2/TOPO synthesised at 90 °C for 30 mins.

features, exhibiting an excitonic shoulder. Attempts to grow larger samples by leaving the reaction for long periods of time (24 hours rather than 0.5 hours at 250 °C) revealed no change in band edge position, indicating no further growth. The colloidal stability of such samples were affected however, with toluene solutions being unstable over 24 hours.

3.6 Luminescence of Q-Cd_3P_2

One of the major features of nanoparticles is the large percentage of surface atoms and therefore the surface properties play an important role. The capping ligand has a dual purpose, stopping the quantum dots from agglomerating and blocking surface defects which act as traps for electrons. The confinement of electrons and the blocking of surface defects (which would lead to deep trap emission), provide for efficient near band edge luminescence in II-VI systems.

Small particles of colloidal cadmium phosphide (Cd_3P_2) have been previously reported to exhibit an unusual emission process (Figure 3.9).[95] Upon excitation, an electron is promoted to the conduction band, forming an electron hole pair (e^-h^+). However, before recombination can take place, another electron is promoted, producing a double excited state $(e^-h^+)_2$. A subsequent recombination process yields a single excited state, with the emission of a photon. This is also accompanied by the emission of an electron.[95]

This has been explained by considering the doubly excited state. The first exciton is reported to relax from its delocalised state covering the entire colloidal particle, to the

surface. This acts as a recombination site for the remaining delocalised pair. The energy of recombination is then utilised for the emission of an electron.

Although these phenomena are incidental during the observation and recording of routine luminescence spectra it is interesting to note, being more unusual than single exciton processes and may also contribute to the instability of colloidally formed nanoparticles.

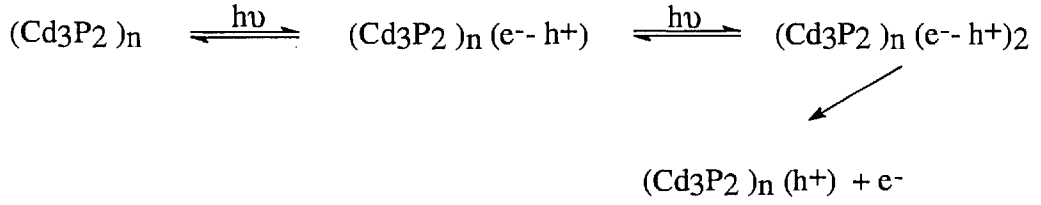


Figure 3.9: Excitation and emission for Cd_3P_2. [95]

Q-Cd_3P_2 produced by colloidal growth are reported to be unstable in air, reacting with atmospheric oxygen.[163] Illumination of colloidal samples is similarly reported to destroy the particle's integrity. These observations are in contrast to those made during the present study; TOPO and 4-ethylpyridine capped nanoparticles exhibit good colloidal stability in air and are resilient to photodegradation.

Samples of TOPO capped particles of Cd_3P_2 synthesised at temperatures between 90 °C and 250 °C were found to display emission maxima between 543 nm and 655 nm (Table 3.3, Figure 3.10).

Particles synthesised at lower temperatures (90 °C) have higher energy emission than particles synthesised at high temperatures (250 °C). The red shift in luminescence with increasing temperature of synthesis is consistent with the theory that larger particles are grown at elevated temperatures. The emissions from samples prepared at 90 °C have a

broad shoulder between 600 and 750 nm. These low intensity shoulders are a common feature in nanocrystalline systems,[35,50] and are attributed to trap states such as surface defects. A substantial Stokes shift (*ca.*100 nm) between the absorption band edge and the luminescence maxima has also been observed in colloidally synthesised Cd_3P_2 dots prepared by Weller *et al.*[162] The origin of Stokes shifts in nanocrystalline semiconductors have been the subject of much speculation, initially being attributed to the binding energy of the exciton,[21] surface defects,[40] and more recently, dark excitons (chapter 1).[40,41] Stoke shifts approaching 100 nm are however unusual and have been assigned to the fact that the M_3P_2 lattice has systematic metal cationic vacancies, which act as efficient trapping sites for electrons.[162] Cd_3P_2/TOPO has Stokes shifts between 100 nm (90 °C) and 150 nm (180 and 220 °C).

Temperature of Synthesis/ °C	Optical absorption band edge/ nm (eV)	Luminescence λ_{max} / nm (eV) (λ_{exc} = 300 nm)
90	444 (2.79)	543 (2.28)
180	470 (2.63)	621 (1.99)
220	476 (2.60)	621 (1.99)
250	556 (2.23)	655 (1.89)

Table 3.3: Comparison of synthesis temperature, band edge and emission maxima. for Cd_3P_2 capped with TOPO.

An unusual feature is the decrease in emission intensity with larger particle size. Quantum dots prepared at 90 °C show strong photoluminescence whilst samples synthesised above 100 °C show a marked decrease. Larger dots could be expected to show lower intensity emission due to the increase in bands for a charge carrier to

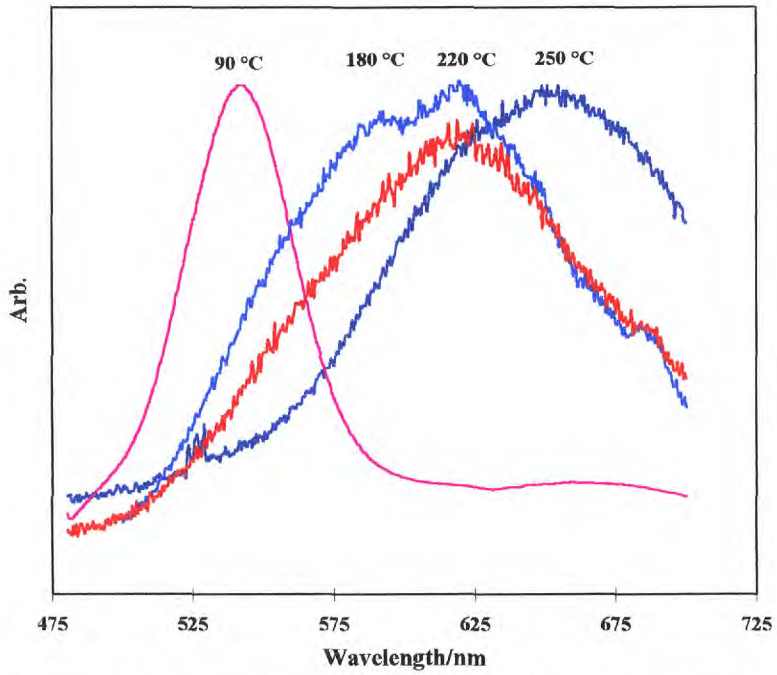


Figure 3.10: Luminescence spectra of TOPO capped Q-Cd_3P_2 prepared at different temperatures (λ_{exc} = 300 nm).

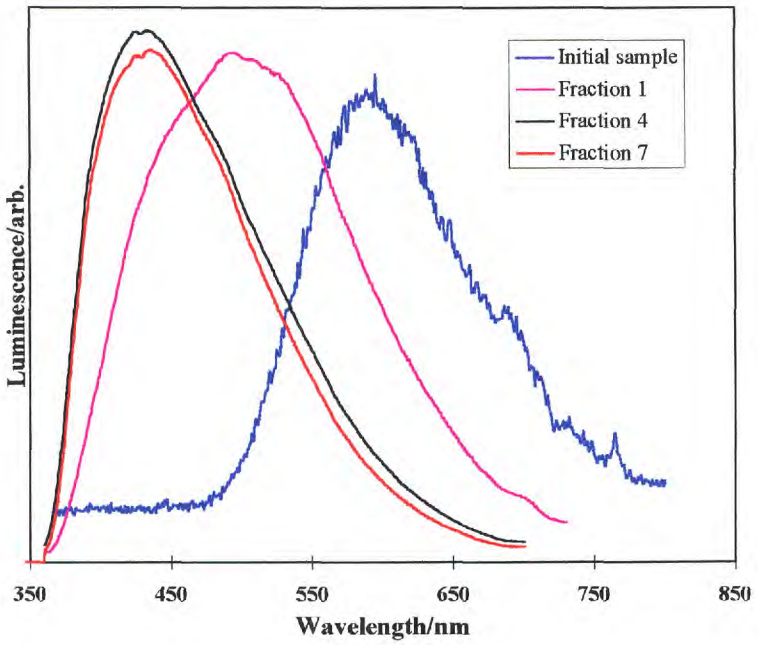


Figure 3.11: Luminescence spectra of Q-Cd_3P_2/4-ethylpyridine synthesised at 167 °C for 24 hours and various size fractions (λ_{exc} = 300 nm).

thermolyse through before recombination. This however, fails to explain such a sudden emission decrease observed in nanocrystals synthesised above a certain temperature. Weak long wavelength luminescence has also been observed in colloidally synthesised Q-Cd_3P_2 dots, where the decrease is attributed to the quantization of the particles.[162] Quantum dots capped with 4-ethylpyridine also exhibit luminescence consistent with Cd_3P_2 dots prepared by Weller *et al.*[163] (Table 3.4). Larger particles with a band edge of 2.44 eV (synthesised at 167 °C for 24 hours) had a weak emission intensity with a λ max. at 590 nm, a Stokes shift of *ca.* 90 nm. Size fractions of the same sample showed an increase in emission, but a decrease in Stokes shift. Fraction 1 had a $\lambda_{max.}$ at 497 nm, and fractions 4 and 7 displayed similar $\lambda_{max.}$ at 434 nm (Figure 3.11).

fraction	Optical absorption band edge/ nm (eV)	Luminescence λ_{max} / nm (eV) (λ_{exc} = 300 nm)
1	505 (2.45)	497 (2.49)
4	425 (2.91)	434 (2.83)
7	403 (3.07)	434 (2.83)

Table 3.4: Comparison of optical properties of different fractions of Cd_3P_2.

This demonstrates that smaller particles exhibit stronger luminescence, due to the smaller number of bands present in smaller nanocrystals. Stokes shifts of up to 100 nm are present in both 4-ethylpyridine and TOPO capped particles. Optical properties are in agreement with the analogous colloidally prepared dots, but are stable when excited in air. This can be attributed in part to the strongly bound organic group passivating the nanocrystal.

3.7 Structural Characterisation of Q-Cd_3P_2

Compounds with the formula M_3P_2 (M = Zn, Cd) are described as having an anti-Mn_2O_3 structure, where each metal atom is surrounded tetrahedrally by 4 phosphorus atoms, and each phosphorus by 6 metal atoms at 6 of the vertices of a distorted cube (Figures A2, A3, Appendix 1).[178] These compounds exhibit less ionic character than the analogous II-VI semiconductors and as a result, small particles of Cd_3P_2 and Zn_3P_2 exhibit poor crystallinity. The relationship between nanocrystal covalency and crystallinity has been discussed by Heath *et al.*[66] The relatively complicated structure also prevents a high degree of crystallinity in nanodispersed Cd_3P_2. Most synthetic pathways to M_3P_2 are reported to result in amorphous materials, or a mixture of amorphous and crystalline product as determined by electron microscopy.[85,86,161-163] There are no reports of X-ray diffraction patterns for Q-Cd_3P_2. Annealing of samples in the electron beam is also reported as a cause of crystallinity observed in some samples.[161,86]

TOPO and 4-ethylpyridine capped particles of Cd_3P_2 reported in this thesis showed no evidence of crystallinity by XRD. Confirmation of the compound's identity was primarily by ICPAES as described earlier, giving the empirical formula Cd_3P_2. HRTEM studies provided evidence for a mixture of crystalline and amorphous materials. Crystalline material was determined to possess a hexagonal type lattice, consistent with colloidal dots of Cd_3P_2.[162] Lattice spacing of 0.92 Å (TOPO capped Cd_3P_2) and 0.90 Å (4-ethylpyridine capped Cd_3P_2) indicate the 226 plane which has an intense reflection in

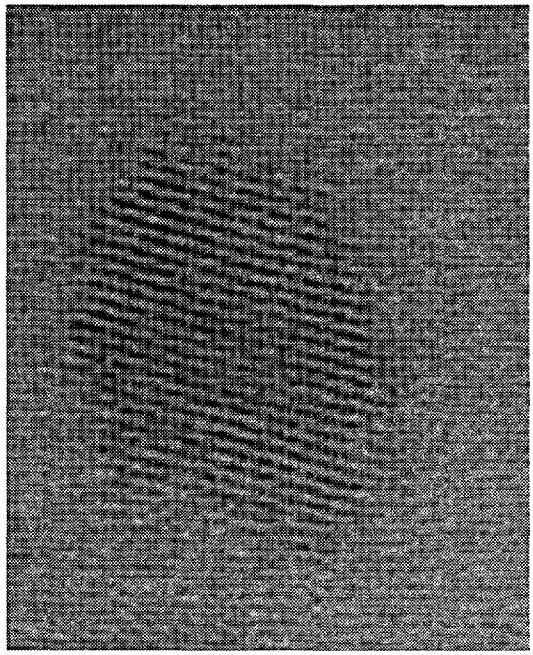


Figure 3.12: HRTEM image of a Cd_3P_2/TOPO nanocrystal (90 °C, 30 mins.), approx. 4 nm diameter, showing lattice fringes.

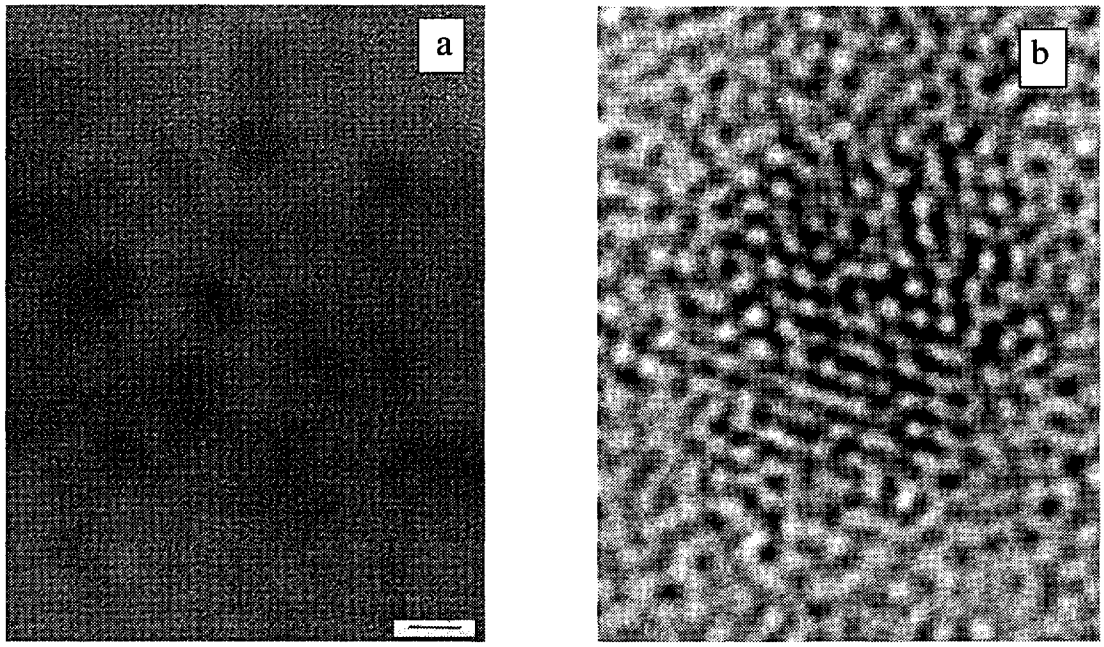


Figure 3.13: HRTEM images of a) Q-Cd_3P_2/4-etpy (167 °C, 24 hours) bar = 3 nm. b) Close up of a dot showing lattice fringes.

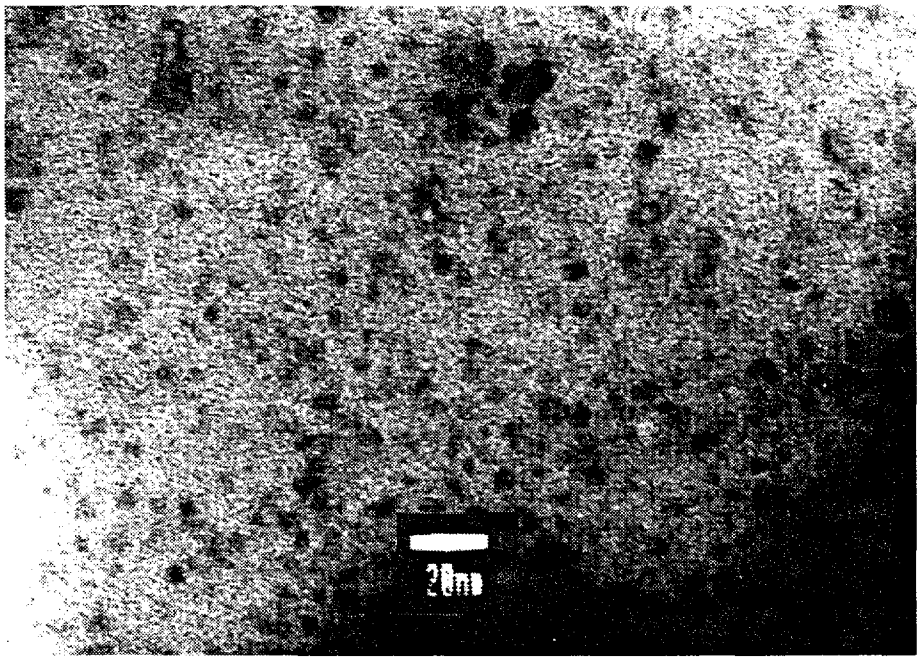


Figure 3.14: TEM image of Q-Cd_3P_2/4-etpy (167°C, 24 hours), bar = 20 nm.

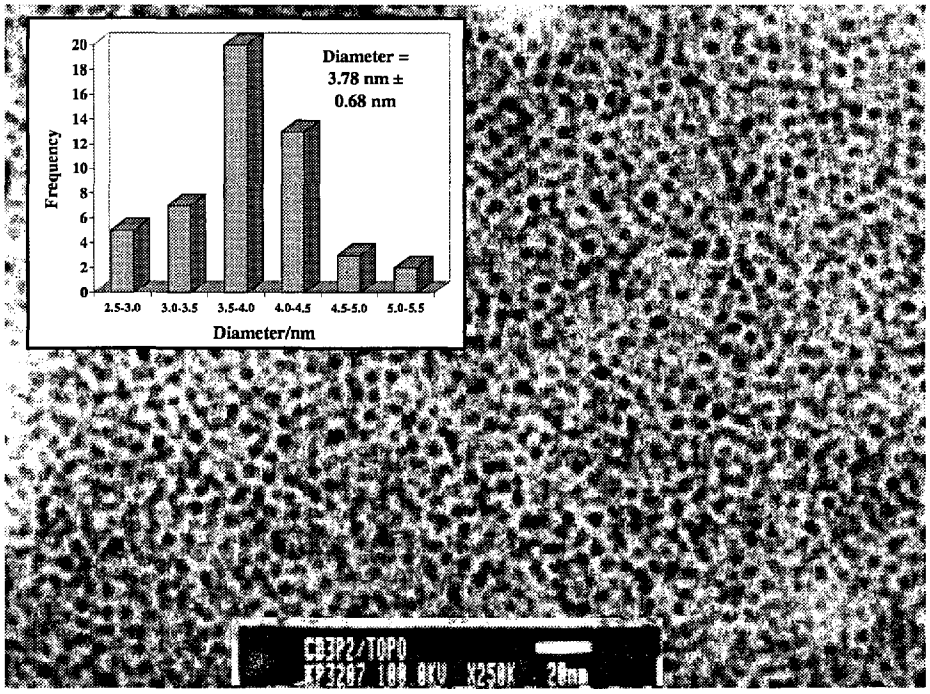


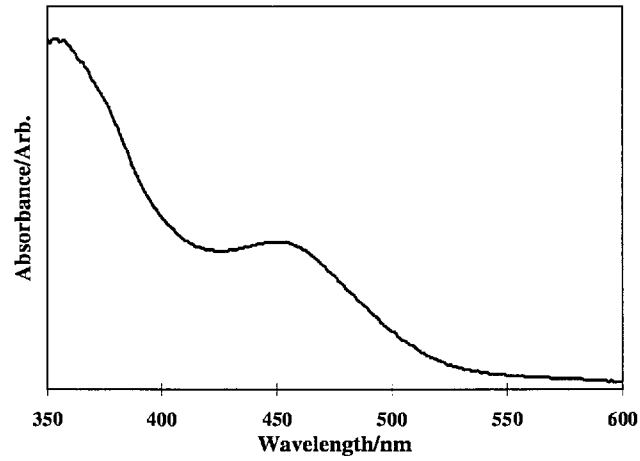
Figure 3.15: TEM of Cd_3P_2/TOPO, synthesised at 90 °C for 30 mins. bar = 20 nm; Inset: histogram of particle size distribution.

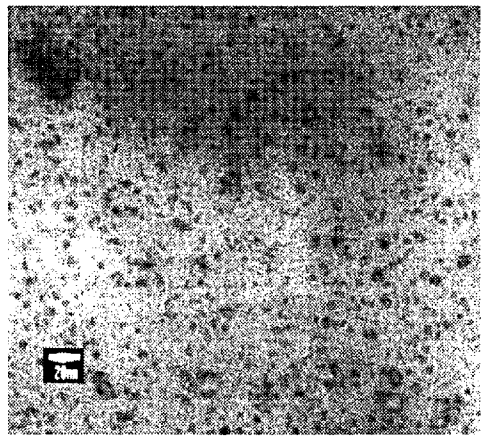
the bulk material (0.91 Å) (Figures 3.12, 3.13).[179] The dots were slightly prolate, with aspect ratios around 1.3. Samples prepared by the thermolysis of $[MeCdP(^tBu)_2]_3$ in 4-ethylpyridine at 167 °C for 24 hours showed dots in the size range 2.5-7 nm, a broader size distribution than the less covalent II-VI analogues.[35] Size selective precipitation by addition of an appropriate non solvent resulted in initial fractions with larger particles, subsequent fractions contained smaller particles as determined by TEM and optical spectroscopy. Comparison of TEM data for Cd_3P_2 (4-ethylpyridine, 167 °C, 24 hours) and two size fractions (Fractions 1 and 7) (Figures 3.14, 3.16 and 3.17) show the reduction in particle size as inferred from the optical data. The initial solution consisted of particles with an average diameter of 4.96 nm ± 0.96 nm (26 %). The next size fraction consisted of particles with a diameter of 4.82 nm ± 1.21 nm (25 %). The seventh size fraction had an average diameter of 3.27 nm ± 0.49 nm (14 %). From these data it can be determined that the larger particles precipitate from the solution initially, followed by smaller particles. The fractionation process also results in a narrowing of the size distribution as would be expected.

TEM of TOPO capped Cd_3P_2, synthesised at 90 °C for 30 mins. revealed particles with an average diameter of 3.78 nm with a standard deviation of 0.68 nm (17.8 %) (Figure 3.15). The standard deviation is large when compared to the analogous II-VI compounds[35] (5%), attributable to difficulties associated with the growth of covalent nanoparticles.[35,66] The predicted diameter using the effective mass approximation (Equation 1.6) is 3.77 nm. This is in good agreement with optical spectra, which infers that TOPO capped particles are smaller than 4-ethylpyridine passivated Q-Cd_3P_2.

Comparison of optical spectra and electron microscopy of 4-ethylpyridine and TOPO capped particles presents an apparent discrepancy. Particles capped with 4-ethylpyridine are larger than TOPO capped particles, despite having a lower boiling point. The larger diameter of 4-ethylpyridine capped dots appears contrary to existing work where the lower synthesis temperatures resulted in smaller particles. Previous studies have reported quantum dots prepared in just one solvent, with no research into the comparison of different solvent systems. Work by Murray *et al.*[35,51] and Alivisatos *et al.*[72] has shown that pyridine is a relatively labile passivating agent and can be easily removed. It is assumed that the growth of quantum dots is in a steady state of equilibrium between capping agent and further shell growth, with the passivating agent temporarily bonding to the surface of a small cluster, desorbing for shell growth, followed by temporary bonding again, and so forth. Weakly bound pyridine will then exchange more readily with further layers of semiconductor; displacement of the strongly bound TOPO species would be expected to be a more energetic process prior to Ostwald ripening. The more labile character of 4-ethylpyridine could therefore explain larger particles despite the lower temperature of synthesis.

Estimates of the particle size using the effective mass model, described by Brus,[23] (Equation 1.6, constants in Appendix 1.) suggests that the optical properties vary markedly with relatively small differences in size for II_3-V_2 compounds. Calculations from equation 1.6 show the band edge shift of 0.79 eV can be attributed to a theoretical diameter increase of just 5.2 Å (Table 3.5). The large shift in absorption with a small diameter increase can be attributed to the large excitonic radius and the high degree of confinement.





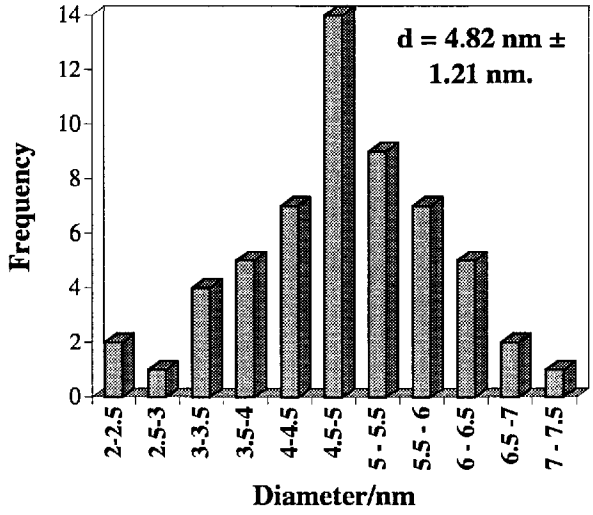
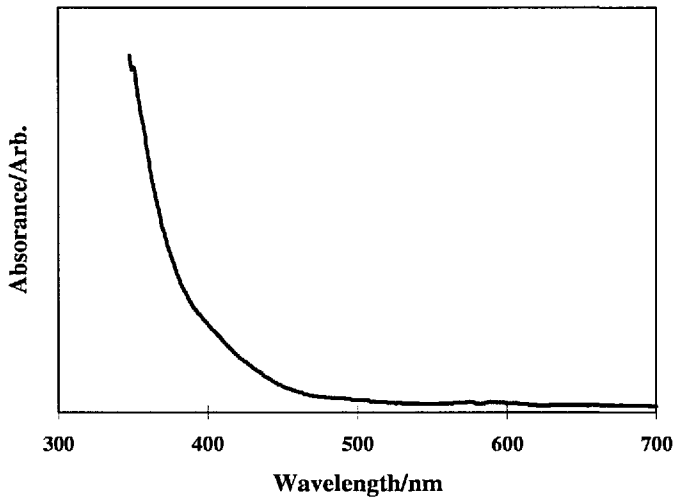
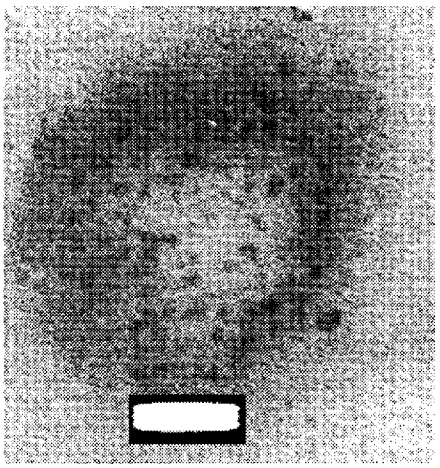


Figure 3.16: Optical absorption spectrum, TEM (bar = 20 nm) and histogram of particle size for 1st size fraction of Cd_3P_2/4-etpy.





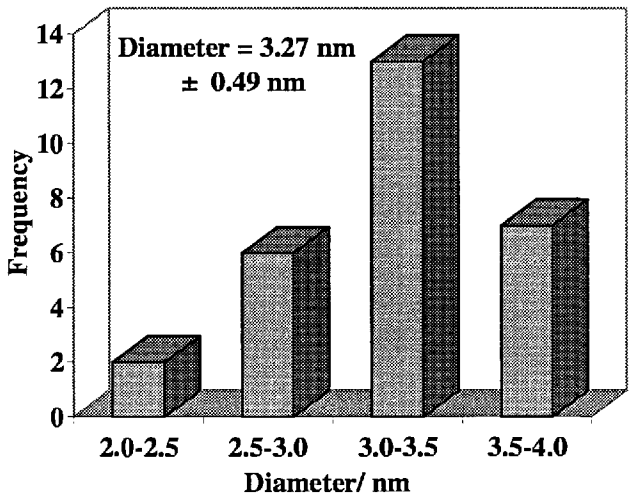


Figure 3.17: Optical absorption spectrum, TEM (bar = 20 nm) and histogram of particle size for 7th size fraction of Cd_3P_2/4-etpy.

Fraction	Optical absorption band edge/nm (eV)	Predicted diameter/ nm.	Observed diameter/nm
1	505 (2.45)	4.02	4.82
7	411 (3.23)	3.50	3.27

Table 3.5: Diameter as a function of band edge, with predicted and actual diameters for some fractions of Q-Cd_3P_2.

As previously reported, nanoparticles of Cd_3P_2 described in this thesis appear resistant to degradation by illumination or exposure to oxygen. The robustness of the nanoparticles can be attributed to the capping ligands passivating the surface. Surface characteristics are very important and the passivating ligand has several roles; the blocking of surface sites, providing an organic stabilising 'monolayer' for the crystal and preventing particle agglomeration. Previous studies on the nature of the capping groups have shown, as detailed in chapter 2, that TOPO binds selectively to the metal sites, whilst TOP binds to the selenium sites, effectively providing a TOPSe capping group.[53,58,59] The ligand 4-ethylpyridine is assumed to bind in a similar manner to TOPO, with the lone electron pair on the heterocyclic N atom binding to metal sites on the nanoparticle surface.

EDAX measurements of Cd_3P_2 prepared in TOPO suggest the presence of TOPO in well washed samples. EDAX on Cd_3P_2 capped with 4-ethylpyridine show the same peaks, with a less intense phosphorus peak as expected (Figure 3.18). Whilst EDAX indicates the passivating agents are present, it does not necessarily follow that the ligands are bound to the surface.

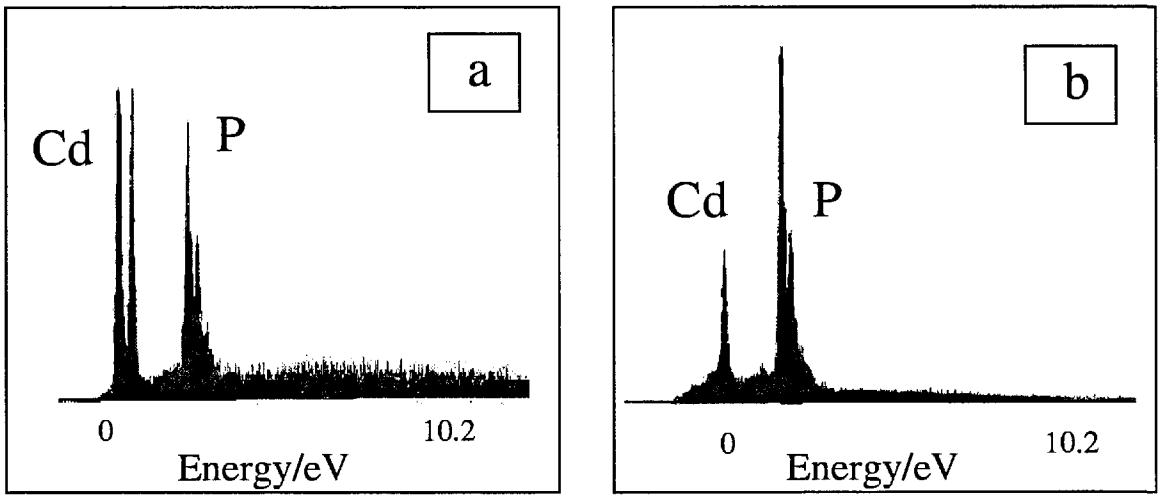


Figure 3.18: EDAX analysis of a) Q-Cd_3P_2/4-etpy b) Q-Cd_3P_2/TOPO.

Infra red spectroscopy of Cd_3P_2/TOPO displayed the ν(C-H) bend from CH_3 at 1457 cm^{-1} and also the shifted ν(P=O) at 1127 cm^{-1}, indicating that the phosphine oxide was strongly bound to the cadmium sites.[53] The presence of bands at 227, 255 and 303 cm^{-1} were consistent with those previously predicted for Cd_3P_2.[180]

Quantum dots capped with 4-ethylpyridine show absorption modes characteristic of an alkylpyridine (Table 3.6), including ring stretches at 1608 and 1394 cm^{-1}.[50,181] Studies on pyridine and alkylpyridine complexes of metal salts report the ν(M-N) stretch between 200 - 600 cm^{-1}, predominantly in the region 210 - 325 cm^{-1}.[181] It is also reported that as alkyl chains get longer, the intensity of the ν(M-N) peak diminishes and broadens. Cd_3P_2 nanocrystals capped with 4-ethylpyridine show a characteristic broad, relatively weak stretch at 315 cm^{-1}, which is consistent with a structure in which the ligand binds through the ring nitrogen to the cadmium sites. Cadmium-phosphorus features were again observed at 231 and 246 cm^{-1}.

Free ligand/ cm^{-1}	Cd_3P_2-4-etpy/ cm^{-1}	assignment
1606	1608	ν(C-C)
1417	1394	ν(C-C)
-	1135	ν(C-H)
1066	1062	ν(C-H)
777	773	ν(C-H)
-	314	ν(Cd-N)
-	231	ν(Cd-P)
-	246	ν(Cd-P)

Table 3.6: Selected IR data on 4-ethylpyridine and 4-ethylpyridine capped Cd_3P_2.

Nuclear magnetic resonance spectroscopy of phosphide containing semiconductor quantum dots has previously extended to three studies.[86,102,182] Gallium phosphide produced in the pores of zeolite Y at different temperatures has been analysed by ^{31}P MAS NMR.[102] High temperature synthesis (300 °C) results in samples which exhibit a single resonance at -143.8 ppm, comparable to the resonance observed in bulk GaP (-146 ppm). Lowering the temperature (200 °C) results in a gradual upfield shift until the resonance is in the form of two peaks at -200 and -233.5 ppm. Similarly, InP produced in the pores of zeolite MCM-41 exhibits a resonance at *ca.* -200 ppm,[182] upfield from the resonance of bulk InP (-148 ppm).

Cadmium phosphide as synthesised by the methanolysis of a silylated precursor and analysed by ^{31}P MAS NMR was reported to have a single broad resonance at -240 ppm, and at -227 ppm when observed in the solution phase.[86] This is again significantly upfield from the reported bulk resonances of -140, -162 and -178 ppm.

Nanoparticles are expected to exhibit an upfield chemical shift for certain NMR active nuclei. Chemical shifts can be assumed to have paramagnetic and diamagnetic shift contributions. Diamagnetic contributions (σ_d) are insensitive to bonding character and are dictated by the ground state of electrons present in atomic or molecular orbitals. Paramagnetic shifts (σ_p) are sensitive to the excited states in orbitals and has been found to be approx. inversely proportional to the energy gap of excited electrons, *i.e.*, the band gap. This can be written:

$$\sigma_p \propto \frac{1}{\Delta E}\left\langle \frac{1}{R^3} \right\rangle \tag{3.1}$$

Hence multi-nuclear NMR, in which the studied nucleus is a core element in the dot's structure, (*i.e.*, ^{77}Se in CdSe, ^{31}P in GaP, *etc.*) will have a reduction in the paramagnetic shift term due to the increase band gap, and an upfield chemical shift. Other factors are important however, including R the distance between the nuclei and the surrounding electrons, crystallinity and lattice structure, which is often ill-defined. In quantum confined systems, the R term may play a significant role, although this is yet to be proved. Particle shape, size and the large number of surface atoms may also have an effect, resulting in lattice deformation to possibly counteract dangling bonds.

Bulk cadmium phosphide is reported to have three major resonances due to three phosphorus environments resulting from orientation of phosphorus atoms around the metal vacancies.[186,187]

^{31}P NMR (solution state and solid state MAS) experiments on TOPO capped Q-Cd_3P_2 provide no evidence for phosphorus from the nanocrystal core with resonances attributable to the capping group only, as described in chapter 2 (Table 3.7). Other

evidence, including EDAX, IR, ICPAES and optical spectroscopy are in contrast to the ^{31}P NMR and indicate the presence of cadmium phosphide; it is tentatively assumed the excess phosphorus from the TOPO masks the resonance from the crystal core.

Solution ^{31}P NMR of 4-ethylpyridine capped Q-Cd_3P_2 shows three broad resonances at 33.6, 38.32 and 53.82 ppm, consistent with 3 phosphorus environments.

Solid state MAS ^{31}P NMR on Cd_3P_2 capped with 4-ethylpyridine shows weak broad resonances at 12.43, 38.81 and 53.44 ppm (Table 3.8). Cross polarisation experiments (CPMAS) in which the spin from the ^{1}H system is transferred to the ^{31}P system gives an increased signal for nuclei proximate to protons. Surface ^{31}P signals should be enhanced as they are closer to the capping group. In such experiments, a resonance at 10.08 ppm was clearly observed. A broad resonance at 37.65 ppm was seen slightly masking the signal at 54.08 ppm. A sharp resonance at 0.90 ppm was also observed and assigned as a surface state. A resonance is also observed at 60.46 ppm and is assigned as a different surface state. It is theoretically possible to have up to 6 different resonances as each of the three phosphorus environments may be at the surface.

The presence of three core resonances suggests similar phosphorus environments for both nanocrystals and bulk materials, however the downfield chemical shift relative to the bulk material is contrary to expected upfield shift observed in other nanocrystals.

The reason for the downfield shift is not clear. The small dimensions of a quantum dot may force electrons closer to the nuclei, making R a small term (Equation 3.1), especially in such a confined system as II_3-V_2 materials. The cubed inverse term will then be large enough to have a significant effect, resulting in an increase in the

paramagnetic shift term which would outweigh any contribution from a change in band gap. This would result in the downfield shift. Certainly all the factors stated above may contribute, additionally the complicated crystal structure of M_3P_2 presents another parameter to consider.

The resonances reported in this thesis also differ from the previously reported solid and solution state ^{31}P NMR of Q-Cd_3P_2. The sol-gel route reported by Buhro reports one resonance, suggesting one phosphorus environment which is not the case.[86] Variations in lattice planes could result in different magnetic environments. The methods of preparation vary immensely, overall this could result in nanoparticles of differing quality and morphology.

Solution state ^{31}P NMR			^{31}P CPMAS NMR	
δ ppm	assignment		δ ppm	assignment
-29.87	Free TOP		32.33	Bound TOPO
35.48	Bound TOPO		45.87	Free TOPO
49.20	Free TOPO		50.03	Free TOPO
53.66	TOPO impurity		54.82	TOPO impurity
66.58	Unidentified			

Table 3.7: Solution and solid state ^{31}P NMR data for TOPO capped Q-Cd_3P_2.

Solution ^{1}H NMR for 4-ethylpyridine capped particles indicate the presence of the passivating species with little deviation in chemical shift from the free ligand. The resonances are broadened making the splitting patterns difficult to assign. This has previously been attributed to a reduction in rotational freedom when bound to the surface site or the inhomogeneous distribution of magnetic environments found on the

nanocrystalline surface.[51,52,65,188] Comparison of ^{1}H NMR of 4-ethylpyridine passivated particles and free 4-ethylpyridine allows assignment of the signals (Table 3.9).

Solution ^{1}H NMR of TOPO capped particles show the resonances associated with the free ligand, *i.e.*, a broad set of three features between 0.75 - 2.0 ppm.

Solution state ^{31}P NMR			^{31}P CPMAS NMR	
δ ppm	assignment		δ ppm	assignment
33.60	Core Phosphorus		0.90	Surface phosphorus
38.32	Core Phosphorus		10.08	Core Phosphorus
53.82	Core Phosphorus		37.65	Core Phosphorus
			54.08	Core Phosphorus
			60.46	Surface phosphorus

Table 3.8: Solution and solid state ^{31}P NMR data for 4-ethylpyridine capped Q-Cd_3P_2.

Free ligand/ splitting/ δ ppm	Cd_3P_2-4-etpy/ splitting/ δ ppm	assignment
t, 1.04	m, 1.20	CH_3
q, 2.42	m, 2.50	CH_2
s, 7.04	s, 7.18	aromatic CH
s, 8.61	s, 8.76	aromatic CH

Table 3.9: ^{1}H NMR data for 4-ethylpyridine and 4-ethylpyridine capped Cd_3P_2.

Zinc Phosphide

3.8 Potential precursors for Zn_3P_2

Diorganophosphides of zinc have been relatively well studied, $Zn(PPh_2)_2$ being synthesised in the 1960's.[168] In an attempt to solve the single crystal structures of such compounds, three new compounds were reported by Wright *et al.* and by Cowley *et al.* The compounds, $[Zn(Bu^t_2P)_2(OH)(\mu\text{-}OH)]_2$,[189] $\{[Zn(Et)(\mu\text{-}PCy_2)]_3{\cdot}THF\}{\cdot}2THF$,[171] and $\{[EtZn(\mu\text{-}PPh_2)]_3{\cdot}(HPPh_2)_2{\cdot}THF\}$[172] have not been used for semiconductor synthesis. $[Zn(Bu^t_2P)_2(OH)(\mu\text{-}OH)]_2$ was synthesised by the serendipitous inclusion of water in experimental work up.

The necessity of ^{t}Bu groups in precursors for Cd_3P_2 lead to the exclusion of $\{[Zn(Et)(\mu\text{-}PCh_2)]_3{\cdot}THF\}{\cdot}2THF$ and $[Zn(Et)(\mu\text{-}PPh_2)]_3{\cdot}(HPPh_2)_2{\cdot}THF$. Attempts were made to produce a novel precursor containing the ^{t}Bu group. An initial attempt involving the reaction between Me_2Zn and HP^tBu_2 in a variety of solvents (hexane, TOP, THF, THF/hexane) in a variety of stoichiometries (1:1, 1:1.5, 1:2, 2:1) was unsuccessful under all conditions.

A more successful approach was devised by the use of Me_2Zn and HP^tBu_2 in a Bawendi style synthesis. The two compounds were mixed in TOP and either injected into TOPO at varying temperatures for TOPO capped nanoparticles, or alternatively mixed with 4-ethylpyridine and heated to obtain 4-ethylpyridine capped dots. The use of a related precursor, H_2P^tBu, as an alternative phosphorus source to the usual precursor

(PH_3) in low pressure MOCVD has reportedly proved successful and several phosphorus containing semiconductors have been synthesised.[190,191] Other alkylphosphines such as cyclopentylphosphine show pre-reaction and are reported to be unsuitable as precursors.[192]

3.9 Optical properties of Q-Zn_3P_2

The thermolysis of Me_2Zn and HP^tBu_2 in hot TOPO or 4-ethylpyridine resulted in nanoparticulate solutions. Isolation of the particles by the addition of a non solvent (methanol/TOPO, light petroleum/4-ethylpyridine) resulted in the production of a white powder for TOPO capped particles and an orange powder for 4-ethylpyridine capped particles. These observation suggests the 4-ethylpyridine capped particles are larger, but it has been observed that size quantization effects for II_3-V_2 compounds are very sensitive to small changes in particle size.

Bulk Zn_3P_2 has a band gap of 1.4 eV (885 nm),[160] which is increased in nanoparticles due to quantum confinement. UV spectra (Figures 3.19) of TOPO capped Zn_3P_2 revealed a distinct blue shift, with a band edge of 3.55 eV (349 nm) when synthesised by the injection of HP^tBu_2 and Me_2Zn into hot TOPO (150 °C for 3 hours). Materials synthesised at 250 °C for 3 hours were found to have a band edge of 3.30 eV (375 nm) (Equation 1.8). The band edge position for both sets of particles indicates growth to similar sizes, as expected the lower temperature of synthesis producing slightly

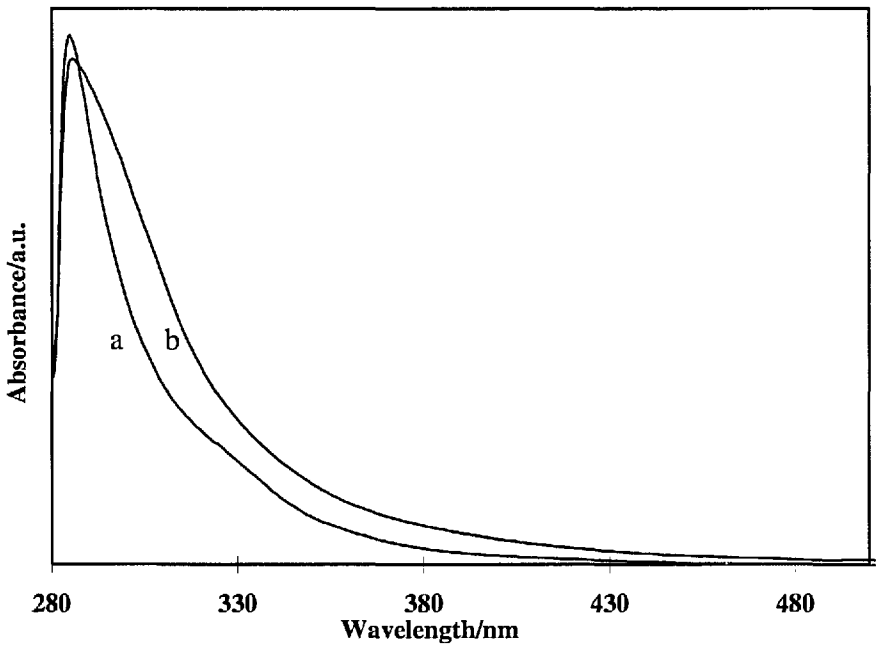


Figure 3.19: Optical absorption spectra of different samples of Q-Zn_3P_2: a) TOPO capped synthesised at 150 ° C; b) TOPO capped synthesised at 250 ° C.

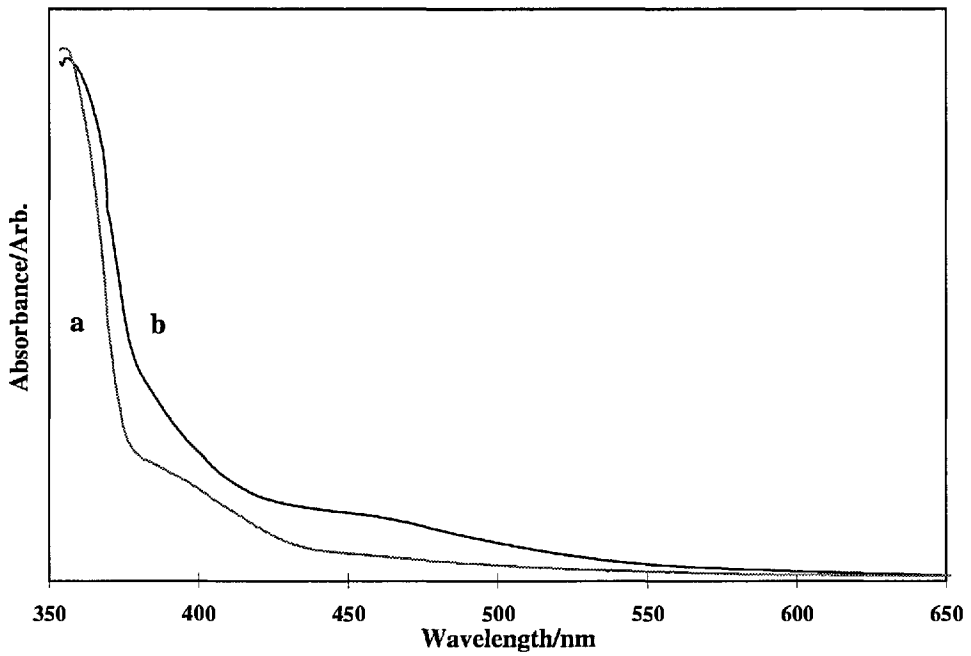


Figure 3.20: Optical absorption spectra of 4-ethylpyridine capped Q-Zn_3P_2, synthesised at 167 ° C; a) 4 hours, b) 30 hours.

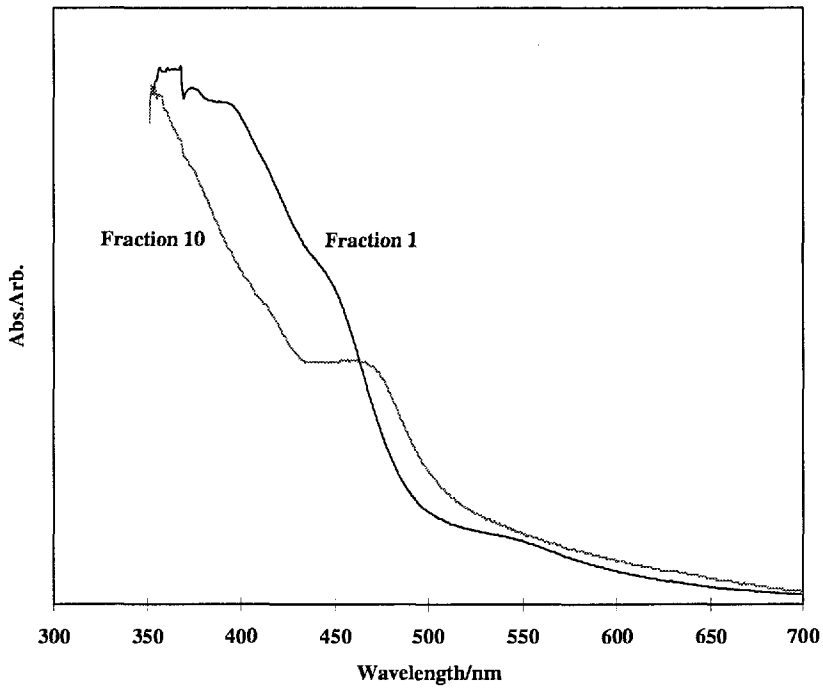


Figure 3.21: Comparison of two size fractions of Q-Zn_3P_2 capped with 4-ethylpyridine.

smaller particles. This is in agreement with TOPO capped Q-Cd_3P_2, where the temperature of synthesis of does not appear to overly effect the size of the particles when compared to the analogous II-VI materials.[50,62] TOPO capped Zn_3P_2 is comparable to the smallest reported particles of colloidal Cd_3P_2, which are also white and are reported to have a band gap of 4.0 eV.[24]

4-ethylpyridine capped particles of Zn_3P_2 synthesised at 167 °C for up to 30 hours have a smaller band gap, indicating slightly larger particles than the TOPO capped Q-Zn_3P_2 (Figure 3.20). The particles were also orange/brown in colour indicating a larger size. An aliquot taken after 4 hours at 167 °C show a band edge of 2.87 eV (431 nm), whilst an aliquot after 30 hours shows a band edge of 2.33 eV (531 nm) (Equation 1.8)

indicating further particle growth after the first aliquot was taken. Size fractionation of 4-ethylpyridine capped Q-Zn_3P_2 was achieved using the same method as for Q-Cd_3P_2/4-etpy.

Increasing size fractionation of the initial solution resulted in solids which exhibited a gradual blue shift in the absorption, indicating the larger particles precipitate first. Fraction 10 produced a pale yellow solid which was found to have a band edge of 3.02 eV (410 nm), the smallest 4-ethylpyridine capped particles obtained (Figure 3.21). An excitonic peak was observed for smaller fraction at *ca.* 450 nm (2.74 eV) indicating an increase in monodispersity due to size fractionation.

3.10 Luminescence of Q-Zn_3P_2

There are no reports in the literature regarding the luminescent behaviour of Q-Zn_3P_2. A sizeable Stokes shift is observed and may be explained as due to metal vacancies in the lattice being efficient trapping sites for electrons. Weak long wavelength luminescence similar to that observed in Q-Cd_3P_2 might be expected,[162] however, all organically capped Q-Zn_3P_2 displayed strong luminescence. The sample synthesised at 250 °C had a relatively broad emission at 563 nm (2.20 eV), with the smaller particles synthesised at 150 °C having a narrower emission at 418 nm (2.95 eV) (Figure 3.22). In all cases there was no low energy emission as commonly associated with surface defects. The narrower emission profile for nanocrystals synthesised at 150 °C can be attributed to a narrower size distribution, which would be expected for lower temperature synthesis. Stoke shifts observed for the samples synthesised at lower temperatures (150 °C) were in

the order of *ca.* 70 nm, whilst the particles synthesised at higher temperatures (250 °C) had Stokes shifts of up to 180 nm.

The increased Stokes shift with increased size distribution suggests that the particle size distribution, which is larger at higher temperature synthesis, may be a factor in optical spectroscopy. The quantum dots exhibit strong luminescence, as expected with small nanoparticles of II_3-V_2 compounds.

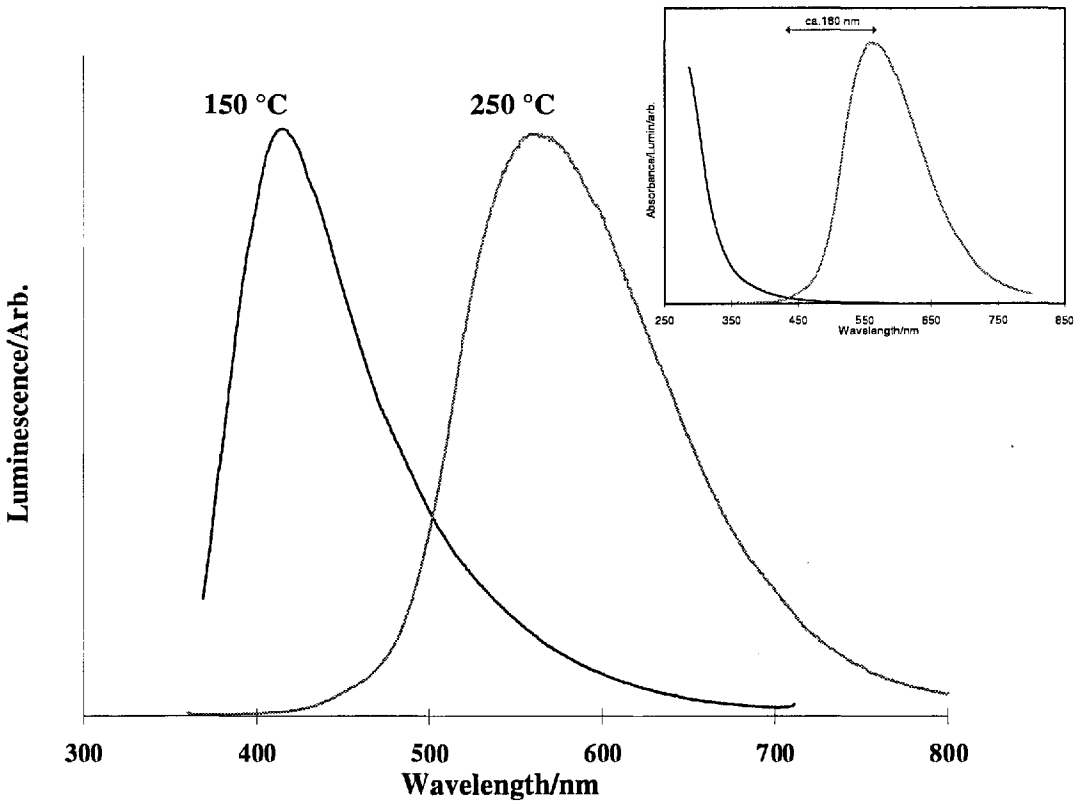


Figure 3.22: Luminescence spectra of Q-Zn_3P_2/TOPO synthesised at two different temperatures; Inset, optical absorption band edge and luminescence spectrum of TOPO capped Q-Zn_3P_2 synthesised at 250 °C, showing the large Stokes shift (λ_{exc} = 300 nm).

4-ethylpyridine capped nanoparticles also exhibit strong luminescence (Figure 3.23) with no evidence of deep traps. Samples prepared at 167 °C for 30 hours were found to have a band edge of 531 nm (2.33 eV) and displayed emission maxima at 575 nm (2.15 eV), a Stokes shift of 44 nm.

The eighth size fractionated sample (with a band edge of 410 nm, 3.02 eV) produced emissions at 474 nm (2.61 eV), a Stokes shift of 64 nm. Emission from fractionated samples had narrower profiles, indicating a narrower size distribution. In all cases, strong luminescence was observed, even with the longest wavelength emission (575 nm). In comparison, Q-Cd_3P_2 displays strong emission profiles in this region (*cf.* TOPO capped, synthesised at 90 °C), but exhibits weak emission above 600 nm.

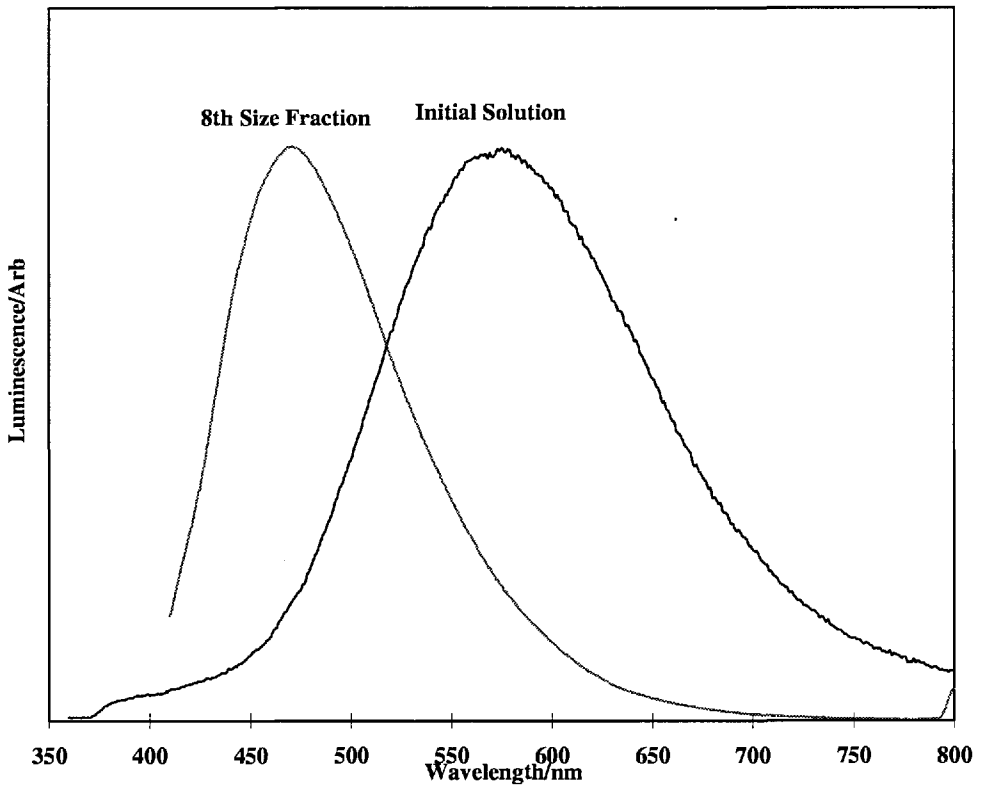


Figure 3.23: Luminescence spectra of Q-Zn_3P_2 capped with 4-ethylpyridine, showing emission from the solution prior to fractionation and the 8th size fraction (λ_{exc} = 400 nm).

3.11 Structural Characterisation of Q-Zn_3P_2

Zn_3P_2 is isostructural with Cd_3P_2 (Zn_3P_2, a = 8.09 Å, c = 11.45 Å; Cd_3P_2, a = 8.75 Å, c = 12.26 Å).[160] Powder X-ray diffraction showed no evidence of crystallinity in any samples of nanometer sized Zn_3P_2.

Confirmation of the compound's identity was confirmed by ICPAES. Analysis of an aliquot taken after 4 hours (167 °C, 4-ethylpyridine) gave a Zn:P ratio of 1.7:1 ($Zn_{3.4}P_2$) and gave no X-ray powder diffraction pattern. After further heating at 167 °C for 50 hours, the ratio had risen to 7.7:1 and a powder diffraction pattern for ZnO was observed. ICPAES of TOPO capped Zn_3P_2 gave Zn:P ratios of 1:1, consistent with excess phosphorus due to the TOPO capping ligand.

HRTEM of 4-ethylpyridine capped Zn_3P_2 (167 °C, 50 hours) displayed a crystalline product with a strong hexagonal pattern, consistent with zinc metal (Figure 3.24) together with the spherical, poorly crystalline Zn_3P_2 quantum dots. Reaction by-products isolated during the purification of the nanoparticles were also identified by XRD as bulk zinc[193] and zinc oxide.[194] HRTEM images of the 4-ethylpyridine capped Q-Zn_3P_2 showed a mixture of amorphous, crystalline and poorly crystalline particles. HRTEM also showed lattice distortions and disordered plane orientations (Figures 3.25, 3.26). Measurement of the lattice fringes do not agree with any known crystal plane of Zn_3P_2,[195] Zn[193] or ZnO.[194]

The particles, between 3.5 - 13 nm in diameter, were slightly prolate, with aspect ratios up to 1.25.

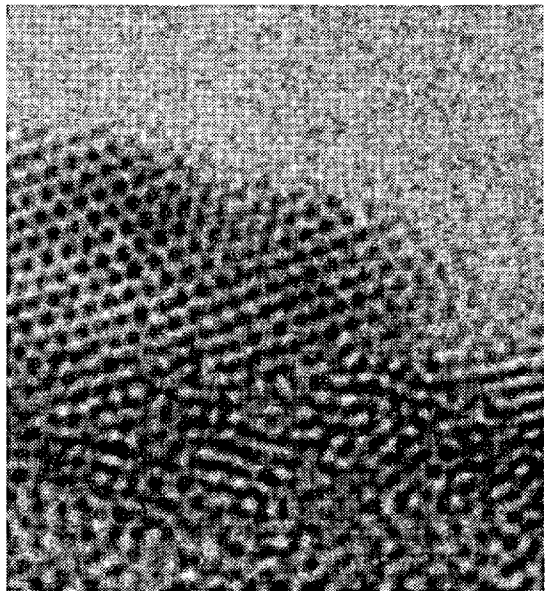


Figure 3.24: HRTEM image of hexagonal zinc metal by-product obtained from Me_2Zn and HP^tBu_2 in 4-etpy for 50 hours.

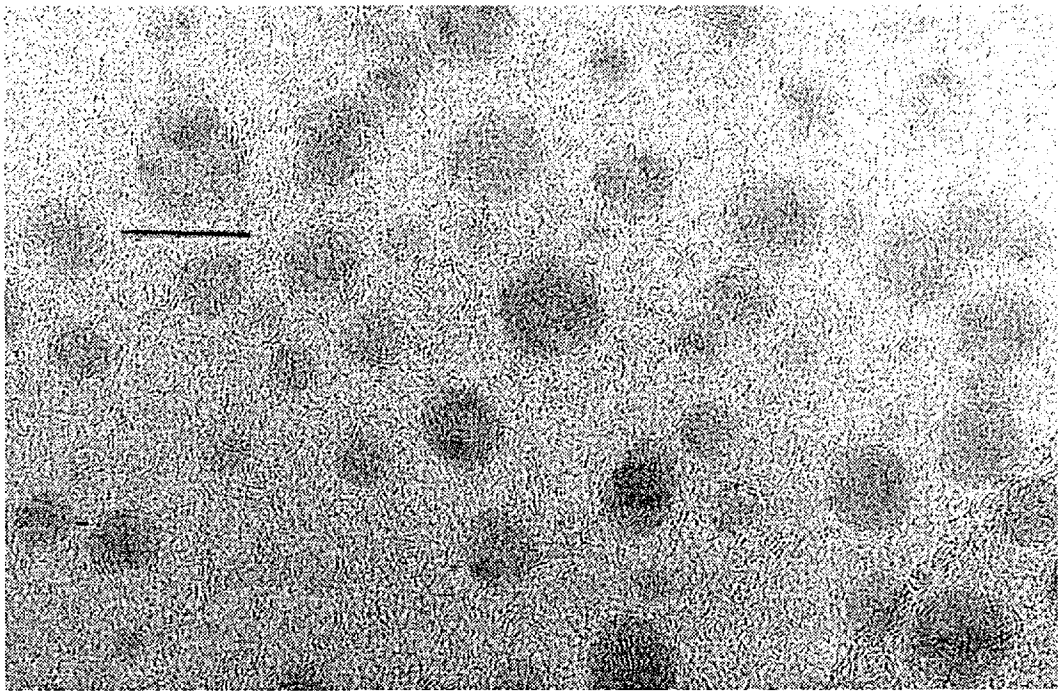


Figure 3.25: HRTEM image of Zn_3P_2 capped with 4-ethylpyridine obtained from Me_2Zn and HP^tBu_2 in 4-etpy for 50 hours, bar = 10 nm.

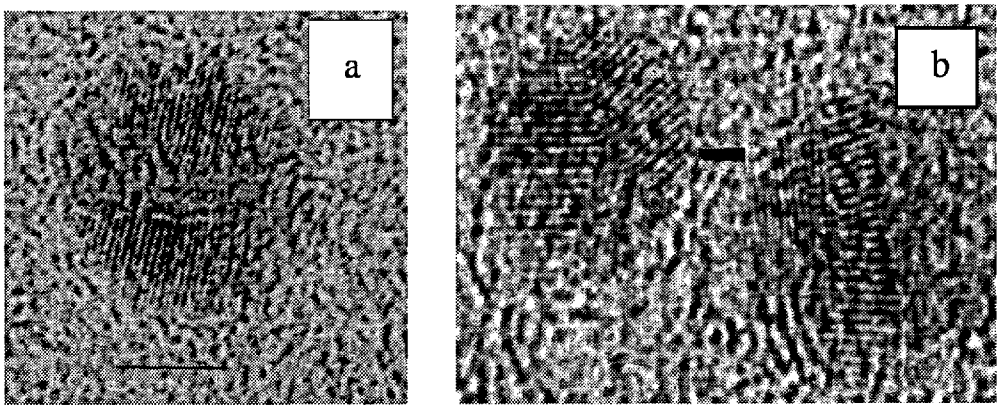


Figure 3.26: HRTEM image of Zn_3P_2 capped with 4-ethylpyridine from Me_2Zn and HP^tBu_2 in 4-etpy for 50 hours, bar = a) 5 nm; b) = 1nm.

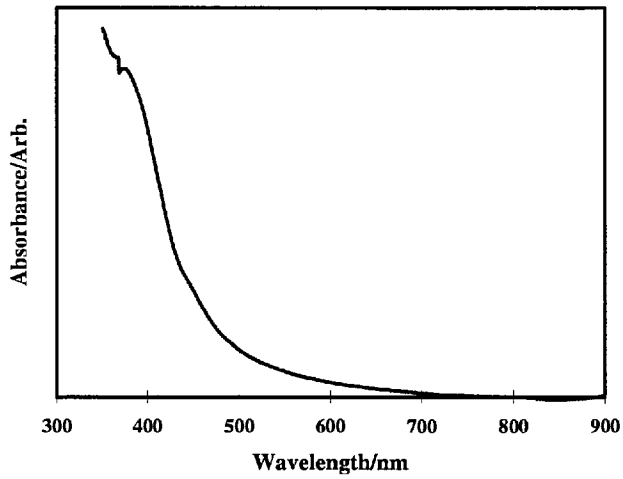
The relevant size distribution and optical spectra of various fractions (fractions 2, 5 and 8) of 4-ethylpyridine capped Q-Zn_3P_2 are shown in figures 3.27, 3.28 and 3.29.

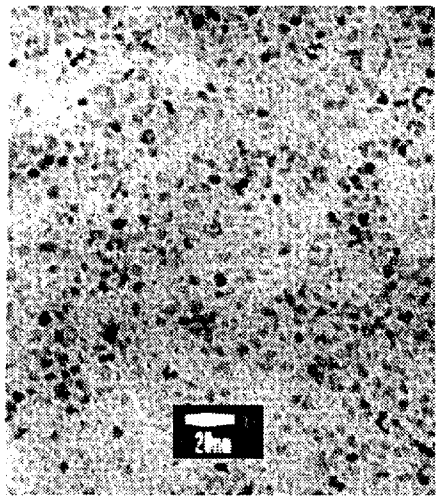
The second size fraction consists of quantum dots with an average diameter of 4.32 nm ± 0.77 nm (17.8 %). The fifth fraction has an average diameter of 3.82 nm ± 0.62 nm (16.2 %), whilst the eighth fraction has an average diameter of 3.59 nm ± 0.57 nm (15.8 %). This demonstrates that size fractionation results in larger particles precipitating from solution first, followed by smaller particle. The size distribution also narrows with fractionation explaining the evolution of an excitonic feature in the electronic spectra.

TEM of TOPO capped nanoparticles, synthesised at 150 °C for 4 hours, showed particles in the range 2-7nm, an average diameter of 4.09 nm ± 0.89 nm (21%) (Figure 3.30). This observation is consistent with the optical spectra which suggests that TOPO capped nanoparticles of Q-Zn_3P_2 were on average smaller than 4-ethylpyridine capped nanoparticles. The large standard deviation in diameter is comparable to TOPO capped Cd_3P_2 and TOPO capped III-V materials reported by Alivisatos *et al.*[65]

Estimates of the particle size by the effective mass approximation described by Brus[23] could not be employed due to a lack of information regarding physical constants for Zn_3P_2. There are no values for the effective mass of holes or electrons for Zn_3P_2. Pseudopotential calculations previously developed by Krishna and Friesner,[32] and employed by Trindade,[50] for the calculation of CdSe, CdS and GaP diameters all rely on a reliable bulk band structure. This method of estimating particle size is not applicable in the present case as there is controversy regarding the validity of the existing pseudopotential model of the band structure of Zn_3P_2.[166] Using an approximation modelled on the anti-fluorite lattice, a discrepancy is observed when comparing the

theoretical band gap to experimental data for macrocrystalline Zn_3P_2. Any estimation of diameter based on experimentally derived band gaps could therefore be inaccurate.





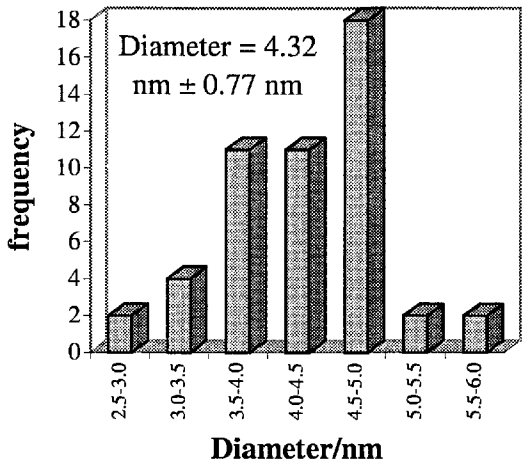
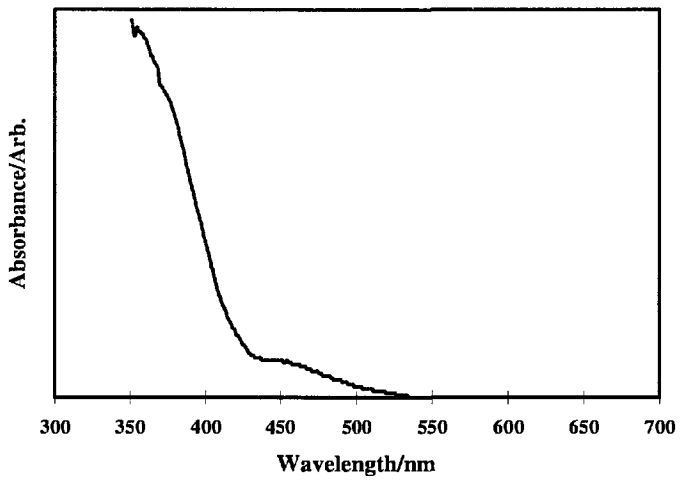
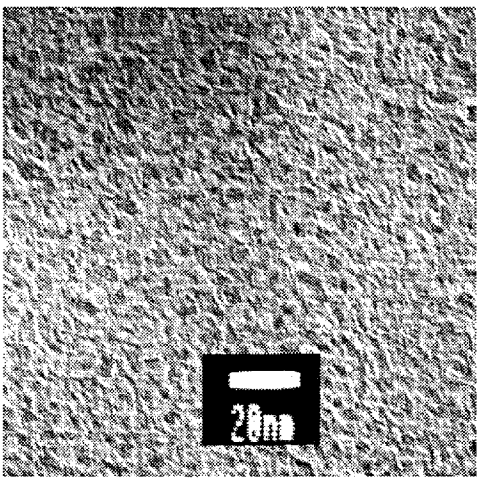


Figure 3.27: Optical absorption spectrum, TEM and histogram of particle size for 2nd size fraction of Zn_3P_2/4-etpy.





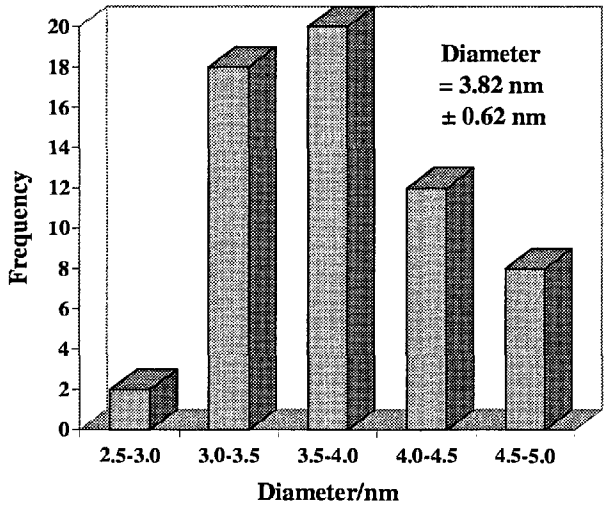
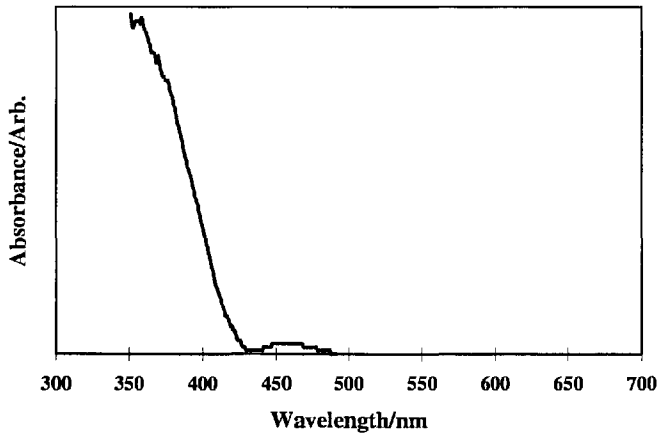
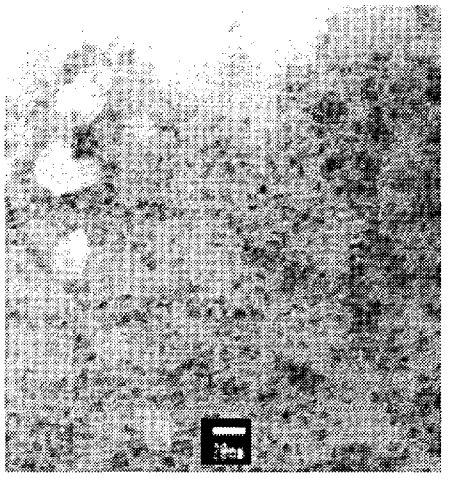


Figure 3.28: Optical absorption spectrum, TEM and histogram of particle size for 5th size fraction of Zn_3P_2/4-etpy.





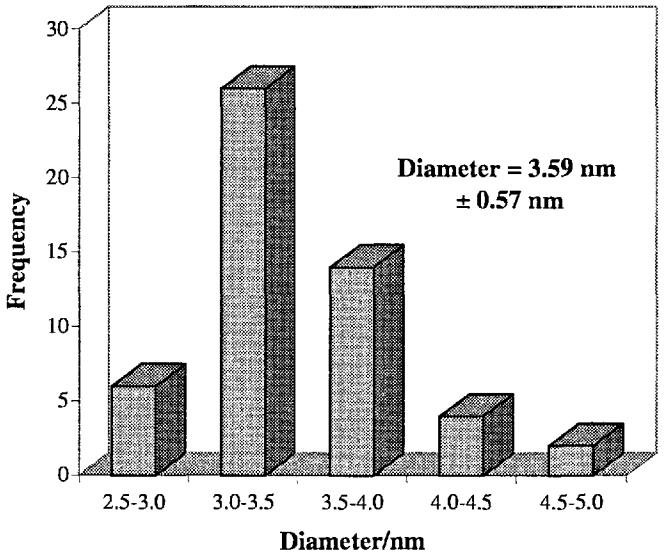


Figure 3.29: Optical absorption spectrum, TEM and histogram of particle size for 8^{th} size fraction of Zn_3P_2/4-etpy.

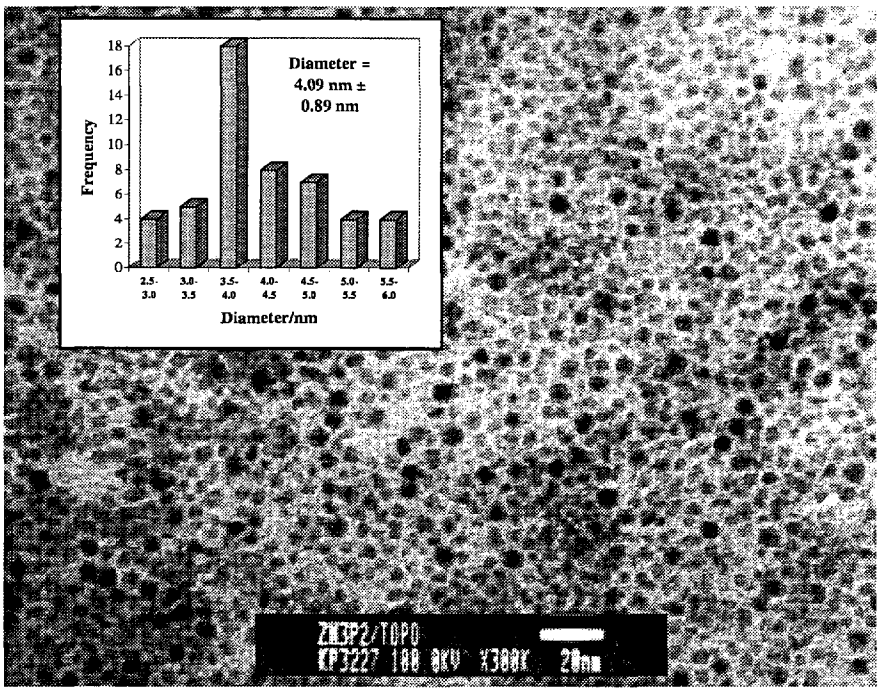


Figure 3.30: TEM image of Q-Zn_3P_2 capped with TOPO, synthesised at 150 °C for 4 hours. Bar = 20 nm.

EDAX analysis of both TOPO capped and 4-ethylpyridine capped particles, whilst not evidence of bonding to the surface, show differing ratios of Zn and P as expected, indicating an increased amount of phosphorus in the TOPO capped samples (Figure 3.31).

Infra-red spectroscopy on TOPO capped Zn_3P_2 shows the characteristic ν(C-H) bending mode from CH_3 at 1465 cm^{-1}. The ν(P=O) stretch, normally observed at 1145 cm^{-1}, found to shift to a lower wave number (1125 cm^{-1})[53] in cadmium phosphide, was found to have shifted in a similar manner when complexed to surface zinc. The ν(P=O) stretch was found as a broad band at 1097 cm^{-1}, a shift of *ca.* 50 cm^{-1}. This is in agreement with previous studies on alkylphosphine oxides bonded to zinc salts, in which a shift of 40 cm^{-1} was found.[196] This suggests that TOPO bonds in a similar manner to surface sites in Zn_3P_2 and Cd_3P_2 dots.

4-ethylpyridine capped Q-Zn_3P_2 shows bending and stretching modes similar to those observed for other quantum dots passivated with 4-ethylpyridine (Table 3.10). The Zn-N band is observed as a broad weak feature at 320 cm^{-1}, suggesting bonding through the ring nitrogen.[181]

Free ligand/ cm^{-1}	Zn_3P_2-4-etpy/ cm^{-1}	assignment
1606	1619	ν(C-C)
1417	1409	ν(C-C)
-	1226	ν(C-H)
1066	1062	ν(C-H)
777	773	ν(C-H)
-	320	ν(Zn-N)

Table 3.10: IR data for 4-ethylpyridine and 4-ethylpyridine capped Q-Zn_3P_2.

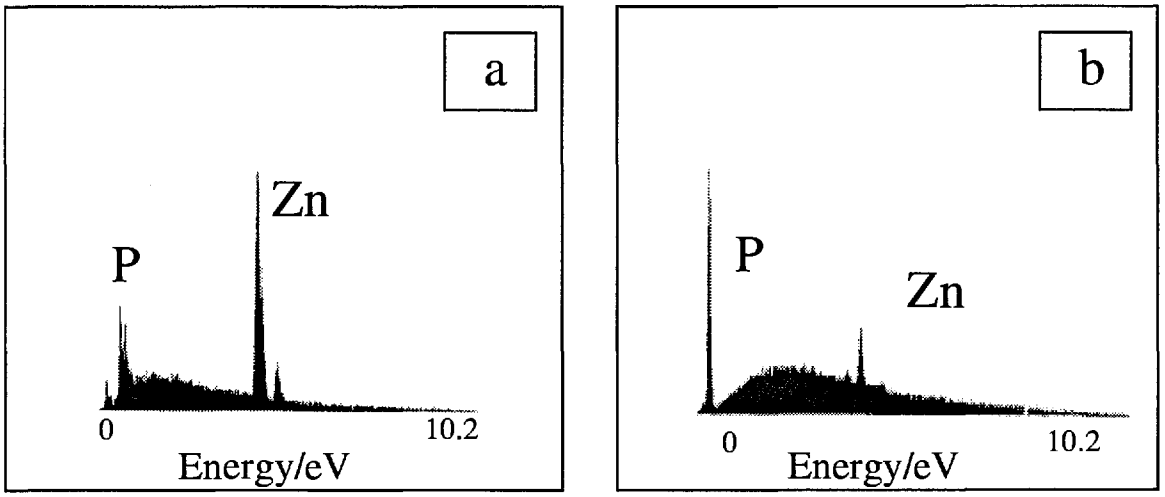


Figure 3.31: EDAX analysis of a)4-ethylpyridine capped Q-Zn_3P_2; b) TOPO capped Q-Zn_3P_2.

Solution state ^{31}P NMR of Q-Zn_3P_2 capped with 4-ethylpyridine displayed features similar to those previously observed with Q-Cd_3P_2. Three distinct broad resonances were observed, suggesting phosphorus environments as predicted for M_3P_2, with phosphorus atoms arranged in three orientations around lattice vacancies[186,187] (Table 3.11). The resonances are significantly downfield. The observation is rather unexpected as MAS NMR on macrocrystalline Zn_3P_2 is reported to show only two of the expected three resonances.[187]

Decoupled ^{31}P MAS NMR of Q-Zn_3P_2 capped with 4-ethylpyridine showed a broad resonance at 32.41 ppm, with weak signals at *ca.* 1 and 60 ppm. Alteration of the spin speed of the sample confirmed the absence of spinning side bands. CPMAS showed resonances at *ca.* 15, 33 and 56 ppm. Each broad resonance had a distinct narrow feature

at 0.9, 40.18 and 62.38 ppm respectively. Due to the enhanced resonance in CPMAS, the narrow features were assigned as phosphorus environments at the surface (Table 3.11).

Solution and solid state ^{31}P NMR on TOPO capped Zn_3P_2 showed typical resonance's for TOPO/TOP species bonded to the surfaces (Table 3.12). No resonance attributable to core phosphorus was observed in TOPO capped Zn_3P_2. This phenomenon was previously observed in TOPO capped Cd_3P_2 and is again attributed to the phosphorus containing passivating ligand masking other resonances.

Solution ^1H NMR of both TOPO and 4-ethylpyridine capped particles show the capping group similar to those observed in Q-Cd_3P_2.

Solution state ^{31}P NMR			CPMAS ^{31}P NMR	
δ ppm	assignment		δ ppm	assignment
32.99	Core Phosphorus		15.00	Core Phosphorus
44.41	Core Phosphorus		0.90	Surface Phosphorus
56.77	Core Phosphorus		33.13	Core Phosphorus
			40.18	Surface phosphorus
			56.74	Core Phosphorus
			62.38	Surface phosphorus

Table 3.11: Solid state and solution state ^{31}P NMR data for 4-ethylpyridine capped Q-Zn_3P_2.

Solution state ^{31}P NMR			Solid state ^{31}P NMR	
δ ppm	assignment		δ ppm	assignment
35.33	Bound TOPO		3.93	-
48.93	Free TOPO		30.70	Bound TOPO
53.29	TOPO impurity		52.76	Free TOPO
57.98	TOPO impurity			
59.73	TOPO impurity			

Table 3.12: Solid state and solution state ^{31}P NMR data for TOPO capped Q-Zn_3P_2.

3.12 Conclusions

Novel chemical routes to high quality nanodispersed quantum dots of Cd_3P_2 and Zn_3P_2 have been developed. Cd_3P_2 was obtained by the controlled thermal decomposition of $[MeCdP^tBu_2]_3$ in TOPO and 4-ethylpyridine. The decomposition of various potential precursors was investigated and those possessing β-hydrogen in the organic moiety were found to be the most successful. Investigation into the decomposition mechanisms outlined a mixture of β-elimination and reductive elimination at different temperatures, the parameters of which could be altered to give products of differing quality.

The results dictated the choice of precursor for use in the synthesis of Zn_3P_2. A methodology was adopted where two precursors were employed (Me_2Zn and HP^tBu_2) in thermolysis in TOPO or 4-ethylpyridine, resulting in organically capped Q-Zn_3P_2.

All nanoparticulates presented in this work were capped with the solvent ligand, either TOPO or 4-ethylpyridine and had optical properties similar to II_3-V_2 compounds prepared by aqueous routes. The nanoparticulates were relatively polydispersed (standard deviation of *ca.* 20 %) and appeared to be a mixture of both crystalline and amorphous particles. The nanoparticles were found to be quantum confined with band gaps shifted to much higher energies. Luminescence appeared strong (except larger particles of Cd_3P_2) and exhibited Stokes shifts relative to the absorption edge, probably due to metal vacancies being efficient trapping sites for charge carriers. The nanoparticles presented here had the advantage over aqueously prepared quantum dots of II_3-V_2 materials by being air stable and resistant to photo-degradation, attributable to the strongly bound organic passivating layer.

The use of diorganophosphide precursors to produce Cd_3P_2 led to the investigation into phosphides of group III metals presented in the next chapter.

Chapter 4 - Synthesis of nanodispersed III-V compounds

4.1 Introduction

III-V compounds are an important class of materials, with many semiconducting applications involving nitride, phosphide, arsenide or antimonide based system.[197] InP is used in optoelectronics as a detector for optical signals and as an infra red emitter.[197] GaP is commonly used in LEDs for emission in the visible spectrum.[198] The advent of nitride compounds has led to diodes and lasers that emit in the blue/green spectral range.[199,200] InP and InAs have a cubic crystalline structure, with direct electronic transitions at point Γ in the Brillouin zone.[201] GaP has the same crystalline structure but has an indirect electronic transition between points Γ and Δ in the Brillouin zone.

Wells *et al.* originally developed a dehalosilylation reaction[69] leading to III-V materials as an alternative to metal alkyls and arsine/phosphine gas, originally employed by Manasevit in MOCVD.[133]

$$InCl_3 + P(SiMe_3)_3 \longrightarrow InP + 3\ ClSiMe_3$$

Micic[67,68] and Alivisatos[65,71] have both adapted the Bawendi method[35] and the dehalosilylation reaction to produce Q-InP and Q-InAs capped with TOPO and amines. The nanoparticles are relatively polydispersed (size distribution of *ca.* 20 %), require heating for several days to acquire a high degree of crystallinity and are reported to be contaminated with oxide waste products. The inherent difficulties in preparing III-V nanoparticles has been discussed by Heath *et al.* as discussed in chapter one.[66]

Single source organometallic routes to GaP, InP, GaAs and InAs have been developed by Wells *et al.* and has been discussed in the first chapter, producing nanocrystals of various sizes, with little discussion devoted to the capping group.[79-81]

4.2 Synthetic methodology

Following the successful use of $[MeCdP^tBu_2]_3$ in preparing Cd_3P_2 in TOPO and 4-ethylpyridine, the analogous diorganophosphides of indium and gallium were investigated.[202] Diorganoarsenides have also been reported but are relatively hard to prepare.[202] An alternative arsenic source was therefore preferred and a precursor previously employed in MOCVD, *tris*(dimethylamino)arsine ($As(NMe_2)_3$) was used.[203] A mixture of $InCl_3$ and $As(NMe_2)_3$ in 4-ethylpyridine was thermolysed at 167 °C resulting in the formation of high quality nanometer sized InAs. The $InCl_3$ was found to form an adduct with 4-ethylpyridine resulting in *mer*[In(4-ethylpyridine)$_3$Cl$_3$](Figure 4.1, Appendix 3). Similar behaviour was discussed by Alivisatos *et al.* when $InCl_3$ complexed to TOPO prior to reaction to produce TOPO capped InP.[65] The complex exists in an approximately octahedral arrangement with *mer* stereochemistry. A similar set of compounds, [In(pyridine)$_3$X$_3$]·pyridine (X = Br, Cl) exist with the same geometry.[204,205] Carty *et al.* calculated steric angles for $InCl_3$·3N systems and predicted *fac* geometry,[206] however strong repulsive interactions between bulky ligands in InX_3·L_3 systems have previously been attributed as the cause of the *mer* geometry.[205] The bond angle between the two *trans* Cl atoms is 172.04 ° hence the complex is only approximately octahedral. A similar

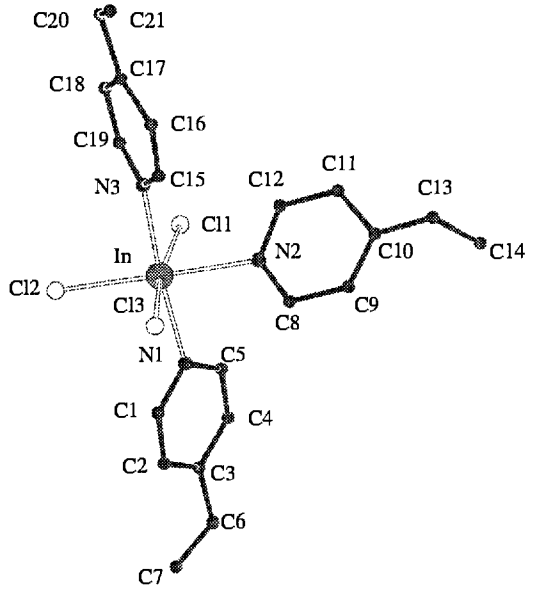


Figure 4.1: Crystal structure of mer[In(4-ethylpyridine)$_3$Cl$_3$].

distortion in bond angles is observed in [In(pyridine)Cl$_3$]·pyridine and [In(pyridine)$_3$Br$_3$]·pyridine. [204,205]The In-N bond lengths (2.31 Å average) are comparable to [In(pyridine)Cl$_3$]·pyridine (2.33 Å average), indicating electron donation strengths of 4-ethylpyridine and pyridine are similar.[204] In-Cl *(trans)* bond lengths (2.46 Å average) are similar to those observed in[In(pyridine)Cl$_3$]·pyridine (2.47 Å average), but the *cis* In-Cl bond length is slightly shorter (2.41 Å). The shortening of the *cis* In-Cl bond was not observed in the simple pyridine complex.[204]

Dimethylamino compounds have previously been used as precursors in low pressure MOCVD for As and Sb containing semiconductors.[203] The surface reaction was previously reported to proceed by elimination of the cyclic compound aziridine as a major decomposition product.[207] It is reasonable to assume that a similar mechanism applies to solution phase decomposition.

Indium Arsenide

Indium arsenide is of particular interest as it has potential for application in industry. Nanoparticles of InAs in the size range 6 - 8 nm are reported to luminesce at *ca.* 1200 nm, an important telecommunication wavelength.[71] The InAs nanoparticles presented here were synthesised by the thermolysis of $InCl_3$ and $As(NMe_2)_3$ in 4-ethylpyridine.

4.3 Optical properties of Q-InAs

The thermolysis of $InCl_3$ and $As(NMe_2)_3$ in 4-ethylpyridine (167 °C, up to 6 days) produced an optically clear deep red solution of nanocrystals. Optical absorption spectra taken at different stages of growth at 167 °C are shown in figure 4.2. Electronic spectroscopy of an aliquot taken after 30 mins. showed a band edge at 2.96 eV (418 nm), with samples left for 6 days showing a band edge of 2.63 eV (471 nm), consistent with further shell growth. The theoretical diameters of such particles are 1.94 nm and 2.07 nm respectively, as calculated from the effective mass approximation (Equation 1.6).

Application of the Brus equation predicts minor shell growth over the 6 days after the first aliquot was taken. This is consistent with observations for TOPO capped III-V materials where the majority of growth is achieved in *ca.* the first hour, with prolonged heating used principally for annealing.[65,71]

Further growth was obtained by injection of more $InCl_3$ and $As(NMe_2)_3$ (1:1 ratio) in 4-ethylpyridine and further refluxing for 3 hours. Optical spectra of the sample

obtained from further application of precursor showed absorption consistent with larger particles (Figure 4.2). An excitonic peak was clearly visible at 451 nm (2.75 eV). An electronic spectrum of the sample suggested a band edge of 2.43 eV (510 nm) (predicted diameter of 2.17 nm).

Addition of further precursor appeared to result in further growth of the nanoparticles as suggested by the shift in electronic spectrum to lower energy. The electronic spectrum also suggested an increase in monodispersity as demonstrated by the emergence of a clear excitonic feature in the optical spectra. The increase in diameter and monodispersity upon further addition of precursor to the reaction has been previously observed and referred to as growth focusing.[208] Size fractionation did not result in any significant separation of different sizes of nanoparticles. Addition of light petroleum to a 4-ethylpyridine solution until flocculation resulted in solid size fractions. Comparison of the electronic spectra of the first 20 fractions showed little difference. Ineffective size selective precipitation has been reported for TOPO capped InP and attributed to a stable oxide layer forming on the quantum dot, inhibiting the effect of the non-solvent.[209] In contrast, II-VI materials are reported to form unstable oxide species, causing nanocrystal surface degradation. The absence of a stable oxide layer allows size fractionation procedures.[53]

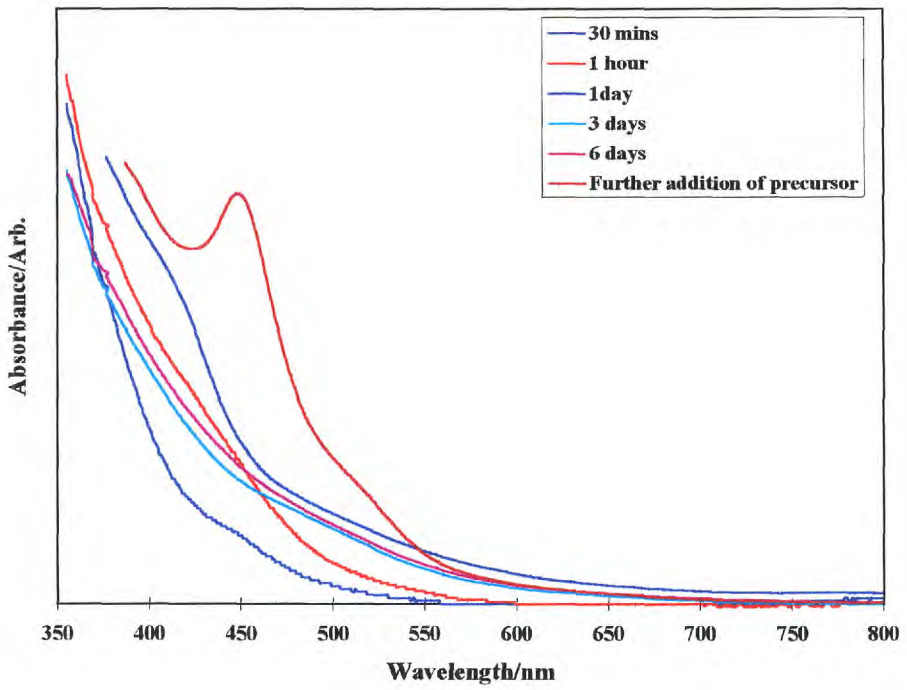


Figure 4.2: Optical absorption spectra of Q-InAs synthesised under different conditions.

Emission spectra for samples isolated at 30 mins, 3 days and 6 days with further precursor added are shown in figure 4.3 and table 4.1. Emission is broad, consistent with emission from nanoparticles with a large size distribution (although not as broad as emission from InP and GaP synthesised from diorganophosphides which will be discussed later). Comparison of the width of emission profiles provides evidence of what has recently been referred to as growth focusing. The emission from samples obtained after 30 mins. had a FWHM of 0.36 eV which increased with growth up to 0.62 eV (3 days). Addition of further precursor resulted in samples with emission profiles with a FWHM of 0.41 eV, indicative of a reduction in the particle size distribution.

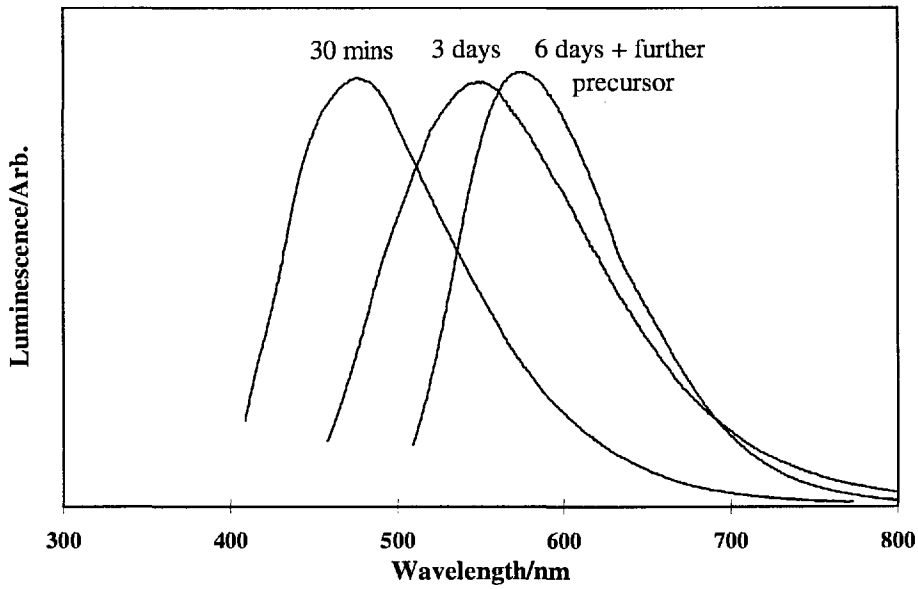


Figure 4.3: Emission spectra from 3 samples of Q-InAs.

The emission spectra have Stokes shifts of up to *ca.* 80 nm. (Table 4.1). The change in Stokes shift with change in particle size has previously been observed with TOPO capped InP.[210] No evidence of surface traps were observed, suggesting that the luminescence is near-band edge due to surface states being filled by the capping ligand 4-ethylpyridine.

Reaction conditions	Band edge/ eV(nm)	Emission $\lambda_{max.}$/ eV (nm)	Stokes shift/ nm	Predicted diameter/ nm
30 mins growth	2.96 (418)	2.59 (478)	60	1.94
3 days growth	2.63 (471)	2.25 (550)	79	2.07
6 days growth + further precursor	2.43 (510)	2.14 (577)	67	2.17

Table 4.1: Selected information on optical properties of Q-InAs.

4.4 Structural Characterisation of Q-InAs

InAs exists in the cubic (zinc blende) phase.[201] The particle diameter predicted from the optical data suggests quantum dots around 2 nm, much smaller than those reported by Alivisatos *et al.*[65,71] and Micic *et al.*[67,68] and therefore expected to show an XRD pattern consistent with particles of a small crystalline domain. The low temperature of synthesis (167 °C) also inhibits the growth of good crystalline particles. EDAX analysis shows the presence of both In and As. A signal from silicon was due to the sample being held on a silicon wafer (Figure 4.4). The XRD pattern on samples prepared at 167 °C for 3 days showed a strong reflection from the 111 plane but poor reflections from the 311 and 220 planes, consistent with poorly crystalline/amorphous material. The width of the reflection from the 111 plane is consistent with particles with a diameter of 0.98 nm, approx. half the diameter predicted by the Brus equation. The Scherrer equation which is used to estimate particle size from XRD patterns relies upon the size of the crystalline domain. Comparison of size predictions to experimental evidence (TEM) shows an anomaly. TEM of samples synthesised over 6 days of growth show the presence of small particles with an average diameter of 2.32 nm ± 0.56 nm (24 %) (Figure 4.5). It may be that the particles are only partly crystalline, with a crystal core of *ca.* 1 nm and an amorphous surface of approx. 0.65 nm. The over-all size is smaller than InAs nanocrystals prepared by other organometallic routes, where the smallest diameters were reported to be 2.5 nm.

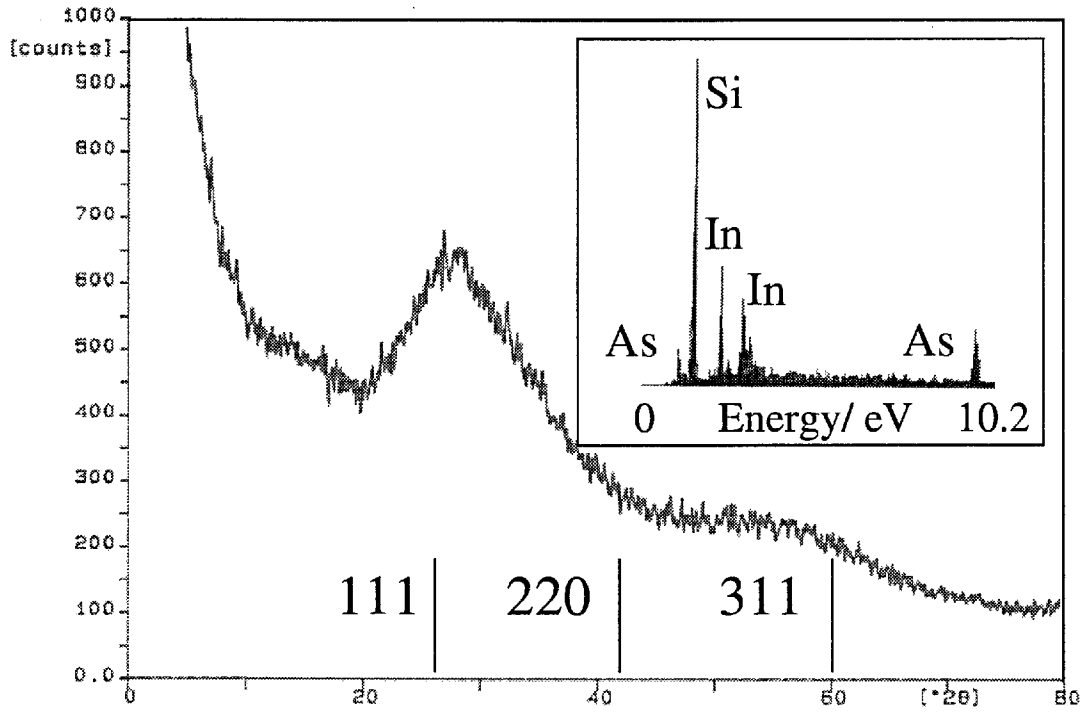


Figure 4.4: XRD pattern for Q-InAs, showing the major Miller indices expected for InAs. Inset; EDAX analysis of InAs nanocrystals.

HRTEM shows dark patches on the copper grid similar to those observed in Cd_3P_2 capped with 4-ethylpyridine which are attributed to amorphous particles (Figure 4.6). No lattice fringes were observed. This agrees with the XRD pattern which predicts either amorphous or very poorly crystalline materials, attributable to the low temperature of synthesis (167 °C) and the extremely small size of the particles prepared.

^{1}H NMR on InAs nanoparticles presented in this thesis shows the presence of the capping group as previously observed with 4-ethylpyridine capped Q-Cd_3P_2 and Q-Zn_3P_2. IR spectroscopy also shows the capping group with band deformations as previously found with nanoparticulates capped with the organic ligand (Chapter 3). The ν(In-N) was

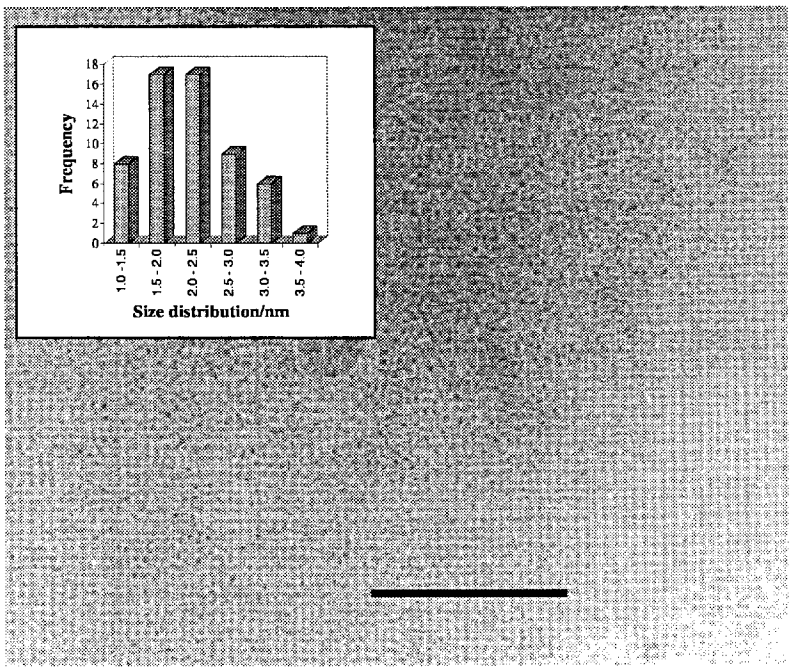


Figure 4.5: TEM image of Q-InAs synthesised at 167 °C for 6 days, bar = 100 nm.

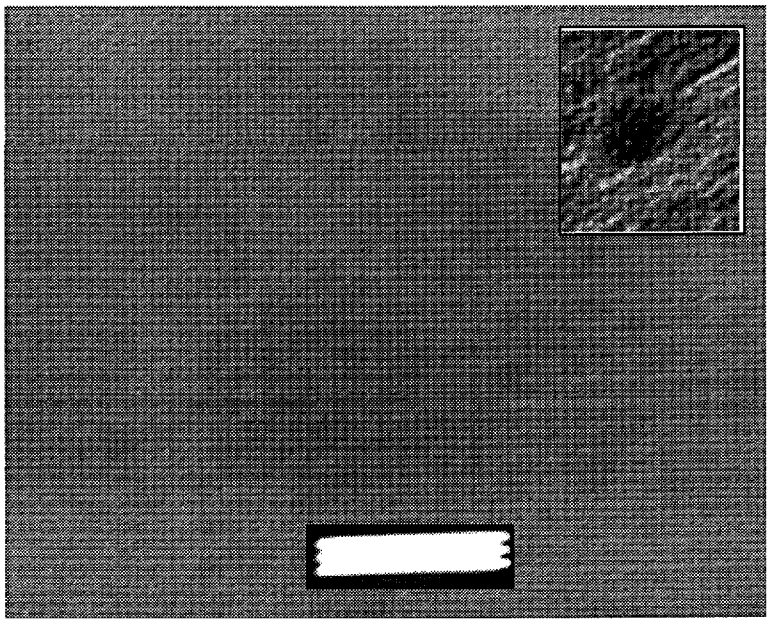


Figure 4.6: HRTEM image of Q-InAs synthesised at 167 °C for 6 days, bar = 20 nm.

Inset; Close up of a single nanocrystal showing amorphous character.

found at 459 cm^{-1} implying that binding to the nanoparticulate surface occurs through the heterocyclic nitrogen.

4.5 Manipulation of Q-InAs

One of the advantages of using a liquid capping agent is that the sample can be redispersed in the solvent used to cap them. In contrast TOPO capped dots are dispersed in hydrocarbons (TOPO is a solid at room temperature). A solution of TOPO capped dots can be manipulated into thin films by controlled crystallisation from solution or by deposition onto Langmuir-Blodgett films (Chapter 1). However, simple spin coating from hydrocarbon solution was attempted using CdSe and CdS prepared as described in chapter 2 and was largely unsuccessful as excess TOPO in solution resulted in uneven films.

4-Ethylpyridine passivated InAs dispersed in 4-ethylpyridine was easily spin coated onto glass substrates. AFM showed the particles deposited onto glass with no evidence of close packing (Figure 4.7) with a top layer depth profile of *ca.* 7 nm. Film thickness was found to be approx. 10 microns by SEM. The diameter of particles appears larger when observed by AFM due to the filament of the microscope lifting up before the tip reaches the nanoparticle (microscopic enlargement).[211] Murray *et al.* have produced super lattices of TOPO capped CdSe by exposing an octane-octanol solution to heat and reduced pressure, inducing crystallisation into an ordered close packed array of particles.[54] By application of a gentle vacuum (*ca.* 0.05 Torr) to a 4-ethylpyridine solution of Q-InAs at

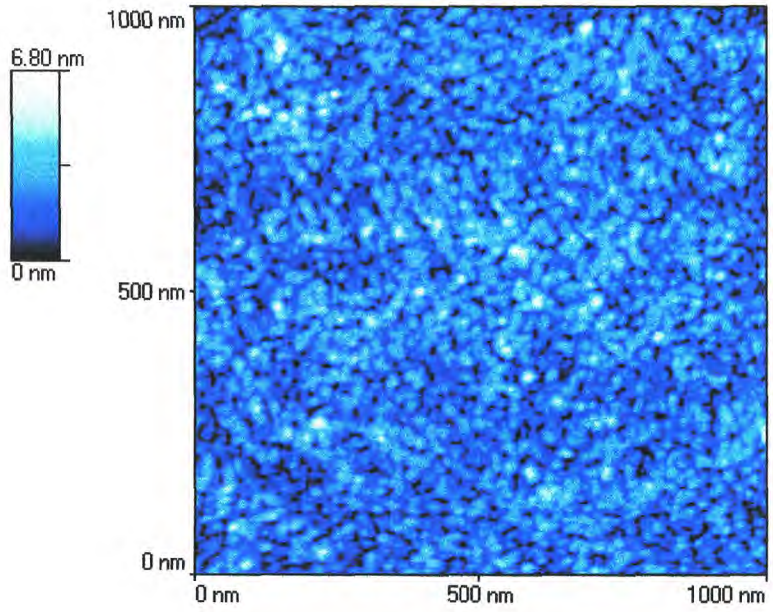


Figure 4.7: AFM image of Q-InAs spin coated on glass.

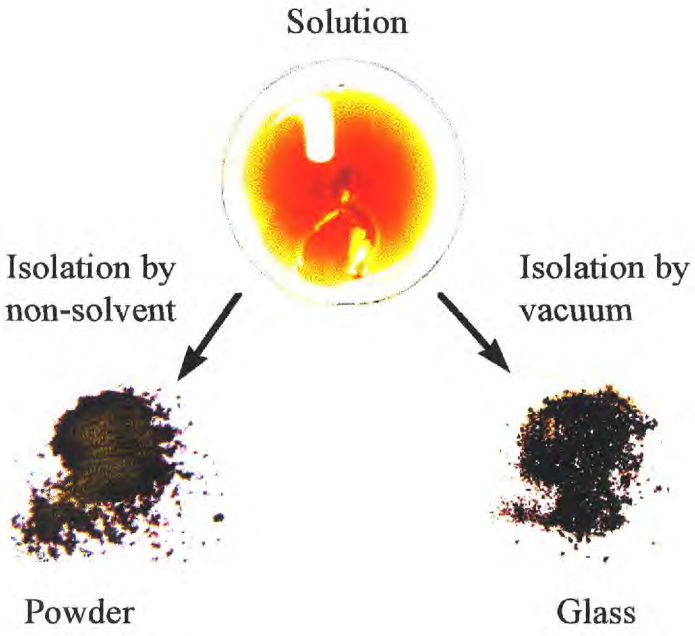


Figure 4.8: Photo of Q-InAs powder (left) and Q-InAs glass (right) from a 4-ethylpyridine solution.

room temperature followed by washing with light petroleum, a glass was formed (Figure 4.8). The glass had an XRD pattern consistent with the nanoparticles used to produce it and exhibited no evidence of super lattice behaviour.[54] The reason for glass formation rather than a super lattice is attributed to the relatively large size distribution of the constituent nanoparticles when compared to analogous II-VI super lattices. Nanoparticulate CdSe prepared by Murray *et al.* had a size distribution of *ca.* 5 %. Prior to manipulation into a super lattice, the CdSe was size fractionated, decreasing the size distribution further.[54] InAs used in this study was found to be unaffected by size fractionation and therefore probably had too large a size distribution for effective crystallisation into a lattice. However, the ease with which Q-InAs was manipulated into a glass is surprising.

Indium and Gallium Phosphide

4.6 Thermolysis of gallium and indium diorganophosphides

The trimeric diorganophosphide of cadmium was found to decompose by at least two pathways (chapter 3), depending on temperature and its organic moiety. It is therefore fair to assume that diorganophosphides of group 13 metals should decompose by the same mechanisms. TGA analysis of $In(P^tBu_2)_3$ and $Ga(P^tBu_2)_3$ showed distinct regions of decomposition, tentatively assigned as predominantly β-hydrogen elimination at lower temperatures (up to *ca.* 150 °C) and predominantly reductive elimination at higher temperatures (150 °C and above) (Figure 4.9).

TGA analysis of $In(P^tBu_2)_3$ showed a gentle curve similar to that observed for the decomposition of $[MeCdP^tBu_2]_3$, with two slightly different decomposition pathways. $Ga(P^tBu_2)_3$ has a sharper profile, with what appears to be three areas of decomposition. The curves are not sharp and indicate multiple decomposition paths. The percentage of remaining compound after thermolysis (Figure 4.9) for $M(P^tBu_2)_3$ (M = In, Ga) is consistent with the loss of three $(CH_3)C{=}CH_2$ groups ($In(P^tBu_2)_3$ - $3(CH_3)C{=}CH_2$ = 69 %, $Ga(P^tBu_2)_3$ - $3(CH_3)C{=}CH_2$ = 66 %). If the compound was losing P^tBu_2 groups, the percentage of remaining compound would be much lower ($In(P^tBu_2)_3$ - 2 P^tBu_2 = 47 %, $Ga(P^tBu_2)_3$ - 2 P^tBu_2 = 40 %).Although this is strong evidence, this in itself conclusive.

GC-MS studies on $In(P^tBu_2)_3$ confirm the mechanism suggested in chapter 3. Thermolysis studies at 100 °C showed two major stages of decomposition at retention times of 0.94 - 1.5 seconds and 5.79 - 6.15 seconds consistently displaying a major

species with a mass of 56, previously attributed to the β-H elimination product $(CH_3)_2C=CH_2$. Other signals were observed showing evidence of the reductive elimination product $P_2{}^tBu_4$, and related fragments (Table 4.2).

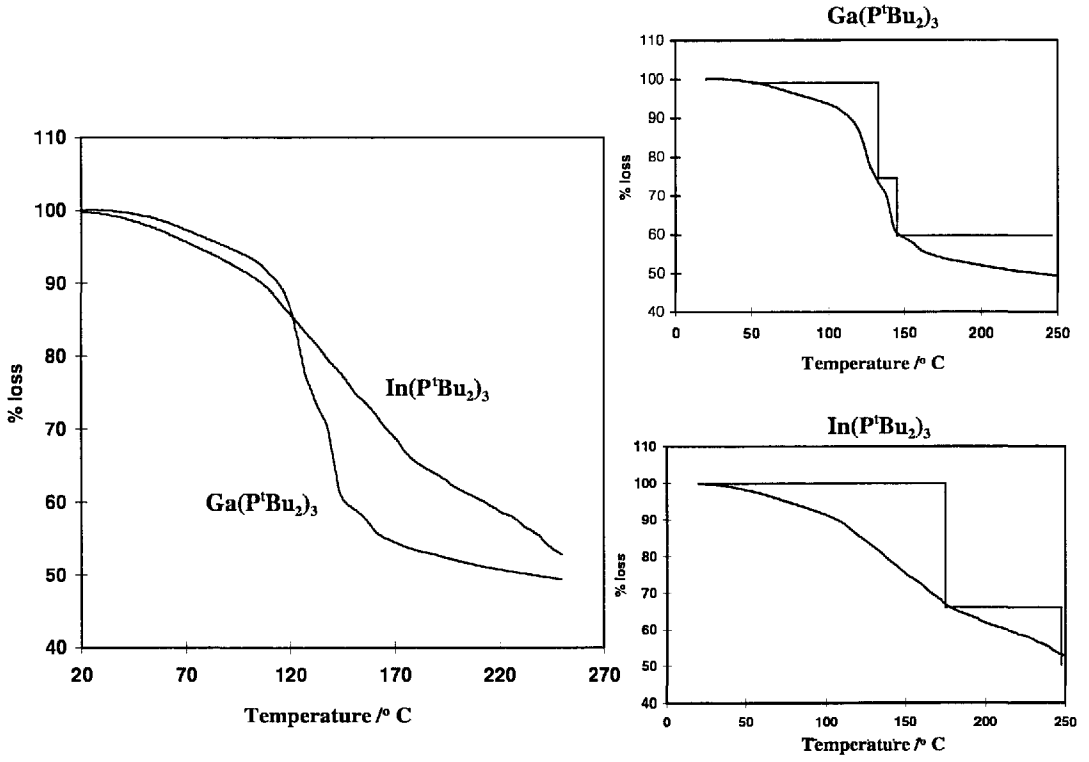


Figure 4.9: TGA analysis of $In(P^tBu_2)_3$ and $Ga(P^tBu_2)_3$.

Other molecular fragments observed were also present in the room temperature mass spectrometry results and were not the process of thermolysis. A species at m/z = 104 was attributed to an oxidation product as the precursor is extremely air sensitive. Signals at 146 were tentatively assigned as HP^tBu_2, an elimination product previously found in the decomposition of $[MeCdP^tBu_2]_3$ (chapter 3).

GC-MS of $In(P^tBu_2)_3$ at 250 °C suggests two major stages of decomposition. Decomposition products were observed between retention times of 1 - 2 seconds and 5.76

- 6.25 seconds, showing evidence of both β-hydrogen elimination and reductive elimination (Table 4.2). The heaviest observed fragment had a mass of 295 and was assigned as a molecular fragment ($InP_3C_6H_{15}$), the second heaviest had a mass of 290 and was assigned as $P_2{}^tBu_4$, the reductive elimination product.

GC-MS of $Ga(P^tBu_2)_3$ showed similar GC results at temperatures of 100, 175 and 250 °C with the majority of signals from either precursor molecular fragments or thermolysis products (Table 4.2).

Thermolysis of $Ga(P^tBu_2)_3$ or $In(P^tBu_2)_3$ in 4-ethylpyridine at 167 °C gave coloured nanoparticulate colloidal solutions. The quantum dot colloids are stable for months in air and are not sensitive to illumination even in the presence of oxygen.

However, thermolysis of $Ga(P^tBu_2)_3$ or $In(P^tBu_2)_3$ in TOPO at temperatures between 100 °C and 250 °C resulted in the formation of an unidentified solid. The solid was soluble in methanol and toluene and therefore would not precipitate from solution making isolation difficult. Once isolated as a waxy solid by evaporation, it was found to be insoluble in non-polar hydrocarbons. ^1H NMR on the solid did not show any resonances consistent with TOPO capped particles, whilst XRD showed evidence of very small particles. This phenomenon has previously been reported during the attempted synthesis of TOPO capped ZnSe by Hines *et al.* where the nanoparticles were reported to be too small to be isolated by solvent/non-solvent interactions, or too large and precipitated out of the reaction solvent.[60] This was attributed to TOPO binding too strongly to the metal and TOP not binding strongly enough. Long chain amines were chosen as a replacement solvent/capping system.

Thermolysis products of $In(P^tBu_2)_3$						Thermolysis products of $Ga(P^tBu_2)_3$		
100 °C			250 °C			175 °C		
Retention time/minutes	**m/z**	**Assignment**	**Retention time/minutes**	**m/z**	**Assignment**	**Retention time/minutes**	**m/z**	**Assignment**
0.94 - 1.5	56	$(CH_3)_2C=CH_2$	1 - 2	56	$(CH_3)_2C=CH_2$	0.96	56	$(CH_3)_2C=CH_2$
5.79 - 6.15	56	$(CH_3)_2C=CH_2$	4.62	119	$P_2{}^tBu$	1.1 - 1.3	56	$(CH_3)_2C=CH_2$
	57	^tBu		176	$P_2{}^tBu_2$	5.38	57	^tBu
	146	HP^tBu_2	5.76 - 6.25	57	^tBu		146	HP^tBu_2
8.5	57	^tBu		146	HP^tBu_2	7.93	56	$(CH_3)_2C=CH_2$
	104	$O=P^tBu$	8.56	57	^tBu		104	$O=P^tBu$
	145	P^tBu_2		104	$O=P^tBu$		146	HP^tBu_2
12.45	57	^tBu		146	HP^tBu_2	12.27	104	$O=P^tBu$
9.82	57	^tBu		177	$P_2{}^tBu_2$		146	HP^tBu_2
	145	P^tBu_2	9.92	57	^tBu		202	P^tBu_3
20.01	57	^tBu	12.23	57	^tBu	18.13	57	^tBu
	176	$P_2{}^tBu_2$					146	HP^tBu_2
	290	$P_2{}^tBu_4$					176	$P_2{}^tBu_2$
	233	$P_2{}^tBu_3$					202	P^tBu_3
	104	$O=P^tBu$					233	$P_2{}^tBu_3$
	146	HP^tBu_2					290	$P_2{}^tBu_4$
20.11	57	^tBu				18.24	57	^tBu
	233	$P_2{}^tBu_3$					233	$P_2{}^tBu_3$

Table 4.2: Selected GC-MS data for the thermolysis of $Ga(P^tBu_2)_3$ and $In(P^tBu_2)_3$ at different temperatures.

Indium Phosphide

4.7 Optical properties of Q-InP

Thermolysis of $In(P^tBu_2)_3$ in 4-ethylpyridine at 167 °C for up to 7 days resulted in a coloured solution. The quantum dots form within 30 minutes after injection of the precursor. Prolonged exposure to heat does not result in further shell growth but is required for annealing of the crystals. III-V materials are less ionic than the analogous II-VI compounds and therefore require extra annealing to obtain a good crystalline core.[66] Bulk indium phosphide has a band gap of 1.27 eV (975 nm),[201] which should shift to higher energies upon confinement. The excitonic diameter has been calculated to be *ca.* 21.3 nm (Equation 1.4) and any crystal with a diameter smaller than this should exhibit quantum confinement effects.

A solution of Q-InP prepared in 4-ethylpyridine at 167 °C for four days gave an electronic spectrum (Figure 4.10, spectrum a) with the onset of absorption at 1.78 eV (696 nm), an increase in the band gap of 0.51 eV.

Samples left for 7 days had an optical absorption profile (Figure 4.10, spectrum b) with a similar band edge position but without the excitonic shoulder, indicating a larger size distribution. Two excitonic peaks were observed at 462 and 590 nm (2.68 and 2.10 eV respectively) for the sample prepared over 4 days. Size fractionation procedures used successfully for Cd_3P_2 and Zn_3P_2 (chapter 3) did not appear to work for InP. After the

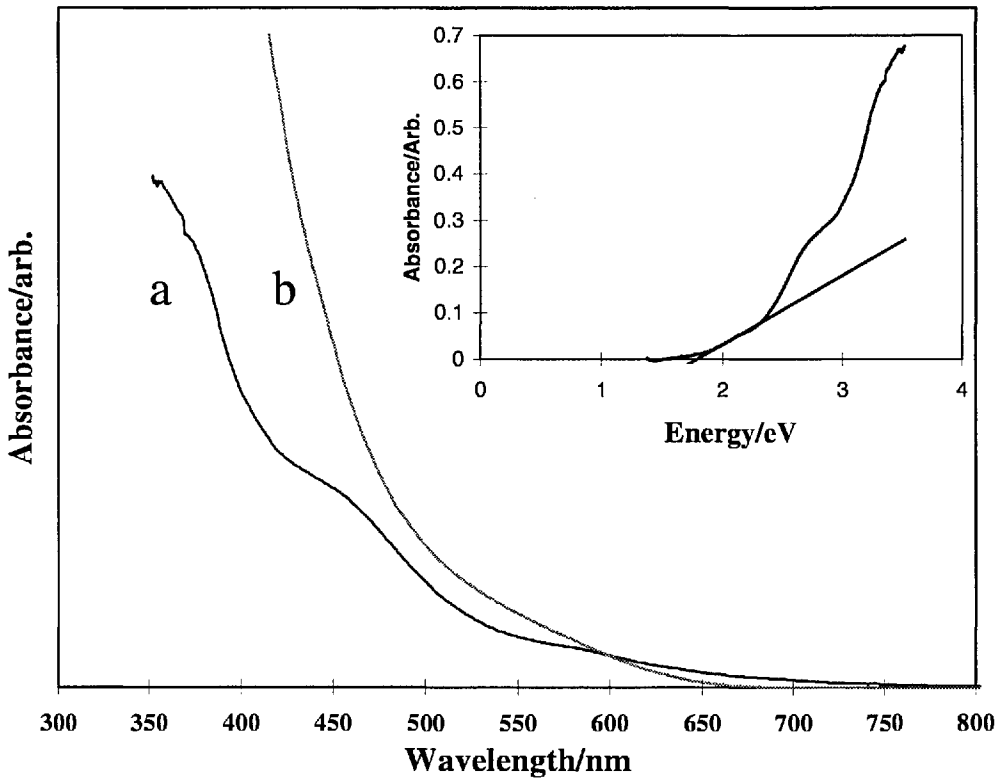


Figure 4.10: Optical electronic spectrum of Q-InP, a) = 167 °C, 4 days; b) 167 °C, 7 days. Inset; Measurement of the band edge by the direct band gap method.

addition of non-solvent, flocculation and isolation of up to 20 fractions, the band edge had not appeared to have significantly shifted. This is attributed to a stable oxide forming on the nanocrystal surface, hindering size fractionation procedures. Luminescence of Q-InP showed a broad near band edge emission with a $\lambda_{max.}$ at 534 nm (2.32 eV), slightly red shifted from the first excitonic transition (Figure 4.11). The Stokes shift of *ca.* 0.5 eV is usually attributed to a dark exciton, although Nozik *et al.* have attributed this phenomenon in InP quantum dots to emission coming from an intrinsic, spin forbidden

state.[209] No evidence was observed for the existence of shallow traps with no red emissions observed in this work.

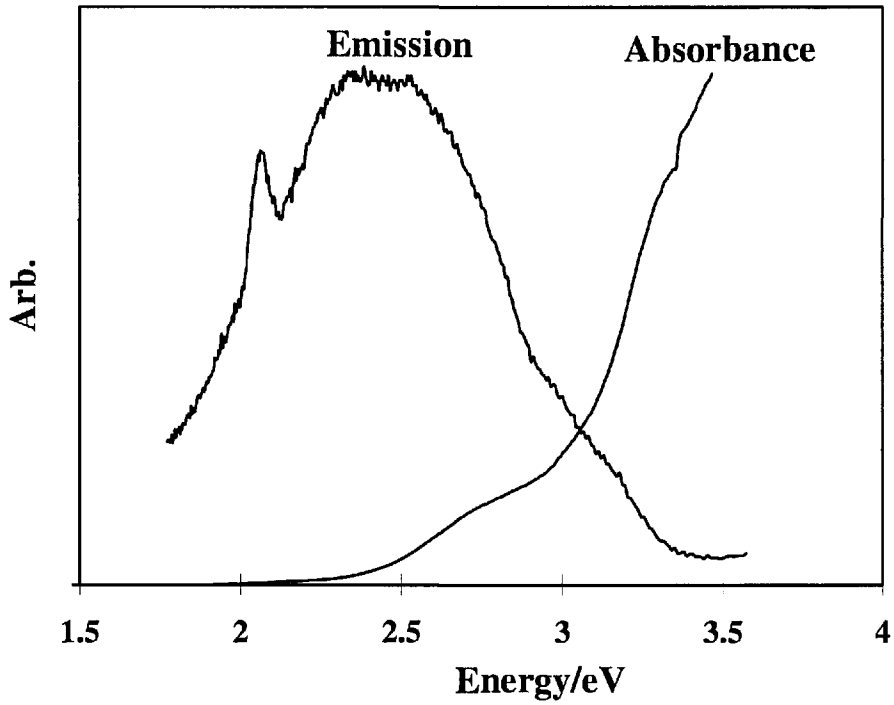


Figure 4.11: Luminescence spectra of Q-InP (167 °C, 4 days), with optical absorption edge showing a slight Stokes shift. (Emission feature at ca. 2 eV is a 2nd order excitation.)

The broadness of the emission can be attributed to the large size distribution when compared to analogous II-VI compounds (FWHM for InP = 0.90 eV, σ = *ca.* 20 %; FWHM for CdSe (250 °C) = 0.24 eV, σ = *ca.* 5%).[35] This is common in TOPO capped III-V materials where harsh growth conditions lead to large size distributions.[65-68,71] The emission profile of InP appears wider than emission from InAs capped with the same ligand.

4.8 Structural characterisation of Q-InP

Macrocrystalline indium phosphide is reported to exist in the cubic zinc blende form.[201] Previous analysis of III-V TOPO capped dots showed a large degree of amorphous character,[68] attributed to the increased covalent nature relative to II-VI dots, demanding the need for higher temperatures to obtain highly crystalline quantum dots. EDAX analysis shows indium and phosphorus signals as expected but is not evidence for the presence of indium phosphide.

The quantum dots of III-V materials presented in this thesis displayed X-ray diffraction patterns consistent with poorly crystalline III-V materials or materials with very small crystalline domains (*ca.* 25 Å as reported previously by Micic *et al.*) (Figure 4.12).[68] The nanoparticles of InP reported in this thesis are *ca.* 7 nm in diameter as shown by TEM. It can therefore be assumed that the nanoparticles of InP have a crystalline core of *ca.* 2.5 nm and an amorphous shell. The amorphous shell is attributable to the low temperature of synthesis (167 °C) which is significantly lower than that previously employed to obtain organically passivated nanocrystals (TOPO capped dots required temperatures between 270 °C and 350 °C to obtain good crystallinity).[65-68,71]

Two broad reflections are observed at 2θ angles of *ca.* 30 and 55 °. The broad reflection at 55° cover reflections from the 220 and 311 planes indicative of the cubic phase. This is not however confirmation of the phase. The large reflection at 30° is consistent with the 111 plane. The reflections observed are typical of quantum dots with an indeterminate crystal core, *i.e.*, neither zinc blende or wurtzite.[140]

TEM experiments show networks of dots on the copper grid, not unlike nanocrystals in a polymer host (Figure 4.13). The nanocrystals do not stand free (*cf.* TOPO capped Cd_3P_2 and Zn_3P_2) but exist in what appears to be a polymeric type matrix.[58,59] Pyridine capped particles are reported to show a propensity to aggregate and cross link, possibly explaining the phenomena.[212,213] The nanocrystals synthesised at 167 °C for four days have an average diameter of 7.24 nm, with a standard deviation of ± 1.24 nm (17.12 %) as show in figures 4.13 and 4.14, which is large when compared to TOPO capped II-VI quantum dot (± 5 %)[35] and comparable to TOPO capped InP (± 20 %).[65] Larger nanoparticles are clearly prolate with aspect ratios of up to 1.4. Samples prepared at 167 °C for 4 days have optical absorption spectra displaying a band edge of 1.78 eV (696 nm) and a predicted diameter of 6.44 nm (Equation 1.6).

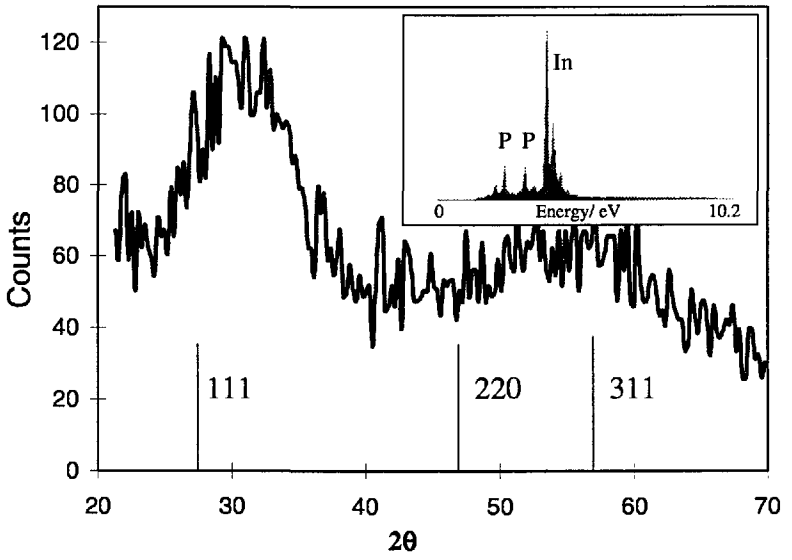


Figure 4.12: XRD pattern for Q-InP (167 °C, 4 days), showing the major Miller indices expected for InP. Inset; EDAX analysis of InP nanocrystals.

HRTEM studies on samples deposited on copper grids show large dark areas similar to those observed in Q-InAs. The lack of lattice fringes implies that the particles are mainly amorphous or poorly crystalline. The presence of the 111 plane in the XRD however lends to the assumption that the particles are slightly crystalline. ICPAES experiments show a high metal content due to the reductive elimination products of the precursor. Samples were found to have In:P ratios as high as 4:1 in reactions left for 7 days in 4-ethylpyridine at 167 °C. Samples left for 4 days were found to have In:P ratios of 1.5:1.

Infra-red spectroscopic studies on 4-ethylpyridine capped InP nanoparticles show bending and stretching modes associated with 4-ethylpyridine[181] and the bands associated with heterocyclic nitrogen bound to a metal,[181] similar to those observed in 4-ethylpyridine capped M_3P_2 (Chapter 3). Bands at 1606 and 1407 cm^{-1} are attributable to ring stretching, with alkyl C-H bond deformations at 775 and 1060 cm^{-1}. A broad feature at 466 cm^{-1} can be attributed to the ν(In-N) bonding mode indicating that the ligand bonds to the surface indium sites as found in 4-ethylpyridine capped InAs.

^{1}H NMR on 4-ethylpyridine capped InP displayed broad resonances consistent with the organic ligand capping the nanocrystal surface (*cf.* Chapter 3). Solution ^{31}P NMR displayed a broad resonance at 33.63 ppm consistent with a species with one phosphorus environment. Decoupled MAS ^{31}P NMR showed a broad single resonance at 31.97 ppm and is attributed to the core of the nanocrystal. CPMAS ^{31}P NMR displayed the single resonance at 32.34 ppm and an intense resonance at 0.95 ppm, assigned as a surface feature. This is shifted from the resonances reported for bulk InP (δ ppm = -148)[214,215]

and contrary to nanocrystalline InP previously reported (*ca.* -200 ppm).[182] The reason for this is again not clear.

Application of a vacuum to a 4-ethylpyridine solution of Q-InP resulted in a glass forming in the same manner as InAs.

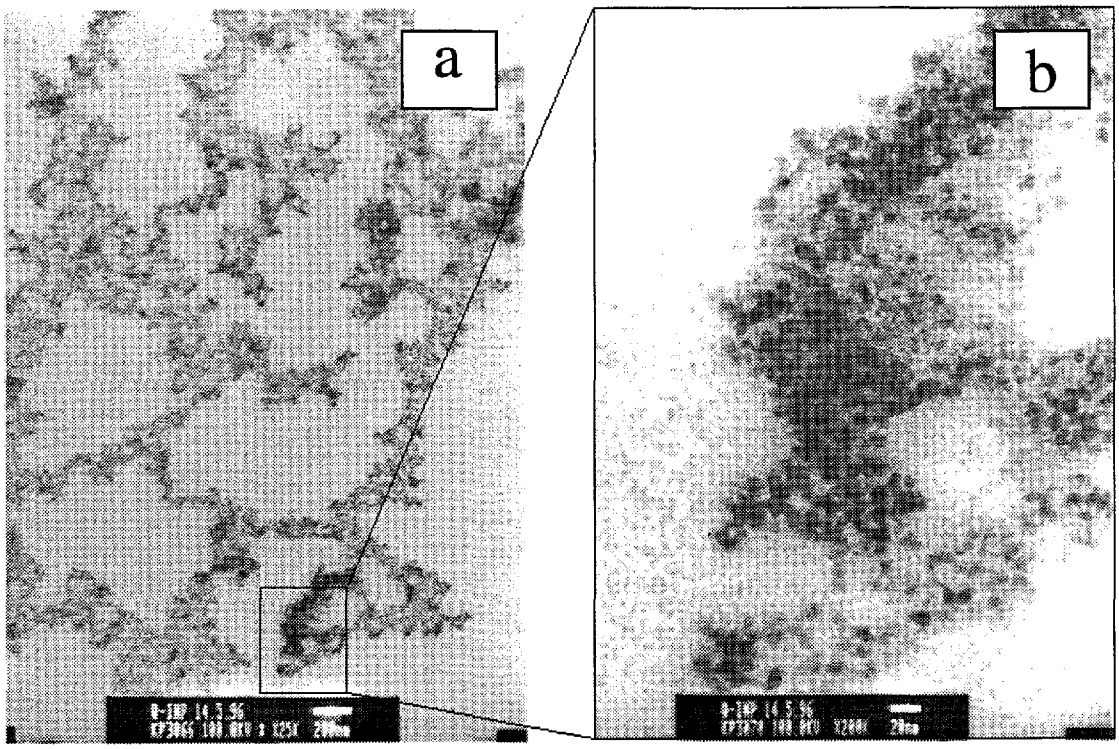


Figure 4.13: TEM images of Q-InP (167 °C, 4 days);

a) bar = 200nm; b) Close up of boxed section, bar = 20 nm.

Gallium Phosphide

4.9 Optical properties of Q-GaP

Organically capped Q-GaP is the least studied of the phosphide III-V nanocrystalline materials. Calculations by Krishna *et al.* show below 30 Å, the direct band gap is predicted to decrease with decreasing particle size and the indirect band gap increase. As a result, GaP is predicted to undergo a transition from an indirect to direct semiconductor at around 20 Å.[32,67,68] The effect on absorption has not been investigated in detail. The absorption of Q-GaP synthesised in 4-ethylpyridine is shown in figure 4.14. Sample (a) was synthesised by thermolysis of $Ga(P^tBu_2)_3$ in 4-ethylpyridine for 7 days. The absorption spectrum obtained was consistent with a solution of polydispersed nanocrystals, attributable to the long growth time.

Sample (b) was prepared by the same route but using a growth time of one hour. The band edge was determined to be 2.43 eV (510 nm) by the direct band gap method, an increase of 0.21 eV. The diameter of the nanocrystals for samples with such a shift in band edge was estimated to be 8.32 nm using the effective mass approximation (Equation 1.6). The optical absorption spectrum of sample (b) is consistent with a more monodispersed product, attributable to the shorter growth time. The excitonic peak visible at *ca.* 430 nm (2.89 eV) is consistent with a predicted direct optical transition in nanoparticulate GaP of diameter of >7.5 nm as predicted by Krishna and Friesner.[32]

Although GaP is not expected to undergo indirect - direct transition until *ca.* 2 nm or less, the band gap is expected to show increased direct character due to the small increase in the direct band gap. The onset of absorption at *ca.* 550 nm is therefore attributed to a indirect transition, whilst the first excitonic peak is considered to be a direct transition.

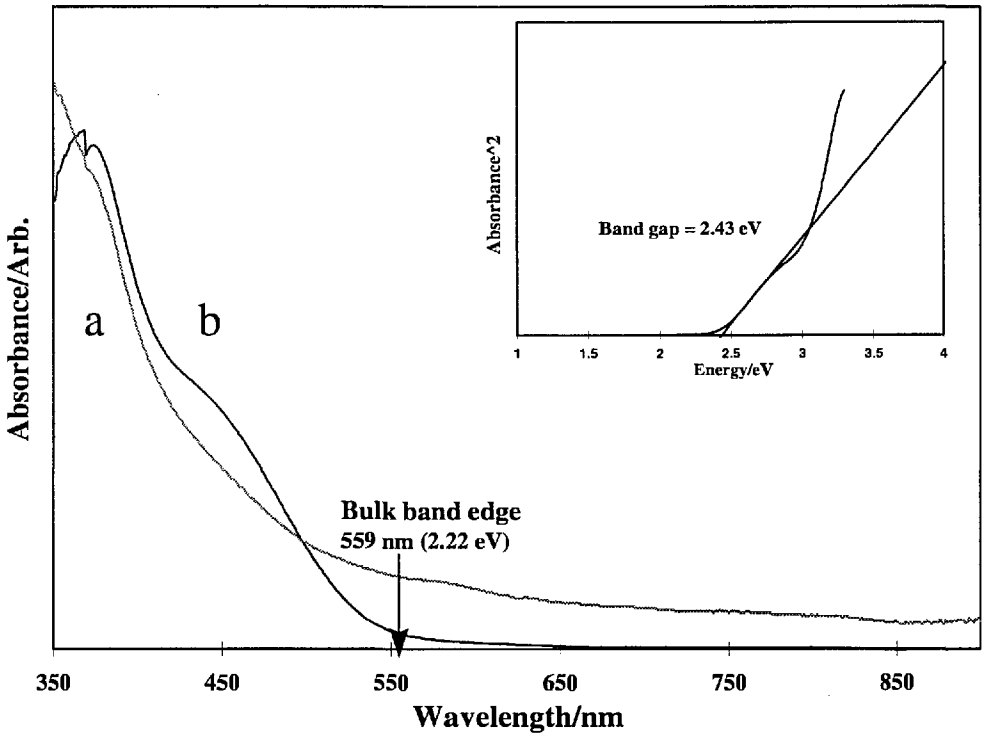


Figure 4.14: Optical absorption spectra of Q-GaP;

a) 167 °C, 7 days. b) 167°C, 1 hour; inset; determination of band edge for sample (b).

Indirect excitonic peaks for such a sample (> 80 Å) are predicted to appear at *ca.* 2.25 eV and are not observed in samples of GaP presented in this thesis.[32]

Luminescence (Figure 4.15) from sample (b) showed a broad emission (FWHM = 0.96 eV) with a $\lambda_{max.}$ at 459 nm (2.70 eV), slightly red shifted from the excitonic peak,

again attributable to the emitting state being a dark exciton or a spin forbidden state. The broadness of the emission profile is comparable to emission from InP quantum dots prepared by the same method and due to the large size distribution (standard deviation *ca.* 20 %). The emission is comparable to TOPO capped GaP.[67,68]

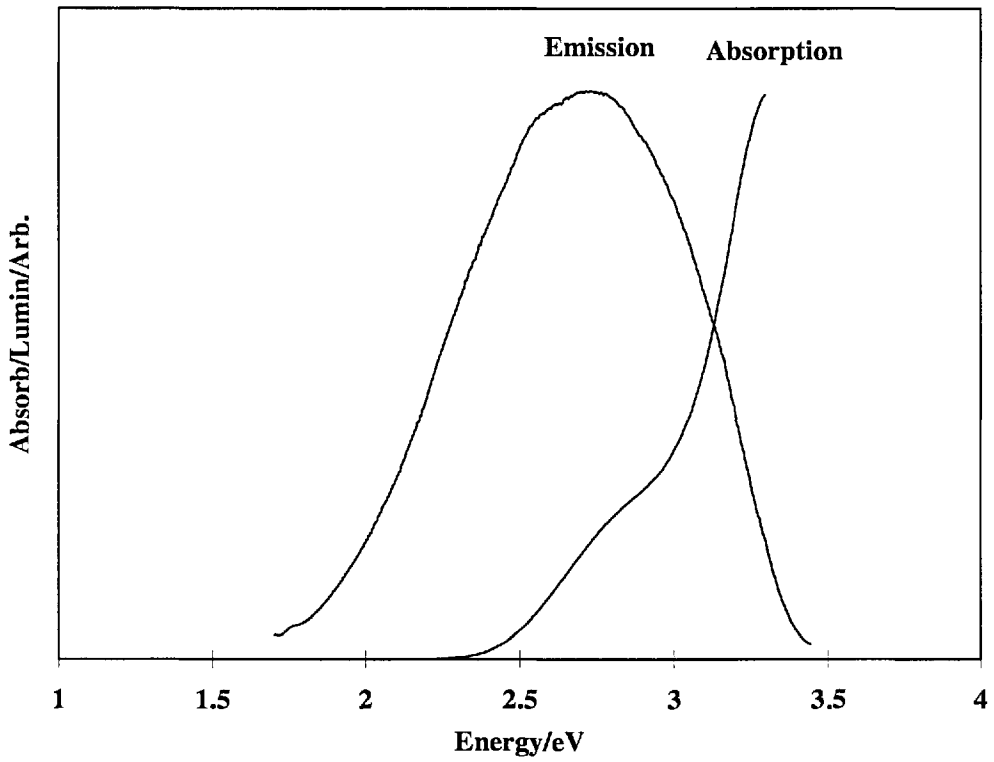


Figure 4.15: Emission spectrum of Q-GaP (167°C, 1 hour) in relation to the optical band edge.

4.10 Structural characterisation of Q-GaP

Macrocrystalline GaP exists in the cubic (zinc blende) phase.[201] XRD on samples synthesised for 1 hour at 167 °C shows typically broadened reflections consistent with small particles of III-V materials of poor crystalline quality (Figure 4.16). The 111 plane is clear, however, the 220 and 311 planes are indistinguishable, indicating a poorly crystalline sample. ICPAES analysis on various samples gave Ga:P ratios of 1.1:1 (aliquot taken after 1 hour) up to 7.4:1 (aliquot taken after 6 days). HRTEM experiments on samples with low Ga:P ratios show small amounts of crystalline particles, unlike InP and InAs, with a cubic lattice, the 111 plane easily identified with spacing of 3.14 Å (Figure 4.17 a).[216] The presence of large amounts of amorphous material was also observed.

HRTEM also shows small particles of Ga metal, *ca.* 1 nm in diameter (Figure 4.17 b). Lattice spacing suggests orthorhombic gallium metal.[217] This is consistent with the GC-MS data for the precursor which indicates the presence of metal which may be due to

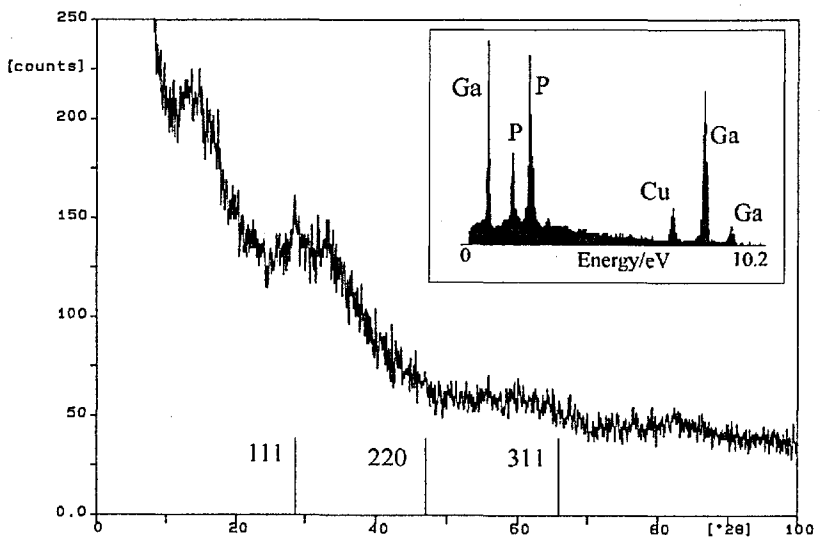


Figure 4.16: XRD pattern for Q-GaP (167 °C, 1 hour), showing the major Miller indices expected for GaP. Inset; EDAX analysis of GaP nanocrystals.

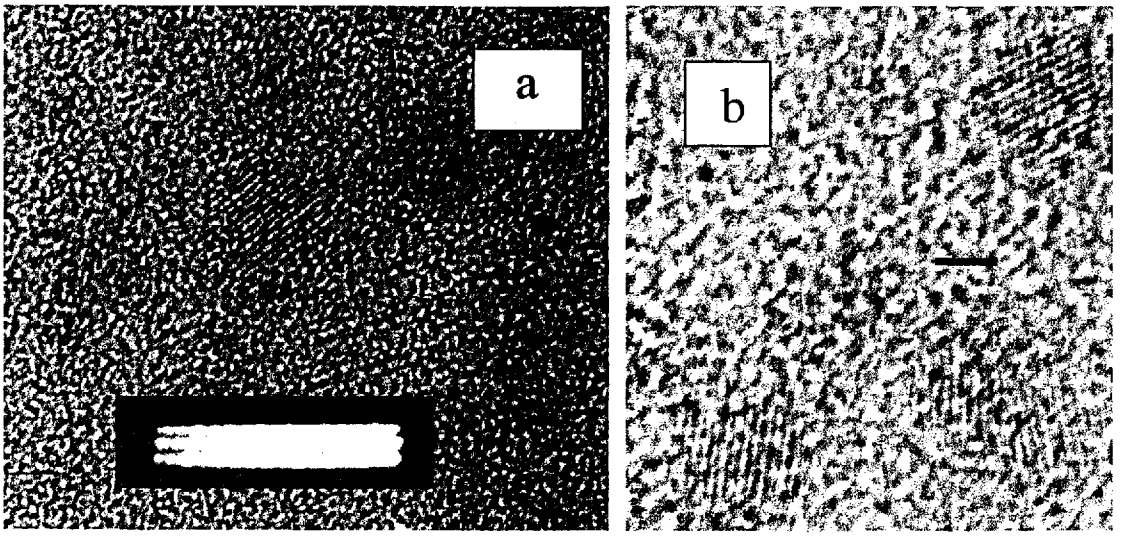


Figure 4.17: a) HRTEM Image of a GaP (167°C, 1 hour) nanoparticle, bar = 10 nm; b) HRTEM image of Ga particles, bar = 1nm.

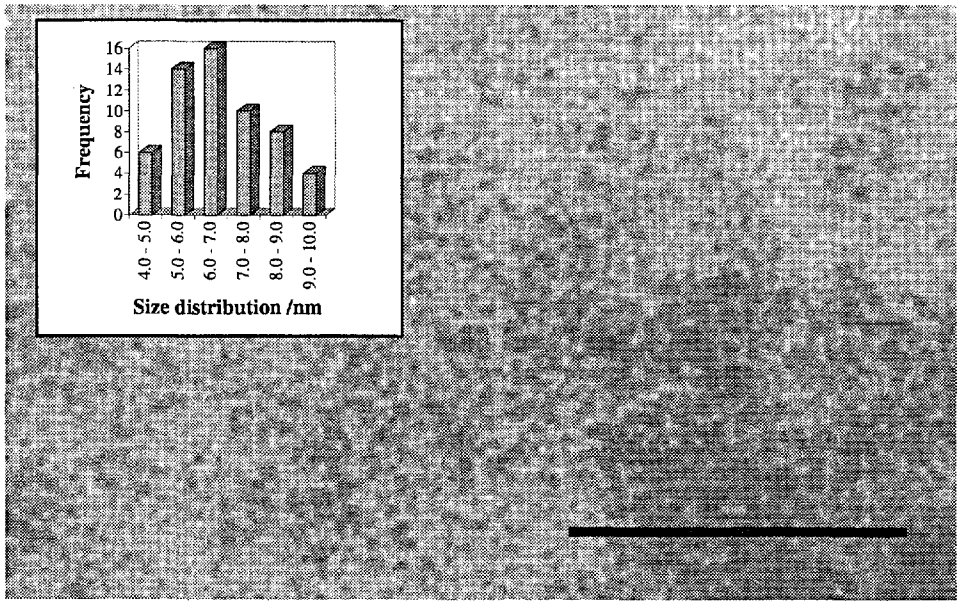


Figure 4.18: TEM image of Q-GaP (167°C, 1 hour), bar = 100 nm.

Inset: Histogram of particle size distribution.

reductive elimination. TEM images of Q-GaP (167 °C, 1 hour) (Figure 4.18) show nanocrystals with aspect ratios of up to 1.3. Samples appeared consistent with 4-ethylpyridine capped quantum dots, showing a propensity to aggregate on the grid, in what may be an example of cross linking.[212,213] Q-GaP produced by thermolysis of the diorganophosphide at 167 °C in 4-ethylpyridine for 1 hour had an average diameter of 6.69 nm ± 1.37 nm (20.4 %) (Predicted diameter of 8.32 nm). The discrepancy in predicted and observed diameter in III-V materials may in part be attributed to the large size distribution.

EDAX analysis of Q-GaP nanoparticles shows the presence of Ga, P and Cu (Figure 4.16, inset). The copper is due to the grid holding the sample. The gallium signal is markedly larger than the phosphorus which can be attributed to the excess metal

content of the samples analysed. IR spectroscopy of 4-ethylpyridine capped GaP quantum dots displayed characteristic bands for the organic ligand (Table 4.3) including a signal at 246 cm^{-1} attributable to ν(Ga-N).[181]

Free ligand/ cm^{-1}	GaP-4etpy/ cm^{-1}	assignment
1606	1606	ν(C-C)
1417	1413	ν(C-C)
1066	1064	ν(C-H)
777	773	ν(C-H)
-	246	ν(Ga-N)

Table 4.3: Selected IR data for 4-ethylpyridine capped GaP.

^{1}H NMR data shows resonances consistent with 4-ethylpyridine, indicating the presence of the ligand on the surface.

Solution ^{31}P NMR shows a single broad resonance at *ca.* 20 ppm, similar to the resonance observed with 4-ethylpyridine capped InP described earlier. ^{31}P MAS NMR shows a broad weak resonance at 31.78 ppm. ^{31}P CPMAS NMR increases the signal to noise ratio showing a clearer resonance at 31.86 ppm, with a shoulder at *ca.* 60 ppm. A small resonance is observed at -2.28 ppm and is assigned as a surface phosphorus environment. Bulk GaP is reported to have a resonance at *ca.* -146 ppm.[214] The down field shift for the quantum dots reported in this work is in contrast to quantum dots of GaP in the pores of zeolites reported previously.[102] The reason for this is unknown.

Again, application of a vacuum to a solution of 4-ethylpyridine capped Q-GaP resulted in formation of a glass.

4.11 Conclusions

Novel routes to quantum dots of InP and GaP have been developed using the thermolysis of the metal diorganophosphide in hot 4-ethylpyridine. Similar decomposition mechanisms were observed when compared to the precursor employed for cadmium phosphide, giving products of mixed purity which again could be controlled by experimental parameters. Quantum dots of InAs were synthesised using the metal salt and *tris*(dimethylamino)arsine in hot 4-ethylpyridine. Experiments carried out in hot TOPO were unsuccessful.

The nanocrystals obtained were poorly crystalline, giving XRD patterns consistent with particles of a small crystalline domain. Electron microscopy showed a mixture of amorphous and a small amount of crystalline dots. The dots were polydispersed (standard deviation of *ca.* 18 %). The structural and optical properties of the nanocrystals were investigated and found to be comparable to previously reported TOPO capped dots of III-V materials. InP and GaP nanocrystals were found to have diameters of *ca.* 7 nm, whilst InAs nanocrystals were approximately 2 nm in diameter.

Colloidal solutions of nanocrystals in 4-ethylpyridine could be manipulated into semi-ordered states under very mild conditions, *i.e.*, application of a vacuum resulted in the formation of a glass. Spin coating the solution onto a glass substrate resulted in thin films. These are important steps if nanocrystals are to be incorporated into devices.

Chapter 5 - Experimental

5.1 Chemicals

Indium chloride (99.99 %, Aldrich), gallium chloride (99.99 %, Aldrich), dimethyl zinc (99.99 %, Epichem), di-*t*-butylphosphine (98 %, Aldrich), dicyclohexylphosphine (98 %, Strem), dicyclopentylphosphine (97 %, Strem), diphenylphosphine (Aldrich), *tris*-dimethylamino arsenic (99 %, Strem), *n*-butyl lithium (1.6 M, Aldrich), dimethyl cadmium (99.99 %, Epichem), 4-ethylpyridine (98 %, Aldrich), dimethylsulfoxide (99.9 %, Aldrich), pyridine (99 %, Aldrich), petroleum spirits, 40-60 (BDH), *n*-hexane (BDH), toluene (BDH), tri-*n*-octylphosphine (90 %, Aldrich), tri-*n*-octylphosphine oxide (90 %, Aldrich), cadmium chloride (99.99 %, Aldrich), sodium diethyldithiocarbamate (99 %, Aldrich), cadmium hydroxide (99.99 %, Aldrich), thiolaceitic acid (96 %, Aldrich), TMEDA (99.5 %, Aldrich), triethylamine (99 %, Aldrich), methanol (BDH), diethylether (BDH), Tetrahydrofuran (BDH), selenium powder (99.5 %, Aldrich), *bis*(trimethylsilyl)sulfide (Lancaster).

5.2 Manipulation of air sensitive compounds

Air sensitive reagents were handled as described in the book by Shriver and Dresden.[218] A double manifold Schlenk line consisting of a 4 vacuum arms (0.05 Torr) and 4 nitrogen arms was used. A rotary oil pump maintained the vacuum and waste products were collected in a cold trap cooled with liquid nitrogen. Nitrogen was supplied by a cylinder connected directly to the nitrogen manifold. Solid chemicals were manipulated in a glove box under a dry nitrogen atmosphere and transferred to suitable

glass ware. Schlenk type glassware was used whilst connected to the manifolds by rubber pressure tubing. Liquid air sensitive chemicals were delivered by cannula or by injection from syringes to Schlenk flasks fitted with rubber septums.

5.3 Solvents

Solvents used for air sensitive chemistry were dried as described below. Solvents used with non air sensitive chemicals were used as received.

Toluene, *n*-hexane, THF and diethylether were refluxed over sodium for 1 hour under a nitrogen atmosphere and then distilled. Methanol was dried over magnesium sulphate. 4-ethylpyridine was frozen and degassed for 2 hours. TOPO was purified as described by Zingaro and White.[142] In a typical purification, 150 g of 90 % pure TOPO was dissolved in 200 ml of petroleum ether. 0.1 M $KMnO_4$ was then added until the solution turned slightly purple. 1M H_2SO_4 was then added until the colour cleared. This procedure was continued until the solution retained a slight brown colour. The organic layer was separated from the aqueous phase and washed 3 times with 100 ml deionised water, then separated again and left to stand for 4 days. The ethereal solution was then slurried with activated alumina and filtered. The resulting solution was left to evaporate in air, leaving the TOPO as a waxy solid. The purity was checked by melting point (54 °C) and ^{1}H NMR.

Dry solvents (except TOPO) were collected in Youngs flasks and stored under nitrogen with 4 Å molecular sieves (BDH).

Deuterated solvents, DMSO-d_6, pyridine-d_5, chloroform-d, and benzene-d_6 were stored under nitrogen in Schlenk tubes with molecular sieves or used as received (N_2 atmosphere, sealed glass ampoules, Goss scientific).

5.4 Synthesis of CdS precursors

5.4.1 Bis(N,N-diethyl)monothiocarbamato-cadmium(II) (cadmium monothiocarbamate)

Cadmium monothiocarbamate was synthesised by Mr. M Chunggaze of our laboratory by bubbling COS gas through 20 ml of diethylamine (< 10 °C) giving the bis(diethylmonothiocarbamato)diethyl ammonium salt. This was immediately reacted with a stoichiometric amount of cadmium acetate, giving cadmium diethylmonothiocarbamate. This was recrystallised from a chloroform-pentane mixture. The compound was analysed by NMR and single crystal X-ray analysis.[137]

5.4.2 Bis(N,N-diethyl)dithiocarbamato-cadmium(II) (cadmium diethyldithiocarbamate)

Cadmium diethyldithiocarbamate was synthesised by the reaction of stoichiometric amounts of cadmium chloride and sodium diethyldithiocarbamate in de-ionised water followed by recrystallisation from dichloromethane. This was analysed by NMR and elemental analysis.[219,220]

5.4.3 Cadmium thioacetate·TMEDA adduct

Cadmium thioacetate·TMEDA was synthesised by reacting cadmium hydroxide, thiolacetic acid and TMEDA in molar ratios of 1:2:1. The product was recrystallised from toluene. This was analysed by NMR and elemental analysis.

$Cd(SOCCH_3)_2$·TMEDA ^1H NMR, (C_6D_6, 25 °C, 400 MHz) δ 1.78 ppm (s, $(CH_3)_2N(CH_2)_2N(CH_3)_2$, 5H), 2.02 ppm (s, $(CH_3)_2N(CH_2)_2N(CH_3)_2$, 20H), 2.45 ppm (s, CH_3CSO, 50H); ^{13}C NMR (100 MHz), δ 34.28 ppm (s, $(CH_3)_2N(CH_2)_2N(CH_3)_2$), 46.78 ppm (s, $(CH_3)_2N(CH_2)_2N(CH_3)_2$), 56.54 ppm (s,$CH_3CSO$), 250.00 ppm (s,$CH_3CSO$). Elemental analysis (calculated): 31.81 % C (31.7), 5.70 % H (5.8), 7.24 % N (7.4).

5.4.4 dimethylcadmium·triethylamine adduct

The 1:1 adduct was formed by the addition of equimolar amounts of Me_2Cd and triethylamine in toluene. This was confirmed by NMR and IR.

Me_2Cd·TEA ^1H NMR, (C_6D_6, 25 °C, 400 MHz) δ -0.2 ppm (s, 6H, $[(CH_3)_2Cd]$), δ 1.2 ppm (t, 9H, $[N(CH_2CH_3)_3]$), δ 2.7 ppm (q, 6H, $[N(CH_2CH_3)_3]$); ^{13}C NMR (100 MHz); δ -3.75 ppm (s, $[(CH_3)_2Cd]$), δ 11.08 ppm (s, $N(CH_3CH_2)_3$), δ 45.84 ppm (s, $N(CH_3CH_2)_3$), IR (cm^{-1}) 511, 692, 916, 1003,1066, 1145, 1203, 1383.

The IR spectrum of Me_2Cd·TEA was comparable to the TEA adduct of dimethylzinc, showing simple adduct behaviour. Absorptions at 692 cm^{-1} and 511 cm^{-1}

have previously been attributed to the $\nu(CH_3)$ rock and ν(Cd-C) asymmetric stretch in dimethylcadmium.[221] Other features observed in the IR spectrum of neat triethylamine.

5.5 Synthesis of diorganophosphide single molecular precursors

Previous work on group II diorganophosphides highlights the extreme air sensitivity of these compounds.[169,171,172,189] ^{1}H, ^{31}P NMR and single crystal analysis are the only previously reported methods of analysis, the compounds being too unstable for IR or mass spectrometry. Mass spectrometry was un-reproducible only allowing for a tentative assignment of the molecular masses. All cadmium diorganophosphides reported have a molecular mass of *ca.* 900 amu suggesting trimeric structures.

No ^{13}C NMR have been previously reported and no methyl resonances have been observed in this work. The compounds presented in this thesis compare favourably to analogous work by other groups, notably Cowley and Wright. [169,171,172,189]

5.5.1 $[MeCdP^{t}Bu_2]_3$

Dimethyl cadmium (*ca.* 1 g) was transferred from a bubbler to a 100 ml flask by dynamic vacuum. 1 molar equivalent of $HP^{t}Bu_2$ was then added, followed by 20 ml of solvent (usually TOP if preparing TOPO capped nanoparticles, 4-ethylpyridine if preparing 4-ethylyridine capped nanoparticles). Reaction of the reagents in a 2:1 ratio had no effect, giving the same product. The reaction mixture was allowed to warm to room temperature and effervesce, producing a pale green solution. Isolation as crystals was achieved by cooling at 0 °C for 2 hours. Removal of the solvent resulted in efflorescence and the formation of an insoluble powder. Samples prepared for NMR analysis were

synthesised as previously described by Beachley *et al.*[170] by carrying out the reaction in a dry deuterated solvent (20 ml benzene-d_6). Single crystal X-ray analysis and NMR confirmed the structure previously reported by Cowley *et al.*[169] (Appendix 2). Yield = 98.60 %.

$[MeCdP^tBu_2]_3$ ^1H NMR, (C_6D_6, 25 °C, 400 MHz) δ 0.13 ppm (s, CH_3), 1.15 ppm (d, $^tBu_2$), 1.30 ppm (satellites $^{111}Cd/^{113}Cd$); ^{31}P NMR, δ 20.39 ppm (s, P^tBu_2); ^{13}C NMR, (100 MHz), δ 31.91 ppm ($C(CH_3)_3$), 34.21 ppm ($C(CH_3)_3$); IR bands (ν/cm^{-1}) (w = weak, s = strong, b = broad.) 1620 w, 1261 w, 1169 s, 1100 s, 1029 s, 923 s, 822 s, 814 s, 721 w , 669 s, c 286 vb,vs.

5.5.2 $[MeCdPR_2]_3$, R = Cp, Cy, Ph

Prepared in a similar manner to $(MeCdP^tBu_2)_3$ using dimethyl cadmium and HPR_2, (R = Cp, Cy and Ph) in a 1:1 ratio. The reactions produced air sensitive white powders which were slightly soluble in hydrocarbons. A variety of solvents were used, including THF, hexane, toluene and TOP in unsuccessful attempts to produce crystals. NMR confirmed structures (*cf.* Wright *et al.*).[171,172]

The metallation reaction between diphenylphosphine and dimethylcadmium appeared to produce a different complex, in which two $HP(Ph)_2$ ligands act as donors in the complex. The NMR data suggest a structure similar to {$[EtZn(\mu\text{-}PPh_2)]_3(HPPh_2)_2$.thf}, previously reported by Wright *et al.*[172] The compound was assigned as $[MeCd(\mu\text{-}PPh_2)]_3(HPPh_2)_2$.

[MeCdPCp$_2$]$_3$ ^{1}H NMR, (C_6D_6, 25 °C, 400 MHz) δ 0.29 ppm (s, CH_3, 9H), 1.3 - 2.1 ppm (m, Cp, 54H); ^{31}P NMR, δ 44.23 ppm (s, PCp_2); ^{13}C NMR, (100 MHz), δ 36.37 ppm (d, C1), 32.57 ppm (d, C2), 26.67(d, C3); IR bands (ν/cm^{-1}) (w = weak, s = strong, b = broad.) 999 (w), 1045(s), 1122 (s) 1232 (w), 1300 (s).

[MeCdPCy$_2$]$_3$ ^{1}H NMR, (C_6D_6, 25 °C, 400 MHz) δ 0.25 ppm (s, CH_3, 9H), 1.0 - 2.0 ppm (m, Ch, 66H); ^{31}P NMR, δ 45.88 ppm (s, PCh_2); ^{13}C NMR, (100 MHz), δ 35.09 ppm (d, *ipso* C), 33.42 ppm (d, *ortho* C), 32.55 (d, *meta* C), 30.05 (d, *para* C); IR bands (ν/cm^{-1}) (w = weak, s = strong, b = broad.) 763 (w), 1276, 1653 (s) 2293 (s, b), 2669 (s).

[MeCd(μ-PPh$_2$)]$_3$(HPPh$_2$)$_2$ ^{1}H NMR, (C_6D_6, 25 °C, 400 MHz) δ 0.54 ppm (s, C*H*$_3$, 9H), 5.19 ppm (d, *H*-PPh_2, 2H) $^1J_{P\text{-}H}$ = 215.51 Hz, 7.0 - 7.6 ppm (m, P-*Ph*, 50H); ^{31}P NMR, δ -39.93 ppm (s, H-*P*Ph_2); δ 17.78 ppm, (s, μ-*P*Ph_2); ^{13}C NMR (100 MHz), δ 134.28 ppm (d, *ortho* C), 128.78 ppm (d, *meta* C), 128.54 ppm (s, *para* C). IR bands (ν/cm^{-1}) (w = weak, b = broad, s= strong) 2935 (s), 2332 (P-H) (w), 1911, 1726, 1261, 721.

5.5.3 $In(P^tBu_2)_3$ and $Ga(P^tBu_2)_3$

The compounds were synthesised as described by Cowley *et al.*[202] and their identity confirmed by ^1H, ^{13}C and ^{31}P NMR. In a typical synthesis, HP^tBu_2 was lithiated by the addition of an equimolar amount of *n*-BuLi in dry hexane. The reaction was stirred for 18 hours under nitrogen. Removal of hydrocarbons *in vacuo* left LiP^tBu_2 as a white solid in nearly 100 % yield.[222] Three molar equivalents of LiP^tBu_2 in ether were then added to either $GaCl_3$ or $InCl_3$ dispersed or dissolved in dry hexane. The reaction proceeded at room temperature under nitrogen for 24 hours, producing highly air sensitive coloured solutions. The compounds were isolated by cannula filtration to remove LiCl, followed by removal of solvent *in vacuo* and storage under nitrogen. Attempts to recrystallise the compounds produced either amorphous solids or crystals too small for single crystal analysis as has previously been reported.[202]

5.6 Synthesis of nanoparticulates in TOPO

5.6.1 Cd_3P_2/TOPO

Nanodispersed Cd_3P_2 passivated with TOPO was synthesised by the rapid injection of a TOP solution of $(MeCdP^tBu_2)_3$ into TOPO at elevated temperatures using Schlenk techniques. In a typical experiment, 20.00 g purified TOPO was heated to 100 °C under a nitrogen atmosphere in a three neck flask, with the central neck attached to a condenser which was in turn connected to the vacuum line manifold. One side neck had a thermometer, the other was sealed with a stopper which was replaced with a rubber septum prior to injection. Whilst at 100 °C the TOPO was thoroughly degassed for 1

hour, then flushed with nitrogen three times. The temperature was then altered to the desired temperature of synthesis (between 100 °C and 250 °C) and left to stabilise. 8 ml of a 0.3 M solution of $(MeCdP^tBu_2)_3$ in TOP was then injected through the rubber septum into the hot TOPO. A drop in temperature of up to 20 °C was normally observed, associated with the nucleation of small particles. The temperature was stabilised back to the injection temperature and the nanoparticles allowed to grow for 30 mins., then removed from the heat source. The reaction flask was allowed to cool to 60 °C where upon 40 ml of dry methanol was added, causing the nanoparticulates to flocculate. The precipitate was isolated by centrifugation (5000 rpm, 10 mins.) and redispersed in toluene. Further centrifugation removed solid waste products such as cadmium, leaving an optically clear colloidal solution. A similar process was used with other molecular precursors such as $(MeCdPR_2)_3$ (R = Cy, Cp) giving a much smaller yield of nanoparticulates and higher yield of waste product.

5.6.2 Zn_3P_2/TOPO

TOPO passivated Zn_3P_2 was prepared using a method similar to that originally described by Murray *et al.*[35] The TOPO was prepared as described in 5.6.1. and the temperature stabilised between 150 °C and 250 °C. However a single source precursor is replaced by a mixture of two precursors. Typically *ca.* 1 g of dimethyl zinc was transferred to a Schlenk flask and frozen. 10 ml TOP was then added followed by 0.6 molar equivalents of HP^tBu_2 (Zn:P ratio of 3:2) and allowed to warm to room temperature. The mixture was then loaded into a syringe and rapidly injected into the hot TOPO. Extreme care was taken not to expose the reaction to air as dimethyl zinc is

pyrophoric. The nanoparticles were allowed to grow for the desired length of time, then isolated as previously described in 5.6.1.

5.6.3 CdS and CdSe/TOPO and DMSO

TOPO capped CdS was synthesised by the injection of a TOP solution of either cadmium monothiocarbamate or cadmium thioacaetate·TMEDA adduct (ca. 0.2 g in 5 ml TOP) into hot TOPO at 250 °C. TOPO preparation and experimental procedure are described in 5.6.1.

The synthesis of CdS or CdSe by the adduct method closely follows the original Murray method.[35] *Ca.* 1 g dimethyl cadmium was transferred to a round bottom flask and combined with an equimolar amount of triethylamine to form the 1:1 adduct. 10 ml TOP and an equimolar amount of either *bis*(trimethylsilyl)sulfide or 0.1 M TOPSe solution (Prepared by dissolving Se powder directly into the correct amount of TOP) was then mixed with the adduct. The reaction mixture was loaded into a syringe and injected into hot TOPO at the desired temperature (100 °C to 250 °C). Isolation of the dots is described in 5.6.1.

DMSO capped CdS was prepared by dissolving 0.5 g cadmium diethyldithiocarbamate into 50 ml DMSO and slowly raising the temperature to reflux (190 °C) for 2 hours. The nanocrystals were isolated by removing the flask from the heat and cooling to room temperature. Addition of 50 ml of dry methanol followed by centrifugation resulted in a solid which was re-dispersed in DMSO. Further centrifugation removed waste solids giving an optically clear solution.

5.7 Synthesis of nanoparticulates in 4-ethylpyridine

5.7.1 Cd_3P_2/4-etpy

Nanodispersed Cd_3P_2 passivated with 4-ethylpyridine was synthesised by the thermolysis of $[MeCdP^tBu_2]_3$ in hot dry 4-ethylpyridine (167 °C) under a nitrogen atmosphere. The experimental set up was the same as for TOPO capped particles.

In a typical experiment 1.3 g (9.1 mmol) Me_2Cd was added to HP^tBu_2 (1.33 g, 9.1 mmol) in 20 ml of dry 4-ethylpyridine. The mixture effervesced and formed a pale green solution of $[MeCdP^tBu_2]_3$. This was then slowly heated to 120 °C for 2 hours, then raised to 167 °C and left for 24 hours. After this, the sample was removed from the heat and allowed to cool to room temperature. Addition of 40 mls petroleum spirits (40-60) caused flocculation of the nanoparticles. Isolation of the nanoparticles by centrifugation yielded a dark powder which could be re-dispersed in either pyridine or 4-ethylpyridine. Further centrifugation resulted in the removal of solid waste, leaving an optically clear red/brown solution.

5.7.2 Zn_3P_2/4-etpy

The procedure closely follows the one described in 5.7.1 above, except dimethyl zinc and HP^tBu_2 (Molar ratios of 3:2) were mixed together prior to reaction. No reaction between the two precursors was observed. Isolation of the nanocrystalline Zn_3P_2 was as described above, giving a brown solution.

5.7.3 InP and GaP/4-etpy

The procedure closely follows the one described in 5.7.1 except the single molecular precursors $M(P^tBu_2)_3$ (M = Ga, In) were dissolved in 4-ethylpyridine prior to heating. Isolation of the nanoparticles into a 4-ethylpyridine solution follows 5.7.1.

5.7.4 InAs/4-etpy

Q-InAs was prepared by a slightly different method than described above. In a typical experiment 0.5 g (2.23 mmol) of dry anhydrous $InCl_3$ was dissolved in 20 ml dry 4-ethylpyridine whilst under nitrogen. Once fully dissolved, 0.48 g (2.23 mmol) $As(NMe_2)_3$ was added and allowed to stir in. The temperature was then slowly raised to 167 °C over 2 hours. To obtain slightly larger dots, 0.28 g (1.26 mmol) dry $InCl_3$ was mixed with 0.26g g (1.26 mmol) $As(NMe_2)_3$ and 10 ml dry 4-ethylpyridine in a separate flask then injected into the original reaction flask at 167 °C. The nanocrystals were isolated as described in 5.7.1.

$InCl_3$ was found to form a complex with 4-ethylpyridine, resulting in $InCl_3{\cdot}(4\text{-etpy})_3$. This could be isolated as crystals by dissolving a small amount (*ca.* 0.5 g) of dry $InCl_3$ in ca. 20 ml of dry 4-ethylpyridine. This was stirred for 2 hours and the volume reduced *in vacuo* to 5 ml. Gradual evaporation of excess 4-ethylpyridine in air resulted in large clear crystals of $InCl_3{\cdot}(4\text{-etpy})_3$. These were analysed by single crystal analysis (Appendix 3), ^1H NMR and elemental analysis.

$InCl_3$·(4-etpy)$_3$ ^{1}H NMR, (C_5D_5N, 25 °C, 400 MHz) δ 1.06 ppm (t, CH_3, 3H), 2.44 ppm (q, CH_2, 2H), 7.21 ppm (s, aromatic CH, 2H), 8.73 ppm (s, aromatic CH, 2H); Elemental analysis (calculated): 46.55 % C (46.46), 5.02 % H (4.97), 7.94 % N (7.74).

5.8 Size fractionation

Size fractionation procedures were employed once the nanocrystals were isolated from the reaction. Drop wise addition of a non solvent (methanol to a toluene solution of TOPO capped particles, or light petroleum to a 4-ethylpyridine solution of 4-ethylpyridine capped particles) until the solution turned cloudy resulted in the flocculation of the larger particles. These could be isolated as solids by centrifugation, followed by redispersion of the solid in the relevant solvent. This procedure could be applied to the same solution up to *ca.* 20 times, each time resulting in smaller and smaller fractions. Optical spectroscopy of the fractions showed the gradual increased blue shift with decreasing particle size and TEM confirmed the results.

5.9 Manipulation of 4-ethylpyridine capped nanoparticulates into glasses and thin films

4-ethylpyridine passivated samples of III-V quantum dots were organised into glasses by simple application of a vacuum. In a typical experiment, 5 ml of concentrated nanoparticulate solution (4-ethylpyridine) was placed in a Schlenk flask and exposed to a vacuum (0.05 Torr). This was left with out stirring for up to 1 week. After 1 week exposure to the vacuum, the samples were washed with light petroleum which resulted in a crystalline looking material.

Thin films of InAs were prepared by Mr. S. Norager of our laboratory, by spin coating a 4-ethylpyridine solution of InAs onto a clean glass substrate using a SCS spin coater model P6708.(Solution dropped on substrate at 100 rpm and spread evenly with a teflon stick. Speed was then ramped up to 2000 rpm for 15 seconds and dried at 6000 rpm for 10 seconds.)

5.10 Instrumentation and physical measurements

5.10.1 UV (electronic) spectroscopy

Solutions containing nanocrystals were placed in a silica cuvette (1 cm path length) in a Philips PU 8710 spectrophotometer. The band gap was determined by fitting the optical data to equation 1.8. Extrapolation of the band edge gave the confined band gap. R^2 fit not less than 0.98.

5.10.2 Photoluminescence spectroscopy

Luminescence spectra were recorded on a Spex Fluromax machine equipped with a Xe lamp (150 W) as a source and a 1527P photomultiplyer tube as a detector. Slits were set at 2 nm and the integration time set at 1 second.

Luminescence spectra were recorded by using a nanoparticulate solution in a luminescence cuvette (4 transparent faces) with a path length of 1 cm. The excitation wavelength used was set at a lower wavelength than the onset of absorption. Several excitation wavelengths were tested to find the optimum. Generally excitation wavelengths were:

CdS = 350 nm	InP = 300 nm	GaP = 300 nm
CdSe = 450 nm	Cd_3P_2 = 350 nm	Zn_3P_2 = 350 nm
InAs = 400 nm		

5.10.3 Infra red spectroscopy

FT-IR were obtained using a Unicam Mattson Polaris spectrometer. Samples were prepared as pressed discs (1% in CsI) or as a nujol mull. Air sensitive compounds were prepared as a nujol mull in a glove box.

5.10.4 Mass spectrometry

Mass spectra were recorded using a V.G. auto spec with a Cs^+ ion beam (FAB) in a 3-nitrobenzyl matrix. Electron impact mass spectra used a beam energy of 70 eV and a source temperature of 200 °C.

5.10.5 NMR spectroscopy

The ^1H, $^{13}C\{^1H\}$ and ^{31}P solution NMR spectra were recordered on a Bruker AM 500 or a DRX 400 in either deuterated pyridine, benzene or chloroform. Solid state ^{31}P MAS NMR and CP-MAS NMR (H_3PO_4 standard) were recorded on a Bruker MSL300 by Mr. D. Butler (Dept. of Chem., UCL (ULIRS)).

5.10.6 X-ray powder diffraction

X-ray powder diffraction patterns were obtained using a Guinier camera and a Philips 1130 X-ray generator (Cu-K_α radiation). Samples were prepared by drying a solution onto a glass substrate or by placing the powder on adhesive tape.

5.10.7 Electron microscopy (HRTEM, TEM)

Samples prepared for TEM were prepared by drop wise addition of a weak solution of nanocrystals onto an amorphous carbon substrate supported on a copper grid (400 mesh, Agar scientific). Excess solvent was removed by a tissue and the grid left to dry.

TEM experiments were carried out using a JEOL-JEM 1200 EX II scanning and transmission electron microscope operating at 100 kV. HRTEM experiments were carried out using a JEOL-JEM-4000EX electron microscope at 400 kV (University of Oxford) or a JEOL JEM 2010 electron microscope operating at 200 kV.

5.10.8 Atomic force microscopy (AFM)

AFM images were obtained using a Topometrix explorer machine in non-contact mode by Dr. Philip Moriarty (Dept. Of Physics, University of Nottingham). Samples were prepared as thin films (described in 5.9) on glass substrates approx. 1cm by 1 cm.

5.10.9 Elemental analysis

Elemental analysis (H, C, N) were carried out by Miss H. O'Callaghan in the microanalytical labs at Imperial College. EDAX analysis were carried out by Mr. K. Pell (Basic Medical Science, QMW college) on samples deposited on either a silicon or copper wafer using a JEOL JSM35CF microscope at 25 kV

5.10.10 Inductively coupled plasma atomic emission spectrophotometry (ICPAES)

Inductively Coupled Plasma Atomic Emission Spectrophotometry (ICPAES) was carried out on an ARL machine. The samples were acid digested (Nitric/Perchloric) and taken to dryness prior to leaching to give a final matrix of 1M HCl. Multi-element analysis by ICPAES was obtained using conventional nebulisation under standard instrumental conditions. The error is typically 0.5 - 1 %.

5.10.11 Thermogravimetric analysis (TGA) and gas chromatography mass-spectrometry (GC-MS)

Thermal gravimetric analyses were carried out using a TGA-50 detector in a nitrogen atmosphere, using an aluminium closed pan with a hole and 10 °C/min heating rate.

GC-MS was carried out using a JEOL AX505X with a HP 5890 gas chromatograph. A bonded phase methyl siloxane BP1 column (SGE) with a thickness of 0.25 μm, internal diameter of 0.22 mm and a length of 25 m. The carrier gas was He at 12 psi at a flow rate of 1 cm^3 min^{-1}. Solutions of ca. 0.25 mg precursor in 0.4 ml dry chloroform were prepared and 1 μl of solution was injected into the machine at various

temperatures (100 °C, 175 °C, 250 °C). The temperature program was 30 °C for 2 minutes, ramped by 8 °C or 12 °C min^{-1} to a maximum of 280 °C. A beam with a 100 μA current and 3 kV voltage was used, with a 2 kV detector.

5.10.12 X-ray single crystal analysis

Single crystal analysis of $[MeCdP^tBu_2]_3$ confirmed the structure previously reported by Cowley *et al.*[169] (Appendix 2). The crystals were found to be solvent dependent and were quickly removed from the Schlenk flask and placed in a stream of liquid nitrogen.

Single crystals of $InCl_3$·(4-ethylpyridine)$_3$ were mounted in Lindemann tubes in air at room temperature.

The crystal data were collected using a Siemens P4/PC diffractometer with Mo-K_α radiation at a temperature of 203 K. The structure was refined using SHELXTL version 5.03.[223]

Appendix 1

Selected information and notes on studied compounds, and sources.

Compound	Structure[a]	Bulk band gap/ eV and Optical transition	$^{*}m_e$	$^{*}m_h$	ε	Bulk exciton diameter/Å[d]
CdS	Wurtzite[b] Zinc blende	2.42, direct	0.19	0.8	5.7	39.3
CdSe	Wurtzite[b] Zinc blende	1.74, direct	0.13	0.45	6.1	64.0
Cd_3P_2	Anti-Mn_2O_3[c]	0.50, direct	0.05	0.5	15.5	360.9
Zn_3P_2	Anti-Mn_2O_3[c]	1.40, direct	-	-	11.0	-
InP	Zinc blende	1.27, direct	0.07	0.65	12.7	212.7
GaP	Zinc blende	2.22, indirect (2.28, direct)	0.10	0.86	9.1	107.5
InAs	Zinc blende	0.36, direct	0.22	0.41	14.6	107.3

Table A1: Electrical properties of studied semiconductors.

Notes

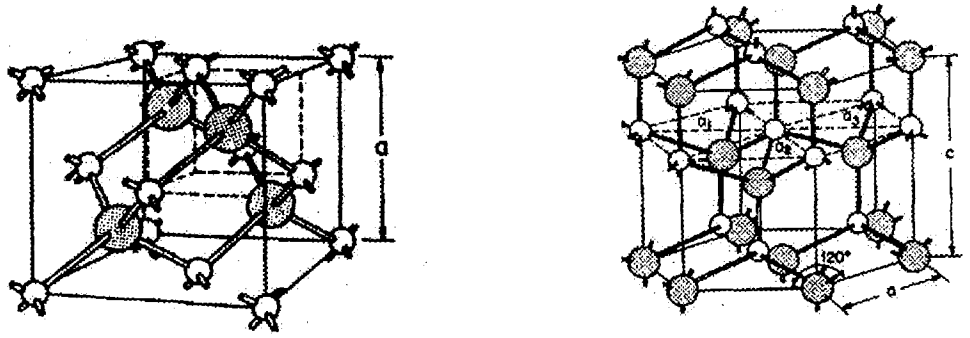
Effective masses for holes/ electrons are given in units of the free electron mass (9.109×10^{-31} Kg). Effective masses and dielectric constants were taken from;

- Landolt-Bornstein, *Numerical Data and Functional Relationships in Science and Technology*, Vol. 17f, *Springer Berlin*, 1983.[201]

- Data in Science and Technology, *Semiconductors other than group IV and III-V, Springer-Verlag.*[160]

a) A. F. Wells, *Structural Inorganic Chemistry*, 3rd Ed, OUP, London, 1962.[178]

b) Wurtzite (ii - hexagonal) is favoured over zinc blende (i - cubic).[64]



i ii

Figure A1: Two possible crystal phases of II-VI materials.[64]

c) Anti-Mn_2O_3 also referred to as an anti -flourite lattice, in which ¼ of the metal sites are vacant.[160]

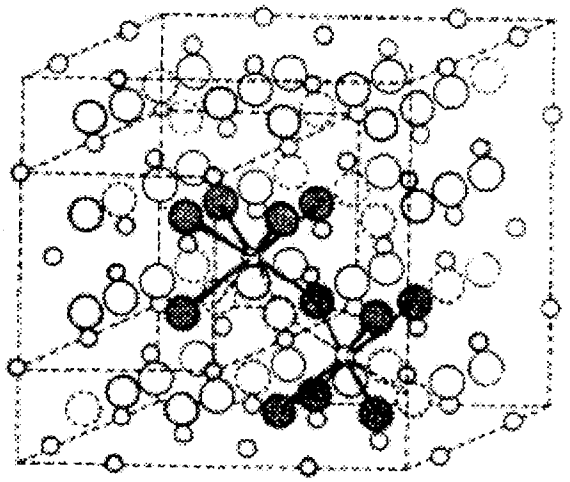


Figure A2: Crystal lattice of Cd_3P_2.[160]

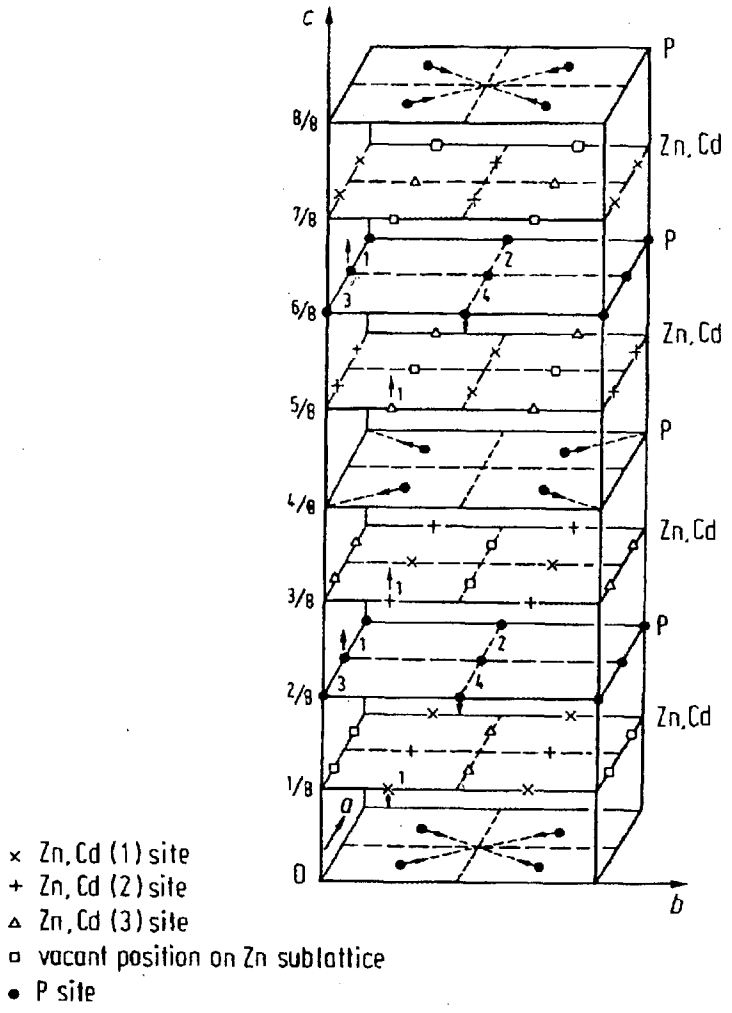


Figure A3: Unit cell of M_3P_2 (M = Zn, Cd) stretched along the c axis. Atoms at ideal positions.[160]

d) All values are calculated from equation 1.4.

Appendix 2

Single crystal X-ray analysis of [MeCdP^{t}Bu$_2$]$_3$ confirms the structure originally reported by Cowley *et al.*[169] The preparation and NMR analysis are described in chapter 3. The X-ray analysis is described in chapter 5.

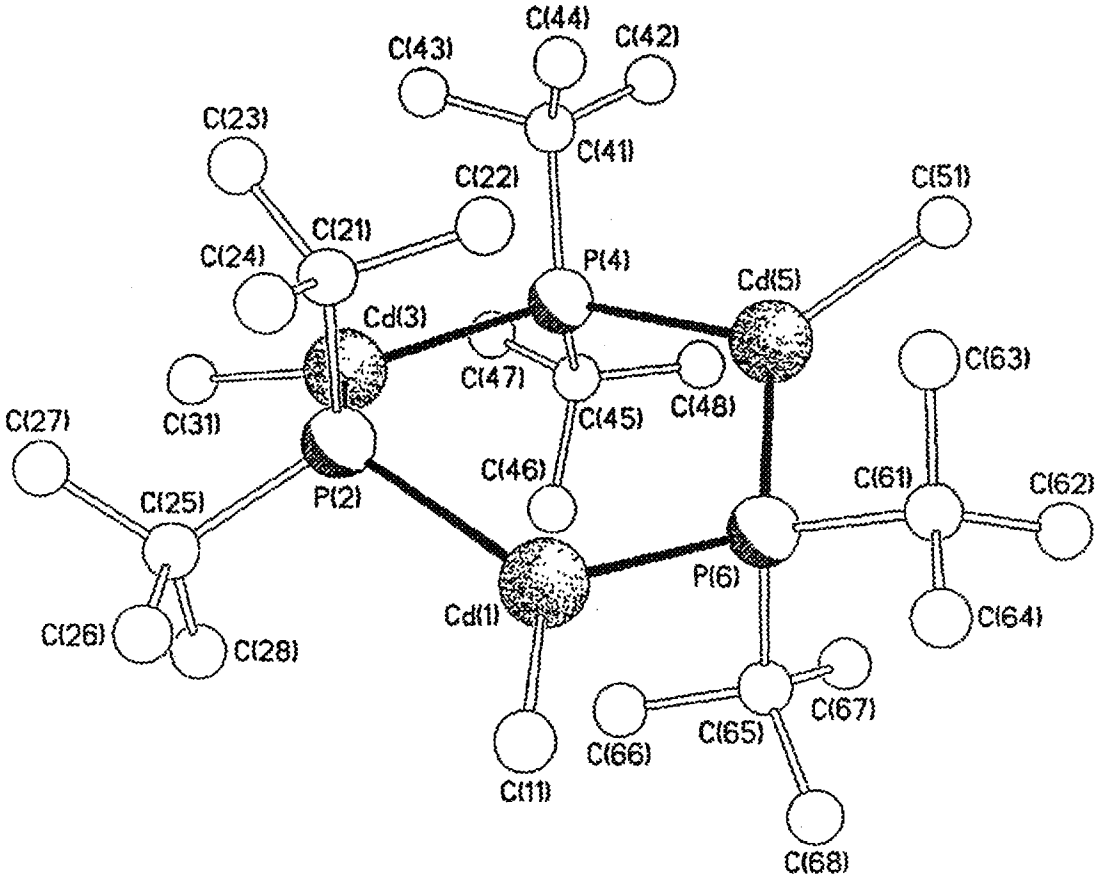


Figure A4: Crystal structure of [MeCdP^{t}Bu$_2$]$_3$.

A2.1 Crystal data and structure refinement for [MeCdP^{t}Bu$_2$]$_3$

Empirical formula	$C_{27}H_{63}P_3Cd_3$	
Formula weight	817.18	
Temperature	203(2) K	
Diffractometer used	Siemens p4/PC	
Wavelength	0.71073 Å	
Crystal system	Monoclinic	
Space group	$P2_1/n$	
Unit cell dimensions	a = 9.104(2) Å	alpha = 90 °
	b = 37.296(3) Å	beta = 104.25(2)°
	c = 11.194(3) Å	gamma = 90°
Volume, Z	3683.5(12) Å^3, 4	
Density (calculated)	1.475 mg/m^3	
Absorption coefficient	1.859 mm^{-1}	
F (000)	1656	
Crystal morphology/ size	Clear rhombs, 0.60 x 0.47 x 0.40 mm	
θ range for data collection	1.95 to 25.00 °	
Limiting indices	$-10 \leq h \leq 9$, $-40 \leq k \leq 44$, $-12 \leq l \leq 13$.	
Reflections collected	6896	
Independent reflections	6470 (R_{int} = 0.0468	
Observed reflections	4485 [$F > 4\sigma(F)$]	

Absorption correction	semi-empirical
Max. and Min. transmission	0.4525 and 0.3600
Refinement method	Full matrix least squares on F^2
Data/ restraints/ parameters	5894/ 0/ 298
Goodness of fit on F^2	1.079
Final R indices [$I>2\sigma(I)$]	R1 = 0.0498, wR2 = 0.01028
R indices (all data)	R1 = 0.0946, wR2 = 0.15531
Largest differences between peak and hole	0.879 and -1.151 eÅ^{-3}

A2.2 Bond lengths for [MeCdP^{t}Bu$_2$]$_3$ /Å

Cd(1)-C(11)	2.171(9)	Cd(5)-P(6)	2.602(2)	C(45)-C(47)	1.529(12)
Cd(1)-P(6)	2.582(2)	P(6)-C(65)	1.883(9)	C(45)-C(48)	1.534(14)
Cd(1)-P(2)	2.592(2)	P(6)-C(61)	1.905(8)	C(45)-C(46)	1.538(14)
P(2)-C(25)	1.891(8)	C(21)-C(23)	1.512(11)	C(61)-C(63)	1.511(13)
P(2)-C(21)	1.896(9)	C(21)-C(24)	1.528(11)	C(61)-C(62)	1.527(13)
P(2)-Cd(3)	2.584(2)	C(21)-C(22)	1.532(12)	C(61)-C(64)	1.526(13)
Cd(3)-C(31)	2.155(9)	C(25)-C(28)	1.529(13)	C(65)-C(68)	1.523(13)
Cd(3)-P(4)	2.567(2)	C(25)-C(27)	1.533(12)	C(65)-C(66)	1.540(13)
P(4)-C(45)	1.893(9)	C(25)-C(26)	1.539(12)	C(65)-C(67)	1.550(13)
P(4)-C(41)	1.898(9)	C(41)-C(44)	1.513(13)		
P(4)-Cd(5)	2.587(2)	C(41)-C(42)	1.535(12)		
Cd(5)-C(51)	2.204(10)	C(41)-C(43)	1.556(13)		

A2.3 Bond angles for [MeCdP^{t}Bu$_2$]$_3$ /°

C(11)-Cd(1)-P(6)	126.2(3)	C(22)-C(21)-P(2)	104.6(5)
C(11)-Cd(1)-P(2)	124.1(3)	C(28)-C(25)-C(27)	109.5(8)
P(6)-Cd(1)-P(2)	109.70(7)	C(28)-C(25)-C(26)	107.9(8)
C(25)-P(2)-C(21)	112.5(4)	C(27)-C(25)-C(26)	109.2(8)
C(25)-P(2)-Cd(3)	102.5(3)	C(28)-C(25)-P(2)	104.0(6)
C(21)-P(2)-Cd(3)	108.2(3)	C(27)-C(25)-P(2)	113.2(6)
C(25)-P(2)-Cd(1)	108.4(3)	C(26)-C(25)-P(2)	112.9(6)
C(21)-P(2)-Cd(1)	101.8(3)	C(44)-C(41)-C(42)	109.5(8)
Cd(3)-P(2)-Cd(1)	123.69(8)	C(44)-C(41)-C(43)	106.2(9)
C(31)-Cd(3)-P(4)	118.8(3)	C(42)-C(41)-C(43)	110.1(8)
C(31)-Cd(3)-P(2)	126.7(3)	C(44)-C(41)-P(4)	106.4(6)
P(4)-Cd(3)-P(2)	114.40(7)	C(42)-C(41)-P(4)	113.1(7)
C(45)-P(4)-C(41)	111.3(4)	C(43)-C(41)-P(4)	111.3(6)
C(45)-P(4)-Cd(3)	107.7(3)	C(47)-C(45)-C(48)	109.2(8)
C(41)-P(4)-Cd(3)	105.7(3)	C(47)-C(45)-C(46)	108.5(8)
C(45)-P(4)-Cd(5)	107.4(3)	C(48)-C(45)-C(46)	108.3(9)
C(41)-P(4)-Cd(5)	105.8(3)	C(47)-C(45)-P(4)	114.0(7)
Cd(3)-P(4)-Cd(5)	118.94(8)	C(48)-C(45)-P(4)	111.4(7)
C(51)-Cd(5)-P(4)	120.7(3)	C(46)-C(45)-P(4)	105.2(6)
C(51)-Cd(5)-P(6)	124.3(3)	C(63)-C(61)-C(62)	109.7(9)

P(4)-Cd(5)-P(6)	114.90(7)	C(63)-C(61)-C(64)	108.5(8)
C(65)-P(6)-C(61)	111.8(4)	C(62)-C(61)-C(64)	110.1(8)
C(65)-P(6)-Cd(1)	99.6(3)	C(63)-C(61)-P(6)	104.1(6)
C(61)-P(6)-Cd(1)	110.0(3)	C(62)-C(61)-P(6)	112.4(6)
C(65)-P(6)-Cd(5)	106.7(3)	C(64)-C(61)-P(6)	111.9(6)
C(61)-P(6)-Cd(5)	105.5(3)	C(68)-C(65)-C(66)	107.4(9)
Cd(1)-P(6)-Cd(5)	123.02(8)	C(68)-C(65)-C(67)	110.1(8)
C(23)-C(21)-C(24)	109.0(7)	C(66)-C(65)-C(67)	108.5(8)
C(23)-C(21)-C(22)	109.5(7)	C(68)-C(65)-P(6)	114.3(7)
C(24)-C(21)-C(22)	108.0(7)	C(66)-C(65)-P(6)	105.2(6)
C(23)-C(21)-P(2)	113.1(6)	C(67)-C(65)-P(6)	111.1(7)
C(24)-C(21)-P(2)	112.4(6)		

Appendix 3

The crystal structure, structure refinement data, bond lengths and bond angles for *mer*[In(4-ethylpyridine)$_3$Cl$_3$]. Preparation and analysis are described in chapter 5.

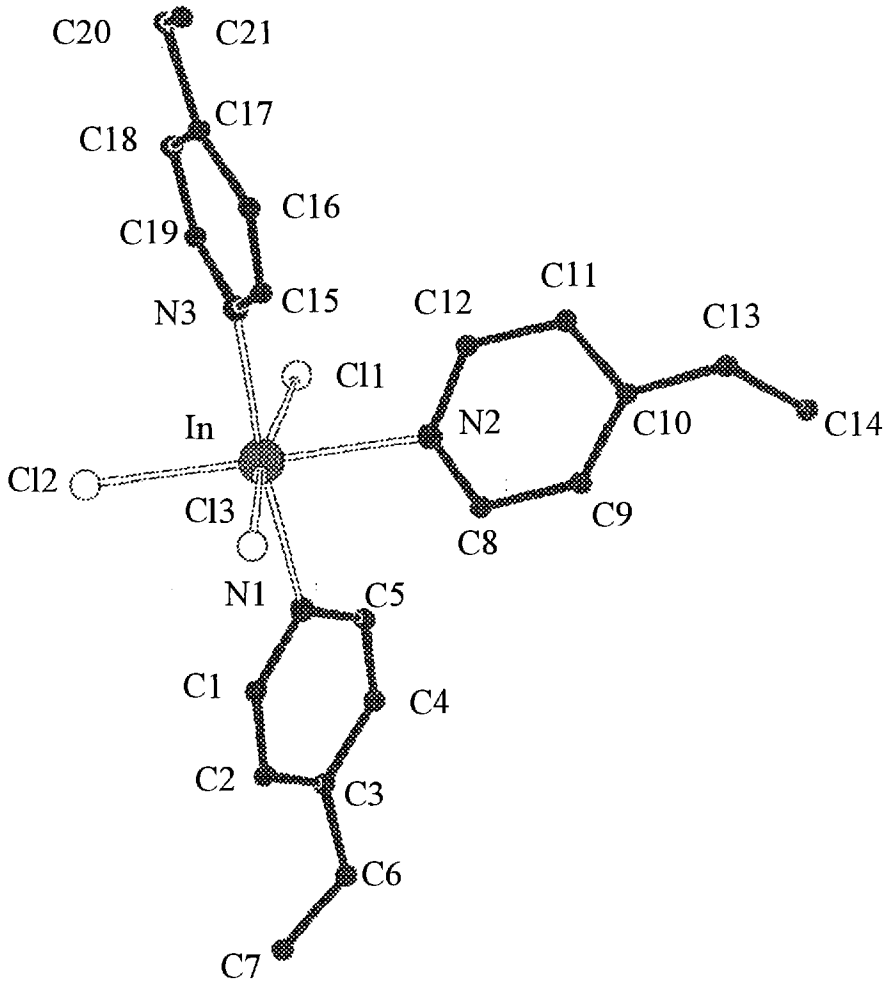


Figure A5: Crystal structure of mer[In(4-ethylpyridine)$_3$Cl$_3$].

A3.1 Crystal data and structure refinement for *mer*[In(4-ethylpyridine)$_3$Cl$_3$]

Empirical formula	$C_{21}H_{27}Cl_3InN_3$	
Formula weight	542.63	
Temperature	293(2) K	
Wavelength	0.71073 Å	
Crystal system	Triclinic	
Space group	P_1	
Unit cell dimensions	a = 9.733(1) Å	alpha = 74.98(1)°
	b = 20.826(2) Å	beta = 83.31(2)°
	c = 25.311(3) Å	gamma = 89.26(2)°
Volume, Z	4921.0(9) Å^3	
Absorption coefficient	1.297 mm^{-1}	
F (000)	2192	
Crystal size	0.38 x 0.35 x 0.425 mm	
θ range for data collection	1.01 to 25.05 °	
Limiting indices	$0 \leq h \leq 11$, $-24 \leq k \leq 24$, $-29 \leq l \leq 30$.	
Reflections collected	18468	
Refinement method	Full matrix least squares on F^2	
Data/ restraints/ parameters	17348/ 0/ 529	
Goodness of fit on F^2	1.177	

Final R indices [I>2σ(I)]	R1 = 0.1028, wR2 = 0.2326
R indices (all data)	R1 = 0.1860, wR2 = 0.2596
Largest differences between peak and hole	2.441 and -1.181 eÅ^{-3}

A3.2 Bond lengths for *mer*[In(4-ethylpyridine)$_3$Cl$_3$]/Å

In(1)-Cl(1)	2.474(2)	In(1)-Cl(2)	2.417(2)
In(1)-Cl(3)	2.461(2)	In(1)-N(1)	2.280(2)
In(1)-N(2)	2.346(3)	In(1)-N(3)	2.310(2)
N(1)-C(1)	1.325(3)	N(1)-C(5)	1.369(3)
N(2)-C(8)	1.355(2)	N(2)-C(12)	1.346(3)
N(3)-C(15)	1.348(4)	N(3)-C(19)	1.316(4)
C(1)-C(2)	1.322(4)	C(2)-C(3)	1.349(6)
C(3)-C(4)	1.394(4)	C(3)-C(6)	1.453(4)
C(4)-C(5)	1.355(5)	C(6)-C(7)	1.325(6)
C(8)-C(9)	1.441(4)	C(9)-C(10)	1.369(5)
C(10)-C(11)	1.428(4)	C(10)-C(13)	1.464(4)
C(11)-C(12)	1.446(5)	C(13)-C(14)	1.547(6)
C(15)-C(16)	1.324(6)	C(16)-C(17)	1.386(5)
C(17)-C(18)	1.509(7)	C(17)-C(20)	1.585(8)
C(18)-C(19)	1.397(4)	C(20)-C(21)	1.527(4)

A3.3 Bond angles for *mer*[In(4-ethylpyridine)$_3$Cl$_3$]/°

Cl(1)-In(1)-Cl(2)	94.5(4)	Cl(1)-In(1)-Cl(3)	172.0(4)
Cl(2)-In(1)-Cl(3)	93.4(5)	Cl(1)-In(1)-N(1)	90.5(4)
Cl(1)-In(1)-N(2)	86.4(3)	Cl(1)-In(1)-N(3)	88.4(5)
Cl(2)-In(1)-N(1)	92.1(6)	Cl(2)-In(1)-N(2)	178.3(6)
Cl(2)-In(1)-N(3)	93.0(8)	Cl(3)-In(1)-N(1)	88.3(4)
Cl(3)-In(1)-N(2)	85.6(5)	Cl(3)-In(1)-N(3)	91.9(6)
N(1)-In(1)-N(2)	89.2(6)	N(1)-In(1)-N(3)	174.7(5)
N(2)-In(1)-N(3)	85.6(5)	In(1)-N(1)-C(1)	121.7(6)
In(1)-N(1)-C(5)	123.9(5)	C(1)-N(1)-C(5)	113.7(2)
In(1)-N(2)-C(8)	119.9(3)	In(1)-N(2)-C(12)	116.5(4)
C(8)-N(2)-C(12)	123.0(4)	In(1)-N(3)-C(15)	120.0(4)
In(1)-N(3)-C(19)	119.4(8)	C(15)-N(3)-C(19)	120.5(4)
N(1)-C(1)-C(2)	124.3(5)	C(1)-C(2)-C(3)	121.3(4)
C(2)-C(3)-C(4)	118.5(5)	C(2)-C(3)-C(6)	124.7(5)
C(4)-C(3)-C(6)	116.5(6)	C(3)-C(4)-C(5)	115.6(4)
N(1)-C(5)-C(4)	126.1(4)	C(3)-C(6)-C(7)	120.6(3)
N(2)-C(8)-C(9)	117.7(6)	C(8)-C(9)-C(10)	123.9(4)
C(9)-C(10)-C(11)	115.0(4)	C(9)-C(10)-C(13)	124.7(5)
C(11)-C(10)-C(13)	119.8(3)	C(10)-C(11)-C(12)	121.2(4)
N(2)-C(12)-C(11)	118.7(4)	C(10)-C(13)-C(14)	109.5(5)

N(3)-C(15)-C(16)	123.2(6)	C(15)-C(16)-C(17)	121.6(2)
C(16)-C(17)-C(18)	114.8(6)	C(16)-C(17)-C(20)	135.1(6)
C(18)-C(17)-C(20)	109.8(7)	C(17)-C(18)-C(19)	117.7(3)
N(3)-C(19)-C(18)	121.4(5)	C(17)-C(20)-C(21)	106.6(5)

References

1. M. Faraday, *Phil. Trans. R. Soc. Lond.* **1857**, *147*, 145.

2. Wo. Ostwald, *Die welt der vernachlassigten dimensionen, Steinkopf,* Dresden. **1915**.

3. A. Henglein, Topp. *Curr. Chem.* **1988,** *143*, 173.

4. M. A. Reed, *Sci. Am.* **1993**, *268*, 98.

5. H. Weller, *Angew. Chem. Int. Ed. Engl.* **1993**, *32*, 41.

6. M. Spiro, *J. Chem. Soc.* **1960**, 3678.

7. M. Spiro, *J. Chem. Soc. Faraday. Trans. 1.* **1979**, 75.

8. A. Henglein, *Chem. Rev.* **1989**, *89*, 1861.

9. M. L. Steigerwald, L. E. Brus, *Acc. Chem. Res.* **1990**, *23*, 183.

10. H. Unchida, T. Matsunaga, H. Yoneyama, T. Sakata, H. Mori, T. Sasaki, *Chem. Mater.* **1993**, *5*, 716.

11. Y. Wang, N. Herron, W. Mahler, A. Suna, *J. Opt. Soc. Am. B.* **1989**, *6*, 808.

12. A. Henglein, *J. Phys. Chem.* **1979**, *83*, 2209.

13. C. K. Grätzel, M. Grätzel, *J. Am. Chem. Soc.* **1979**, *101*, 7741.

14. D. Meisel, *J. Am. Chem. Soc.* **1979**, *101*, 6133.

15. J. R. Darwent, G. Porter, *J. Chem. Soc., Chem., Comm.* **1981**, 145.

16. J. R. Darwent, *J. Chem. Soc. Faraday. Trans. 2.* **1981**, *77*, 1703.

17. H. M. Rosenberg, *The solid state,* 3rd Ed, Oxford University Press, **1988.**

18. P. A Cox, *The electronic structure and chemistry of solids,* 6th Ed, Oxford University Press, **1995**.

19. R. Hoffmann, *Solids and surfaces, a chemist's view of bonding in extended structures*, VCH Press, New York, **1988**.

20. D. R Lide, *CRC handbook of chemistry and physics*, CRC press, Boca Raton, **1996**, 77th ed. 12-98.

21. R. Turton, *The quantum dot*, **1995**, W. H. Freeman, Oxford.

22. N. Chestoy, T. D. Harris, R. Hull, L. E. Brus, *J. Phys. Chem.* **1986**, *90*, 3393.

23. L. E. Brus, *J. Phys Chem.* **1986,** *90*, 2555.

24. H. Weller, *Adv. Mater.* **1993**, *5*, 88.

25. J. H. Fendler, F. C. Meldrum, *Adv. Mater.* **1995**, *7*, 607.

26. L. E. Brus, *New J. Chem.* **1987**, *11*, 123.

27. L. E. Brus, *J. Phys. Chem.* **1983**, *79*, 5566.

28 H. Weller, H. M. Schmidt, U. Koch, A. Fojtik, S. Baral, A. Henglein, W. Kunath, K. Weiss, E. Dieman, *Chem. Phys. Lett.* **1986**, *124*, 557.

29. Y. Nosaka, *J. Phys. Chem.* **1991**, *95*, 5054.

30. Y. Wang, N. Herron, *J. Phys. Chem.* **1991**, *95*, 525.

31. P. E. Lippens, M. Lannoo, *Phys. Rev. B.* **1989**, *39*, 10935.

32. M. V. R. Krishna, R. A. Friesner, *J. Phys. Chem.* **1991**, *95*, 8309.

33. A. L. Efros, A. L. Efros, *Sov. Phys. Semicond. (Engl. Transl.).* **1982**, *16*, 772.

34. S. F. Bertram, *Handbook of X-rays,* (Ed. E. F. Kaelbe) McGraw-Hill, New York, **1967**.

35. C. B. Murray, D. J. Norris, M. G. Bawendi, *J. Am. Chem. Soc.* **1993**, *115*, 8706.

36. T. Vossmeyer, L. Katiskas, M. Giersig, I. G. Popovic, K. Driesner, A. Chemseddne, A. Eychmuller, H. Weller, *J. Phys. Chem.* **1994**, *98*, 7665.

37. L. Spanhel, M. Haase, H. Weller, A. Henglein, *J. Am. Chem. Soc.* **1987**, *109*, 5649.

38. K. Sookal, B. S. Cullum, S. Michel Angel, C. J. Murphy, *J. Phys. Chem.* **1996,** *100*, 4551.

39. H. Weller, U. Koch, M. Gutierrez, A. Henglein, *Ber. Bunsen-Ges. Phys. Chem.* **1987**, *91*, 88.

40. A. L. Efros, M. Rosen, M. Kuno, M. Nirmal, D. J. Norris, M. Bawendi, *Phys. Rev. B.* **1996**, *54*, 4843.

41. M. Nirmal, D. J. Norris, M. Kuno, M. G. Bawendi, A. L. Efros, M. Rosen, *Phys. Rev. Lett.* **1995**, *75*, 3728.

42. A. Henglein, P. Mulvaney, T. Linnert, *Faraday. Discuss.* **1991,** *92*, 31.

43. M. T. Reetz, W. Helbig, *J. Am. Chem. Soc.* **1994**, *116*, 7401.

44. M. Brust, J. Fink, D. Bethel, D. J. Schriffren, C. Kiely, *J. Chem. Soc., Chem. Comm.* **1995,** 1655.

45. J. Tanori, M. P. Pileni, *Adv. Mater.* **1995**, *7*, 862.

46. R. A. Andrievskii, *Russ. Chem. Rev.* **1994**, *63*, 411.

47. A. Kornowski, M. Giersig, M. Vogel, A. Chemseddine, H. Weller, *Adv. Mater.* **1993**, *5*, 634.

48. A. Fojtik, A. Henglein, *Chem. Phys. Lett.* **1994**, *221*, 363.

49. J. G. Brennan, T. Siegrist, P. J. Carrol, S. M. Stuczynski, L. E. Brus, M. L. Steigerwald, *J. Am. Chem. Soc.* **1989**, *111*, 4141.

50. T. Trindade, Ph.D. thesis, University of London, **1996**.

51. M. Kuno, J. K. Lee, B. O. Dabbousi, F. V. Mikulec, M. G. Bawendi, *J. Chem. Phys.* **1997**, *106*, 9869.

52. L. R. Becerra, C. B. Murray, R. G. Griffin, M. G. Bawendi, *J. Chem. Phys.* **1994**, *100*, 3297.

53. J. E. Bowen-Katari, V. L. Colvin, A. P. Alivisatos, *J. Phys. Chem.* **1994**, *98*, 4109.

54. C. B. Murray, C. R. Kagan, M. G. Bawendi, *Science.* **1995**, *270*, 1335.

55. B. O. Dabbousi, C. B. Murray, M. F. Rubner, M. G. Bawendi, *Chem. Mater.* **1994,** *6*, 216.

56. M. Danek, K. F. Jensen, C. B. Murray, M. G. Bawendi, *J. Cryst. Growth.* **1994,** *145*, 714.

57. N. C. Greenham, X. Peng, A. P. Alivisatos, *Synth. Metal.* **1997**, *84*, 545.

58. D. E. Fogg, L. H. Radzilowski, B. O. Dabbousi, R. R. Schrock, E. L. Thomas, M. G. Bawendi, *Macromolecules,* **1997**, *30*, 8433.

59. D. E. Fogg, L. H. Radzilowski, R. Blanski, R. R. Schrock, E. L. Thomas, *Macromolecules,* **1997,** *30*, 417.

60. M. A. Hines, P. Guyot-Sionnest, *J. Phys. Chem. B.* **1998**, *102*, 3655.

61. X. Peng, T. E. Wilson, A. P. Alivisatos, P. G. Schulz, *Angew. Chemie. Int. Ed. Engl.* **1997,** *36*, 145.

62. T. Trindade, P. O'Brien, X. Zhang, *Chem. Mater.* **1997**, *9*, 523.

63. T. Trindade, P. O'Brien, X. Zhang, M. Motevalli, *J. Mat. Chem.* **1997**, *7*, 1011.

64. P. O'Brien, A. C. Jones, *CVD of compound semiconductors.* VCH Press, FRG, **1997**.

65. A. A. Guzelian, J. E. B. Katari, U. Banin, A. V. Kadavanich, X. Peng, A. P. Alivisatos, K. Hamed, E. Juban, R. H. Wolters, C. C. Arnold, J. R. Heath, *J. Phys. Chem.* **1996**, *100*, 7212.

66. J. R. Heath, J. J. Shiang, *Chem. Soc. Rev.* **1998**, *27*, 65.

67. O. I. Micic, A. J. Nozik, *J. Lumin.* **1996**, *70*, 95.

68. O. I. Micic, J. R. Sprague, C. J. Curtis, K. M. Jones, J. L. Machol, A. J. Nozik, H. Giessen, B. Fluegel, G. Mohs, N. Peyghambarian, *J. Phys. Chem.* **1995,** *99*, 7754.

69. R. L. Wells, C. G. Pitt, A. T. McPhail, A. P. Purdy, S. Shafieezad, H. B. Hallock, *Chem. Mater.* **1989**, *1*, 4.

70. S. Mann, J. Webb, R. J. P. Williams, *Biomineralization*, VCH, Weinheim, **1989**.

71. A. A. Guzelian, U. Banin, A. V. Kadavanich, X. Peng, A. P. Alivisatos, *Appl. Phys. Lett.* **1996**, *69*, 1432.

72. X. Peng, M. C. Schlamp, A. V. Kadanavich, A. P. Alivisatos, *J. Am. Chem. Soc.* **1997**, *119*, 7019.

73. M. A. Hines, P. Guyot-Sionnest, *J. Phys. Chem.* **1996**, *100*, 468.

74. M. Danek, K. F. Jensen, C. B. Murray, M. G. Bawendi, *Chem. Mater.* **1996**, *8*, 173.

75. M. C. Schlamp, X. Peng, A. P. Alivisatos, *J. Appl. Phys.* **1997**, *82*, 5837.

76. T. Cassagneau, T. E. Mallouk, J. H. Fendler, *J. Am. Chem. Soc.* **1998**, *120*, 7848.

77. V. L. Colvin, M. C. Schlamp, A. P. Alivisatos, *Nature.* **1994**, *370*, 354.

78. D. L. Klein, R. Roth, A. K. L. Lim, A. P. Alivisatos, P. L. McEuen, *Nature.* **1997**, *389*, 699.

79. S. S. Kher, R. L. Well, *Chem. Mater.* **1994**, *6*, 2056.

80. R. L. Wells, M. F. Self, A. T. McPhail, S. R. Aubuchon, R. C. Woudenberg, J. P. Jasinski, *Organometallics.* **1993**, *12*, 2832.

81. J. F. Janik, R. L. Wells, V. G. Young, A. L. Rheingold, L. A. Guzei, *J. Am. Chem. Soc.* **1998**, *120*, 532.

82. M. A. Olshavsky, A. N. Goldstein, A. P. Alivisatos, *J. Am. Chem. Soc.* **1990**, *112*, 9438.

83. H. Uchida, C. J. Curtis, A. J. Nozik, *J. Phys. Chem.* **1991**, *95*, 5382.

84. H. Uchida, C. J. Curtis, P. V. Kamat, K. M. Jones, A. J. Nozik, *J. Phys. Chem.* **1992**, *62*, 1156.

85. S. C. Goel, M. Y. Chang, W. E. Buhro, *J. Am. Chem. Soc.* **1990**, *112*, 5636.

86. M. A. Matchett, A. M. Viano, N. L. Adolphi, R. D. Stoddard, W. E. Buhro, M. S. Conradi, P. C. Gibson, *Chem. Mater.* **1992**, *4*, 508.

87. S. Schulz, L. Martinez, J. L. Ross, *Adv. Mater. Opt. Electron.* **1996**, *6*, 185.

88. V. K. La Mer, R. H. Dinegar, *J. Am. Chem. Soc.* **1950**, *72*, 4847.

89. T. Johnson, V. K. La Mer, *J. Am. Chem. Soc.* **1947**, *69*, 1184.

90. R. J. Hunter, *Foundations of colloid science*, Vol. 1, 6th Ed., Oxford University Press, **1993**, p. 13 - 17.

91. A. Henglein, *Pure Appl. Phys.* **1984**, *56*, 1215.

92. R. Rossetti, J. L. Ellison, J. M. Gibson, L. Brus, *J. Chem. Phys.* **1984**, *80*, 4464.

93. R. Rossetti, R. Hull, J. M. Gibson, *J. Chem. Phys.* **1985**, *82*, 552.

94. H. Weller, A. Fojtik, A. Henglein, *Chem. Phys. Lett.* **1985**, *117*, 485.

95. M. Haase, H. Weller, A. Henglein, *Ber. Bunsenges. Phys. Chem.* **1988**, *92*, 1103.

96. Y. Wang, N. Herron, *J. Phys. Chem.* **1987**, *91*, 257.

97. H. J. Wazke, J. H. Fendler, *J. Phys. Chem.* **1987**, *91*, 854.

98. T. Abe, Y. Tachibana, T. Uematsu, M. Iwamoto, *J. Chem. Soc., Chem. Comm.* **1995**, 1617.

99. Y. Wang, A. Suna, W. Mahler, R. Kasowski, *J. Chem. Phys.* **1987**, *87*, 7315.

100. A. R. Kortan, R. Hull, R. L. Opila, M. G. Bawendi, M. L. Stiegerwald, P. J. Carrol, L. E. Brus, *J. Am. Chem. Soc.* **1990**, *112*, 1327.

101. M. L. Steigerwald, A. P. Alivisatos, J. M. Gibson, T. D. Harris, R. Kortan, A. J. Muller, A. M. Thayer, T. M. Duncan, D. C. Douglas, L. E. Brus, *J. Am. Chem. Soc.* **1988**, *110*, 3046.

102. J. E. McDougall, H. Eckert, G. D. Stucky, N. Herron, Y. Wang, K. Moller, T. Bein, D. Cox, *J. Am. Chem. Soc.* **1989**, *111*, 8006.

103. S. W. Haggata, X. Li, D. J. Cole-Hamilton, J. R. Fryer, *J. Mater. Chem.* **1996**, *6*, 1771.

104. S. W. Haggata, D. J. Cole-Hamilton, J. R. Fryer, *J. Mater. Chem.* **1997**, *7*, 1969.

105. X. Li, J. R. Fryer, D. J. Cole-Hamilton, *J. Chem. Soc., Chem. Comm.* **1994,** 1715.

106. A. Hasselbarth, A. Eychmuller, R. Eichberger, M. Giersi, A. Mews, H. Weller, *J. Phys. Chem.* **1993**, *97*, 5333.

107. A. Mews, A. Eychmuller, M. Giersig, D. Schoos, H. Weller, *J. Phys. Chem.* **1994,** *98*, 934.

108. D. Schoos, A. Mews, A. Eychmuller, H. Weller, *Phys. Rev. B.* **1994**, *49*, 17072.

109. H. S. Zhou, I. Honma, H. Komiyama, J. W. Haus, *J. Phys. Chem.* **1993**, *97*, 895.

110. A. Eychmuller, A. Hasselbarth, H. Weller, *J. Lumin.* **1992**, *53*, 113.

111. B. O. Daboussi, J. Rodriguez, F. V. Mikulec, J.R. Heine, H. Matoussi, R. Ober, K. F. Jensen, M. G. Bawendi, *J. Phys. Chem. B.* **1997,** *101*, 9463.

112. C. F. Hoener, K. A. Allan, A. J. Bard, A. Campion, M. Fox, T. E. Mallouk, S. E. Webber, J. M. White, *J. Phys. Chem.* **1992**, *96*, 3812.

113. D. Hommel, K. Leonardi, H. Heinke, H Selke, K. Ohkawa, F. Gindele, U. Woggon, *Phys. Stat. Solidi. B.* **1997**, *202*, 835.

114. Y. Tian, T. Newton, N. A. Kotov, D. M. Guldi, J. Fendler, *J. Phys. Chem.* **1996**, *100*, 8927.

115. A. Eychmuller, A. Mews, H. Weller, *Chem. Phys. Lett.* **1993**, *208*, 59.

116. A. Mews, U. Banin, A. V. Kadanavich, A. P. Alivisatos, *Ber. Bunsenges. Phys. Chem.* **1997**, *101*, 1621.

117. X. Peng, R. Lu, Y. Y. Zhao, L. Qu, H. Chen, T. Li, *J. Phys. Chem.* **1994**, *98*, 13323.

118. H. Weller, *Angew. Chem. Int. Ed. Engl.* **1996**, *35*, 1079.

119. O. V. Salata, P. J. Dobson, P. J. Hull, J. L. Hutchinson, *Thin Solid Films.* **1994**, *251*, 1.

120. O. V. Salata, P. J. Dobson, P. J. Hull, J. L. Hutchinson, *Appl. Phys. Lett.* **1994**, *65*, 189.

121. M. Gao, M. Gao, X. Zhang, Y. Yang, B. Yang, J. Shen, *J. Chem. Soc., Chem. Comm.* **1994**, 2777.

122. D. Bethell, D. J. Schriffren, *Nature.* **1996**, *382*, 581.

123. C. A. Mirkin, R. L. Letsinger, R. C. Mucic, J. J. Storhoff, *Nature.* **1996**, *382*, 607.

124. A. P. Alivisatos, K. P. Johnsson, X. G. Peng, T. E. Wilson, C. J. Loweth M. P. Bruchez, P. G. Schulz, *Nature*. **1996**, *382*, 609.

125. B. O. Dabbousi, M. G. Bawendi, O. Onitsuka, M. F. Rubner, *Appl. Phys. Lett.* **1995**, *66*, 1316.

126. M. Gao, B. Richter, S. Kirtein, *Adv. Mater.* **1997**, *9*, 802.

127. F. Hakini, M. G. Bawendi, R. Tumminelli, J. R. Haavlsto, US Patent no. 5,260,957.

128. M. Grätzel, *Renew. Energy*. **1994**, *5*, 118.

129. B. Oregan, M. Grätzel, *Nature*. **1991**, *353*, 737.

130. M. Grätzel, K. Kalyanasundaram, *Current Science*. **1994**, *10*, 706.

131. J. E. Moser, P. Bonhote, L. Walder, M. Grätzel, *Chimica*. **1997**, *51*, 28.

132. D. L. Feldheim, C. D. Keating, *Chem. Soc. Rev*. **1998,** *27*, 1.

133. H. M. Manasevit, *Appl. Phys. Lett*. **1968**, *12*, 156.

134. P. O'Brien, R. Nomura, *J. Mater. Chem*. **1995**, *5*, 1761.

135. O. F. Z. Khan, P. O'Brien, P. A. Hamilton, J. R. Walsh, A. C. Jones, *Chemtronics* **1989**, *4*, 224.

136. M. Nyman, M. J. Hampden-Smith, E. N. Duesler, *Chem. Vap. Deposition*. **1996**, *2*, 171.

137. M. Chunggaze, M. A. Malik, P. O'Brien, *Adv. Mater. Opt. Electron*. **1997**, *7*, 311.

138. J. I. Pankove, *Optical processes in semiconductors*, Dover publications, New York, **1970.**

139. D. R Lide, *CRC handbook of chemistry and physics*, CRC press, 73rd student ed. Boca Raton, **1993**, 12-86.

140. M. G. Bawendi, A. R. Kortan, M. L. Steigerwald, L. E. Brus, *J. Chem. Phys*. **1989**, *91*, 7282.

141. M. R. Lazell, P. O'Brien, Unpublished results.

142. R. A. Zingaro, J. C. White, *J. Inorg. Nucl. Chem*. **1960**. *12*, 315.

143. M. Kolosky, J. Vialle, T. Cotel, *J. Chromatography*. **1984**, *299*, 436.

144. D. P. Riley, J. D. Oliver, *Inorg. Chem.* **1986,** *25*, 1814.

145. V. Yu. Kukushkin, V. K. Bel'skii, V. E. Konovalov, R. R. Shifrina, A. I. Moiseev, R. A. Vasova, *Inorg. Chem. Chimica. Acta.* **1991**, *183*, 57.

146. B. B. Wayland, R. F. Schramm, *Inorg. Chem.* **1969**, *8*, 971.

147. C. G. Fuentes, S. J. Patel, *J. Inorg. Nucl. Chem.* **1970**, *32*, 1575.

148. K. Nakamoto, *Infra-red and raman spectra of inorganic and co-ordination compounds*, 5th Ed, Part B, pg. 102, J. Wiley and Sons. New York, **1997**.

149. F. A. Cotton, R. Francis, W. D. Horrocks, *J. Phys. Chem.* **1960**, *64*, 1534.

150. W. Zdanowicz, L. Zdanowicz, *Ann. Rev. Mat. Sci.* **1975**, *5*, 301.

151. S. I. Radautsan, E. K. Arushanov, A. N. Nateprov, G. P. Chuiko, *Cadmium arsenide and cadmium phosphide*, Shtiintsa, Kishinev, **1976**.

152. V. B. Larzarev, V. Ya. Schevchenka, Ya. H. Greenberg, V. V. Sobolein, *II-V Semiconducting Compounds*, Nauska, Moscow, **1978**.

153. E. K. Arushanov, *Prog. Crystal. Growth. Charact.* **1981**, *3*, 211.

154. M. Bushan, A. Catalano, *Appl. Phys. Lett.* **1981**, *38*, 39.

155. J. M. Pawlikowski, *Infra-Red. Phys.* **1988**, *28*, 177.

156. E. K. Arushanov, *Prog. Crystal. Growth. Charact.* **1992**, *25*, 131.

157. M. J. Ludowiski, *J. Appl. Phys.* **1985**, *58*, R31.

158. W. E. Buhro, *Polyhedron*, **1994**, *13*, 1131.

159. G. Fritz, *Comments Inorg. Chem.* **1982**, *1*, 329.

160. O. Madelung, *Data in science and technology: semiconductors other than group IV elements and III-V compounds,* Springer Verlag.

161. W. E. Buhro, *Private communication.*

162. A. Kornowski, R. Eichberger, M. Giersig, H. Weller, E. Eychmuller, *J. Phys. Chem.* **1996**, *100*, 12467.

163. H. Weller, A. Fojtik, A. Henglein, *Chem. Phys. Lett.* **1985**, *117*, 485.

164. J. Misiewicz, L. Byra, K. Jezierski, J. Szatkowski, N. Mirowska, Z. Gurnienny, E. Placeczek-Poloko, *Microelectronics Journal.* **1994**, *25*, 23.

165. C. W. F. T. Pistorius, J. B. Clark, J. Coertzer, G. J. Kruger, O. A. Kuuze, *High Temp-High Press.* **1977**, *9*, 471.

166. J, Misiewicz, J. Andrezejewski, *Phys. Stat. Sol.* **1994**, *184*, K7.

167. A. H. Cowley, R. A. Jones, *Angew. Chem. Int. Ed. Engl.* **1989**, *28*, 1208.

168. K. Issleib, H. O. Froelich, *Chem. Ber.* **1962**, *95*, 375.

169. B. L. Benac, A. H. Cowley, R. A. Jones, C. M. Nunn, T. C. Wright, *J. Am. Chem. Soc.* **1989**, *111*, 4986.

170. O. T. Beachley, J. D. Maloney, *Organometallics.* **1997**, *16*, 4016.

171. A. J. Edwards, M. A. Power, P. R. Raithby, C. A. Russel, D. S. Wright, *Organometallics.* **1993**, *12*, 4687.

172. M. G. Davidson, A. J. Edwards, M. A. Power, P.R. Raithby, C.A Russel, A. Steiner, K. L. Verhorevoort, D. S Wright, *J. Chem. Soc., Chem. Comm.* **1995**, 1989.

173. Y. Yokoyama, K. Takahashi, *Bull. Chem. Soc. Jpn.* **1987**, *60*, 3485.

174. M. Chunggaze, J. McAleese, P. O'Brien, D. J. Otway, *J. Chem. Soc., Chem Comm.* **1998**, 833.

175. M. Chunggaze, M. A. Malik, P. O'Brien, *Adv. Mater*, submitted.

176. P. O'Brien, M. A. Malik, M. Chunggaze, T. Trindade, J. R. Walsh, A. C. Jones, *J. Cryst. Growth.* **1996**, *170*, 23.

177. M. Baudler, A. Zarkadas, *Chem. Ber.* **1972**, *105*, 3844.

178. A. F. Wells, *Structural inorganic chemistry*, 3rd ed. Oxford, London, **1962**.

179. X- ray powder diffraction file, ASTM special technical publication, 48-j, 2-1181.

180. M. J. Gelten, *Lect. Notes Phys.* **1982**, 152, 167.

181. M. Goldstein, E. F. Mooney, A. Anderson, H. A. Gebbie, *Spectrochimica. Acta.* **1965**, *21*, 105.

182. J. R. Agger, M. W. Anderson, M. E. Pemble, O. Terasaki, Y. Nozue, *J. Phys. Chem. B.* **1998**, *102*, 3345.

183. N. F. Ramsey, *Phys. Rev.* **1950**, *78*, 699.

184. A. M. Thayer, M. L. Steigerwald, T. M. Duncan, D. C. Douglass, *Phys. Rev. Lett.* **1988**, *60*, 2673.

185. P. J. Hore, *Nuclear magnetic resonance,* Oxford Chemistry primers, OUP, Oxford, **1995,** pp. 14.

186. S. M. Holl, T. Kowalewski, J. Schaefer, *Sol. State. Nucl. Mag. Res.* **1996**, *6*, 39.

187. N. L. Adolphi, R. D. Stoddard, S. C. Goel, W. E. Buhro, P. C. Gibbins, M. S. Conradi, *J. Phys. Chem. Solids.* **1992**, *53*, 1275.

188. J. R. Sackleben, E. W. Wooten, L. Emsley, A. Pines, V. L. Colvin, A. P. Alivisatos, *Chem. Phys. Lett.* **1992**, *198*, 431.

189. A. M. Arif, A. H. Cowley, R. A. Jones, S. U. Koschmieder, *J. Chem. Soc., Chem. Comm.* **1987**, 1319.

190. J. Komeno, *J. Cryst. Growth.* **1994**, *145*, 468.

191. S. H. Li, N. I. Buchan, C. A. Larsen, G. B. Stringfellow, *J. Cryst. Growth.* **1989**, *96*, 906.

192. H. H. Abdul-Ridha, J. E. Bateman, G. H. Fan, M. E. Pemble, I. M. Povey, *J. Electrochem. Soc.* **1994**, *141*, 1886.

193. X- ray powder diffraction file, ASTM special technical publication, 4-831.

194. X- ray powder diffraction file, ASTM special technical publication, 21-1486

195. X- ray powder diffraction file, ASTM special technical publication, 47-1441.

196. F. A. Cotton, R. D. Barnes, E. Bannister, *J. Chem. Soc.* **1960**, 2199.

197. A. Katz, *Indium phosphide and related material: processing, technology and devices*, **1992.**

198. A. Bar-Lev, *Semiconductors and electronic devices*, 2nd ed., Prentice Hall, New York, **1984**.

199. S. P. Benbaars, *Proceedings of the IEEE.* **1997**, *85*, 1740.

200. S. N. Mohammed, A. A. Salvador, H. Morkoc, *Proceedings of the IEEE.* **1995**, *83*, 1306.

201. H. Landolt, *Numerical data and functional relationships in science and technology*, Landolt-Bernstein, Vol. 17 a + d, 1984, Springer, Berlin.

202. A. M. Arif, B. L. Benac, A. H. Cowley, R. A. Jones, K. B. Kidd, C. M. Nunn, *New J. Chem.* **1988**, *12*, 553.

203. C. R. Abernathy, P. W. Wisk, S. J. Pearton, F. Ren, D. A. Bohling, G. T. Muhr, *J. Crystal Growth.* **1992**, *124*, 64.

204. S. E. Jeffs, R. W. H. Small, I. J. Worrall, *Acta. Cryst. C.* **1984**, *40*, 1329.

205. R. W. H. Small, I. J. Worrall, *Acta. Cryst. B.* **1982**, *38*, 932.

206. A. J. Carty, D. G. Tuck, *Prog. Inorg. Chem.* **1975**, *19*, 243.

207. S. Salim, J. P. Lu, K. F. Jensen, D. A. Bohling, *J. Crystal Growth.* **1992,** *124*, 16.

208. X. Peng, J. Wickham, A. P. Alivisatos, *J. Am. Chem. Soc.* **1998**, *120*, 5343.

209. O. I. Micic, K. M. Jones, A. Cahill, A. J. Nozik, *J. Phys. Chem. B.* **1998**, *102*. 9791.

210. O. I. Micic, H. M. Cheong, H. Fu, A. Zunger, J. R. Sprague, A. Mascarenhas, A. J. Nozik, *J. Phys. Chem. B.* **1997,** *101,* 4904.

211. S. N. Maganov, M-H. Whangbo, *Adv. Mater.* **1994**, *6*, 355.

212. H. Noglik, W. J. Pietro, *Chem. Mater.* **1994**, *6*, 1593.

213. N. Felidj, G. Levi, J. Pantigny, J. Aubard, *New J. Chem.* **1998**, *22*, 725.

214. T. M. Duncan, R. F. Karlicek, W. A. Bonner, F. A. Thiel, *J. Phys. Chem. Solids.* **1984,** *45*, 389.

215. N. L. Adolphi, M. S. Conradi, W. E. Buhro, *J. Phys. Chem. Solids.* **1992**, *53*, 1073.

216. X- ray powder diffraction file, ASTM special technical publication, 12-191.

217. X- ray powder diffraction file, ASTM special technical publication, 5-601.

218. D. F. Shriver, M. A. Drezden, *The manipulation of air sensitive compounds*, 2nd ed., Wiley-Interscience, New York, **1986.**

219. M. B. Hursthouse, M. A. Mailk, M. Motevalli, P.O'Brien, *Polyhedron.* **1992**, *11*, 45.

220. M. Bonamico, G. Mazzone, A. Viciago, L. Zambonelli, *Acta. Cryst.* **1965**, *19*, 898.

221. J. R. Walsh, Ph.D. Thesis, University of London, **1990.**

222. S. W. Haggata, Ph.D. Thesis, University of London, **1995**.

223. G. M. Sheldrick, *SHELXTL v. 5.03, a program for crystal structure refinement*, University of Gottingen, FRG, **1993**.